

UNCLASSIFIED

AD NUMBER
AD342723
CLASSIFICATION CHANGES
TO: unclassified
FROM: secret
LIMITATION CHANGES
TO: Approved for public release, distribution unlimited
FROM: Controlling DoD Organization: Defense Atomic Support Agency, Washington, DC.
AUTHORITY
DASA ltr dtd 2 May 1966; DASA ltr dtd 2 May 1966

THIS PAGE IS UNCLASSIFIED

SECRET

AD 342723

DEFENSE DOCUMENTATION CENTER

FOR

SCIENTIFIC AND TECHNICAL INFORMATION

CAMERON STATION, ALEXANDRIA, VIRGINIA



SECRET

NOTICE: When government or other drawings, specifications or other data are used for any purpose other than in connection with a definitely related government procurement operation, the U. S. Government thereby incurs no responsibility, nor any obligation whatsoever; and the fact that the Government may have formulated, furnished, or in any way supplied the said drawings, specifications, or other data is not to be regarded by implication or otherwise as in any manner licensing the holder or any other person or corporation, or conveying any rights or permission to manufacture, use or sell any patented invention that may in any way be related thereto.

NOTICE:

THIS DOCUMENT CONTAINS INFORMATION
AFFECTING THE NATIONAL DEFENSE OF
THE UNITED STATES WITHIN THE MEAN-
ING OF THE ESPIONAGE LAWS, TITLE 18,
U.S.C., SECTIONS 793 and 794. THE
TRANSMISSION OR THE REVELATION OF
ITS CONTENTS IN ANY MANNER TO AN
UNAUTHORIZED PERSON IS PROHIBITED
BY LAW.

CATALOGED BY DDC 342 723
AS AD No.

SECRET

This document consists of 151 pages
Not 134 125 copies.

DASA-1362

DOWNGRADED AT 12 YEAR INTER-
VALS; NOT AUTOMATICALLY
DECLASSIFIED. DOD DIR 5200.10

**DEBRIS HAZARDS,
A FUNDAMENTAL STUDY**

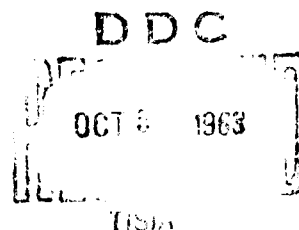
Final Report

by

Edward B. Ahlers

SECRET

THIS MATERIAL CONTAINS INFORMATION AFFECTING THE
NATIONAL DEFENSE OF THE UNITED STATES WITHIN THE
MEANING OF THE ESPIONAGE LAWS, TITLE 18, U.S.C.,
SECS. 793 AND 794, THE TRANSMISSION OR REVELATION
OF WHICH IN ANY MANNER TO AN UNAUTHORIZED PERSON
IS PROHIBITED BY LAW.



SECRET

IIT RESEARCH INSTITUTE
Technology Center
Chicago 16, Illinois

DASA-1362

DEBRIS HAZARDS, A FUNDAMENTAL STUDY

by
Edward B. Ahlers

for
Defense Atomic Support Agency
Washington 25, D. C.

Contract No. DA-49-146-XZ-097
IITRI Project No. 8231

000000
11-11-61
A

Reproduction of this document in whole or in part is permitted for any
purpose of the United States Government.

Qualified requestors may obtain copies for this report from DDC.

SECRET

SECRET

FOREWORD

This is the Final Report on IIT Research Institute Project K231, "Fundamental Study of Debris Hazards," conducted for the Defense Atomic Support Agency, Washington, D. C., under Contract DA-49-146-XZ-097. All work done under the initial contract on the basic study of debris hazards which provided for supplemental research to analyze data and develop expressions to facilitate the formulation of debris damage predictive schemes for several specific situations done under Modification No. 1, are reported.

Work performed on "DANNY BOY TASK II - Debris Investigations," under Contract Modification No. 2, was described in the preliminary and final test reports, "Throwout Study of an Underground Nuclear Detonation," published by the Department of Defense - U. S. AEC as POR01814 (ITR-1814) and POR-1814 (WT-1814).

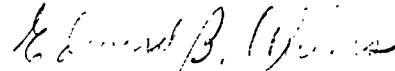
Work done on "DANNY BOY TASK I - Pre-Shot Predictions," also under Contract Modification No. 2, was reported as a separate report entitled, "Hydrodynamic Analysis for a Buried Underground Nuclear Explosion." Work performed on "DANNY BOY TASK III - Post-Test Crater Analysis," under Contract Modification No. 3 will also be submitted as a separate report.

The cooperation and assistance of the Armed Services Explosives Safety Board, (especially Mr. Russel G. Perkins, Chief of Explosives Branch) in allowing project engineers use of their explosions files is greatly appreciated.

IITRI personnel contributing to these studies include E. B. Ahlers, D. I. Feinstein, B. Gain, P. C. Hermann, J. Lukes and Dr. K. E. McKee. Mr. C. A. Miller conducted the analysis of horizontal motion of debris particles under the influence of the blast winds. Mr. R. L. Barnett developed the analysis of the motion of tree debris.

Respectfully submitted,

IIT RESEARCH INSTITUTE



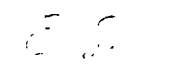
Edward B. Ahlers
Project Engineer

REVIEWED BY:



C. A. Miller, Manager
Structures Research

APPROVED:



E. Sevin, Associate Director
Solid Mechanics Research Division

IIT RESEARCH INSTITUTE

SECRET

SECRET

ABSTRACT

Predicting the mechanical debris, associated with nuclear detonation, stemming from several sources (blast-induced flight of structural fragments, pickup of material from the ground by blast winds, and crater throwout) is a significant problem. Designers of hardened sites are concerned with materials which may accumulate atop silo doors or damage vulnerable above-grade antenna systems. Military operations are concerned with the hazards to troops and equipment from the use of nuclear demolition and tactical devices. Potential users of nuclear excavating devices are concerned with hazards to personnel, utilities and equipment.

This report describes the collection and analysis of data on various aspects of debris formation and dispersion, and examples of data utilization in estimating debris environment in several situations. The approach in the study was to collect extensive data from past experimental and analytical investigations bearing on debris formation and dispersion. By further study the most meaningful formats were summarized to be used as inputs to approximate solutions for debris environment predictions.

An extensive regression study of several hundred HE incidents, accidental and experimental, is made to relate the maximum range of debris to explosion parameters and crater dimensions. Results showing consistency with the limited available nuclear data relating to crater throwout are also presented to describe the nature of the debris distribution function in general terms.

Fragmentation data from HE events and laboratory experiments are used to indicate the nature of fragment-size distributions from structural demolition.

An analytical study of the motion of debris fragments caused by blast winds considers debris trajectories for various times of structural failure, fragment sizes, positive and negative phase winds, and initial elevations of the fragment.

Specific estimates are made of the debris hazards to troops of flying tree limbs in the proximity of forest stands, the vulnerability of troop personnel to throwout debris from cratering and stream-bed charges, and the debris environment about hardened antenna systems.

Useful estimates of debris environment can be made for many targeting situations with data contained in this report. Refinement of data is certainly essential, especially in experimental definition of fragmentation patterns of ideal structural elements, and in definition of crater lip contours near their extremities, i. e., the throwout debris within and beyond the extremities of the lip.

IIT RESEARCH INSTITUTE

SECRET

SECRET

TABLE OF CONTENTS

<u>Chapter</u>		<u>Page</u>
ONE	INTRODUCTION.	1
1.1	Report Organization	3
1.2	Summary and Conclusions	15
1.3	Recommendations	17
TWO	DEBRIS CHARACTERISTICS OF HIGH EXPLOSIVE AND NUCLEAR DETONATIONS.	18
2.1	Application of HE Data from Planned and Accidental Explosions	19
2.2	Measures of Maximum Debris Distance	21
	2.2.1 Details of Regression Analysis	21
	2.2.2 Regression Study of Maximum Debris Distance	26
	2.2.3 Correlation of Maximum Debris Distance with Crater Dimension	55
2.3	Debris Dispersion Patterns.	55
	2.3.1 Theoretical Models	55
	2.3.2 Debris Dispersion Patterns of HE Explosions	79
THREE	FRAGMENTATION, EXPERIMENTAL OBSERVATIONS	113
3.1	Fragmentation of Coal	114
3.2	Fragmentation of Explosively Detonated Stone Blocks	115
3.3	Fragmentation of Concrete Shielding of Reactor Models	115
3.4	Fragmentation of a Reinforced Concrete Ordnance Structure	129
3.5	Fragmentation of Concrete Walls	131
FOUR	FRAGMENTATION, ANALYTICAL CONSIDERATIONS.	138
4.1	State of Knowledge of Fracture Mechanics	138
4.2	Mathematical Model	140
4.3	Example	144
FIVE	DEBRIS TRANSPORT BY BLAST WINDS.	150
5.1	General Treatment of Problem	150
5.2	Numerical Results.	158
	5.2.1 Zero Initial Conditions Excluding a Negative Phase	158
	5.2.2 Zero Initial Conditions Including a Negative Phase	160
	5.2.3 Effect of Initial Conditions	166
SIX	VULNERABILITY OF FIELD TROOPS TO TREE DEBRIS	170
6.1	Previous Studies	170
6.2	Problem Approach	171
6.3	Results.	180

SECRET

SECRET

TABLE OF CONTENTS (Con't.)

<u>Chapter</u>		<u>Page</u>
SEVEN	VULNERABILITY OF FIELD TROOPS TO THROWOUT DEBRIS FROM CRATERING AND STREAM-BED CHARGES	181
7.1	Method of Solution.	182
7.2	Fragment and Size Distribution Method	183
	7.2.1 Nomographic Calculation of Safe Distances Based on Size Distribution.	192
	7.2.2 Explosive Equivalence	203
	7.2.3 Comparison with DANNY BOY Results	204
7.3	Throwout Debris from Stream-Bed Charges	206
	REFERENCES	212
<u>Appendix</u>		
A	MAXIMUM DEBRIS DISTANCE AND EXPLOSION PARAMETERS FOR SELECTED EXPLOSIONS	A-1
B	COMPUTER PROGRAM FOR REGRESSION STUDY OF HE DETONATIONS	B-1
C	MAXIMUM DEBRIS DISTANCE AND CRATER DIMENSIONS FOR SELECTED EXPLOSIONS	C-1
D	FRAGMENT-SIZE DISTRIBUTION AND DISPERSION OF FRAGMENTS FROM PANTEX ORDNANCE PLANT EVENT	D-1
E	FRAGMENTATION DATA ON EXPLODED DRY SANDSTONE BLOCKS	E-1
F	CONCRETE FRAGMENT WEIGHTS AND DIMENSIONS FOR 1/24-SCALE SHIELDED REACTOR MODELS	F-1
G	CONCRETE FRAGMENT WEIGHTS AND DIMENSIONS FOR 1/12-SCALE SHIELDED REACTOR MODELS	G-1
H	TRAJECTORY OF AN AIR PARTICLE DURING THE POSITIVE PHASE OF A NUCLEAR BLAST	H-1
J	THE VULNERABILITY OF ANTENNA SYSTEMS	J-1
J-1	Estimates Based on High-Explosive Debris Data	J-4
J-2	Estimates Based on Nuclear Test Results	J-7
J-3	Estimates Based on Analytical Studies.	J-12
	J-3.1 Application of RAND Crater Model	J-13
	J-3.2 Trajectory Analysis	J-19
	J-3.3 Numerical Results	J-22
J-4	General Consistency of Results	J-25

SECRET

SECRET

LIST OF ILLUSTRATIONS

<u>Figure</u>		<u>Page</u>
1.1	Quadratic Regression Line: Maximum Debris Distance versus Equivalent Yield.	5
1.2	Linear Regression Line: $W^{1/3}$ -Scaled Maximum Debris Distance vs $W^{1/3}$ -Scaled Crater Volume	6
1.3	Comparison of Theoretical and Actual Fragment Dispersion Pattern.	7
1.4	Fragment-Size Distribution at Various Ground Ranges for a Reinforced Concrete Structure	8
1.5	Cumulative Fragment-Size Distribution for a Reinforced Concrete Ordnance Structure	10
1.6	Cumulative Distribution of Total Fragment Weight for a Reinforced Concrete Ordnance Structure	11
2.1	Graphical Representation of Least-Squares Linear Regressive Line	23
2.2	Normal Distribution of Events About Least-Squares Regression Line	25
2.3	Linear Regression Line: Maximum Debris Distance vs Equivalent Yield.	39
2.4	Quadratic Regression Line: Maximum Debris Distance vs Equivalent Yield.	41
2.5	Linear Regression Line: $W^{1/3}$ -Scaled Maximum Debris Distance vs Equivalent Yield	43
2.6	Quadratic Regression Line: $W^{1/3}$ -Scaled Maximum Debris Distance vs Equivalent Yield	45
2.7	Linear Regression Line: Maximum Debris Distance vs Impulse.	47
2.8	Quadratic Regression Line: Maximum Debris Distance vs Impulse.	48
2.9	Linear Regression Line: $W^{1/3}$ -Scaled Maximum Debris Distance vs $W^{1/3}$ -Scaled Impulse	49
2.10	Quadratic Regression Line: $W^{1/3}$ -Scaled Maximum Debris Distance vs $W^{1/3}$ -Scaled Impulse	50

SECRET

SECRET

LIST OF ILLUSTRATIONS (Con't.)

<u>Figure</u>	<u>Page</u>
2.11 Linear Regression Line: Maximum Debris Distance vs Crater Volume.	53
2.12 Quadratic Regression Line: Maximum Debris Distance vs Crater Volume.	56
2.13 Linear Regression Line: Maximum Debris Distance vs Crater Diameter.	57
2.14 Quadratic Regression Line: Maximum Debris Distance vs Crater Diameter.	58
2.15 Linear Regression Line: Maximum Debris Distance vs Crater Depth	59
2.16 Quadratic Regression Line: Maximum Debris Distance vs Crater Depth	60
2.17 Linear Regression Line: $W^{1/3}$ -Scaled Maximum Debris Distance vs $W^{1/3}$ -Scaled Crater Volume	63
2.18 Quadratic Regression Line: $W^{1/3}$ -Scaled Maximum Debris Distance vs $W^{1/3}$ -Scaled Crater Volume	64
2.19 Linear Regression Line: $W^{1/3}$ -Scaled Maximum Debris Distance vs $W^{1/3}$ -Scaled Crater Diameter.	65
2.20 Quadratic Regression Line: $W^{1/3}$ -Scaled Maximum Debris Distance vs $W^{1/3}$ -Scaled Crater Diameter.	66
2.21 Linear Regression Line: $W^{1/3}$ -Scaled Maximum Debris Distance vs $W^{1/3}$ -Scaled Crater Depth	67
2.22 Quadratic Regression Line: $W^{1/3}$ -Scaled Maximum Debris Distance vs $W^{1/3}$ -Scaled Crater Depth	68
2.23 Wall Panel Under Explosive Impulse from Line-Source Charge	69
2.24 Roof Panel Fragmented by Line-Source Charge	70
2.25 Structural Arch Subject to Impulse Load from Line-Source Charge	71
2.26 Trajectory of Individual Fragment	71
2.27 Theoretical Fragment Distribution Functions	73

SECRET

SECRET

LIST OF ILLUSTRATIONS (Con't.)

<u>Figure</u>		<u>Page</u>
2.28	Typical Structure Subjected to Fragmentation by Internal Detonation.	75
2.29	Comparison of Theoretical and Actual Fragment Dispersion Patterns	77
2.30	Debris Dispersion Patterns for Selected Explosions	81
2.31	First-Order Logarithmic Curves of Debris Dispersion for Selected Explosions	83
2.32	Second-Order Logarithmic Curves of Debris Dispersion for Selected Explosions	84
2.33	Modified Second-Order Logarithmic Curves of Debris Dispersion for Selected Explosions.	85
2.34	Parabolic Curves of Debris Dispersion for Selected Explosions	87
2.35	Logarithmic Parabolas of Debris Dispersion for Selected Explosions	88
2.36	Second-Order Semi-Logarithmic Curves of Debris Dispersion for Selected Explosions.	89
2.37	Debris Dispersion and Standard Error for 1945 Badger Ordnance Works Explosion	91
2.38	Pre-shot View of Pantex Ordnance Plant Test Structure from Southeast.	92
2.39	Pre-shot View of Pantex Ordnance Plant Test Structure from Northwest	93
2.40	Post-shot View of Pantex Ordnance Plant Test Structure	94
2.41	Area of Fragment Distribution from Pantex Ordnance Plant Test Structure.	95
2.42	Debris Dispersion for Reinforced Concrete Structure Logarithmic Plot with Second-Order Regression Line	98
2.43	Debris Dispersion for Reinforced Concrete Structure Semi-log Plot with First-Order Regression Line	99

SECRET

SECRET

LIST OF ILLUSTRATIONS (Con't.)

<u>Figure</u>		<u>Page</u>
2.44	Debris Dispersion for Reinforced Concrete Structure Semi-log Plot with Second-Order Regression Line	100
2.45	Areal Dispersion for Reinforced Concrete Structure Logarithmic Plot with Second-Order Regression Line . . .	101
2.46	Areal Dispersion for Reinforced Concrete Structure Semi-log Plot with First-Order Regression Line	103
2.47	Areal Dispersion for Reinforced Concrete Structure Semi-log Plot with Second-Order Regression Line	105
2.48	Average Fragment Weight vs Ground Range for a Reinforced Concrete Structure	107
2.49	Fragment Quantities at Various Ground Ranges for a Reinforced Concrete Structure	108
2.50	Fragment-Size Distribution at Various Ground Ranges for a Reinforced Concrete Structure	109
2.51	Fragment Distances for Various Weight Classes for a Reinforced Concrete Structure	111
2.52	Fragment-Distance Distribution for Various Weight Classes for a Reinforced Concrete Structure	112
3.1	The Ideal Law of Breakage	116
3.2	Cumulative Fragment-Size Distribution for Exploded Dry Sandstone Blocks	117
3.3	Model Reactor with Concrete Shielding	119
3.4	Cumulative Fragment Distributions for 1/24-Scale Shielded Reactor Vessels (all recorded fragments)	120
3.5	Cumulative Fragment Distributions for 1/24-Scale Shielded Reactor Vessels (all fragments over 0.1 lb) . . .	121
3.6	Cumulative Fragment Distributions for 1/12-Scale Shielded Reactor Vessels	123
3.7	Fragmentation Measures for 1/12- and 1/24-Scale Shielded Reactor Model Tests	125

SECRET

SECRET

LIST OF ILLUSTRATIONS (Con't.)

<u>Figure</u>		<u>Page</u>
3.8	Fragmentation Measures for 1/24-Scale Shielded Reactor Models Full and 3/4-Full of Water.	126
3.9	Fragmentation Measures for Selected 1/24-Scale Shielded Reactor Model Tests.	127
3.10	Fragmentation Measures for Selected 1/24-Scale Shielded Reactor Model Tests.	128
3.11	Fragment-Size Distribution for a Reinforced Concrete Ordnance Structure	130
3.12	Distribution of Total Fragment Weight by Fragment-Size Classes for a Reinforced Concrete Structure	132
3.13	Cumulative Fragment-Size Distribution for a Reinforced Concrete Ordnance Structure	133
3.14	Cumulative Distribution of Total Fragment Weight for a Reinforced Concrete Ordnance Structure	134
3.15	Placement of Wall Targets in JANGLE U Event.	135
3.16	Size Distribution of Fragments from Wall Targets in JANGLE U Event	136
4.1	Fragmentation Model	141
4.2	Motion of Mass at Failure ($\delta = 5$)	145
4.3	Motion of Mass at Failure ($\delta = 10$).	146
4.4	Motion of Mass at Failure ($\delta = 100$)	147
5.1	General Debris Particle	151
5.2	Dynamic Pressure Variation	156
5.3	Positive Phase Duration	157
5.4	Velocity-Distance Plot for $2 < \theta < 10$	159
5.5	Velocity-Distance Plot for $0.2 < \theta \leq 1$	161
5.6	Comparison of Distance Traveled by Different Size Particles.	163
5.7	Velocity-Distance Plot Including Negative Phase for $1 < \theta < 10$	164

SECRET

SECRET

LIST OF ILLUSTRATIONS (Con't.)

<u>Figure</u>		<u>Page</u>
5.8	Velocity-Distance Plot Including Negative Phase for $0.2 < \theta < 1$	165
5.9	Comparison of Exact and Approximate Method of Handling Initial Conditions	168
6.1	Relative Positions of Troops, Forest, and Ground Zero. . .	172
6.2	Wind Particle Trajectories During the Positive Phase of a Nuclear Blast.	175
6.3	Trace of Branchwood for Low Yield Weapons.	176
6.4	Forest Stand After a Nuclear Explosion (2.4 psi overpressure)	177
6.5	Forest Stand After a Nuclear Explosion (3.8 psi overpressure)	177
6.6	Horizontal Displacement of Tree Limbs	178
7.1	High Explosion Crater 13 (40,000 lbs), Buckboard Mesa, Nevada Test Site, Nye County, Nevada	185
7.2	Area Mean Distance vs Fragment Size.	188
7.3	Distribution Law Exponent vs Scaled Depth of Burial	189
7.4	Scaled Distribution Law Coefficient vs Scaled Depth of Burial	190
7.5	Crater Radius vs Yield, Surface Shots, Various Fails. . . .	191
7.6	Distribution Law Exponent and Constant vs Scaled Depth of Burial	193
7.7	Nomographic Chart No. 1 for Computing Values of C and n .	194
7.8	Nomographic Chart No. 2 for Computing Debris Distance . .	195
7.9	Asymmetry vs Yield.	199
7.10	Plan and Section of the DANNY BOY Crater	200
7.11	Debris Diameter Ratio vs Scaled Depth of Burial	201
7.12	Debris Diameter for HE Charges in Various Soils	202
7.13	Per cent of Efficiency vs Scaled Depth of Burst.	204

SECRET

SECRET

LIST OF ILLUSTRATIONS (Con't.)

<u>Figure</u>		<u>Page</u>
7.14	Estimated Maximum Fragment Distances for DANNY BOY Event.	205
7.15	Plumes from Low-Yield Underwater Explosions.	209
7.16	Plume from Shallow Underwater Nuclear Explosions.	210
H-1	Detailed Flow Diagram for the Particle Velocity Integration .	H-4
J-1	Fragment Distribution from 20-MT Weapon Based on Pantex Test.	J-6
J-2	Throwout Density, Area I, DANNY BOY Event	J-8
J-3	Throwout Density, Area II, DANNY BOY Event	J-9
J-4	Throwout Density, Area III, DANNY BOY Event.	J-10
J-5	Debris Density for 1-KT Weapon Based on DANNY BOY Results	J-11
J-6	Velocity Field in Crater ($\tau = 0.1026$ msec)	J-14
J-7	Velocity Field in Crater ($\tau = 52.49$ msec).	J-15
J-8	Velocity Field in Crater ($\tau = 80.01$ msec).	J-16
J-9	Velocity Field in Crater ($\tau = 105$ msec).	J-17
J-10	Crater Divisions.	J-18
J-11	Weapon Parameter for 20-MT Weapon	J-23
J-12	Debris Density for 1-KT Weapon Based on Brode's Model of Crater Formation	J-26

SECRET

SECRET

LIST OF TABLES

<u>Figure</u>		<u>Page</u>
2.1	Regression Lines for Maximum Debris Distance in Terms of Explosion Parameters.	29
2.2	Regression Lines for Maximum Debris Distance in Terms of Crater Dimensions	61
3.1	Model Tests Selected for Plotting	118
6.1	Damage Criteria for Forests	178
6.2	Safe Distances to Prevent Casualties from Tree Debris . . .	179
7.1	Debris Distances for Cratering Tests in Basalt	187
7.2	Debris Contours for Cratering Explosions in Basalt	197
J-1	Limit of Antenna Vulnerability Based on HE Data	J-4
J-2	Debris Density for Antenna System Location at 4.0 Miles Ground Range	J-12
J-3	Initial Table Velocity.	J-19
J-4	Trajectory Analysis Data for 20-MT Weapon	J-23

SECRET

SECRET

CHAPTER ONE

INTRODUCTION

While most nuclear weapons effects -- radiation, thermal, air blast, ground shock, and radioactive fallout -- have been investigated extensively since 1946, little study has been devoted to the creation and distribution of structural debris. This stems in part from the fact that under earlier concepts of vulnerability, yields of weapons and the accuracy of their delivery, the design hardness levels under consideration were such that structural debris was not a prime hazard. Developments in the yield of weapons, delivery accuracy, and design hardness levels make the effect of flying debris a serious consideration. With the utilization of tactical nuclear weapons by field troops, knowledge of debris environment is an important consideration in the deployment of troops. Design specifications for survival of hardened retaliatory weapons sites shortly beyond the edge of the plastic zone of the crater require a knowledge of the deposition of crater throwout material. The siting of communications systems presents particularly serious problems since they are especially vulnerable where substantial flying debris arises.

The investigation was initiated to conduct a series of analytical and experimental studies of the behavior of debris. The following tasks were included:

Fundamental Studies of Debris Behavior

Measures of the maximum fragment distance were developed from HE data and compared with nuclear results. The shape of debris distribution functions was studied in detail. Experimental and analytical work on fragment size-distribution was revised. An analytical model for the transport of debris under blast wind loading was developed.

SECRET

SECRET

- **Specific Vulnerability Studies**

Several vulnerability studies were included, both as applications of the collected data, and to provide measures of vulnerability to flying debris under targeting situations of considerable interest and significance. These studies included:

- Vulnerability of field troops from branch wood within or near forest stands.
- Vulnerability of field troops to crater-emanated debris from very-low yield cratering charges.
- Vulnerability of field troops to crater-emanated debris from very-low yield stream bed charges.
- Vulnerability of antenna systems crater-emanated debris from high-yield nuclear bursts.

- **Crater Throwout Study of an Underground Nuclear Detonation**

This task was conducted as DANNY BOY Project 1.5 with findings reported under separate cover (Ref. 1, 2). DANNY BOY Project 1.5 involved the following activities:

- Compilation of data relating the initial and terminal positions of a series of more than 1100 "ideal" objects (steel plates, spheres, cylinders and cubes; wood cubes and boards; and common brick) emplaced on the ground surface and in drill holes in the crater zone prior to the shot.
- Compilation of data on the distribution of natural throwout debris beyond the limit of the crater lip, i. e. , beyond the ground range where the ground surface is completely obscured by debris.
- Compilation of analysis and plotting of the data in various manners to describe the behavior of crater throwout for this deep underground burst.

SECRET

SECRET

1.1 Report Organization

This report is organized into seven chapters. Each of the six chapters following the Introduction concerns a pertinent aspect of the overall debris problem. Thus, the report is a series of related, but self-contained, studies rather than a continuous-reading document. The contents of the report are summarized by chapters as follows.

Chapter One, Introduction

The first chapter provides a general introduction to the debris problem. The major conclusions drawn from the investigation are presented. Finally, recommendations for additional research are made.

Chapter Two, Debris Characteristics of High Explosive and Nuclear Detonations

Previous nuclear weapon effects tests have produced little data concerning the formation and distribution of structural debris, with the following exceptions:

Project 4.5 of Operation JANGLE included measurements of the debris from airport-type runways and reinforced-concrete wall panels erected over the crater zone of an underground burst.

Project 33.2 of Operation PLUMBBOB studied the behavior of debris (including window glass, military debris, gravel, stones, and spheres) in response to air blast at various ground ranges. Findings of this investigation had not been published at the time of this investigation.

Other Operation PLUMBBOB studies were concerned with fragments of biological interest, such as glass splinters capable of penetrating abdominal walls.

DANNY BOY Project 1.5, a study of crater throwout, was recently completed.

SEDAN, a recent nuclear event, included an experimental investigation of crater throwout.

SECRET

SECRET

While debris information from past nuclear tests provided only limited data for analysis, extensive measurements were found to be available in reports of planned and accidental HE detonations. These data were collected, studied, and plotted in various manners to define general patterns in debris behavior. Where possible, "check points" from nuclear experience are introduced to indicate their consistency with HE results. Hundreds of explosion reports were reviewed in this task. Data from a series of more than 200 selected explosions were used to obtain expressions relating maximum debris distance to equivalent yield, and to an estimate of the explosive impulse. A smaller series of explosions was used to derive expressions relating maximum debris distance to crater dimensions. Maximum debris distance is correlated with explosion parameters and crater dimensions using the method of least squares; scaled and unscaled relationships are developed using both linear and quadratic relationships. In each regression line so obtained, the standard error and correlation coefficient have been computed as a measure of closeness of fit. Figure 1. 1, which expresses the quadratic correlation between maximum debris distance and equivalent yield, and Fig. 1. 2, which shows the correlation between scaled maximum debris distance and scaled crater volume, are typical of these regression results. Note particularly, the consistency of JANGLE U results with the HE findings. The much lower position of the DANNY BOY results can be explained on the basis of the very deep burial of the device in this event, which resulted in trajectories with pronounced vertical components in the ejecta. Actually, it may be argued that the HE detonations are more like the buried nuclear burst than surface nuclear bursts, because of the absence of substantial blast winds.

To define the probability of personnel or equipment being hit by missiles, and, for the shorter ground ranges, the quantity of material likely to be deposited atop a silo door, it is necessary to estimate the distribution of fragments within the maximum ground range. Several approaches to this problem were pursued. A theoretical model for fragment distribution from ground zero to maximum debris distance was derived by assuming wall and roof panels to fragment into equisized fragments upon detonation of a nearby line charge. Comparison of this model with several explosions shows

SECRET

SECRET

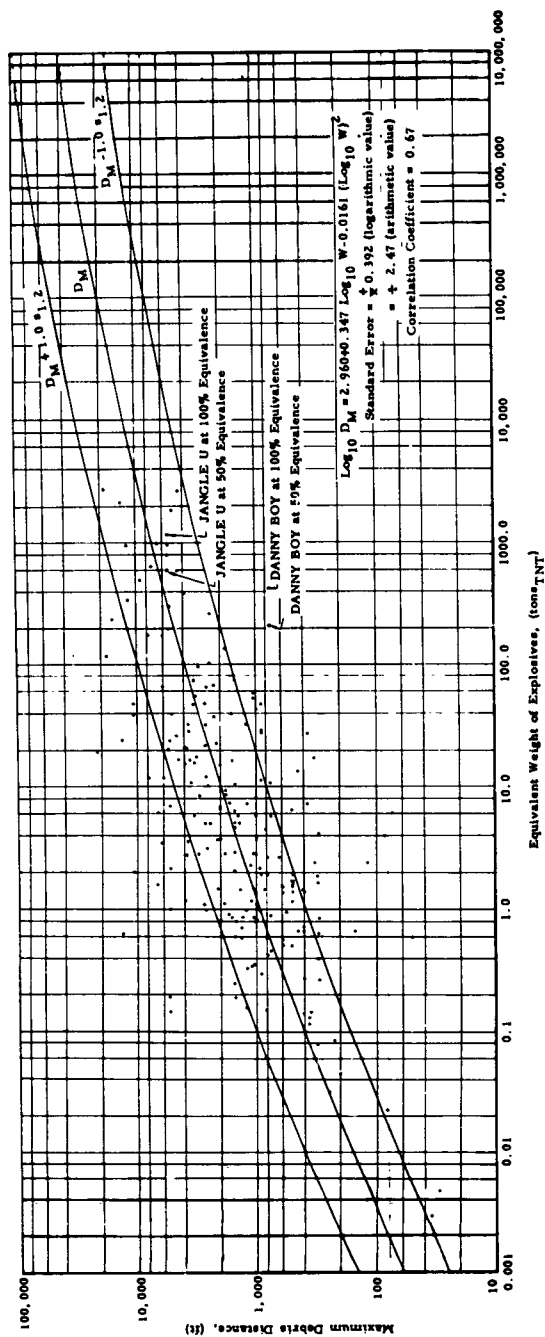


Figure 1.1 Quadratic Regression Line: Maximum Debris Distance versus Equivalent Yield

SECRET

SECRET

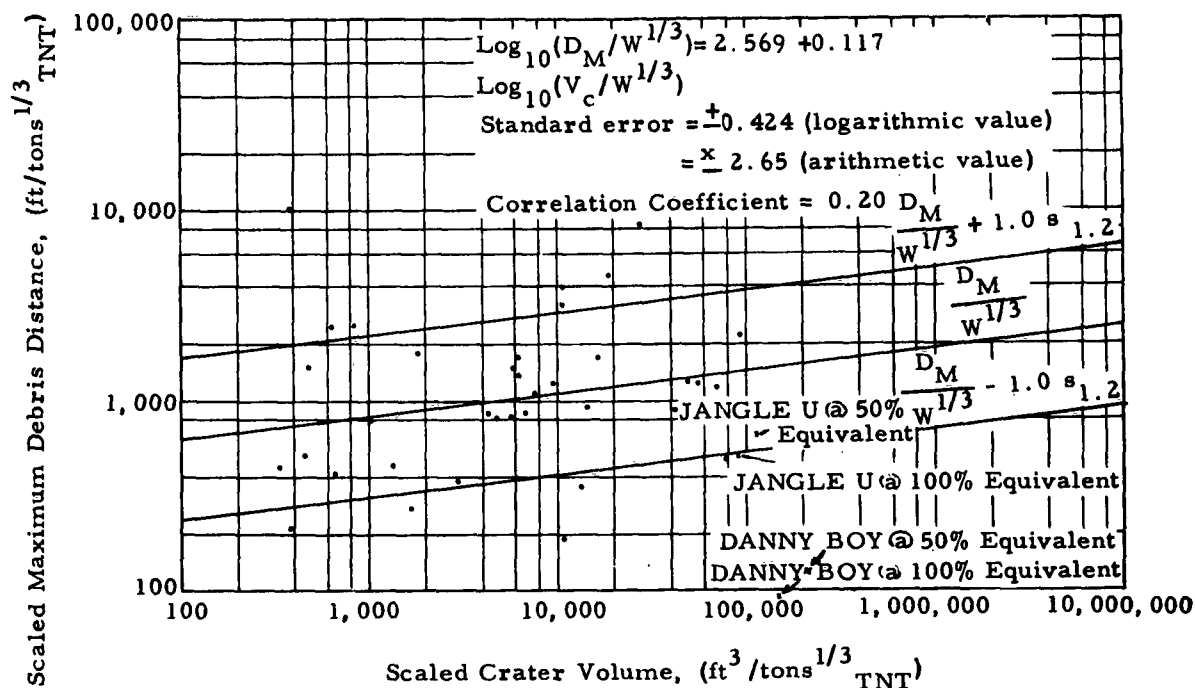


Figure 1.2 Linear Regression Line: W^{1/3}-Scaled Maximum Debris Distance Vs. W^{1/3}-Scaled Crater Volume

that the shape of the curves is similar (Fig. 1.3). Next, debris distribution patterns of a series of six ordnance explosions were plotted in various matters to note their similarity. Thirdly, debris distribution of an ordnance structure (involving over 30,000 recorded fragments with a total weight of about 43 tons) was plotted in detail. Contrary to expectation based on drag effects, the large fragments from this explosion did not travel as far as the smaller ones (Fig. 1.4). This is probably because fragments subject to forces sufficient to cause large acceleration were also subject to a greater degree of breakup.

SECRET

SECRET

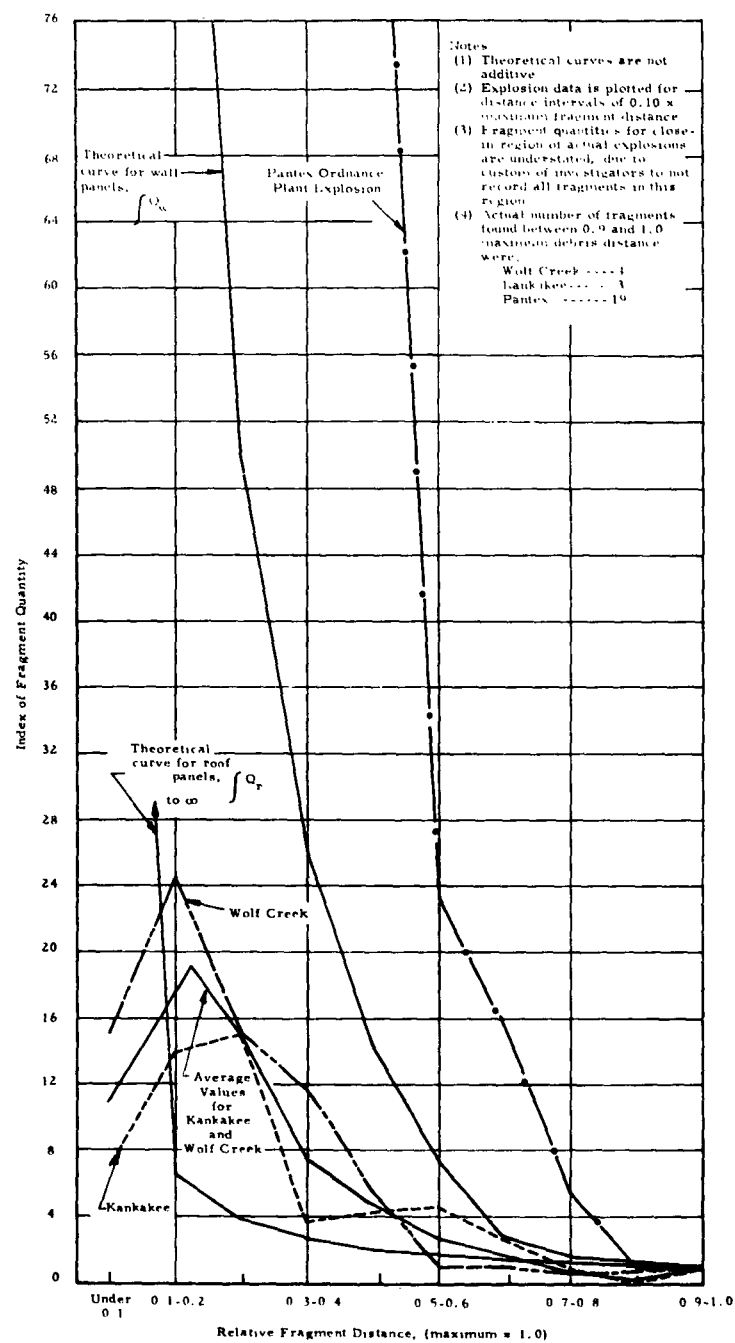


Figure 1.3 Comparison of Theoretical and Actual Fragment Dispersion Patterns

SECRET

SECRET

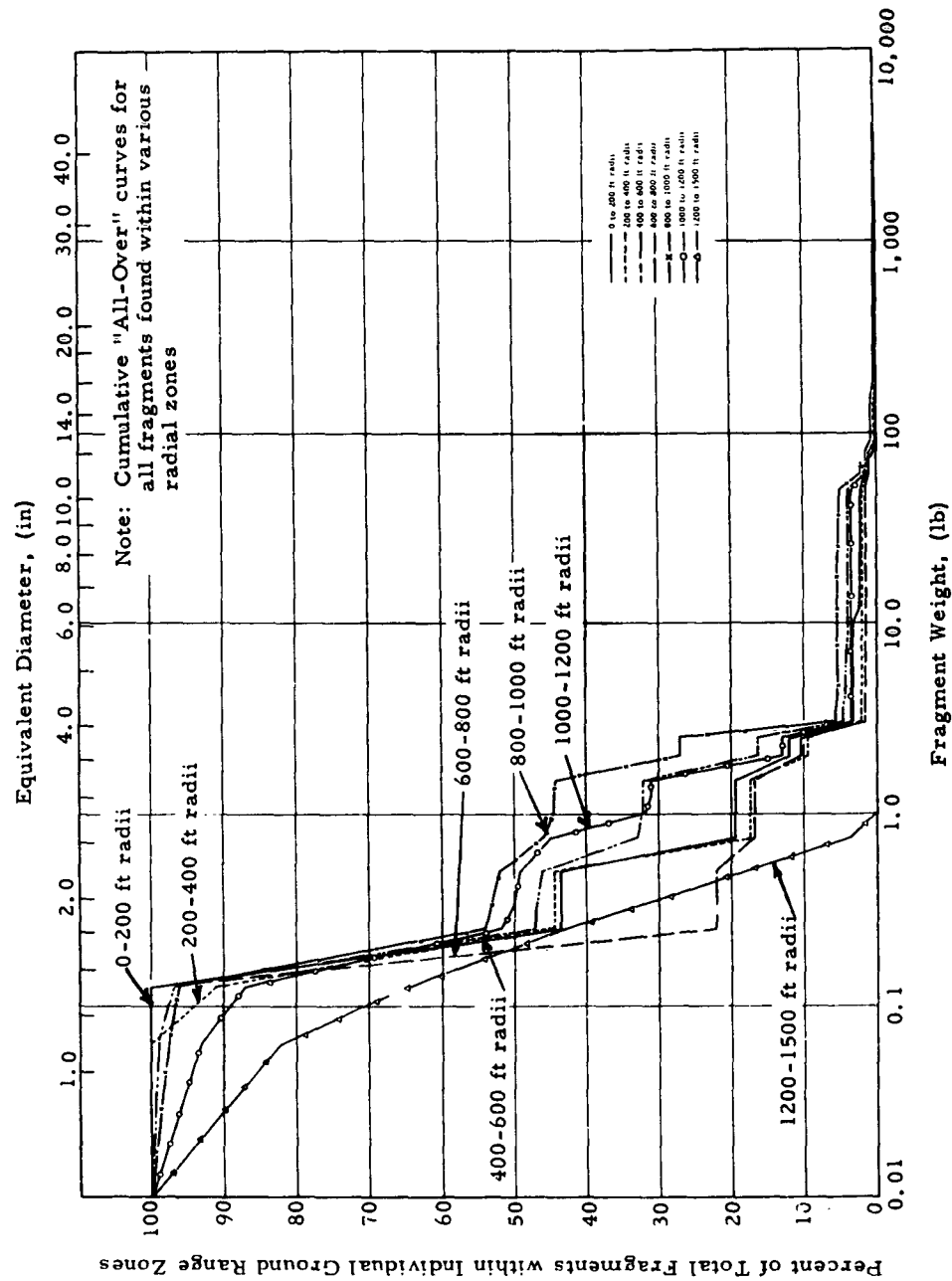


Figure 1.4 Fragment-Size Distribution at Various Ground Ranges for a Reinforced Concrete Structure

SECRET

SECRET

Chapter Three, Fragmentation Experimental Observations

Since energy levels of the flying fragments are a measure of their potential to penetrate shields, impart shock loading to equipment, or incapacitate personnel, it is well to define the expected size-distribution of fragments. No definitive experimental investigation of structural fragmentation has yet been made, even on idealized structural elements, by which the fragment-size distribution is related to structural strength and loading parameters. For this reason an attempt was made to collect and summarize past experimental work on fragmentation of materials and structures, and to describe the general fragment-size distribution patterns that have been observed. Five such investigations are described;

The British Coal Utilization Research Association
studies on coal breakage from random forces,

Safety in Mines Research Establishment (of Great
Britain) research on explosively detonated stone
blocks.

Stanford Research Institute model tests on frag-
mentation of reactor containment structures
from internal explosions,

The Pantex Ordnance Plant detailed fragment counts
from the planned explosion of a reinforced concrete
ordnance structure,

Project 4.5 of Operation JANGLE studies of fragment
size distributions from reinforced concrete wall
panels erected over the crater zone.

Experimentation has shown that the higher the loading on the source material the smaller the fragments produced, and that a wide range of fragment sizes are produced by any loading. An "Ideal Law of Breakage" which shows excellent fit to the experimental data has evolved from coal-crushing investigations. The extensive data from over 30,000 concrete fragments in the Pantex Ordnance Plant event allowed a detailed study of the fragment-size distribution. It is interesting to note that only about 3 percent of the fragments recorded in this event (above 1-ounce in size) weighed more than three pounds, but that these accounted for nearly 75 percent of the total weight of all fragments. This tends to support the hypothesis that for many problems involving impact of fragments, there may be an optimum

SECRET

SECRET

fragment-size for purposes of design predictions. Figures 1.5 and 1.6 show these distributions. The only major structural fragmentation study conducted on nuclear detonations was the test of wall panels on the JANGLE U event. Size distributions of the larger fractions were plotted as part of that project and it was noted that the JANGLE data did not preclude the possibility that the concrete fragment-size distribution caused by the underground nuclear shot followed the same pattern as mined coal or ore in a crusher.

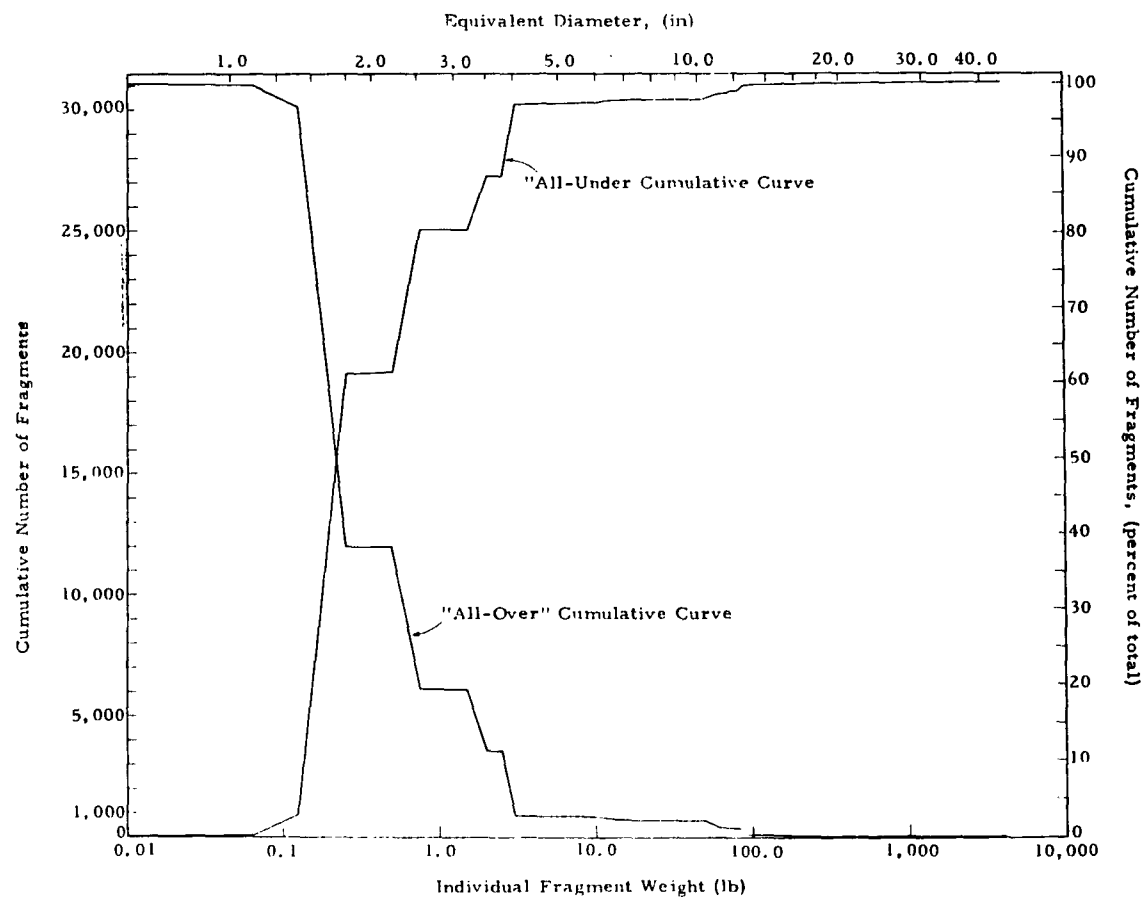


Figure 1.5 Cumulative Fragment-Size Distribution for a Reinforced Concrete Ordnance Structure

SECRET

SECRET

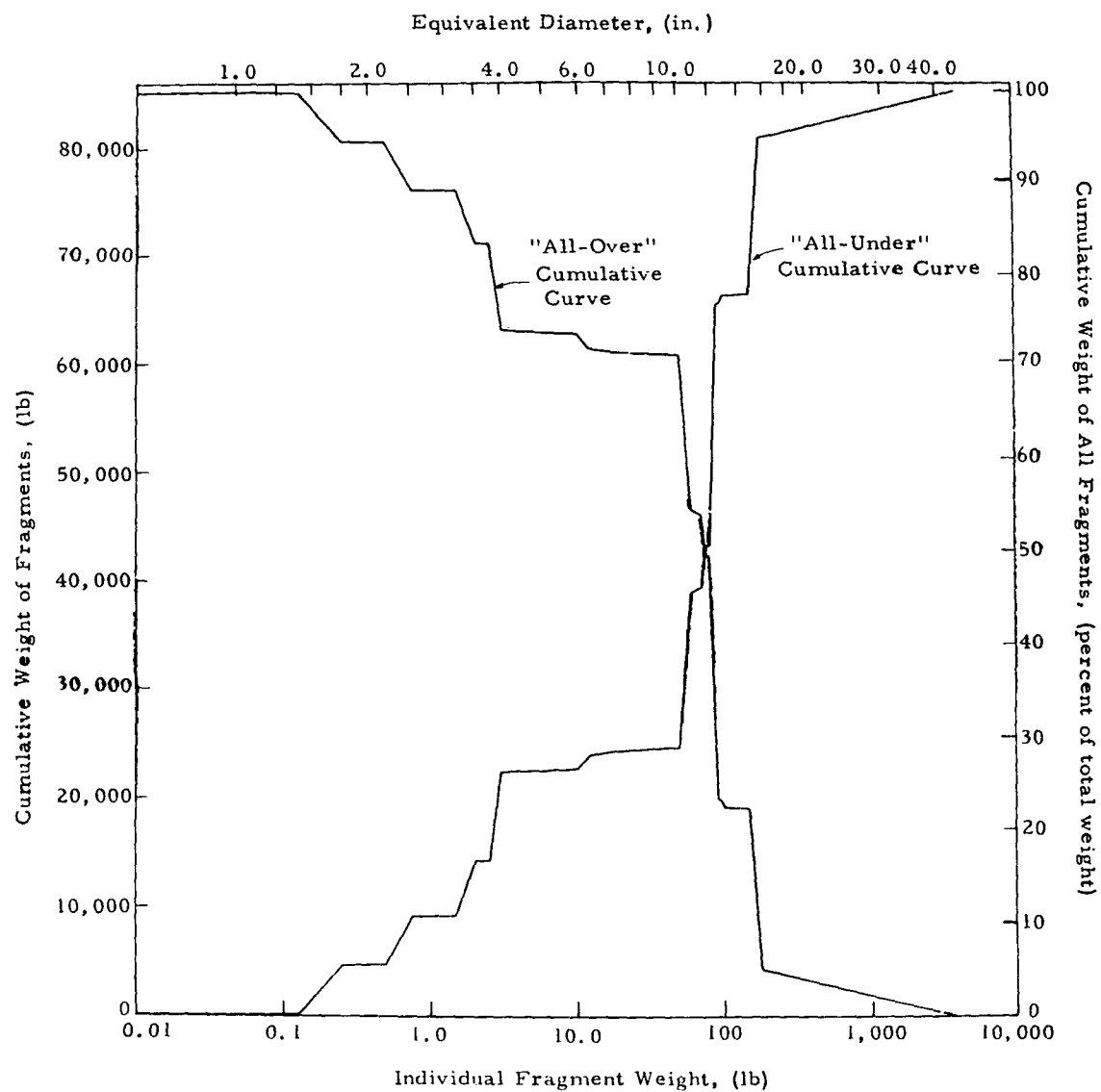


Figure 1-6 Cumulative Distribution of Total Fragment Weight
for a Reinforced Concrete Ordnance Structure

SECRET

SECRET

Chapter Four, Fragmentation, Analytical Considerations

Prediction of the number and size into which a structural component fragments, when subjected to blast loading, is totally beyond the current state-of-the-art of fracture mechanics. Thus, a relatively simple mathematical model was formulated to be used to predict debris formation, which can be adapted to include advances in fracture mechanics. The model selected for this study, is a simple extension of the single-degree-of-freedom structural model long used to analyze the elastic-plastic response of structural components subjected to blast loading. The response of the single-degree-of-freedom system with an elastic, perfectly plastic spring is determined. In particular the mass, velocity, and the time when the mass reaches a certain displacement, called the fracture displacement, are of interest. The magnitude of the fracture displacement and the description of particles formed when this displacement is reached must await further analytical and experimental developments in fracture mechanics.

Chapter Five, Debris Transport by Blast Winds

The motion of a particle acted on by the nuclear blast winds is analyzed on the assumption that initial conditions of the particle motion are known. The model used assumes that the force acting on the particle is proportional to the square of the relative velocity between the particle and air. Blast parameters are assumed constant over the range of travel of the debris, and it is further assumed that the apparent lengthening of the positive phase duration due to the debris motion in the direction of shock propagation can be handled by a simple adjustment of positive phase duration. These assumptions are necessary to reduce the equation of motion for any debris particle to a one-parameter nonlinear differential equation. Without making these two assumptions, it would be necessary to treat each weapon yield and placement as a separate problem and no general observation could be made regarding debris behavior. The equation of motion is numerically integrated and results are obtained for a wide range of overpressures and particle sizes. It is possible to use the results directly to determine distance-time plots for any debris. The effect of negative

SECRET

SECRET

phase winds on particle motion is also studied. While a complete description of the negative phase wind is not available, reasonable estimates of this wind can drastically change the motion of the debris particle.

Chapter Six, Vulnerability of Field Troops to Tree Debris

The study of the vulnerability of engineer and field troops to hazards from tree debris is one of three specific debris problems of interest to the Office of the Chief of Engineers, U.S. Army. The objective of this study was to define a "safe distance" for positioning troops to avoid casualties from falling trees and limbs. The safe distance may actually fall inside or outside the forest and both cases are represented. Since any individual tree may fail at the base under blast loading, tree height is considered the minimum safe distance in any situation. Making certain simplifying assumptions (i. e. , zero strength tree limbs, plane blast wave loading, unobstructed trajectories, and that personnel struck by tree limbs are certain casualties), tree limbs are followed in their trajectories from the time of shock arrival to their impact with the ground. Results show that for the lower yields (1 KT, for example) trajectories become vertical early. A uniform translation of all branches is thus obtained, the area in front of the forest up to the "safe distance" being similar in appearance to that of the forest floor after all branchwood was allowed to drop vertically. For the higher yield weapons (20 MT, for example) trajectories terminate before they become vertical. Results are similar with the exception that the highest branches of the first few rows of trees pile up in a lower density than those following closer-in trajectories. Results of this study are summarized in the following table, which lists safe distances in terms of tree height, weapon yield, and overpressure levels.

Chapter Seven, Vulnerability of Field Troops to Throw Out Debris from Cratering and Stream Bed Charges

Methods for estimating safe distances for positioning troops in the proximity of very-low-yield cratering and stream-bed charges, based on debris criteria, were studied. As with the preceding tree debris vulner-

SECRET

SECRET

SAFE DISTANCES TO PREVENT CASUALTIES FROM TREE DEBRIS

Yield of Weapon	Height of Tree, feet	Safe Distance Falls Inside of Forest Safe Distance from Ground Zero	Safe Distance Falls Outside of Forest									
			Safe Distance from Ground Zero for Various Overpressures at the Front of the Forest, (yd)					Safe Distance from Forest for Various Overpressures at the Front of the Forest, (yd)				
			5 psi	10 psi	15 psi	20 psi	30 psi	5 psi	10 psi	15 psi	20 psi	30 psi
0.05 KT	20	311 - 376 yards	193	130	109	98	87	7	8	10	12	16
	40		200	136	113	100	87	14	14	14	14	16
	60		206	142	119	106	91	20	20	20	20	20
	80		213	149	126	113	98	27	27	27	27	27
	100		220	156	133	120	105	34	34	34	34	34
	120		226	162	139	126	111	40	40	40	40	40
	160		239	175	152	139	124	53	53	53	53	53
	200		253	189	166	153	138	67	67	67	67	67
0.1 KT	20	392 - 473 yards	241	164	137	123	108	7	10	12	15	19
	40		248	168	139	123	108	14	14	14	15	19
	60		254	174	145	128	109	20	20	20	20	20
	80		261	181	152	135	116	27	27	27	27	27
	100		268	188	159	142	123	34	34	34	34	34
	120		274	194	165	148	129	40	40	40	40	40
	160		287	207	178	161	142	53	53	53	53	53
	200		301	221	192	175	156	67	67	67	67	67
0.5 KT	20	670 - 809 yards	410	279	235	210	186	10	16	21	26	33
	40		414	279	235	210	186	14	16	21	26	33
	60		420	283	235	210	186	20	20	21	26	33
	80		427	290	241	211	186	27	27	27	27	33
	100		434	297	248	218	187	34	34	34	34	34
	120		440	303	254	224	193	40	40	40	40	40
	160		453	316	267	237	206	53	53	53	53	53
	200		467	330	281	251	220	67	67	67	67	67
1 KT	20	845 - 1021 yards	517	351	295	264	233	12	20	26	32	41
	40		519	351	295	264	233	14	20	26	32	41
	60		525	351	295	264	233	20	20	26	32	41
	80		532	358	296	264	233	27	27	27	32	41
	100		539	365	303	266	233	34	34	34	34	41
	120		545	371	309	272	233	40	40	40	40	41
	160		559	385	323	286	246	54	54	54	54	54
	200		572	398	336	299	259	67	67	67	67	67
1 MT	20	8,448 - 10,208 yards	5,119	3,430	2,856	2,526	2,182	68	121	165	203	265
	40		5,137	3,460	2,895	2,574	2,243	86	151	204	251	326
	60		5,147	3,475	2,916	2,599	2,273	96	166	225	276	356
	80		5,153	3,485	2,927	2,612	2,290	102	176	236	289	373
	100		5,157	3,490	2,934	2,620	2,299	106	181	243	297	382
	120		5,160	3,493	2,937	2,623	2,302	109	184	246	300	385
	160		5,163	3,495	2,938	2,623	2,302	112	186	247	300	385
	200		5,163	3,495	2,938	2,623	2,302	112	186	247	300	385
20 MT	20	22,932 - 27,709 yards	13,792	9,128	7,505	6,553	5,528	81	146	200	247	325
	40		13,821	9,179	7,575	6,639	5,640	110	197	270	333	437
	60		13,842	9,215	7,624	6,699	5,718	131	233	319	393	515
	80		13,858	9,243	7,662	6,746	5,779	147	261	357	440	576
	100		13,871	9,267	7,693	6,786	5,829	160	285	388	480	626
	120		13,882	9,287	7,720	6,818	5,872	171	305	415	512	669
	160		13,901	9,304	7,764	6,872	5,940	190	322	459	566	737
	200		13,916	9,345	7,799	6,914	5,994	205	363	494	608	791

SECRET

SECRET

ability problem, these two cases were studied to supply data needed by the Office of the Chief of Engineers, U. S. Army. Numerous reports on debris from HE cratering tests were studied to obtain measures of the relationship between debris distance, weapon yield, depth of burst, fragment size, and soil characteristics. The U. S. Geological Survey report on a series of HE cratering tests in basalt (Area 18 at Nevada Test Site) provided data on relationships between the first four of these factors (Ref. 24). Using these data, nomographic procedures were presented for estimating average debris distance for various fragment sizes in basalt, for various combinations of yield and depth of burst. An asymmetry factor is introduced to obtain maximum rather than average debris distances, based on measurements of the ray-like patterns in the USGS study. Using data from the Panama Canal series of cratering tests in various media (Ref. 29), distance ratios are plotted obtaining estimates of debris distances in media other than basalt, and for the stream-bed charge. Debris distances found by this method, using DANNY BOY explosion parameters, are consistent with photographic observations of the debris deposit from this event.

1.2 Summary and Conclusions

Various aspects of the debris problem -- fragmentation characteristics of materials and structures, transport of the debris particles by the blast winds, and the ultimate distribution of material resulting from these factors -- are studied in this investigation. Both analytical and experimental studies of the phenomena are considered. In some cases, behavior is defined empirically from collected historical data, in other cases, by analytically derived expressions and exhibits.

Fundamental data are collected to provide a basis for initial estimates of the nature of the debris problem in specific targeting situations. Historical data (HE detonations) are used to derive empirical expressions correlating maximum debris distance with equivalent TNT yields, impulse, and crater dimensions. These serve to make initial approximations of the limiting ground range of debris problems. Data compiled on relative distribution of debris particles can be used to make initial estimates of fragment quantities at various ground ranges. Estimates made from these

SECRET

SECRET

data are, at best, crude. For the most part they are based on HE data and nuclear - HE equivalence. Use of the latter is questionable -- especially since extreme differences in blast winds exist between nuclear and HE. As with most HE results, the experimental findings include great degrees of scatter.

The existence of definite debris patterns is graphically demonstrated in this report. The only phenomenon lending itself to analytical treatment is the transport of debris particles by the blast winds. A relatively complete treatment of the phenomenon is made. Fragmentation of materials and structures is reviewed in detail -- but this study simply cannot be carried very far without considerable experimentation.

The following conclusions are drawn from this study:

- (1) Data in this report can be used to determine debris distribution under a variety of targeting situations.
- (2) In many situations initial estimates of the severity of the debris problem can be made from the data compiled.
- (3) Progress has been made in providing data and methods for estimating the existence and severity of debris problems, but the approximations are crude.
- (4) The various debris phenomena (fragment-size distributions for materials and structures, debris dispersion patterns, and variations with explosion parameters) follow characteristic patterns which can be established experimentally.
- (5) The feasibility of predicting debris effects of nuclear explosions has been demonstrated by examples. Because random and/or uncontrollable (and unpredictable) factors influence debris behavior, prediction of these effects will never have a high degree of precision.
- (6) Debris prediction methods can be greatly improved by experimental data which can be developed on future full-scale nuclear test programs.

SECRET

SECRET

Problems exist which cannot be solved without further investigation, primarily experimental. Knowledge of fragmentation of actual structures, or even structural elements, is sub-minimal. Little is known of fragment quantities and the fragment-size distribution which can be expected from structural elements, and even less is known of the variations in the characteristics which would be caused by different levels of impulsive loading. Likewise, the time of failure of structural elements is a completely unknown factor. The analytical treatment of fragment transport by blast winds, included in this report, requires experimental verification. The problem of crater throwout debris and the resultant buildup of the crater lip is significant in terms of the mass of material likely to be accumulated atop hardened sites. The work on crater throwout debris begun on Project DANNY BOY under this contract should also be expended to cover variations in parameters.

1.3 Recommendations

On the basis of the findings of work performed under this contract, it is recommended that further analytical and experimental investigation be made in the following areas.

- (1) Further study of the data accumulated in this report, aimed toward codifying estimating procedures.
- (2) Further analysis of the accumulated data from the crater throwout debris study from the DANNY BOY event.
- (3) Inclusion of crater throwout debris studies in possible forthcoming tests, to study effects of variations in parameters -- other yields, depths of burial, and soils.
- (4) Experimental investigation of fragmentation of photo-type wall and roof panels -- studying time of failure, fragment-size distribution, fragment dispersion, and effects of variations in the loading pulse. This work could be performed under a combination of HE and full-scale nuclear testing.

SECRET

SECRET

CHAPTER TWO
DEBRIS CHARACTERISTICS OF HIGH EXPLOSIVE
AND NUCLEAR DETONATIONS

Little data on formation and dispersion of structural debris have been collected from full-scale nuclear tests. Since debris hazards were not initially considered a major problem, tests of structures and structural elements did not include measurements of fragmentation or debris transport. One exception was Project 4. 5 of Operation JANGLE, in which reinforced concrete wall and runway panels were erected above the expected crater zone and debris measurements taken (Ref. 5). The vulnerability of parked aircraft was emphasized in this study, thus major interest was centered about the maximum ground range of aircraft damage from blast and from debris. A second exception was Project 33. 2 of Operation PLUMBBOB in which the behavior of missiles (including window glass, military debris, gravel, spheres and native stone) emplaced at various ground ranges was studied. Findings of Project 33. 2 Operation PLUMBBOB had not been published at the time of this investigation. Other debris studies on Operation PLUMBBOB involved such fragments as small glass fragments capable of penetrating abdominal walls, which are of biological interest but which cannot be regarded as structural debris. More recently, crater throwout debris studies included in underground nuclear test programs on DANNY BOY and SEDAN have investigated objects emplaced on the ground surface and within the expected crater, and their post-shot locations relative to original positions. These crater throwout studies involved deep-buried shots in which the debris was not influenced substantially by blast winds, as it would be with a surface or shallow-buried shot.

From the beginning of this investigation, it was apparent that fragmentation and debris dispersion data from past full-scale nuclear tests would provide only limited information for analysis. It became obvious, however, that an extensive body of data was available in explosion reports from HE events -- both planned and accidental -- and that these could be studied to define general debris behavior patterns. The limited nuclear data could

SECRET

SECRET

then be introduced as "check points" on the HE studies. Several hundred selected reports on HE detonations were studied to determine the relationship between the maximum debris distance and various explosion parameters; these were then used to define the expected limit of the debris hazard. The least-squares method was used to correlate maximum debris distance with equivalent yield, computed values of impulse, and crater dimensions. It is of particular interest to note that comparisons of maximum debris distance from the JANGLE and DANNY BOY studies are consistent with the HE results.

In addition to defining the maximum debris distance, it was necessary to estimate the distribution of debris fragments at distances shorter than maximum. Quantitative data are needed for any estimate of probability of equipment or personnel being hit by flying fragments in the debris zone. Several approaches to this problem were taken. A theoretical model for the distribution of fragments from ground zero to maximum debris distance was developed by assuming structural wall and roof panels to fail into equi-sized fragments, with radial initial velocity vectors, upon detonation of a line-charge placed near them. Comparison with debris-distribution patterns of several explosions show that curves are of similar shapes. Next, the debris-distribution patterns of a series of six HE detonations involving ordnance structures were plotted together in various manners to note their similarity. Thirdly, debris distribution from a reinforced concrete ordnance structure was plotted in various ways. The availability of data, from this event, on the weights and terminal locations of over 30,000 fragments with a total weight of about 43 tons permitted highly detailed treatment of debris distribution. An interesting observation of this study is that the large fragments did not travel as far as the smaller fragments. This seemingly contradicts expectations based on air drag effects, but the comparison is inappropriate since the particles subject to forces sufficient to cause large motions are also subject to a greater degree of fragmentation.

2.1 Application of HE Data from Planned and Accidental Explosions

Past HE detonations, both planned and accidental, are an extensive source of data on the behavior of structural debris. Explosion reports customarily include some or all of the following information.

SECRET

SECRET

Total weight of explosive involved
Weight of explosive exploding at one time
Kind of explosive
Source structure
Crater dimensions
Maximum debris distance
Distances at which individual fragments were found
Distances at which various degrees of structural damage occurred

Several detailed compilations of explosion reports have been made (Ref. 6, 7, 8). Explosion reports make it possible to plot debris distances -- frequently only the maximums -- against various explosion parameters. Statistical measures of the consistency of these data can also be made.

Although the validity of debris data from individual explosion reports is limited in certain respects, the availability of many reports does permit averaging the data and constructing graphical and statistical measures of debris behavior. Plots of maximum debris distance in terms of equivalent explosive weight which permit estimates of expected debris ranges are included here. While scaling from HE to nuclear is generally a questionable procedure, these plots can be, and in fact have been, applied in determining whether or not debris problems are likely to exist at various ground ranges.

Certain limitations in the use of data taken mostly from reports on accidental explosions are apparent. Extreme variations exist in the range of explosion environments. Explosion source structures include steamers, freight cars, munitions plants, warehouses and igloos. Some of the explosions occurred in the open field. The relative degree of confinement afforded by these structures certainly affects the loading on the flying fragments. The amount of material available for fragmentation is a function of the source structure and, for larger explosions, of the surrounding neighborhood as well. In some cases, explosion data may be questioned as to the accuracy of the weight of explosives involved in accidental explosions, whether high or low order detonation took place, and the quantity of explosives involved in individual detonations of a series of consecutive explosions. Also, the

SECRET

SECRET

trajectories of fragments from HE detonations will range from the horizontal to the vertical, the farthest-flung may have initial trajectory angles of around 45° from the horizontal. This behavior is unlike fragment trajectories resulting from a structure failing under loading from the plane blast wave of a nuclear explosion.

2.2 Measures of Maximum Debris Distance

A series of 206 accidental and planned explosions was selected from those tabulated in references 6 and 8 and subjected to a regression study to develop estimating expressions for maximum debris distance -- a measure of maximum range of vulnerability to debris hazards. Selected explosions are listed in Appendix A, which tabulates maximum debris distances and the major explosion parameters. Maximum debris distance was correlated with equivalent weight of explosives and impulse; various scaled relationships between these functions were also studied. A total of 40 linear and 40 quadratic regression lines was determined by computer methods, together with standard errors and correlation coefficients for each line. (Results of this correlation study are included in Table 2.1 and Fig. 2.3 through 2.10.)

2.2.1 Details of Regression Analysis

The plots of maximum debris distance and explosion parameters, (Fig. 2.3 through 2.10) show a great degree of scatter among data points. It is quite apparent that this dispersion is, in all cases, far too great to permit visual location of any average line through the data points. Statistical devices must be used to describe the plotted relationships satisfactorily. Simple (linear) and quadratic correlations were therefore made, using least-squares methods.

It should be noted that the computation of a regression line does not necessarily assure a functional relationship between the factors correlated; in this case it merely describes what has historically occurred. Thus, the computation and drawing of a regression line describing the correlation between maximum debris distance and equivalent weight of explosives does not mean that the two factors are functionally related by some physical law to the exclusion of such other considerations as configuration and strength

SECRET

SECRET

of structures and impulse distance. If, however, the association between maximum debris distance and some explosion parameter were found to be sufficiently close, it could be possible to estimate, with some calculable degree of accuracy, the maximum debris distance for other explosions on the basis of the observed relationship found in this sample of 206 explosions.

The computed regression lines were derived by the method of least squares -- one of the most widely used methods of curve fitting -- which yields the equation of the line from which the summation of the squares of the deviations of all the plotted points is a minimum. Application of the least-squares linear regression line is demonstrated in Fig. 2.1.

Derivations of equations for least-squares regression lines can be found in most engineering statistics texts. The linear least squares line of the form

$$X_{12} = a_{12} + b_{12} X_2$$

is obtained by solving the simultaneous equations

$$\begin{aligned} Na_{12} + b_{12} \sum X_2 &= \sum X_1 \\ a_{12} \sum X_2 + b_{12} \sum X_2^2 &= \sum X_1 X_2 \end{aligned}$$

to obtain the coefficients a_{12} and b_{12} .

Similarly, the quadratic least-squares regression line of the form

$$X_{12} = a'_{12} + b' X_2 + c' X_2^2$$

is obtained by solving the set of three simultaneous equations:

$$\left. \begin{aligned} Na'_{12} + b'_{12} \sum X_2 + c'_{12} \sum X_2^2 &= \sum X_1 \\ a'_{12} \sum X_2 + b'_{12} \sum X_2^2 + c'_{12} \sum X_2^3 &= \sum x_1 X_2 \\ a'_{12} \sum X_2^2 + b'_{12} \sum X_2^3 + c'_{12} \sum X_2^4 &= \sum x_1 X_2^2 \end{aligned} \right\} \quad (2.1)$$

The advantages of deriving least-squares lines in this study are that (1) reproducible associative relationships are developed in accordance with accepted statistical procedures, and (2) measures of probable error and closeness of fit can be computed. The standard error is a measure of

SECRET

SECRET

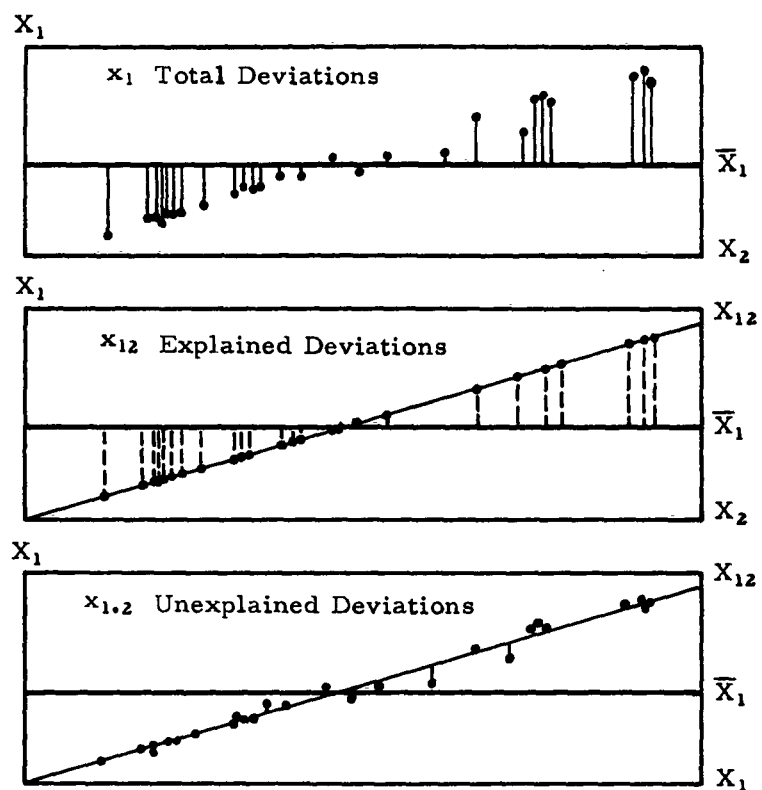


Figure 2.1 Graphical Representation of Least-Squares Linear Regression Line

X_1, X_2 = a set of bivariate data

\bar{X}_1 = arithmetic mean of X_1

X_{12} = least-squares regression line values of X_1

x_{12} = deviations explained by regression of X_1 on X_2

$x_{1.2}$ = $X_1 - X_{12}$ = residual or unexplained deviations

N = number of items in sample.

SECRET

SECRET

the distribution of data points about the regression line, and is defined as

$$\begin{aligned}
 s_{1.2} &= \sqrt{\frac{\sum_{n=1}^n (\text{unexplained deviations})^2}{\text{Degrees of Freedom}}} \\
 &= \sqrt{\frac{\sum_{n=1}^n (X_1 - X_{12})^2}{(N-2)}} \quad \text{(Linear least-squares line)} \\
 &= \sqrt{\frac{\sum_{n=1}^n (X_1 - X_{12})^2}{(N-3)}} \quad \text{(Quadratic least-squares line)}
 \end{aligned} \tag{2.2}$$

The standard error about the least-squares regression line may be interpreted in a manner analogous to the standard deviation of a frequency distribution as represented by the normal curve. It is a measure of the distribution of data points about the least-squares regression line, and its interpretation is demonstrated graphically in Fig. 2.2. The upper chart in Fig. 2.2 shows the relative frequency of events producing data points within various multiples of the standard error about the regression line if the distribution is normal. About two-thirds of all values would be within $X_{12} \pm s_{1.2}$, and all but 27 out 10,000 would fall within $X_{12} \pm 3s_{1.2}$. The lower chart is a more appropriate expression of this distribution for vulnerability analysis. This chart shows the frequency of events occurring below the various multiples of standard error about the regression line. Its use is best shown by example.

If we let D_1 equal maximum debris distance and W_2 , and W_3 the various equivalent yields, then the probability of a piece of debris being thrown as far as D_1 or beyond is 0.14 percent for W_1 , 2.9 percent for W_2 and 15.9 percent for W_3 . Similarly, for a weapon of yield W_3 the probability of a piece of debris being thrown a distance equal to or beyond D_1 is 15.9 percent; and is 2.9 percent for D_2 and 0.14 percent for D_3 .

SECRET

SECRET

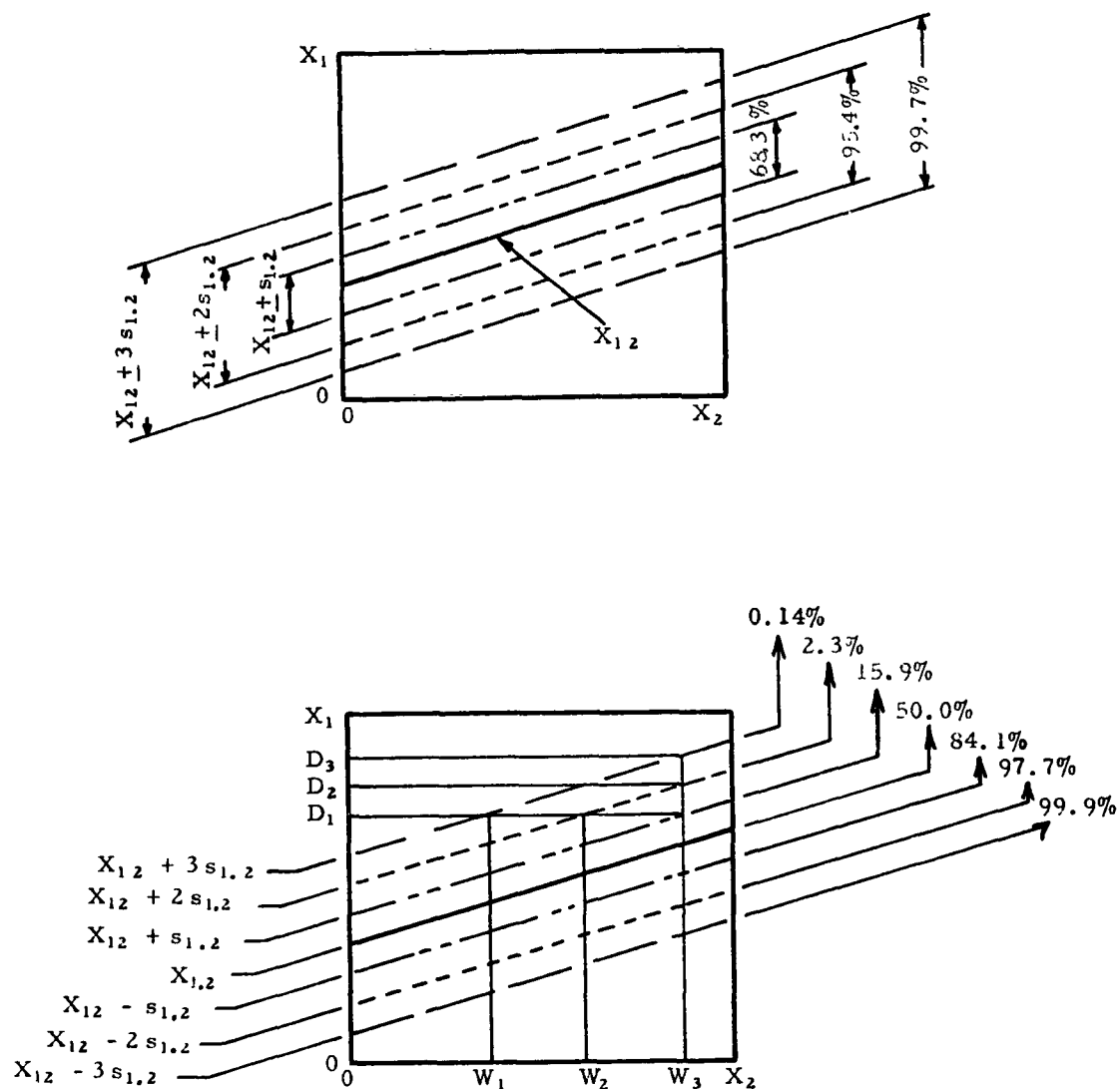


Figure 2.2 Normal Distribution of Events
about Least-Squares Regression Line

SECRET

SECRET

Standard error is expressed in units of the dependent variable and, as such, is not amenable to comparison with unlike quantities -- or moreover, with any general standard of closeness-of-fit. The correlation coefficient is a measure of scatter in dimensionless terms, and is defined as the square root of the ratio of the explained variation Σx_{12}^2 to the total variation Σx_1^2 ,

$$r = \sqrt{\frac{\Sigma x_{12}^2}{\Sigma x_1^2}}.$$

The correlation coefficient can be computed for the linear case by the expression

$$r = \sqrt{\frac{\Sigma X_{12}^2 - \bar{X} \Sigma X_1}{\Sigma X_1^2 - \bar{X} \Sigma X_1}}$$

and for the quadratic case by

$$r = \sqrt{1 - \frac{N-1}{N-3} \frac{\left(\Sigma X_1^2 - \frac{(\Sigma X_1)^2}{N} \right) - b'_{12} \left(\Sigma X_1 X_2 - \frac{\Sigma X_1 \Sigma X_{12}}{N} \right) - c'_{12} \left(\Sigma X_1 X_2 - \frac{\Sigma X_1 \Sigma X_2^2}{N} \right)}{\Sigma X_1^2 - \frac{(\Sigma X_1)^2}{N}}}.$$

The sign of r is positive for a regression line of positive slope, and negative for a regression line with a negative slope.

In general a correlation coefficient of +0.90 or greater indicates high positive correlation, and between zero and +0.10 indicates a low positive correlation. Positive correlation coefficients below +0.90 generally do not engender high degrees of confidence. A correlation coefficient of +0.50 or thereabouts is decidedly marginal.

2.2.2 Regression Study of Maximum Debris Distance

The quantities of explosives involved in the 206 explosions studied ranged from 8 lb to 9,000,000 lb, providing more than seven cycles of data. The total weight of explosive materials involved was about 50,000,000 lb. Since the largest explosion in this compilation involved 9,000,000 lb (4.5 kilotons of ammonium nitrate), extension of the regression lines to the magnitudes of nuclear weapon yields involves an extrapolation of one or two

SECRET

SECRET

orders of magnitude beyond the limits of plotted data. Their use in estimating maximum debris distance in the range of high-yield nuclear weapons requires extrapolation of three or four orders of magnitude beyond the limits of the plotted data. Thus, while there is no specific interest in the very small HE detonations, they are included in the total sample to extend the range of basic data -- while extrapolating several orders of magnitude beyond the limits of the data can be considered questionable under many circumstances, it is better to do so with seven cycles of data input than with a lesser amount.

A total of 40 linear and 40 quadratic regression lines, in logarithmic terms, was derived by computer methods. Each of the debris distance parameters,

Log_{10} maximum debris distance (ft)

Log_{10} cube-root maximum debris distance ($\text{ft}^{1/3}$)

Log_{10} 2/3-power maximum debris distance ($\text{ft}^{2/3}$)

Log_{10} $W^{1/3}$ -scaled maximum debris distance $\left(\frac{\text{ft}}{\text{tons}_{\text{TNT}}^{1/3}} \right)$

Log_{10} $W^{2/3}$ -scaled maximum debris distance $\left(\frac{\text{ft}}{\text{tons}_{\text{TNT}}^{2/3}} \right)$

was correlated against each of the explosion parameters:

Log_{10} equivalent yield (tons_{TNT})

Log_{10} impulse $\left(\frac{\text{lb-msec}}{\text{sq in.}} \right)$

Log_{10} cube-root equivalent yield ($\text{tons}_{\text{TNT}}^{1/3}$)

Log_{10} cube-root impulse $\left(\frac{\text{lb-msec}}{\text{sq in.}} \right)^{1/3}$

Log_{10} 2/3-power equivalent yield ($\text{tons}_{\text{TNT}}^{2/3}$)

Log_{10} 2/3-power impulse $\left(\frac{\text{lb-msec}}{\text{sq in.}} \right)^{2/3}$

Log $W^{1/3}$ -scaled impulse $\left(\frac{\text{lb-msec}}{\text{in}^2 - \text{tons}_{\text{TNT}}^{1/3}} \right)$

Log $W^{2/3}$ -scaled impulse $\left(\frac{\text{lb-msec}}{\text{in}^2 - \text{tons}_{\text{TNT}}^{2/3}} \right)$

SECRET

SECRET

The selection of associative relationships to be correlated was arbitrary. No analytical basis for a fixed relationship existed, and no justification for scaled relationships was apparent. By computer methods, the computation of a large number of correlations required little additional effort beyond that for the one or two obvious correlations, and provided the opportunity to check the relative closeness of fit for various approaches. The computer program outlined in Appendix B was written to type out coefficients for the regression lines, the standard error and the correlation coefficient. Regression study results are tabulated in Table 2.1. As this table shows, most correlation coefficients were between 0.51 and 0.69, which is not a high positive correlation. No single correlation appeared significantly better than all others. The quadratic correlations were only marginally better than the linear correlations. The improved correlation coefficients for the quadratic cases can sometimes be regarded as suspect, in fact, especially if they yield expressions indicating a continually increasing slope with increasing explosion size.

Several correlations were selected for plotting, together with their respective data points. These are presented in the following figures.

Fig. 2.3 Maximum Debris Distance Vs Equivalent Yield
(linear log-log scale)

Fig. 2.4 Maximum Debris Distance Vs Equivalent Yield
(quadratic log-log scale)

Fig. 2.5 $W^{1/3}$ -Scaled Maximum Debris Distance Vs
Equivalent Yield

Fig. 2.6 $W^{1/3}$ -Scaled Maximum Debris Distance Vs
Equivalent Yield

Fig. 2.7 Maximum Debris Distance Vs Impulse
(linear log-log scale)

Fig. 2.8 Maximum Debris Distance Vs Impulse
(quadratic log-log scale)

Fig. 2.9 $W^{1/3}$ -Scaled Maximum Debris Distance Vs
 $W^{1/3}$ -Scaled Impulse
(linear log-log scale)

Fig. 2.10 $W^{1/3}$ -Scaled Maximum Debris Distance Vs
 $W^{1/3}$ -Scaled Impulse
(quadratic log-log scale)

Text follows on page 51

SECRET

REGRESSION LINES FOR MAXIMUM DEBRIS D

Ta



Factors Correlated	Type of Correlation	Logarithmic Form
		Regression Line
Log ₁₀ Cube-Root Maximum Debris Distance (ft ^{1/3}) Versus Log ₁₀ Equivalent Yield (tons _{TNT})	Linear	$\text{Log}_{10} D_M^{1/3} = 0.982 + 0.107 \text{Log}_{10} W$
	Quadratic	$\text{Log}_{10} D_M^{1/3} = 0.986 + 0.116 \text{Log}_{10} W - 0.00536 (\text{Log}_{10} W)^2$
Log ₁₀ Cube-Root Maximum Debris Distance (ft ^{1/3}) Versus Log ₁₀ Impulse (lb-msec/in. ²)	Linear	$\text{Log}_{10} D_M^{1/3} = 0.525 + 0.139 \text{Log}_{10} I$
	Quadratic	$\text{Log}_{10} D_M^{1/3} = 0.457 + 0.177 \text{Log}_{10} I - 0.00503 (\text{Log}_{10} I)^2$
Log ₁₀ Cube-Root Maximum Debris Distance (ft ^{1/3}) Versus Log ₁₀ Cube-Root Equivalent Yield (tons _{TNT} ^{1/3})	Linear	$\text{Log}_{10} D_M^{1/3} = 0.982 + 0.322 \text{Log}_{10} W^{1/3}$
	Quadratic	$\text{Log}_{10} D_M^{1/3} = 0.986 + 0.347 \text{Log}_{10} W^{1/3} - 0.0484 (\text{Log}_{10} W^{1/3})^2$
Log ₁₀ Cube-Root Maximum Debris Distance (ft ^{1/3}) Versus Log ₁₀ Cube-Root Impulse (lb-msec/in. ²) ^{1/3}	Linear	$\text{Log}_{10} D_M^{1/3} = 0.525 + 0.416 \text{Log}_{10} I^{1/3}$
	Quadratic	$\text{Log}_{10} D_M^{1/3} = 0.457 + 0.531 \text{Log}_{10} I^{1/3} - 0.0454 (\text{Log}_{10} I^{1/3})^2$
Log ₁₀ Cube-Root Maximum Debris Distance (ft ^{1/3}) Versus Log ₁₀ ² / ₃ - Power Equivalent Yield (tons _{TNT} ^{2/3})	Linear	$\text{Log}_{10} D_M^{1/3} = 0.982 + 0.161 \text{Log}_{10} W^{2/3}$
	Quadratic	$\text{Log}_{10} D_M^{1/3} = 0.986 + 0.173 \text{Log}_{10} W^{2/3} - 0.0121 (\text{Log}_{10} W^{2/3})^2$
Log ₁₀ Cube-Root Maximum Debris Distance (ft ^{1/3}) Versus Log ₁₀ ² / ₃ - Power Impulse (lb-msec/in. ²) ^{2/3}	Linear	$\text{Log}_{10} D_M^{1/3} = 0.525 + 0.208 \text{Log}_{10} I^{2/3}$
	Quadratic	$\text{Log}_{10} D_M^{1/3} = 0.457 + 0.265 \text{Log}_{10} I^{2/3} - 0.0113 (\text{Log}_{10} I^{2/3})^2$
Log ₁₀ Cube-Root Maximum Debris Distance (ft ^{1/3}) Versus Log ₁₀ W ^{1/3} - Scaled Impulse (lb-msec/in. ² - tons _{TNT} ^{1/3})	Linear	$\text{Log}_{10} D_M^{1/3} = -0.779 + 0.544 \text{Log}_{10} \left(\frac{I}{W^{1/3}} \right)$
	Quadratic	$\text{Log}_{10} D_M^{1/3} = 4.689 - 2.893 \text{Log}_{10} \left(\frac{I}{W^{1/3}} \right) + 0.537 \left[\text{Log}_{10} \left(\frac{I}{W^{1/3}} \right) \right]^2$
Log ₁₀ Cube-Root Maximum Debris Distance (ft ^{1/3}) Versus Log ₁₀ W ^{2/3} - Scaled Impulse (lb-msec/in. ² - tons _{TNT} ^{2/3})	Linear	$\text{Log}_{10} D_M^{1/3} = 2.104 - 0.333 \text{Log}_{10} \left(\frac{I}{W^{2/3}} \right)$
	Quadratic	$\text{Log}_{10} D_M^{1/3} = 3.388 - 1.153 \text{Log}_{10} \left(\frac{I}{W^{2/3}} \right) + 0.131 \left[\text{Log}_{10} \left(\frac{I}{W^{2/3}} \right) \right]^2$

SECRET

SECRET

2

Table 2.1

S FOR MAXIMUM DEBRIS DISTANCE IN TERMS OF EXPLOSION PARAMETERS

Logarithmic Form		Exponential Form		Correlation Coefficient	Figure Number
Regression Line	Standard Error	Regression Line	Standard Error		
$D_M^{1/3} = 0.982 + 0.107 \log_{10} W$	± 0.131	$D_M^{1/3} = 9.60 W^{0.107}$	$\frac{x}{\div} 1.35$	0.67	
$D_M^{1/3} = 0.986 + 0.116 \log_{10} W - 0.00536 (\log_{10} W)^2$	± 0.131	$D_M^{1/3} = 9.68 W^{0.116} (10)^{-0.00536 (\log_{10} W)^2}$	$\frac{x}{\div} 1.35$	0.67	
$D_M^{1/3} = 0.525 + 0.139 \log_{10} I$	± 0.128	$D_M^{1/3} = 3.35 I^{0.139}$	$\frac{x}{\div} 1.34$	0.68	
$D_M^{1/3} = 0.457 + 0.177 \log_{10} I - 0.00503 (\log_{10} I)^2$	± 0.128	$D_M^{1/3} = 2.87 I^{0.177} (10)^{-0.00503 (\log_{10} I)^2}$	$\frac{x}{\div} 1.34$	0.68	
$D_M^{1/3} = 0.982 + 0.322 \log_{10} W^{1/3}$	± 0.131	$D_M^{1/3} = 9.60 (W^{1/3})^{0.322}$	$\frac{x}{\div} 1.35$	0.67	
$D_M^{1/3} = 0.986 + 0.347 \log_{10} W^{1/3} - 0.0484 (\log_{10} W^{1/3})^2$	± 0.131	$D_M^{1/3} = 9.68 (W^{1/3})^{0.347} (10)^{-0.0484 (\log_{10} W^{1/3})^2}$	$\frac{x}{\div} 1.35$	0.67	
$D_M^{1/3} = 0.525 + 0.416 \log_{10} I^{1/3}$	± 0.128	$D_M^{1/3} = 3.35 (I^{1/3})^{0.416}$	$\frac{x}{\div} 1.34$	0.68	
$D_M^{1/3} = 0.457 + 0.531 \log_{10} I^{1/3} - 0.0454 (\log_{10} I^{1/3})^2$	± 0.128	$D_M^{1/3} = 2.87 (I^{1/3})^{0.531} (10)^{-0.0454 (\log_{10} I^{1/3})^2}$	$\frac{x}{\div} 1.34$	0.68	
$D_M^{1/3} = 0.982 + 0.161 \log_{10} W^{2/3}$	± 0.131	$D_M^{1/3} = 9.60 (W^{2/3})^{0.161}$	$\frac{x}{\div} 1.35$	0.67	
$D_M^{1/3} = 0.986 + 0.173 \log_{10} W^{2/3} - 0.0121 (\log_{10} W^{2/3})^2$	± 0.131	$D_M^{1/3} = 9.68 (W^{2/3})^{0.173} (10)^{-0.0121 (\log_{10} W^{2/3})^2}$	$\frac{x}{\div} 1.35$	0.66	
$D_M^{1/3} = 0.525 + 0.208 \log_{10} I^{2/3}$	± 0.128	$D_M^{1/3} = 3.35 (I^{2/3})^{0.208}$	$\frac{x}{\div} 1.34$	0.68	
$D_M^{1/3} = 0.457 + 0.265 \log_{10} I^{2/3} - 0.0113 (\log_{10} I^{2/3})^2$	± 0.128	$D_M^{1/3} = 2.87 (I^{2/3})^{0.265} (10)^{-0.0113 (\log_{10} I^{2/3})^2}$	$\frac{x}{\div} 1.34$	0.68	
$D_M^{1/3} = -0.779 + 0.544 \log_{10} \left(\frac{I}{W^{1/3}} \right)$	± 0.145	$D_M^{1/3} = 0.166 \left(\frac{I}{W^{1/3}} \right)^{0.544}$	$\frac{x}{\div} 1.39$	0.57	
$D_M^{1/3} = 4.689 - 2.893 \log_{10} \left(\frac{I}{W^{1/3}} \right) + 0.537 \left[\log_{10} \left(\frac{I}{W^{1/3}} \right) \right]^2$	± 0.142	$D_M^{1/3} = 4.89 \times 10^4 \left(\frac{I}{W^{1/3}} \right)^{-2.893} (10)^{-0.537 \left[\log_{10} \left(\frac{I}{W^{1/3}} \right) \right]^2}$	$\frac{x}{\div} 1.39$	0.59	
$D_M^{1/3} = 2.104 - 0.333 \log_{10} \left(\frac{I}{W^{2/3}} \right)$	± 0.151	$D_M^{1/3} = 1.270 \times 10^2 \left(\frac{I}{W^{2/3}} \right)^{-0.333}$	$\frac{x}{\div} 1.42$	0.51	
$D_M^{1/3} = 3.388 - 1.153 \log_{10} \left(\frac{I}{W^{2/3}} \right) + 0.131 \left[\log_{10} \left(\frac{I}{W^{2/3}} \right) \right]^2$	± 0.150	$D_M^{1/3} = 2.444 \times 10^3 \left(\frac{I}{W^{2/3}} \right)^{-1.154} (10)^{0.130 \left[\log_{10} \left(\frac{I}{W^{2/3}} \right) \right]^2}$	$\frac{x}{\div} 1.41$	0.51	

Table 2.1 (C)

Factors Correlated	Type of Correlation	Logarithmic Form
		Regression Line
Log ₁₀ Maximum Debris Distance (ft) Versus Log ₁₀ Equivalent Yield (tons _{TNT})	Linear	Log ₁₀ D _M = 2.950 + 0.322 Log ₁₀ W
	Quadratic	Log ₁₀ D _M = 2.960 + 0.347 Log ₁₀ W - 0.0161 (Log ₁₀ W) ²
Log ₁₀ Maximum Debris Distance (ft) Versus Log ₁₀ Impulse (lb-msec/in. ²)	Linear	Log ₁₀ D _M = 1.578 + 0.416 Log ₁₀ I
	Quadratic	Log ₁₀ D _M = 1.373 + 0.531 Log ₁₀ I - 0.0151 (Log ₁₀ I) ²
Log ₁₀ Maximum Debris Distance (ft) Versus Log ₁₀ Cube-Root Equivalent Yield (tons _{TNT} ^{1/3})	Linear	Log ₁₀ D _M = 2.950 + 0.968 Log ₁₀ W ^{1/3}
	Quadratic	Log ₁₀ D _M = 2.960 + 1.042 Log ₁₀ W ^{1/3} - 0.145 (Log ₁₀ W ^{1/3}) ²
Log ₁₀ Maximum Debris Distance (ft) Versus Log ₁₀ Cube-Root Impulse (lb-msec/in. ²) ^{1/3}	Linear	Log ₁₀ D _M = 1.578 + 1.250 Log ₁₀ I ^{1/3}
	Quadratic	Log ₁₀ D _M = 1.373 + 1.593 Log ₁₀ I ^{1/3} - 0.136 (Log ₁₀ I ^{1/3}) ²
Log ₁₀ Maximum Debris Distance (ft) Versus Log ₁₀ $\frac{2}{3}$ - Power Equivalent Yield (tons _{TNT} ^{2/3})	Linear	Log ₁₀ D _M = 2.950 + 0.483 Log ₁₀ W ^{2/3}
	Quadratic	Log ₁₀ D _M = 2.960 + 0.520 Log ₁₀ W ^{2/3} - 0.0362 (Log ₁₀ W ^{2/3}) ²
Log ₁₀ Maximum Debris Distance (ft) Versus Log ₁₀ $\frac{2}{3}$ - Power Impulse (lb-msec/in. ²) ^{2/3}	Linear	Log ₁₀ D _M = 1.578 + 0.624 Log ₁₀ I ^{2/3}
	Quadratic	Log ₁₀ D _M = 1.373 + 0.795 (Log ₁₀ I ^{2/3}) - 0.0340 (Log ₁₀ I ^{2/3}) ²
Log ₁₀ Maximum Debris Distance (ft) Versus Log ₁₀ W ^{1/3} - Scaled Impulse (lb-msec/in. ² - tons _{TNT} ^{1/3})	Linear	Log ₁₀ D _M = - 2.338 + 1.634 Log ₁₀ $\left(\frac{I}{W^{1/3}}\right)$
	Quadratic	Log ₁₀ D _M = 14.08 - 8.69 Log ₁₀ $\left(\frac{I}{W^{1/3}}\right)$ + 1.612 $\left[\text{Log}_{10} \left(\frac{I}{W^{1/3}}\right)\right]^2$
Log ₁₀ Maximum Debris Distance (ft) Versus Log ₁₀ W ^{2/3} - Scaled Impulse (lb-msec/in. ² - tons _{TNT} ^{2/3})	Linear	Log ₁₀ D _M = 6.317 - 1.001 Log ₁₀ $\left(\frac{I}{W^{2/3}}\right)$
	Quadratic	Log ₁₀ D _M = 10.17 - 3.462 Log ₁₀ $\left(\frac{I}{W^{2/3}}\right)$ + 0.390 $\left[\text{Log}_{10} \left(\frac{I}{W^{2/3}}\right)\right]^2$

SECRET

Table 2.1 (Continued)

2

SECRET

Logarithmic Form		Exponential Form		Correlation Coefficient	Figure Number
Regression Line	Standard Error	Regression Line	Standard Error		
$= 2.950 + 0.322 \log_{10} W$	± 0.392	$D_M = 892 W^{0.322}$	$\frac{x}{\div} 2.47$	0.67	2.3
$= 2.960 + 0.347 \log_{10} W - 0.0161 (\log_{10} W)^2$	± 0.392	$D_M = 912 W^{0.347} (10)^{-0.0161 (\log W)^2}$	$\frac{x}{\div} 2.47$	0.67	2.4
$= 1.578 + 0.416 \log_{10} I$	± 0.385	$D_M = 38 I^{0.416}$	$\frac{x}{\div} 2.43$	0.68	2.7
$= 1.373 + 0.531 \log_{10} I - 0.0151 (\log_{10} I)^2$	± 0.386	$D_M = 24 I^{0.531} (10)^{-0.0151 (\log_{10} I)^2}$	$\frac{x}{\div} 2.43$	0.68	2.8
$= 2.950 + 0.968 \log_{10} W^{1/3}$	± 0.392	$D_M = 892 (W^{1/3})^{0.968}$	$\frac{x}{\div} 2.47$	0.67	
$= 2.960 + 1.042 \log_{10} W^{1/3} - 0.145 (\log_{10} W^{1/3})^2$	± 0.392	$D_M = 912 (W^{1/3})^{1.042} (10)^{-0.145 (\log_{10} W^{1/3})^2}$	$\frac{x}{\div} 2.47$	0.67	
$= 1.578 + 1.250 \log_{10} I^{1/3}$	± 0.385	$D_M = 38 (I^{1/3})^{1.250}$	$\frac{x}{\div} 2.43$	0.68	
$= 1.373 + 1.593 \log_{10} I^{1/3} - 0.136 (\log_{10} I^{1/3})^2$	± 0.386	$D_M = 24 (I^{1/3})^{1.593} (10)^{-0.136 (\log_{10} I^{1/3})^2}$	$\frac{x}{\div} 2.43$	0.68	
$= 2.950 + 0.483 \log_{10} W^{2/3}$	± 0.392	$D_M = 892 (W^{2/3})^{0.484}$	$\frac{x}{\div} 2.47$	0.67	
$= 2.960 + 0.520 \log_{10} W^{2/3} - 0.0362 (\log_{10} W^{2/3})^2$	± 0.392	$D_M = 912 (W^{2/3})^{0.520} (10)^{-0.0362 (\log_{10} W^{2/3})^2}$	$\frac{x}{\div} 2.47$	0.67	
$= 1.578 + 0.624 \log_{10} I^{2/3}$	± 0.385	$D_M = 38 (I^{2/3})^{0.624}$	$\frac{x}{\div} 2.43$	0.68	
$= 1.373 + 0.795 (\log_{10} I^{2/3} - 0.0340 (\log_{10} I^{2/3})^2)$	± 0.386	$D_M = 24 (I^{2/3})^{0.795} (10)^{-0.0340 (\log_{10} I^{2/3})^2}$	$\frac{x}{\div} 2.43$	0.68	
$= -2.338 + 1.634 \log_{10} \left(\frac{I}{W^{1/3}} \right)$	± 0.434	$D_M = 0.00459 \left(\frac{I}{W^{1/3}} \right)^{1.634}$	$\frac{x}{\div} 2.72$	0.57	
$14.08 - 8.69 \log_{10} \left(\frac{I}{W^{1/3}} \right) + 1.612 \left[\log_{10} \left(\frac{I}{W^{1/3}} \right) \right]^2$	± 0.426	$D_M = 1.211 \times 10^{14} \left(\frac{I}{W^{1/3}} \right)^{-8.69} (10)^{-1.612 \left[\log_{10} \left(\frac{I}{W^{1/3}} \right) \right]^2}$	$\frac{x}{\div} 2.66$	0.59	
$= 6.317 - 1.001 \log_{10} \left(\frac{I}{W^{2/3}} \right)$	± 0.456	$D_M = 2.078 \times 10^6 \left(\frac{I}{W^{2/3}} \right)^{-1.001}$	$\frac{x}{\div} 2.84$	0.51	
$= 10.17 - 3.462 \log_{10} \left(\frac{I}{W^{2/3}} \right) + 0.390 \left[\log_{10} \left(\frac{I}{W^{2/3}} \right) \right]^2$	± 0.451	$D_M = 1.483 \times 10^{10} \left(\frac{I}{W^{2/3}} \right)^{-3.462} (10)^{0.390 \left[\log_{10} \left(\frac{I}{W^{2/3}} \right) \right]^2}$	$\frac{x}{\div} 2.83$	0.51	

Table 2.1 (C)

Factors Correlated	Type of Correlation	Logarithmic Form
		Regression Line
$\log_{10} \frac{2}{3}$ - Power Maximum Debris Distance (ft ^{2/3}) Versus \log_{10} Equivalent Yield (tons _{TNT})	Linear	$\log_{10} D_M^{2/3} = 1.968 + 0.215 \log_{10} W$
	Quadratic	$\log_{10} D_M^{2/3} = 1.974 + 0.231 \log_{10} W - 0.0108 (\log_{10} W)^2$
$\log_{10} \frac{2}{3}$ - Power Maximum Debris Distance (ft ^{2/3}) Versus \log_{10} Impulse (lb-msec/in. ²)	Linear	$\log_{10} D_M^{2/3} = 1.052 + 0.278 \log_{10} I$
	Quadratic	$\log_{10} D_M^{2/3} = 0.916 + 0.354 \log_{10} I - 0.0101 (\log_{10} I)^2$
$\log_{10} \frac{2}{3}$ - Power Maximum Debris Distance (ft ^{2/3}) Versus \log_{10} Cube-Root Equivalent Yield (tons _{TNT} ^{1/3})	Linear	$\log_{10} D_M^{2/3} = 1.968 + 0.646 \log_{10} W^{1/3}$
	Quadratic	$\log_{10} D_M^{2/3} = 1.974 + 0.695 \log_{10} W^{1/3} - 0.0969 (\log_{10} W^{1/3})^2$
$\log_{10} \frac{2}{3}$ - Power Maximum Debris Distance (ft ^{2/3}) Versus \log_{10} Cube-Root Impulse (lb-msec/in. ²) ^{1/3}	Linear	$\log_{10} D_M^{2/3} = 1.052 + 0.834 \log_{10} I^{1/3}$
	Quadratic	$\log_{10} D_M^{2/3} = 0.916 + 1.062 \log_{10} I^{1/3} - 0.0909 (\log_{10} I^{1/3})^2$
$\log_{10} \frac{2}{3}$ - Power Maximum Debris Distance (ft ^{2/3}) Versus $\log_{10} \frac{2}{3}$ - Power Equivalent Yield (tons _{TNT} ^{2/3})	Linear	$\log_{10} D_M^{2/3} = 1.968 + 0.322 \log_{10} W^{2/3}$
	Quadratic	$\log_{10} D_M^{2/3} = 1.974 + 0.347 \log_{10} W^{2/3} - 0.0242 (\log_{10} W^{2/3})^2$
$\log_{10} \frac{2}{3}$ - Power Maximum Debris Distance (ft ^{2/3}) Versus $\log_{10} \frac{2}{3}$ - Power Impulse (lb-msec/in. ²) ^{2/3}	Linear	$\log_{10} D_M^{2/3} = 1.052 + 0.15 \log_{10} I^{2/3}$
	Quadratic	$\log_{10} D_M^{2/3} = 0.916 + 0.530 \log_{10} I^{2/3} - 0.0227 (\log_{10} I^{2/3})^2$
$\log_{10} \frac{2}{3}$ - Power Maximum Debris Distance (ft ^{2/3}) Versus $\log_{10} W^{1/3}$ - Scaled Impulse (lb-msec/in. ² - tons _{TNT} ^{1/3})	Linear	$\log_{10} D_M^{2/3} = 1.560 + 1.090 \log_{10} \left(\frac{I}{W^{1/3}} \right)$
	Quadratic	$\log_{10} D_M^{2/3} = 9.405 - 5.803 \log_{10} \left(\frac{I}{W^{1/3}} \right) + 1.077 \left[\log_{10} \left(\frac{I}{W^{1/3}} \right) \right]^2$
$\log_{10} \frac{2}{3}$ - Power Maximum Debris Distance (ft ^{2/3}) Versus $\log_{10} W^{2/3}$ - Scaled Impulse (lb-msec/in. ² - tons _{TNT} ^{2/3})	Linear	$\log_{10} D_M^{2/3} = 4.214 - 0.0667 \log_{10} \left(\frac{I}{W^{2/3}} \right)$
	Quadratic	$\log_{10} D_M^{2/3} = 6.786 - 2.310 \log_{10} \left(\frac{I}{W^{2/3}} \right) + 0.0260 \left[\log_{10} \left(\frac{I}{W^{2/3}} \right) \right]^2$

SECRET

SECRET

2

Table 2.1 (Continued)

Logarithmic Form		Exponential Form		Correlation Coefficient	Figure Number
Regression Line	Standard Error	Regression Line	Standard Error		
$\frac{2}{3} = 1.968 + 0.215 \log_{10} W$	± 0.262	$D_M^{2/3} = 92.9 W^{0.215}$	$\frac{x}{\div} 1.83$	0.67	
$\frac{2}{3} = 1.974 + 0.231 \log_{10} W - 0.0108 (\log_{10} W)^2$	± 0.262	$D_M^{2/3} = 94.3 W^{0.231} (10)^{-0.0107 (\log_{10} W)^2}$	$\frac{x}{\div} 1.83$	0.67	
$\frac{2}{3} = 1.052 + 0.278 \log_{10} I$	± 0.257	$D_M^{2/3} = 11.28 I^{0.278}$	$\frac{x}{\div} 1.81$	0.68	
$\frac{2}{3} = 0.916 + 0.354 \log_{10} I - 0.0101 (\log_{10} I)^2$	± 0.257	$D_M^{2/3} = 8.24 I^{0.354} (10)^{-0.0101 (\log_{10} I)^2}$	$\frac{x}{\div} 1.81$	0.68	
$\frac{2}{3} = 1.968 + 0.646 \log_{10} W^{1/3}$	± 0.262	$D_M^{2/3} = 92.86 (W^{1/3})^{0.646}$	$\frac{x}{\div} 1.83$	0.67	
$\frac{2}{3} = 1.974 + 0.695 \log_{10} W^{1/3} - 0.0969 (\log_{10} W^{1/3})^2$	± 0.262	$D_M^{2/3} = 94.27 (W^{1/3})^{0.695} (10)^{-0.0969 (\log_{10} W^{1/3})^2}$	$\frac{x}{\div} 1.83$	0.67	
$\frac{2}{3} = 1.052 + 0.834 \log_{10} I^{1/3}$	± 0.257	$D_M^{2/3} = 11.28 (I^{1/3})^{0.834}$	$\frac{x}{\div} 1.81$	0.68	
$\frac{2}{3} = 0.916 + 1.062 \log_{10} I^{1/3} - 0.0909 (\log_{10} I^{1/3})^2$	± 0.257	$D_M^{2/3} = 8.24 (I^{1/3})^{1.062} (10)^{-0.0909 (\log_{10} I^{1/3})^2}$	$\frac{x}{\div} 1.81$	0.68	
$\frac{2}{3} = 1.968 + 0.322 \log_{10} W^{2/3}$	± 0.262	$D_M^{2/3} = 92.86 (W^{2/3})^{0.322}$	$\frac{x}{\div} 1.83$	0.67	
$\frac{2}{3} = 1.974 + 0.347 \log_{10} W^{2/3} - 0.0242 (\log_{10} W^{2/3})^2$	± 0.262	$D_M^{2/3} = 94.27 (W^{2/3})^{0.347} (10)^{-0.0242 (\log_{10} W^{2/3})^2}$	$\frac{x}{\div} 1.83$	0.67	
$\frac{2}{3} = 1.052 + 0.416 \log_{10} I^{2/3}$	± 0.257	$D_M^{2/3} = 11.28 (I^{2/3})^{0.416}$	$\frac{x}{\div} 1.81$	0.68	
$\frac{2}{3} = 0.916 + 0.530 \log_{10} I^{2/3} - 0.0227 (\log_{10} I^{2/3})^2$	± 0.257	$D_M^{2/3} = 8.24 (I^{2/3})^{0.530} (10)^{-0.0227 (\log_{10} I^{2/3})^2}$	$\frac{x}{\div} 1.81$	0.68	
$\frac{2}{3} = 1.560 + 1.090 \log_{10} \left(\frac{I}{W^{1/3}} \right)$	± 0.290	$D_M^{2/3} = 2.756 \times 10^{-2} \left(\frac{I}{W^{1/3}} \right)^{1.090}$	$\frac{x}{\div} 1.95$	0.57	
$\frac{2}{3} = 9.405 - 5.803 \log_{10} \left(\frac{I}{W^{1/3}} \right) + 1.077 \left[\log_{10} \left(\frac{I}{W^{1/3}} \right) \right]^2$	± 0.284	$D_M^{2/3} = 2.54 \times 10^9 \left(\frac{I}{W^{1/3}} \right)^{-5.80} (10)^{1.077 \left[\log_{10} \left(\frac{I}{W^{1/3}} \right) \right]^2}$	$\frac{x}{\div} 1.92$	0.59	
$\frac{2}{3} = 4.214 - 0.0667 \log_{10} \left(\frac{I}{W^{2/3}} \right)$	± 0.303	$D_M^{2/3} = 1.636 \times 10^4 \left(\frac{I}{W^{2/3}} \right)^{-0.0667}$	$\frac{x}{\div} 2.01$	0.51	
$\frac{2}{3} = 6.786 - 2.310 \log_{10} \left(\frac{I}{W^{2/3}} \right) + 0.0260 \left[\log_{10} \left(\frac{I}{W^{2/3}} \right) \right]^2$	± 0.301	$D_M^{2/3} = 6.107 \times 10^6 \left(\frac{I}{W^{2/3}} \right)^{-2.310} (10)^{0.0262 \left[\log_{10} \left(\frac{I}{W^{2/3}} \right) \right]^2}$	$\frac{x}{\div} 2.00$	0.51	

Table 2.1 (Cont)

Factors Correlated	Type of Correlation	Logarithmic Form	
		Regression Line	
$\log_{10} W^{1/3}$ - Scaled Maximum Debris Distance (ft/tons _{TNT} ^{1/3}) Versus \log_{10} Equivalent Yield (tons _{TNT})	Linear	$\log_{10} \left(\frac{D_M}{W^{1/3}} \right) = 2.950 - 0.0105 \log_{10} W$	
	Quadratic	$\log_{10} \left(\frac{D_M}{W^{1/3}} \right) = 2.960 + 0.0140 \log_{10} W - 0.0161 (\log_{10} W)^2$	
$\log_{10} W^{1/3}$ - Scaled Maximum Debris Distance (ft/tons _{TNT} ^{1/3}) Versus \log_{10} Impulse (lb-msec/in. ²)	Linear	$\log_{10} \left(\frac{D_M}{W^{1/3}} \right) = 2.941 + 0.00048 \log_{10} I$	
	Quadratic	$\log_{10} \left(\frac{D_M}{W^{1/3}} \right) = 2.401 + 0.302 \log_{10} I - 0.399 (\log_{10} I)^2$	
$\log_{10} W^{1/3}$ - Scaled Maximum Debris Distance (ft/tons _{TNT} ^{1/3}) Versus \log_{10} Cube-Root Equivalent Yield (tons _{TNT} ^{1/3})	Linear	$\log_{10} \left(\frac{D_M}{W^{1/3}} \right) = 2.950 - 0.0316 \log_{10} W^{1/3}$	
	Quadratic	$\log_{10} \left(\frac{D_M}{W^{1/3}} \right) = 2.960 + 0.042 \log_{10} W^{1/3} - 0.145 (\log_{10} W^{1/3})^2$	
$\log_{10} W^{1/3}$ - Scaled Maximum Debris Distance (ft/tons _{TNT} ^{1/3}) Versus \log_{10} Cube-Root Impulse (lb-msec/in. ²) ^{1/3}	Linear	$\log_{10} \left(\frac{D_M}{W^{1/3}} \right) = 2.941 + 0.00144 \log_{10} I^{1/3}$	
	Quadratic	$\log_{10} \left(\frac{D_M}{W^{1/3}} \right) = 2.401 + 0.907 \log_{10} I^{1/3} - 0.360 (\log_{10} I^{1/3})^2$	
$\log_{10} W^{1/3}$ - Scaled Maximum Debris Distance (ft/tons _{TNT} ^{1/3}) Versus $\log_{10} \frac{2}{3}$ - Power Equivalent Yield (tons _{TNT} ^{2/3})	Linear	$\log_{10} \left(\frac{D_M}{W^{1/3}} \right) = 2.950 - 0.0158 \log_{10} W^{2/3}$	
	Quadratic	$\log_{10} \left(\frac{D_M}{W^{1/3}} \right) = 2.960 + 0.0210 \log_{10} W^{2/3} - 0.0362 (\log_{10} W^{2/3})^2$	
$\log_{10} W^{1/3}$ - Scaled Maximum Debris Distance (ft/tons _{TNT} ^{1/3}) Versus $\log_{10} \frac{2}{3}$ - Power Impulse (lb-msec/in. ²) ^{2/3}	Linear	$\log_{10} \left(\frac{D_M}{W^{1/3}} \right) = 2.941 + 0.00072 \log_{10} I^{2/3}$	
	Quadratic	$\log_{10} \left(\frac{D_M}{W^{1/3}} \right) = 2.401 + 0.453 \log_{10} I^{2/3} - 0.0898 (\log_{10} I^{2/3})^2$	
$\log_{10} W^{1/3}$ - Scaled Maximum Debris Distance (ft/tons _{TNT} ^{1/3}) Versus $\log_{10} W^{1/3}$ - Scaled Impulse (lb-msec/in. ² - tons _{TNT} ^{1/3})	Linear	$\log_{10} \left(\frac{D_M}{W^{1/3}} \right) = 2.067 + 0.260 \log_{10} \left(\frac{I}{W^{1/3}} \right)$	
	Quadratic	$\log_{10} \left(\frac{D_M}{W^{1/3}} \right) = 2.504 - 0.0150 \log_{10} \left(\frac{I}{W^{1/3}} \right) + 0.0429 \left[\log_{10} \left(\frac{I}{W^{1/3}} \right) \right]^2$	
$\log_{10} W^{1/3}$ - Scaled Maximum Debris Distance (ft/tons _{TNT} ^{1/3}) Versus $\log_{10} W^{2/3}$ - Scaled Impulse (lb-msec/in. ² - tons _{TNT} ^{2/3})	Linear	$\log_{10} \left(\frac{D_M}{W^{1/3}} \right) = 2.382 + 0.178 \log_{10} \left(\frac{I}{W^{2/3}} \right)$	
	Quadratic	$\log_{10} \left(\frac{D_M}{W^{1/3}} \right) = 3.369 - 0.452 \log_{10} \left(\frac{I}{W^{2/3}} \right) + 0.100 \left[\log_{10} \left(\frac{I}{W^{2/3}} \right) \right]^2$	

SECRET

Table 2.1 (Continued)

Logarithmic Form		Exponential Form		Correlation Coefficient	Figure Number
Regression Line	Standard Error	Regression Line	Standard Error		
$\frac{M}{I^{1/3}} = 2.950 - 0.0105 \log_{10} W$	± 0.392	$\frac{D_M}{W^{1/3}} = 892 W^{-0.0105}$	$\frac{x}{\div} 2.47$	0.029	2.5
$\frac{M}{I^{1/3}} = 2.960 + 0.0140 \log_{10} W - 0.0161 (\log_{10} W)^2$	± 0.392	$\frac{D_M}{W^{1/3}} = 912 W^{0.0140} (10)^{-0.0161 (\log_{10} W)^2}$	$\frac{x}{\div} 2.47$	0.059	2.6
$\frac{M}{I^{1/3}} = 2.941 + 0.00048 \log_{10} I$	± 0.392	$\frac{D_M}{W^{1/3}} = 874 I^{0.00048}$	$\frac{x}{\div} 2.47$	0.0012	
$\frac{M}{I^{1/3}} = 2.401 + 0.302 \log_{10} I - 0.399 (\log_{10} I)^2$	± 0.391	$\frac{D_M}{W^{1/3}} = 252 I^{0.302} (10)^{-0.399 (\log_{10} I)^2}$	$\frac{x}{\div} 2.46$	0.053	
$\frac{M}{I^{1/3}} = 2.950 - 0.0316 \log_{10} W^{1/3}$	± 0.392	$\frac{D_M}{W^{1/3}} = 892 (W^{1/3})^{-0.0316}$	$\frac{x}{\div} 2.47$	0.029	
$\frac{M}{I^{1/3}} = 2.960 + 0.042 \log_{10} W^{1/3} - 0.145 (\log_{10} W^{1/3})^2$	± 0.392	$\frac{D_M}{W^{1/3}} = 912 (W^{1/3})^{0.042} (10)^{-0.145 (\log_{10} W^{1/3})^2}$	$\frac{x}{\div} 2.47$	0.059	
$\frac{M}{I^{1/3}} = 2.941 + 0.00144 \log_{10} I^{1/3}$	± 0.392	$\frac{D_M}{W^{1/3}} = 874 (I^{1/3})^{0.00144}$	$\frac{x}{\div} 2.47$	0.0010	
$\frac{M}{I^{1/3}} = 2.401 + 0.907 \log_{10} I^{1/3} - 0.360 (\log_{10} I^{1/3})^2$	± 0.391	$\frac{D_M}{W^{1/3}} = 252 (I^{1/3})^{0.907} (10)^{-0.360 (\log_{10} I^{1/3})^2}$	$\frac{x}{\div} 2.46$	0.053	
$\frac{M}{I^{1/3}} = 2.950 - 0.0158 \log_{10} W^{2/3}$	± 0.392	$\frac{D_M}{W^{1/3}} = 892 (W^{2/3})^{-0.0158}$	$\frac{x}{\div} 2.47$	0.029	
$\frac{M}{I^{1/3}} = 2.960 + 0.0210 \log_{10} W^{2/3} - 0.0362 (\log_{10} W^{2/3})^2$	± 0.392	$\frac{D_M}{W^{1/3}} = 912 (W^{2/3})^{0.0210} (10)^{-0.0362 (\log_{10} W^{2/3})^2}$	$\frac{x}{\div} 2.47$	0.059	
$\frac{M}{I^{1/3}} = 2.941 + 0.00072 \log_{10} I^{2/3}$	± 0.392	$\frac{D_M}{W^{1/3}} = 873 (I^{2/3})^{0.00072}$	$\frac{x}{\div} 2.47$	0.0012	
$\frac{M}{I^{1/3}} = 2.401 + 0.453 \log_{10} I^{2/3} - 0.0898 (\log_{10} I^{2/3})^2$	± 0.391	$\frac{D_M}{W^{1/3}} = 252 (I^{2/3})^{0.453} (10)^{-0.0898 (\log_{10} I^{2/3})^2}$	$\frac{x}{\div} 2.46$	0.053	
$\frac{M}{I^{1/3}} = 2.067 + 0.260 \log_{10} \left(\frac{I}{W^{1/3}} \right)$	± 0.390	$\frac{D_M}{W^{1/3}} = 117 \left(\frac{I}{W^{1/3}} \right)^{0.260}$	$\frac{x}{\div} 2.45$	0.12	2.9
$\frac{M}{I^{1/3}} = 2.504 - 0.0150 \log_{10} \left(\frac{I}{W^{1/3}} \right) + 0.0429 \left[\log_{10} \left(\frac{I}{W^{1/3}} \right) \right]^2$	± 0.391	$\frac{D_M}{W^{1/3}} = 320 \left(\frac{I}{W^{1/3}} \right)^{-0.0150} (10)^{0.0429 \left[\log_{10} \left(\frac{I}{W^{1/3}} \right) \right]^2}$	$\frac{x}{\div} 2.46$	0.072	2.10
$\frac{M}{I^{1/3}} = 2.382 + 0.178 \log_{10} \left(\frac{I}{W^{2/3}} \right)$	± 0.390	$\frac{D_M}{W^{1/3}} = 241 \left(\frac{I}{W^{2/3}} \right)^{0.178}$	$\frac{x}{\div} 2.45$	0.12	
$\frac{M}{I^{1/3}} = 3.369 - 0.452 \log_{10} \left(\frac{I}{W^{2/3}} \right) + 0.100 \left[\log_{10} \left(\frac{I}{W^{2/3}} \right) \right]^2$	± 0.390	$\frac{D_M}{W^{1/3}} = 234 \left(\frac{I}{W^{2/3}} \right)^{-0.452} (10)^{0.100 \left[\log_{10} \left(\frac{I}{W^{2/3}} \right) \right]^2}$	$\frac{x}{\div} 2.46$	0.081	

Table 2.1 (Cont)

Factors Correlated	Type of Correlation	Logarithmic Form	
		Regression Line	
$\text{Log}_{10} W^{2/3}$ - Scaled Maximum Debris Distance (ft/tons $_{\text{TNT}}^{2/3}$) Versus Log_{10} Equivalent Yield (tons $_{\text{TNT}}$)	Linear	$\text{Log}_{10} \left(\frac{D_M}{W^{2/3}} \right) = 2.950 - 0.345 \text{Log}_{10} W$	
	Quadratic	$\text{Log}_{10} \left(\frac{D_M}{W^{2/3}} \right) = 2.960 - 0.320 \text{Log}_{10} W - 0.0161 (\text{Log}_{10} W)^2$	
$\text{Log}_{10} W^{2/3}$ - Scaled Maximum Debris Distance (ft/tons $_{\text{TNT}}^{2/3}$) Versus Log_{10} Impulse (lb-msec/in. 2)	Linear	$\text{Log}_{10} \left(\frac{D_M}{W^{2/3}} \right) = 4.309 - 0.417 \text{Log}_{10} I$	
	Quadratic	$\text{Log}_{10} \left(\frac{D_M}{W^{2/3}} \right) = 3.432 + 0.0731 \text{Log}_{10} I - 0.0648 (\text{Log}_{10} I)^2$	
$\text{Log}_{10} W^{2/3}$ - Scaled Maximum Debris Distance (ft/tons $_{\text{TNT}}^{2/3}$) Versus Log_{10} Cube-Root Equivalent Yield (tons $_{\text{TNT}}^{1/3}$)	Linear	$\text{Log}_{10} \left(\frac{D_M}{W^{2/3}} \right) = 2.905 - 1.035 \text{Log}_{10} W^{1/3}$	
	Quadratic	$\text{Log}_{10} \left(\frac{D_M}{W^{2/3}} \right) = 2.960 - 0.961 \text{Log}_{10} W^{1/3} - 1.453 (\text{Log}_{10} W^{1/3})^2$	
$\text{Log}_{10} W^{2/3}$ - Scaled Maximum Debris Distance (ft/tons $_{\text{TNT}}^{2/3}$) Versus Log_{10} Cube-Root Impulse (lb-msec/in. 2) $^{1/3}$	Linear	$\text{Log}_{10} \left(\frac{D_M}{W^{2/3}} \right) = 4.309 - 1.251 \text{Log}_{10} I^{1/3}$	
	Quadratic	$\text{Log}_{10} \left(\frac{D_M}{W^{2/3}} \right) = 3.432 + 0.219 \text{Log}_{10} I^{1/3} - 0.585 (\text{Log}_{10} I^{1/3})^2$	
$\text{Log}_{10} W^{2/3}$ - Scaled Maximum Debris Distance (ft/tons $_{\text{TNT}}^{2/3}$) Versus $\text{Log}_{10} \frac{2}{3}$ - Power Equivalent Yield (tons $_{\text{TNT}}^{2/3}$)	Linear	$\text{Log}_{10} \left(\frac{D_M}{W^{2/3}} \right) = 2.950 - 0.517 \text{Log}_{10} W^{2/3}$	
	Quadratic	$\text{Log}_{10} \left(\frac{D_M}{W^{2/3}} \right) = 2.960 - 0.480 \text{Log}_{10} W^{2/3} - 0.0362 (\text{Log}_{10} W^{2/3})^2$	
$\text{Log}_{10} W^{2/3}$ - Scaled Maximum Debris Distance (ft/tons $_{\text{TNT}}^{2/3}$) Versus $\text{Log}_{10} \frac{2}{3}$ - Power Impulse (lb-msec/in. 2) $^{2/3}$	Linear	$\text{Log}_{10} \left(\frac{D_M}{W^{2/3}} \right) = 4.309 - 0.625 \text{Log}_{10} I^{2/3}$	
	Quadratic	$\text{Log}_{10} \left(\frac{D_M}{W^{2/3}} \right) = 3.432 + 0.1096 \text{Log}_{10} I^{2/3} - 0.1457 (\text{Log}_{10} I^{2/3})^2$	
$\text{Log}_{10} W^{2/3}$ - Scaled Maximum Debris Distance (ft/tons $_{\text{TNT}}^{2/3}$) Versus $\text{Log}_{10} W^{1/3}$ - Scaled Impulse (lb-msec/in. 2 - tons $_{\text{TNT}}^{1/3}$)	Linear	$\text{Log}_{10} \left(\frac{D_M}{W^{2/3}} \right) = 6.486 - 1.118 \text{Log}_{10} \left(\frac{I}{W^{1/3}} \right)$	
	Quadratic	$\text{Log}_{10} \left(\frac{D_M}{W^{2/3}} \right) = -9.111 + 8.69 \text{Log}_{10} \left(\frac{I}{W^{1/3}} \right) - 1.531 \left[\text{Log}_{10} \left(\frac{I}{W^{1/3}} \right) \right]^2$	
$\text{Log}_{10} W^{2/3}$ - Scaled Maximum Debris Distance (ft/tons $_{\text{TNT}}^{2/3}$) Versus $\text{Log}_{10} W^{2/3}$ - Scaled Impulse (lb-msec/in. 2 - tons $_{\text{TNT}}^{2/3}$)	Linear	$\text{Log}_{10} \left(\frac{D_M}{W^{2/3}} \right) = 1.565 + 1.361 \text{Log}_{10} \left(\frac{I}{W^{2/3}} \right)$	
	Quadratic	$\text{Log}_{10} \left(\frac{D_M}{W^{2/3}} \right) = -3.451 + 2.565 \text{Log}_{10} \left(\frac{I}{W^{2/3}} \right) - 1.910 \left[\text{Log}_{10} \left(\frac{I}{W^{2/3}} \right) \right]^2$	

SECRET

Table 2.1 (Continued)

Logarithmic Form		Exponential Form		Correlation Coefficient	Figure Number
Regression Line	Standard Error	Regression Line	Standard Error		
$\frac{D}{3} = 2.950 - 0.345 \log_{10} W$	± 0.392	$\frac{D_M}{W^{2/3}} = 892 W^{-0.345}$	$\frac{x}{\div} 2.47$	0.69	
$\frac{D}{3} = 2.960 - 0.320 \log_{10} W - 0.0151 (\log_{10} W)^2$	± 0.392	$\frac{D_M}{W^{2/3}} = 912 W^{-0.320} (10)^{-0.0161 (\log_{10} W)^2}$	$\frac{x}{\div} 2.47$	0.69	
$\frac{D}{3} = 4.309 - 0.417 \log_{10} I$	± 0.407	$\frac{D_M}{W^{2/3}} = 2.04 \times 10^4 I^{-0.417}$	$\frac{x}{\div} 2.55$	0.66	
$\frac{D}{3} = 3.432 + 0.0731 \log_{10} I - 0.0648 (\log_{10} I)^2$	± 0.402	$\frac{D_M}{W^{2/3}} = 2.71 \times 10^3 I^{0.0731} (10)^{-0.0648 (\log_{10} I)^2}$	$\frac{x}{\div} 2.52$	0.67	
$\frac{D}{3} = 2.905 - 1.035 \log_{10} W^{1/3}$	± 0.392	$\frac{D_M}{W^{2/3}} = 892 (W^{1/3})^{-1.035}$	$\frac{x}{\div} 2.47$	0.69	
$\frac{D}{3} = 2.960 - 0.961 \log_{10} W^{1/3} - 1.453 (\log_{10} W^{1/3})^2$	± 0.392	$\frac{D_M}{W^{2/3}} = 912 (W^{1/3})^{-0.961} (10)^{-1.453 (\log_{10} W^{1/3})^2}$	$\frac{x}{\div} 2.47$	0.69	
$\frac{D}{3} = 4.309 - 1.251 \log_{10} I^{1/3}$	± 0.407	$\frac{D_M}{W^{2/3}} = 2.04 \times 10^4 (I^{1/3})^{-1.251}$	$\frac{x}{\div} 2.55$	0.66	
$\frac{D}{3} = 3.432 + 0.277 \log_{10} I^{1/3} - 0.585 (\log_{10} I^{1/3})^2$	± 0.402	$\frac{D_M}{W^{2/3}} = 2.71 \times 10^3 (I^{1/3})^{0.219} (10)^{-0.585 (\log_{10} I^{1/3})^2}$	$\frac{x}{\div} 2.52$	0.67	
$\frac{D}{3} = 2.950 - 0.517 \log_{10} W^{2/3}$	± 0.392	$\frac{D_M}{W^{2/3}} = 892 (W^{2/3})^{-0.517}$	$\frac{x}{\div} 2.47$	0.69	
$\frac{D}{3} = 2.960 - 0.480 \log_{10} W^{2/3} - 0.0362 (\log_{10} W^{2/3})^2$	± 0.392	$\frac{D_M}{W^{2/3}} = 912 (W^{2/3})^{-0.480} (10)^{-0.0362 (\log_{10} W^{2/3})^2}$	$\frac{x}{\div} 2.47$	0.69	
$\frac{D}{3} = 4.309 - 0.625 \log_{10} I^{2/3}$	± 0.407	$\frac{D_M}{W^{2/3}} = 2.04 \times 10^4 (I^{2/3})^{-0.625}$	$\frac{x}{\div} 2.55$	0.66	
$\frac{D}{3} = 3.432 + 0.1096 \log_{10} I^{2/3} - 0.1457 (\log_{10} I^{2/3})^2$	± 0.402	$\frac{D_M}{W^{2/3}} = 2.71 \times 10^3 (I^{2/3})^{0.1096} (10)^{-0.1457 (\log_{10} I^{2/3})^2}$	$\frac{x}{\div} 2.52$	0.67	
$\frac{A}{73} = 6.486 - 1.118 \log_{10} \left(\frac{I}{W^{1/3}} \right)$	± 0.504	$\frac{D_M}{W^{2/3}} = 3.06 \times 10^6 \left(\frac{I}{W^{1/3}} \right)^{-1.118}$	$\frac{x}{\div} 3.19$	0.38	
$\frac{M}{73} = -9.111 + 8.69 \log_{10} \left(\frac{I}{W^{1/3}} \right) - 1.531 \left[\log_{10} \left(\frac{I}{W^{1/3}} \right) \right]^2$	± 0.497	$\frac{D_M}{W^{2/3}} = 7.74 \times 10^{-10} \left(\frac{I}{W^{1/3}} \right)^{8.69} (10)^{-1.531 \left[\log_{10} \left(\frac{I}{W^{1/3}} \right) \right]^2}$	$\frac{x}{\div} 3.14$	0.40	
$\frac{M}{273} = 1.565 + 1.361 \log_{10} \left(\frac{I}{W^{2/3}} \right)$	± 0.403	$\frac{D_M}{W^{2/3}} = 2.72 \times 10^{-2} \left(\frac{I}{W^{2/3}} \right)^{1.361}$	$\frac{x}{\div} 2.53$	0.67	
$\frac{M}{273} = -3.451 + 2.565 \log_{10} \left(\frac{I}{W^{2/3}} \right) - 1.910 \left[\log_{10} \left(\frac{I}{W^{2/3}} \right) \right]^2$	± 0.403	$\frac{D_M}{W^{2/3}} = 3.54 \times 10^{-4} \left(\frac{I}{W^{2/3}} \right)^{2.57} (10)^{-1.910 \left[\log_{10} \left(\frac{I}{W^{2/3}} \right) \right]^2}$	$\frac{x}{\div} 2.53$	0.67	

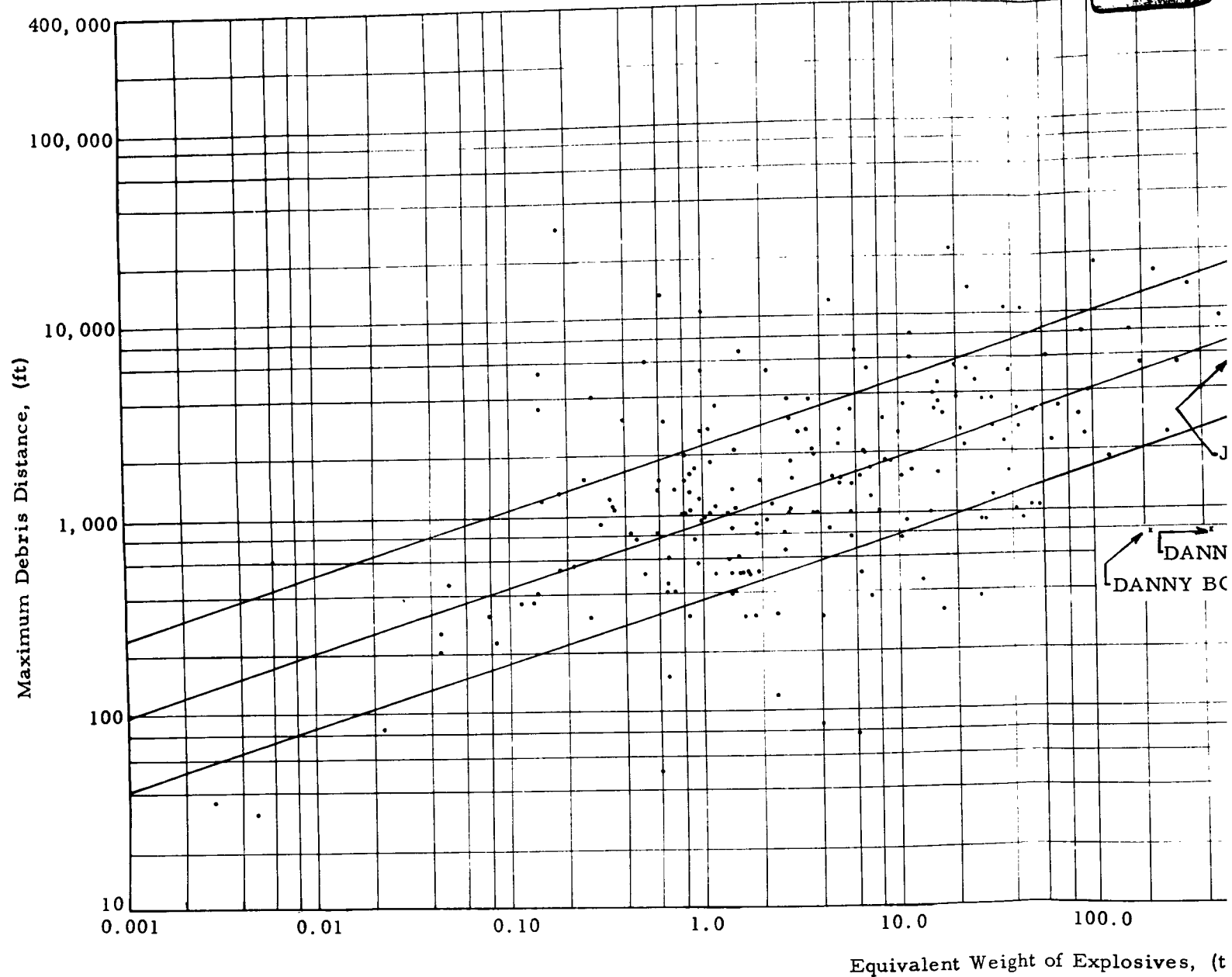
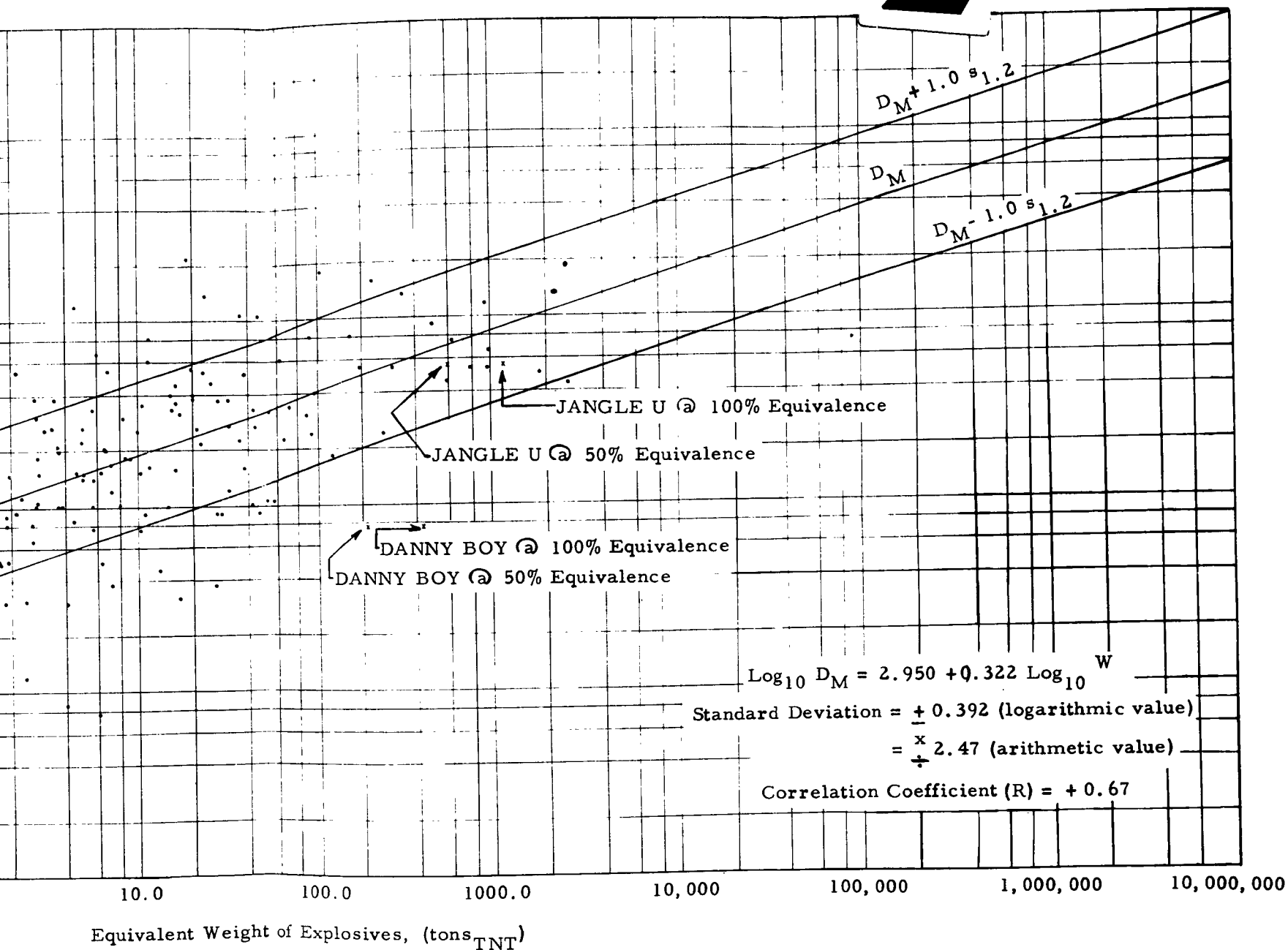


Figure 2.3 Linear Regression Line: Maximum Debris Distance versus Equivalent Yield

SECRET

2

SECRET



versus Equivalent Yield

1

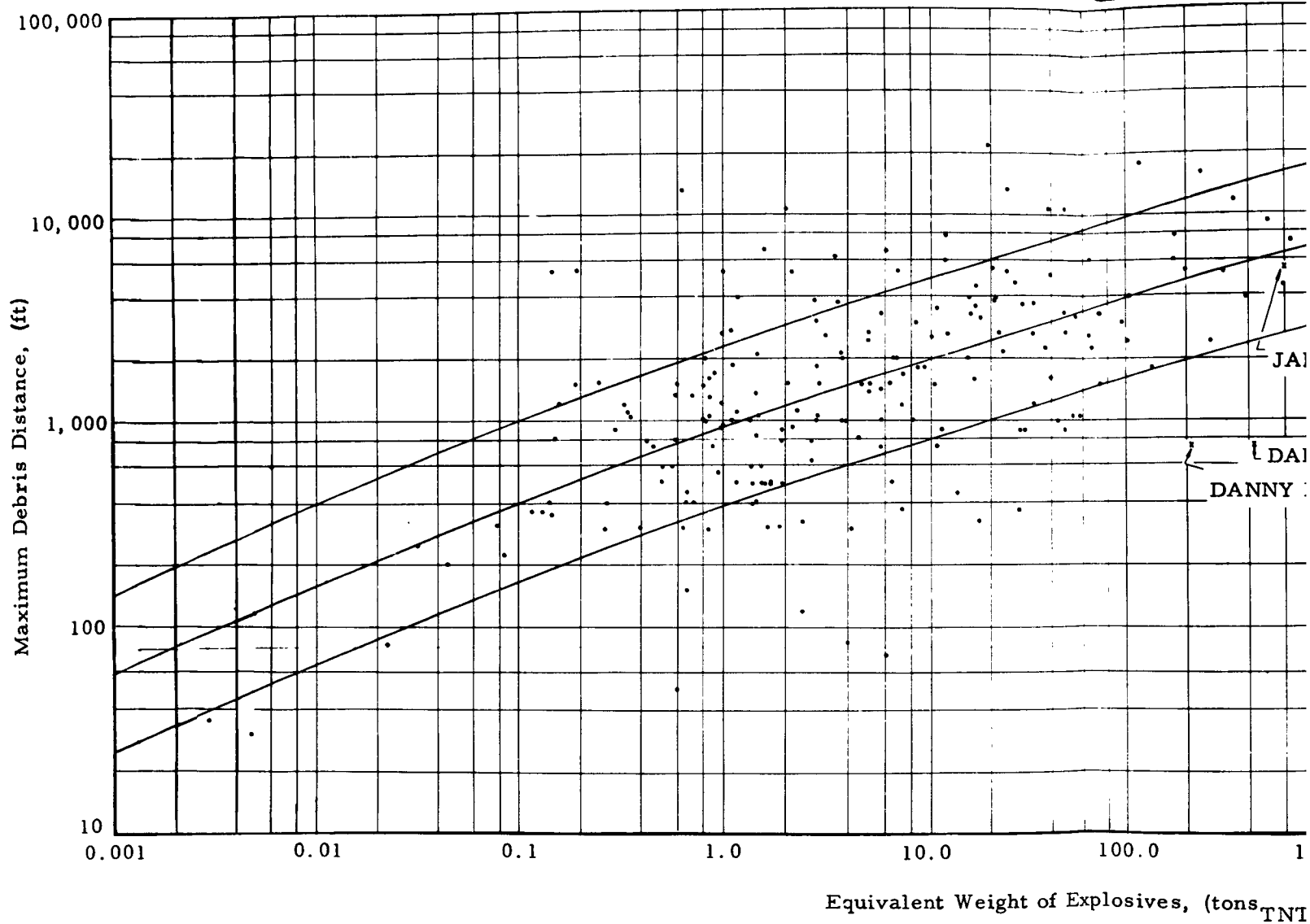
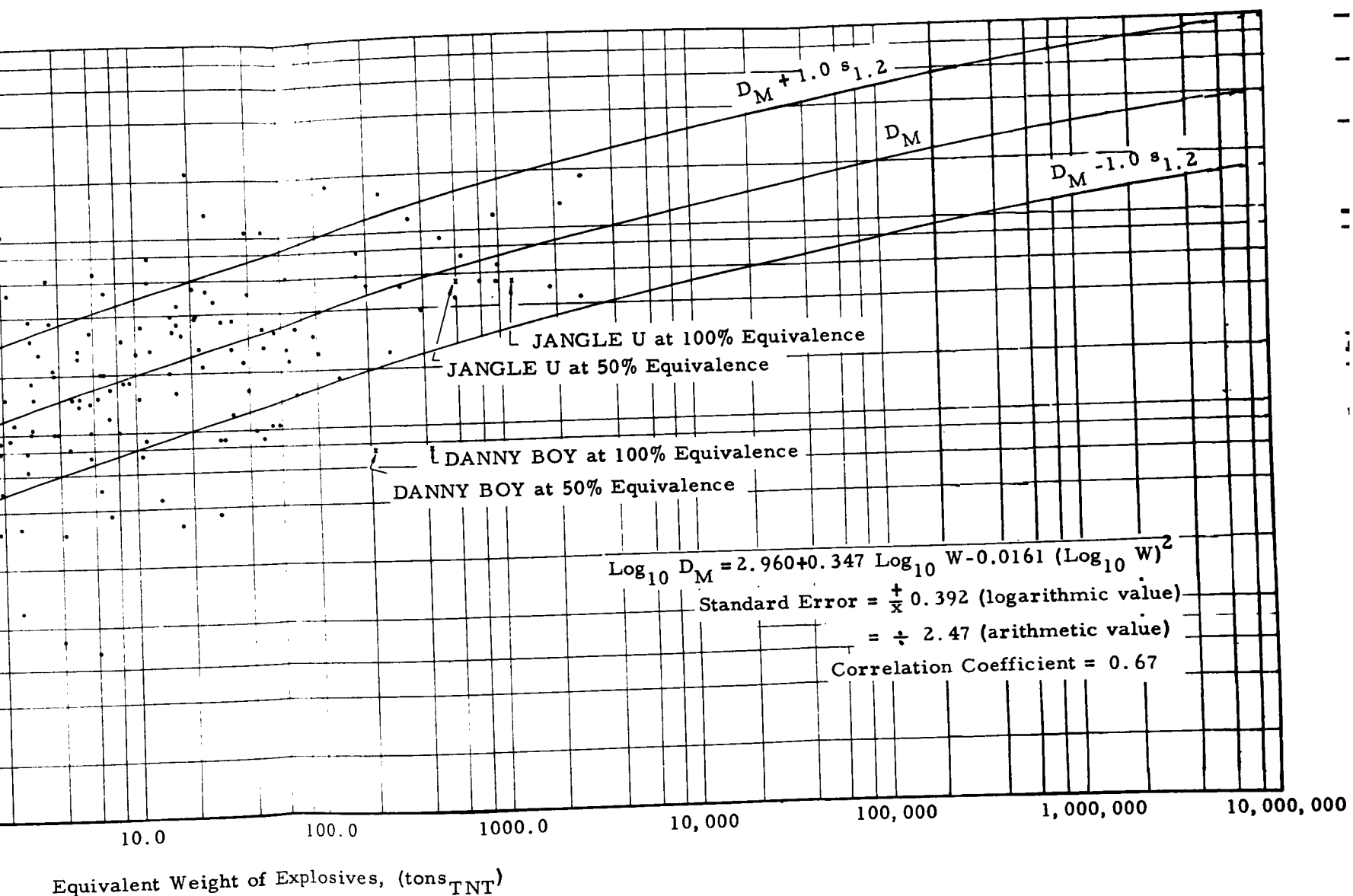


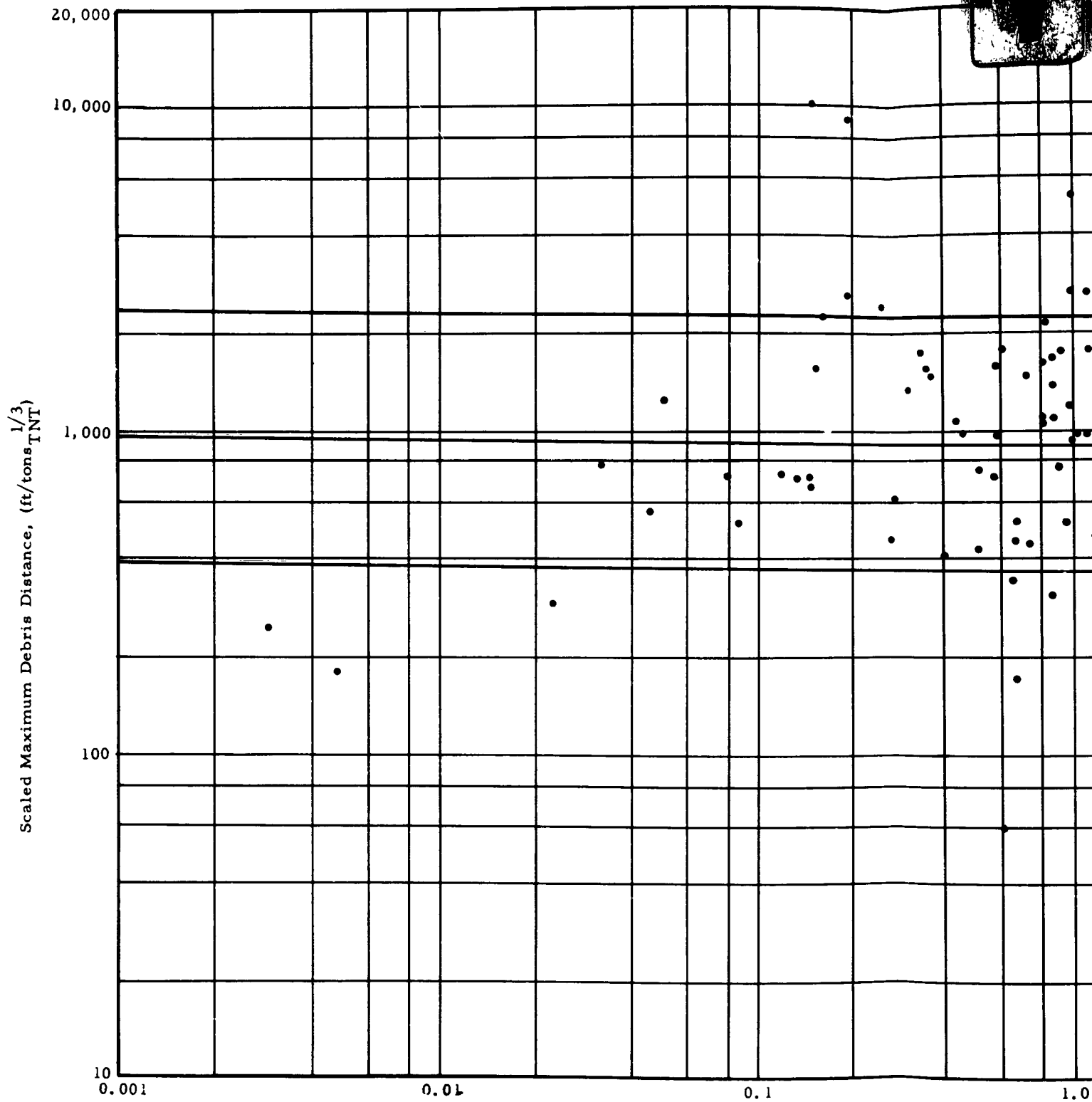
Figure 2.4 Quadratic Regression Line: Maximum Debris Distance
versus Equivalent Yield

SECRET

SECRET

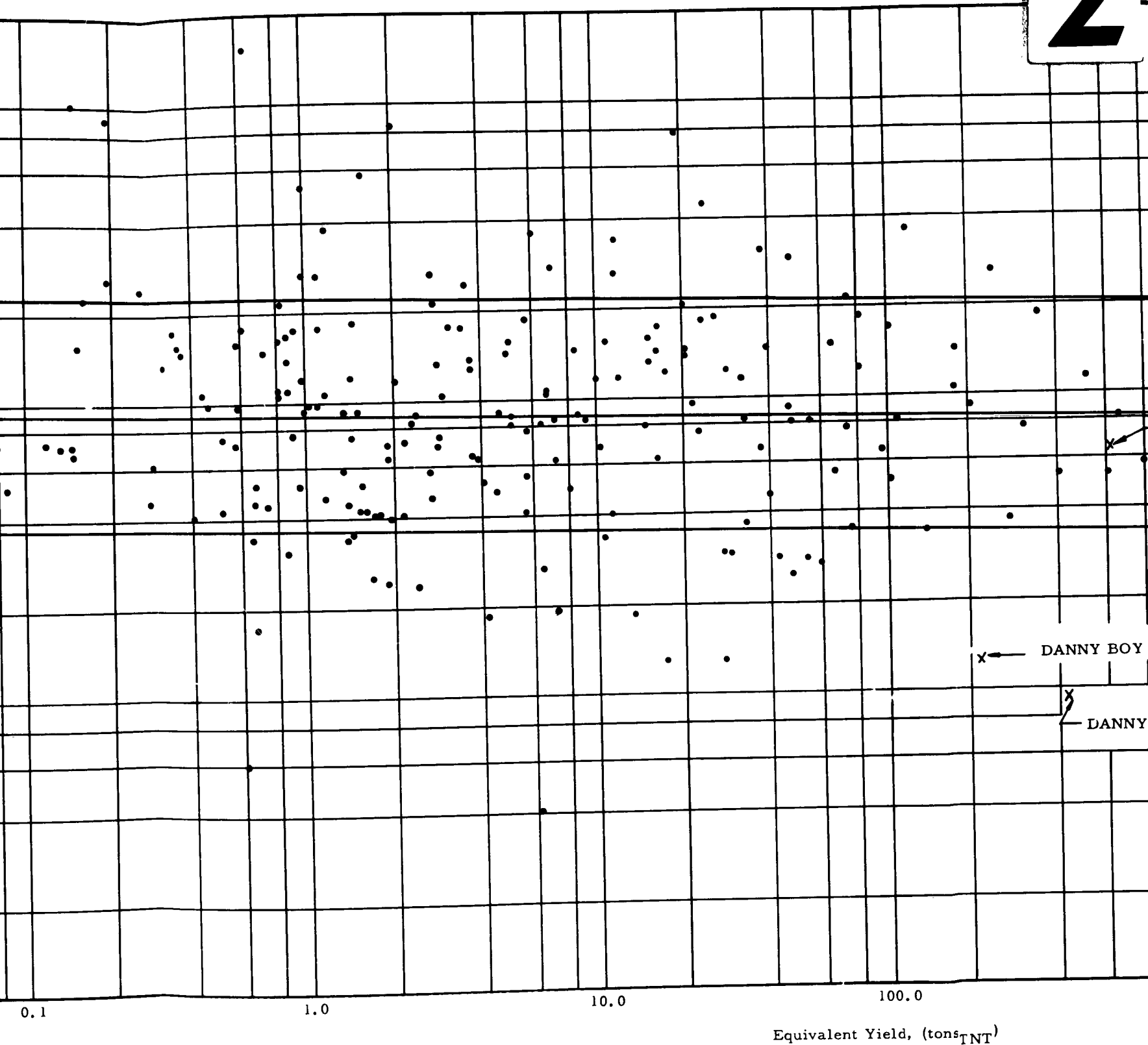
2

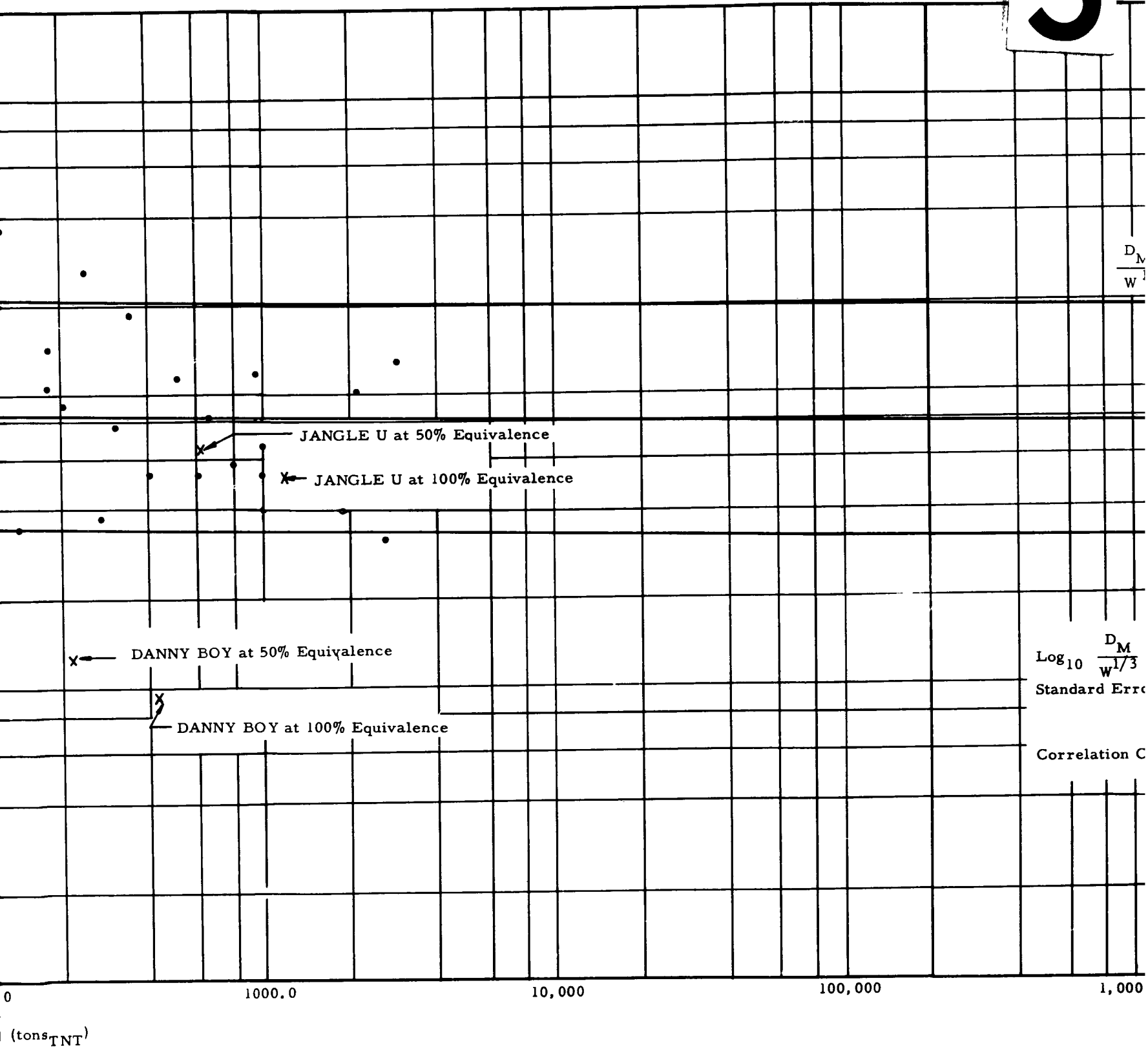




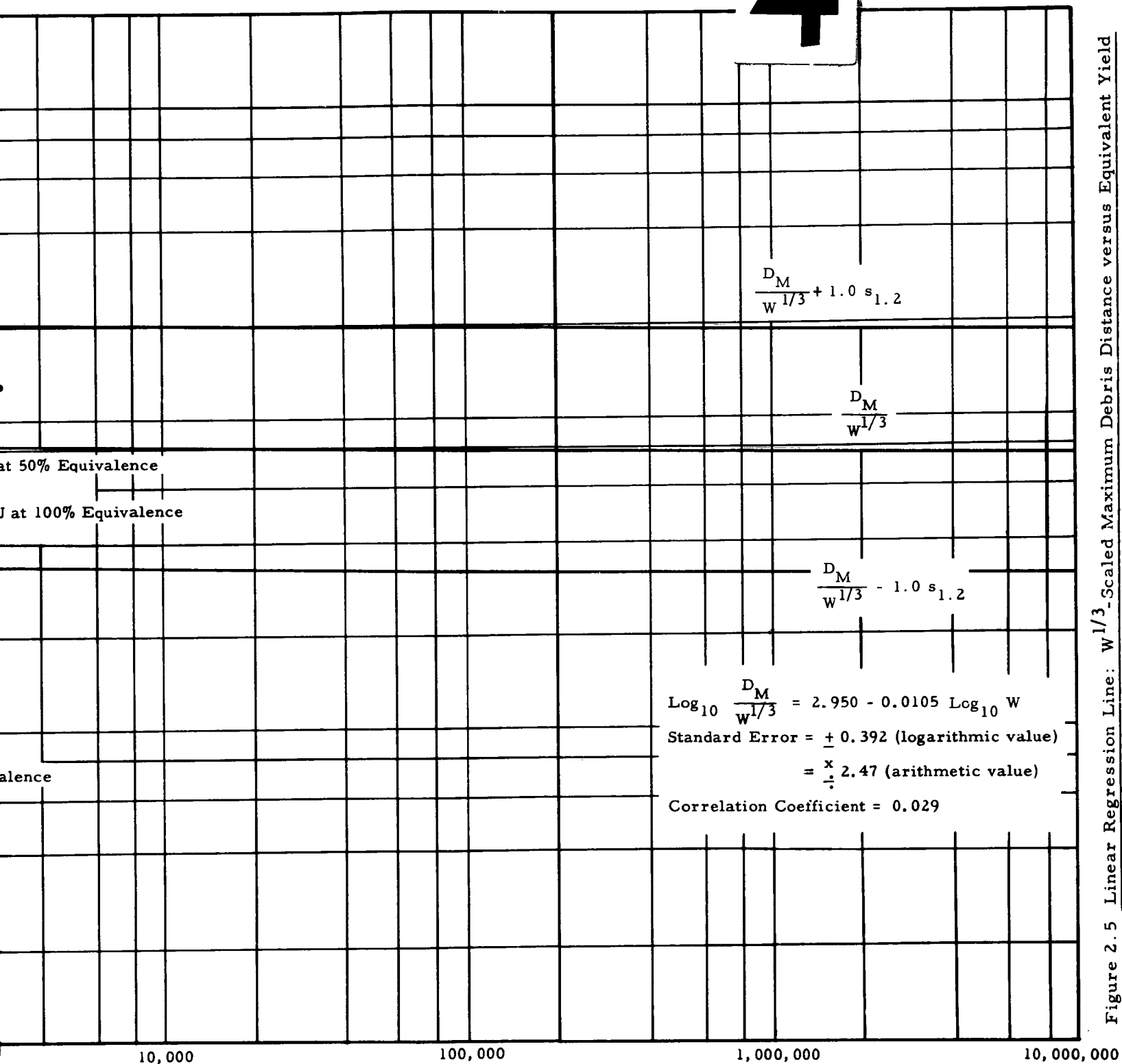
SECRET

2

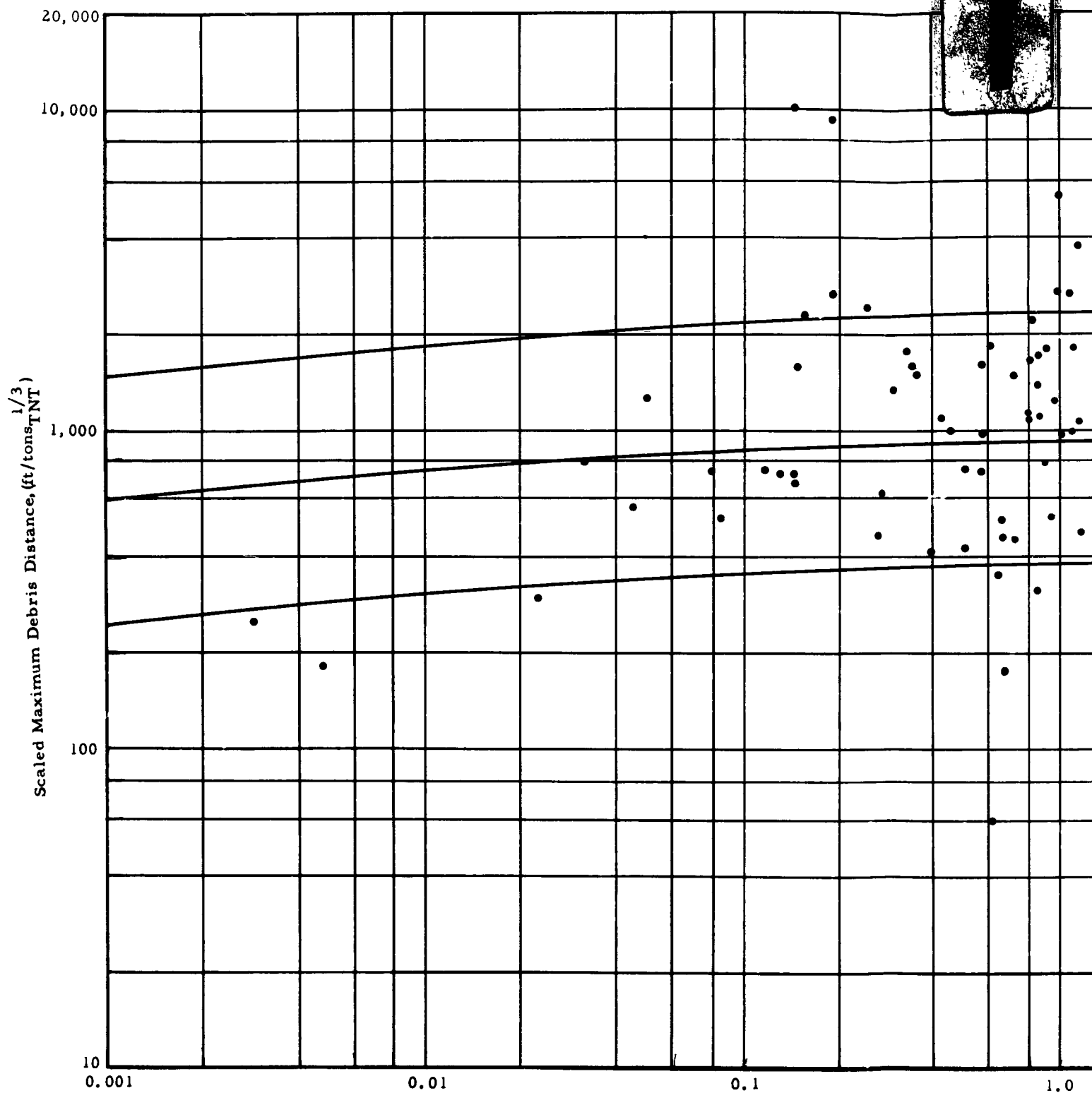




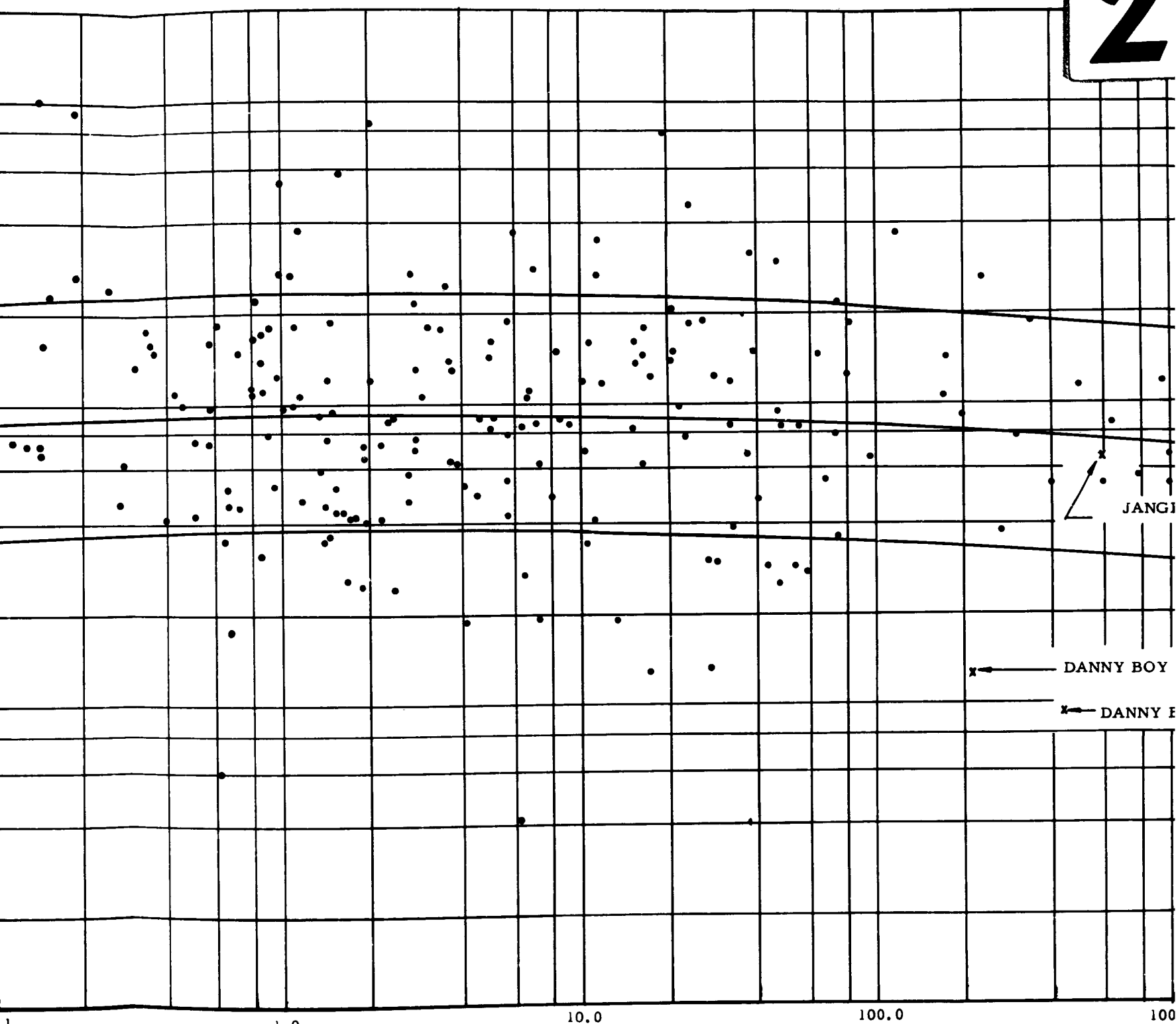
4



1



SECRET



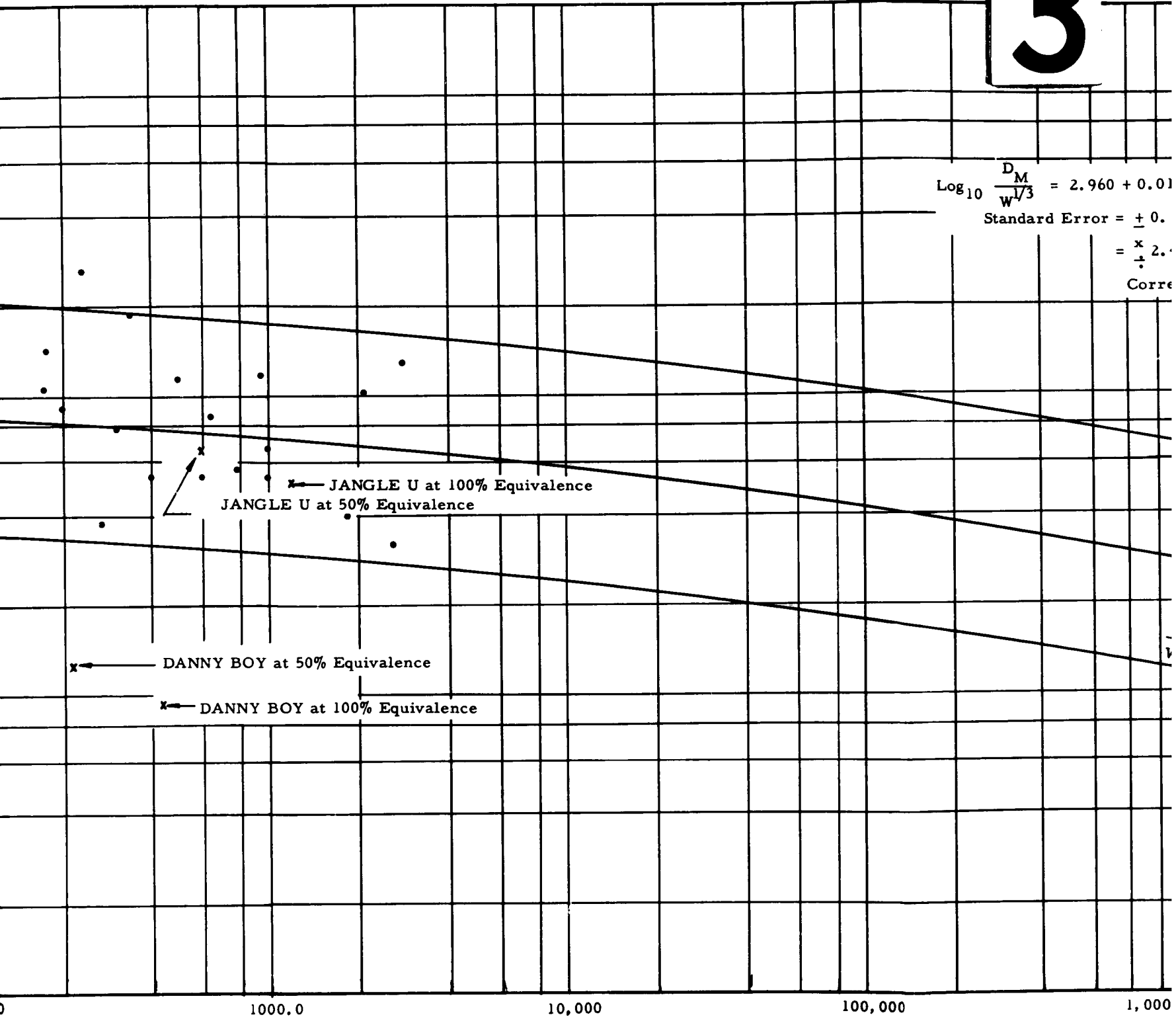
Equivalent Yield, (tons_{TNT})

$$\log_{10} \frac{D_M}{W^{1/3}} = 2.960 + 0.01$$

Standard Error = ± 0.01

$= \frac{x}{\frac{1}{2}}$

Corre



(tons_{TNT})

4

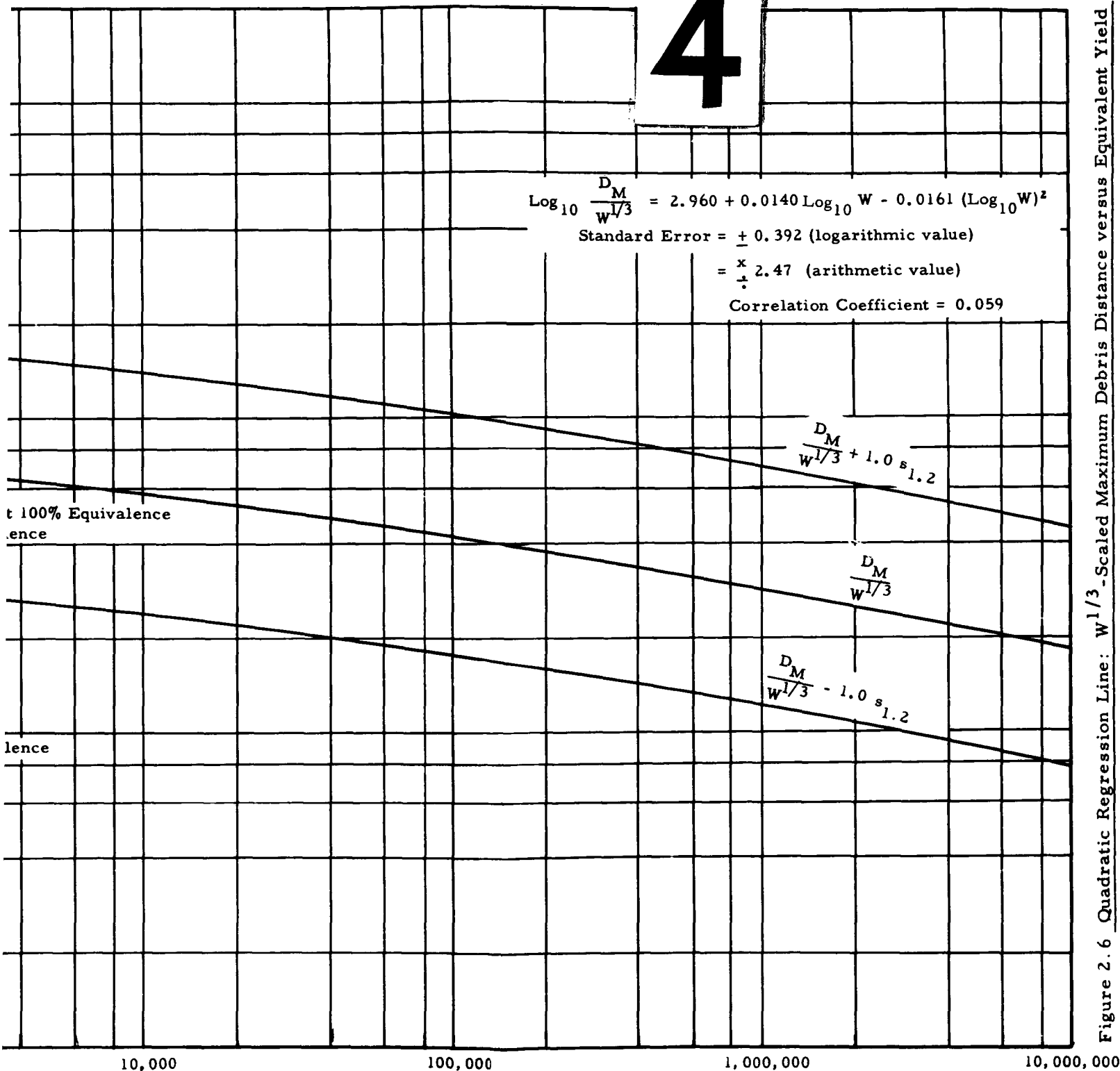


Figure 2.6 Quadratic Regression Line: $W^{1/3}$ -Scaled Maximum Debris Distance versus Equivalent Yield

SECRET

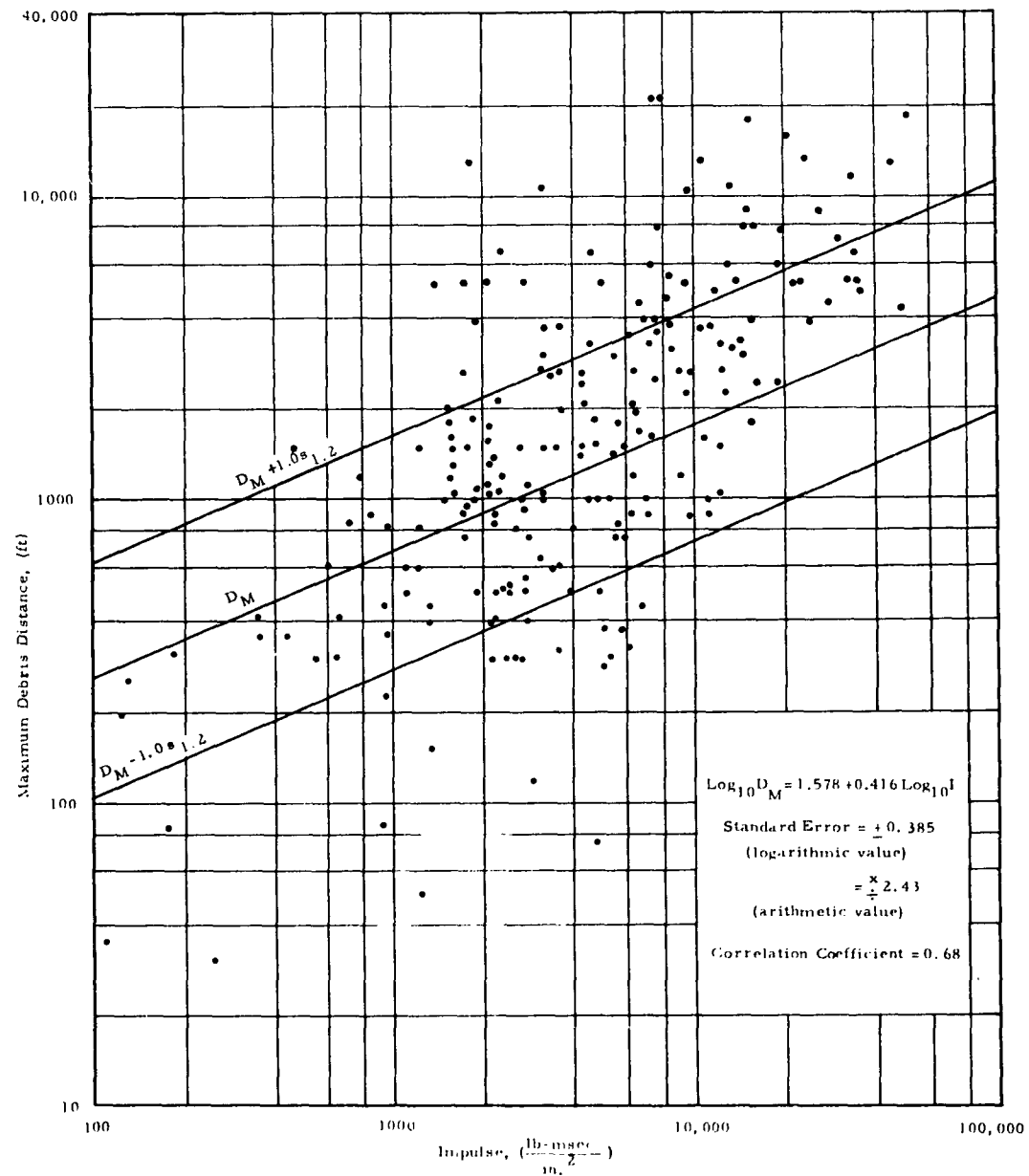


Figure 2.7 Linear Regression Line:
Maximum Debris Distance versus Impulse

SECRET

SECRET

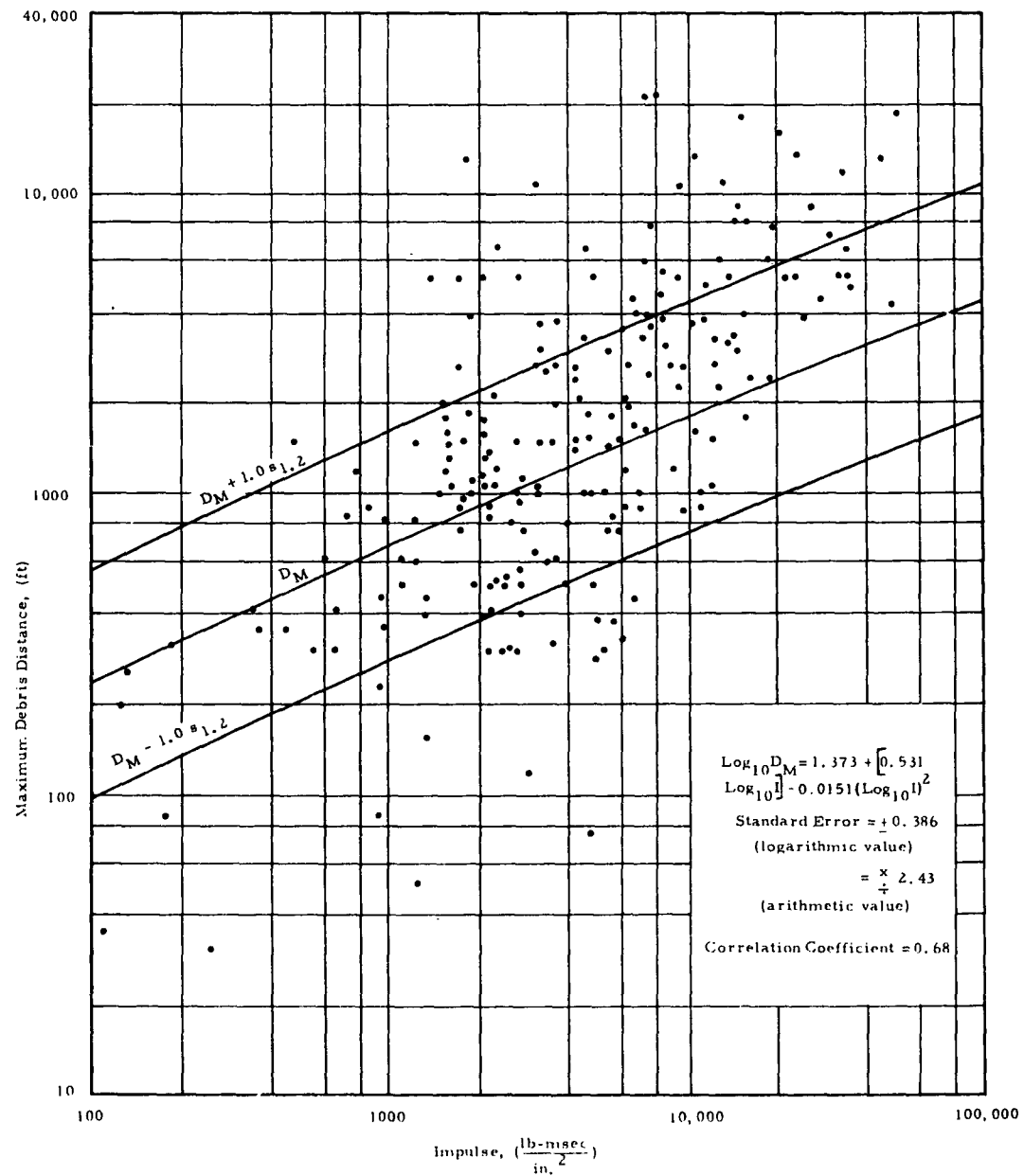


Figure 2.8 Quadratic Regression Line: Maximum Debris Distance versus Impulse

SECRET

SECRET

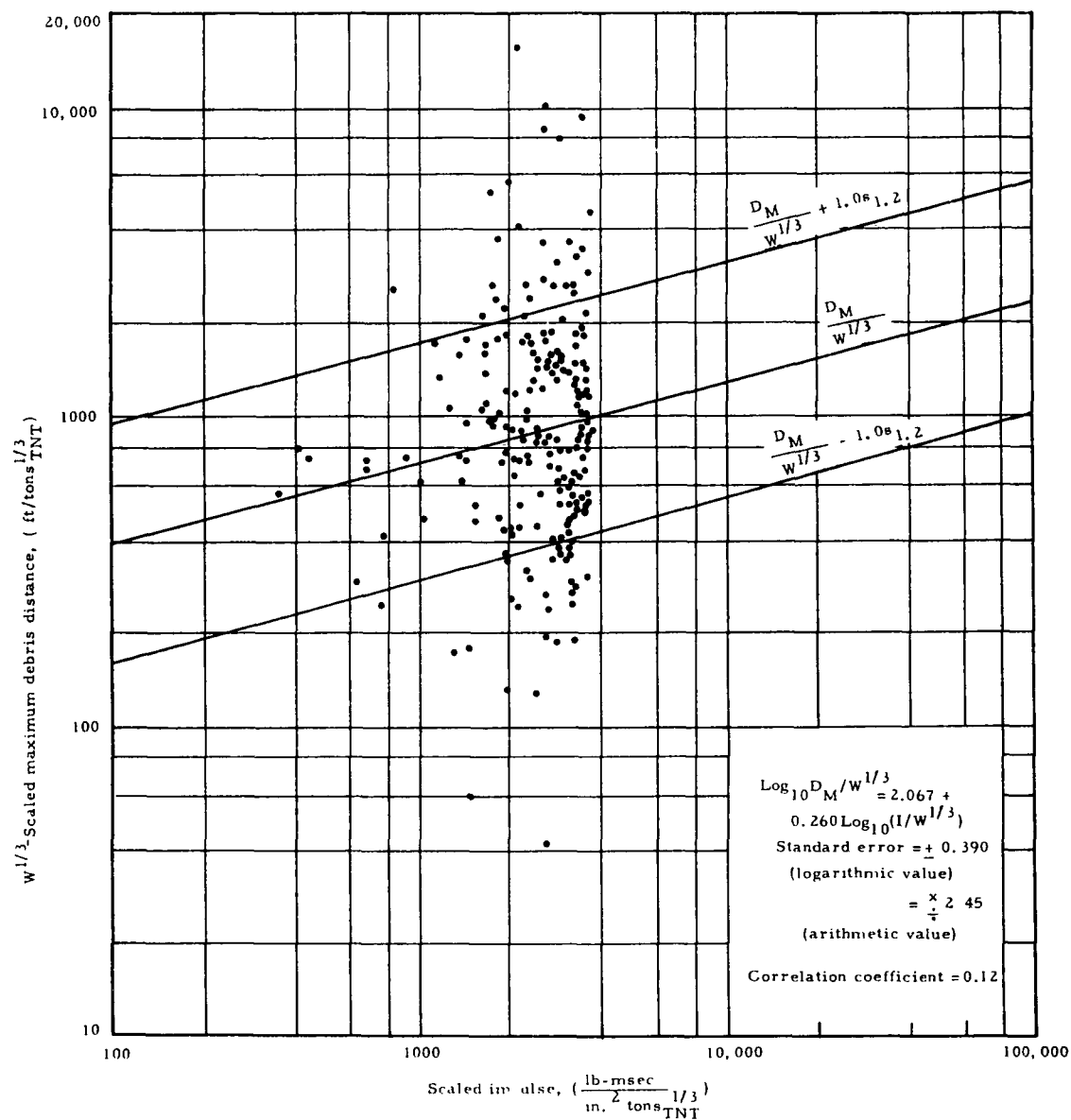


Figure 3.2 Linear Regression Line: W^{1/3}-Scaled Maximum Debris Distance versus W^{1/3}-Scaled Impulse

SECRET

SECRET

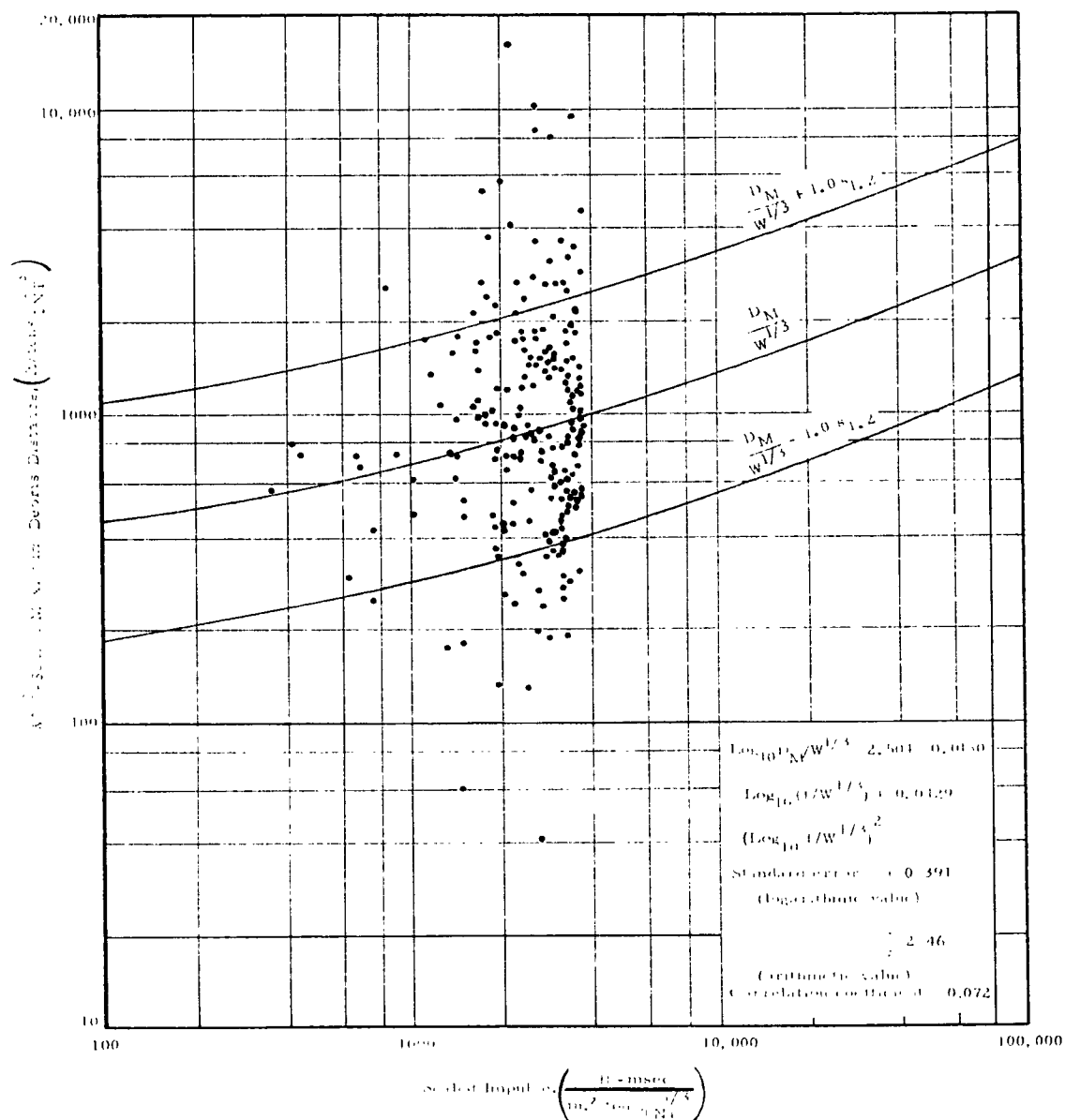


Figure 2.10 Quadratic Regression Line: $W^{1/3}$ -Scaled Maximum Debris Distance versus $W^{1/3}$ -Scaled Impulse

SECRET

SECRET

Maximum debris distance data from the JANGLE U shot and the DANNY BOY event are included in Fig. 2.3 to 2.6 to show their consistency with the HE data. Maximum debris distance for the DANNY BOY event was taken at 750 ft, the distance to a lobe of detached dust observed in post-shot aerial photographic observation (Ref. 9). The DANNY BOY event involved a 0.430-KT device buried at 110 ft. Maximum debris distance for JANGLE U was taken at 550 ft -- the farthest-thrown recorded fragment of the reinforced concrete runways and wall panels built within the crater zone. The JANGLE U shot involved a 1.2-KT device buried at 17 ft. These points are consistent with the HE results, especially when considered in relation to the regression line and the one-standard-error limit. The DANNY BOY event data compare less favorably with the HE regression lines than do the JANGLE U findings. The much greater depth of burial in DANNY BOY, where the device was placed at "optimum" depth, accounts for this. The resultant trajectories observed in DANNY BOY had pronounced vertical components. The favorable comparison of the underground nuclear events with the HE results is not surprising. Because of the absence of extreme blast winds, the HE detonations may be more closely akin to the underground nuclear burst than to surface or above-grade nuclear bursts, as far as debris behavior is concerned.

Lack of similarity between contained HE explosions and nuclear explosions under various siting and target conditions is obvious. The application of these curves to specific targeting situations can certainly be questioned. The dearth of actual debris measurements from full-scale nuclear tests is also realized. In view of these factors, the necessity of using available data such as this, tempered by engineering judgment, is apparent. Use of these charts will permit the making of order-of-magnitude estimates of maximum debris distance. Such estimates can at least indicate whether debris is a problem under various targeting conditions. A first-order estimate of maximum debris range measured from ground zero can be obtained from the correlations of maximum debris distance and equivalent yield. The correlations of maximum debris distance with impulse can be applied to the problem of an individual structure located intermediate between ground zero and the target whose vulnerability is questioned. Consideration of the

SECRET

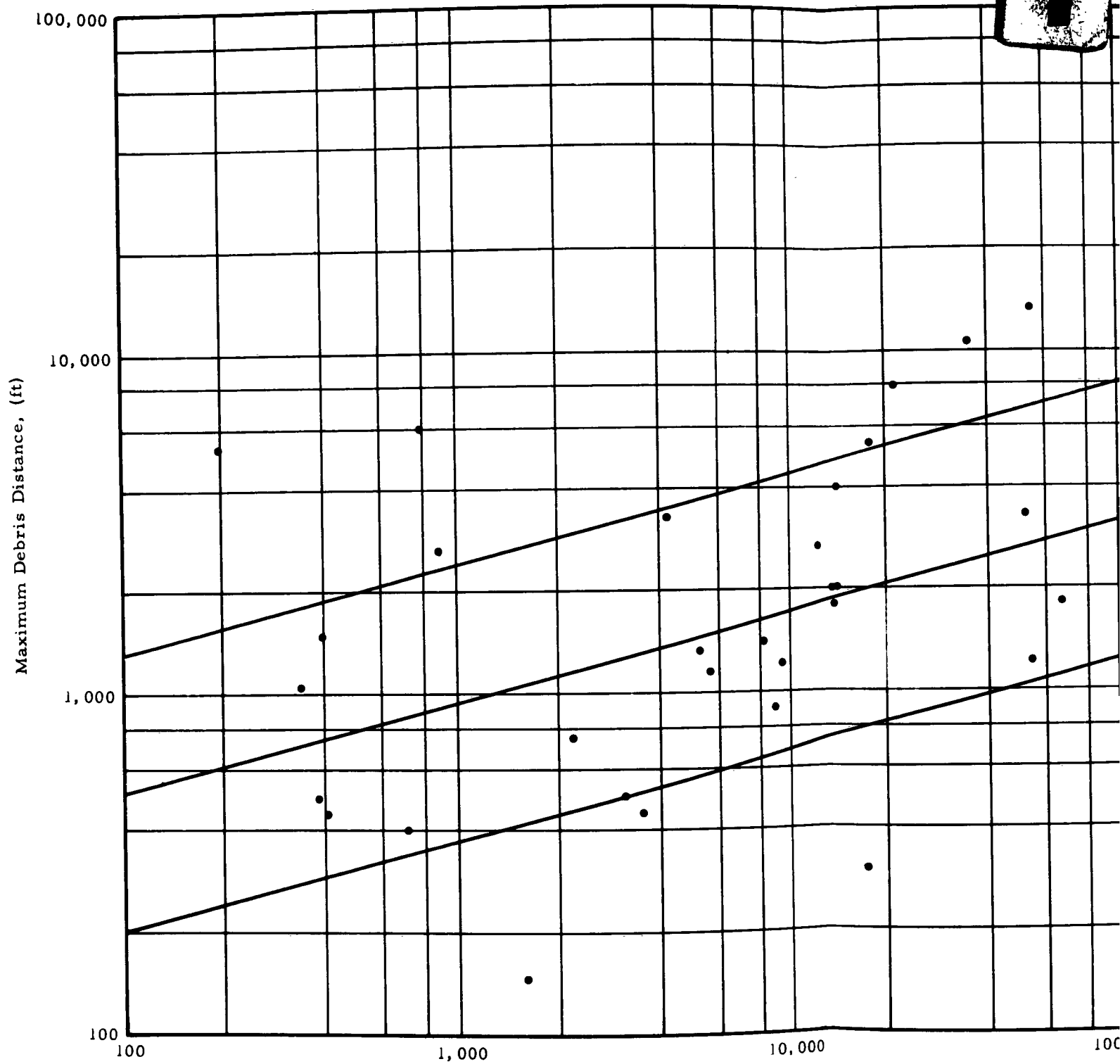
SECRET

standard error provides an indication of the likelihood of the target being within maximum debris distance.

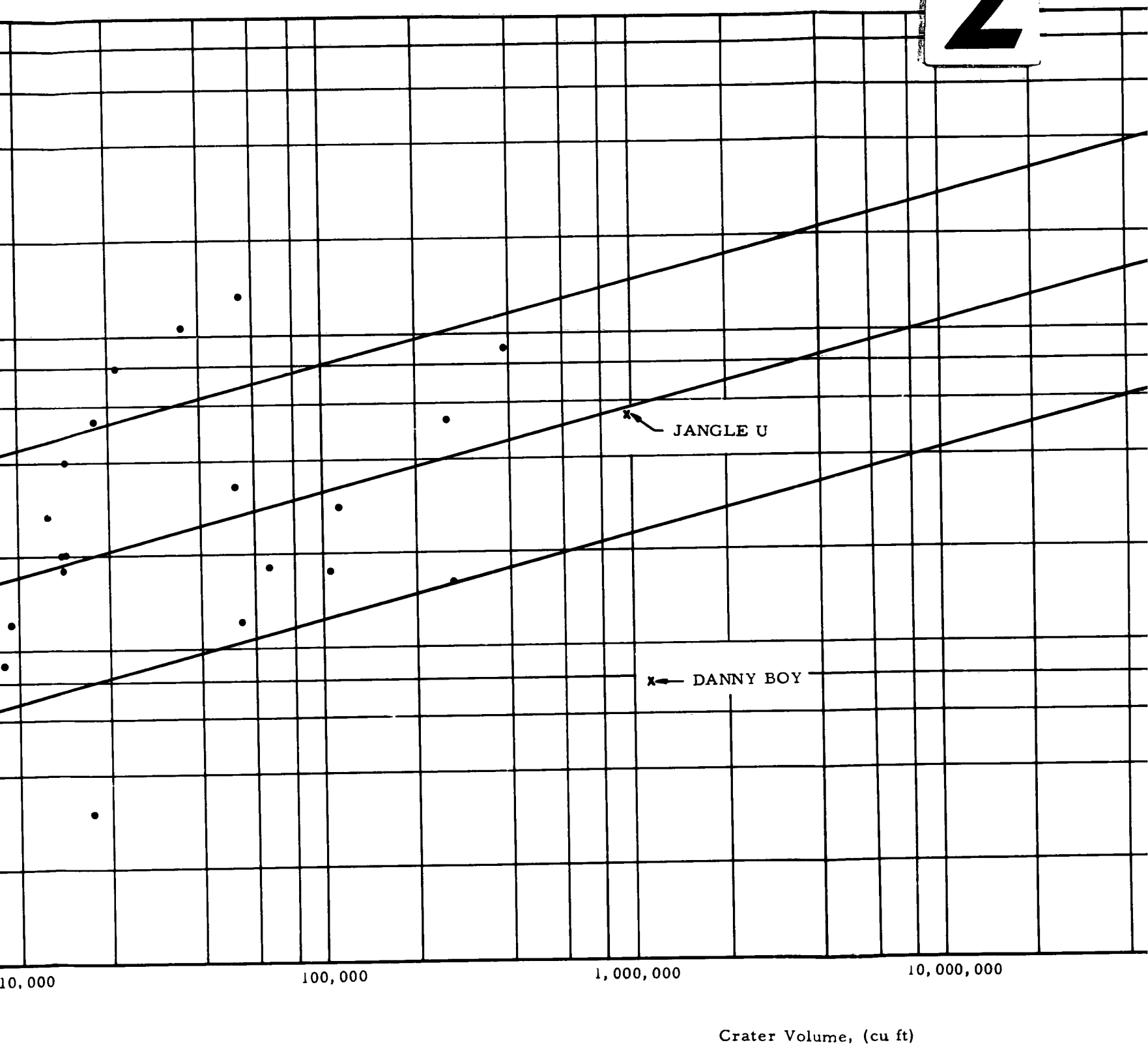
These charts, in themselves, do not provide any means for estimating the probability of the target being hit by debris, or estimating the number of pieces of debris likely to hit the target. They estimate maximum debris distance only-- the location of the furthest-thrown fragment. The problem of areal density of debris (the number of fragments per unit area) will be considered separately.

Considerable difficulty was experienced in keeping within the accurate capacity of the electronic computer in these regression studies. The matrix solution to the simultaneous equations for the least-squares lines involves taking small differences between very large numbers which are summations of products or summations of powers of numbers. As these summations increase in size, the process taxes the accurate capacity of the computer. Although where necessary, recourse was made to double precision (16 digits) on the IBM 7090/401 computer, it was still not possible to ascribe a high degree of mathematical precision to the constants in the regression results. Thus we see that mathematically the correlation coefficient for the quadratic case should not be lower than that in the linear case, or else the quadratic expression should have a zero coefficient to the squared independent variable. Regardless of this, we have observed that computed values of correlation coefficients were sometimes lower for the quadratic case, and that computed values of standard errors were frequently higher for the quadratic case. In these instances the differences in values of correlation coefficients and standard errors for the linear and quadratic cases were small -- actually marginal. The first digit of the standard error and correlation coefficient is good, the second digit probably merits some confidence. The constants in the regression lines are of unknown precision. The relative position of the lines among the scattered data points and the ratio of numbers of data points within and without the plus-and-minus-one standard error bands are reasonable.

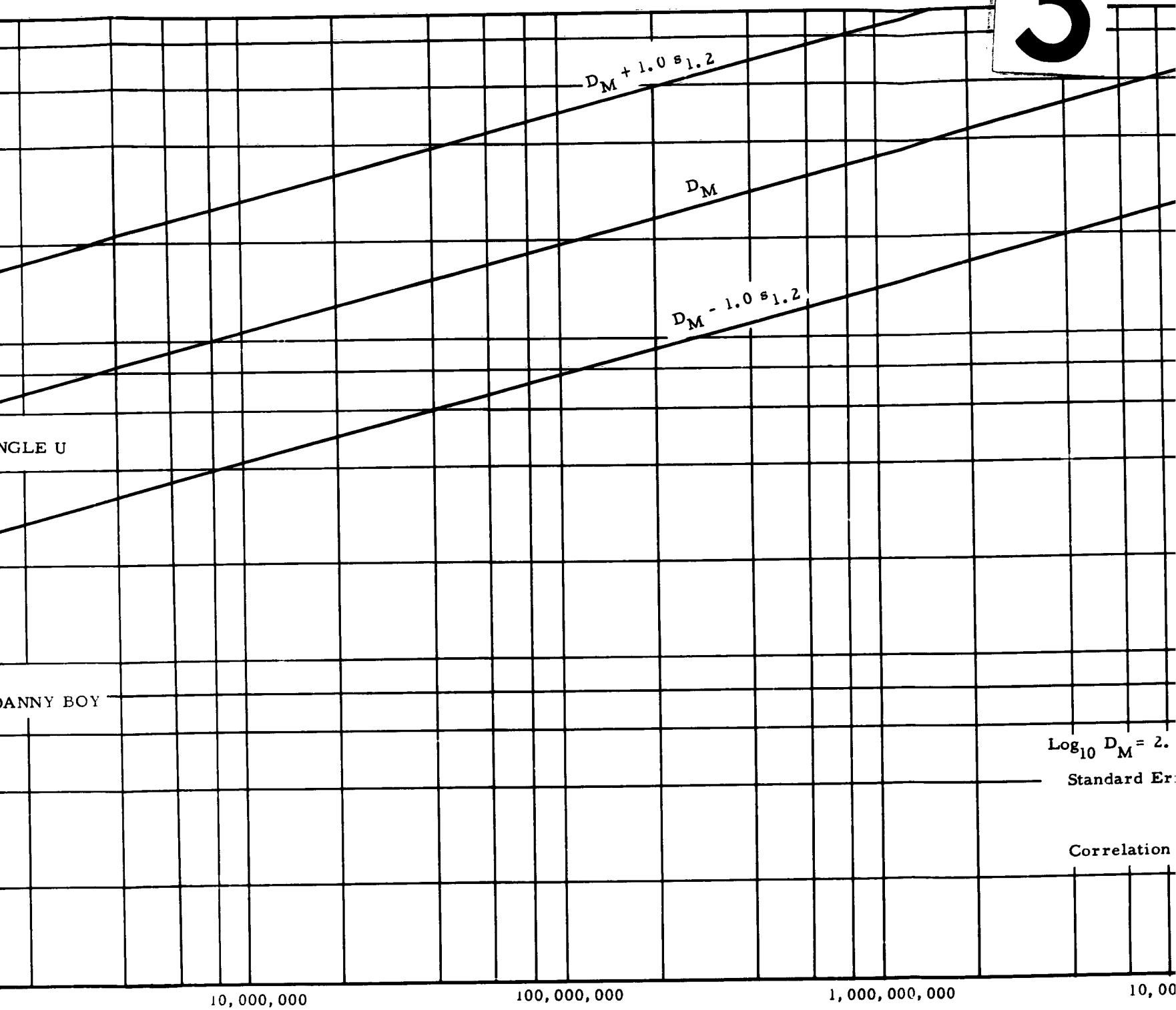
SECRET



SECRET



3



4

SECRET

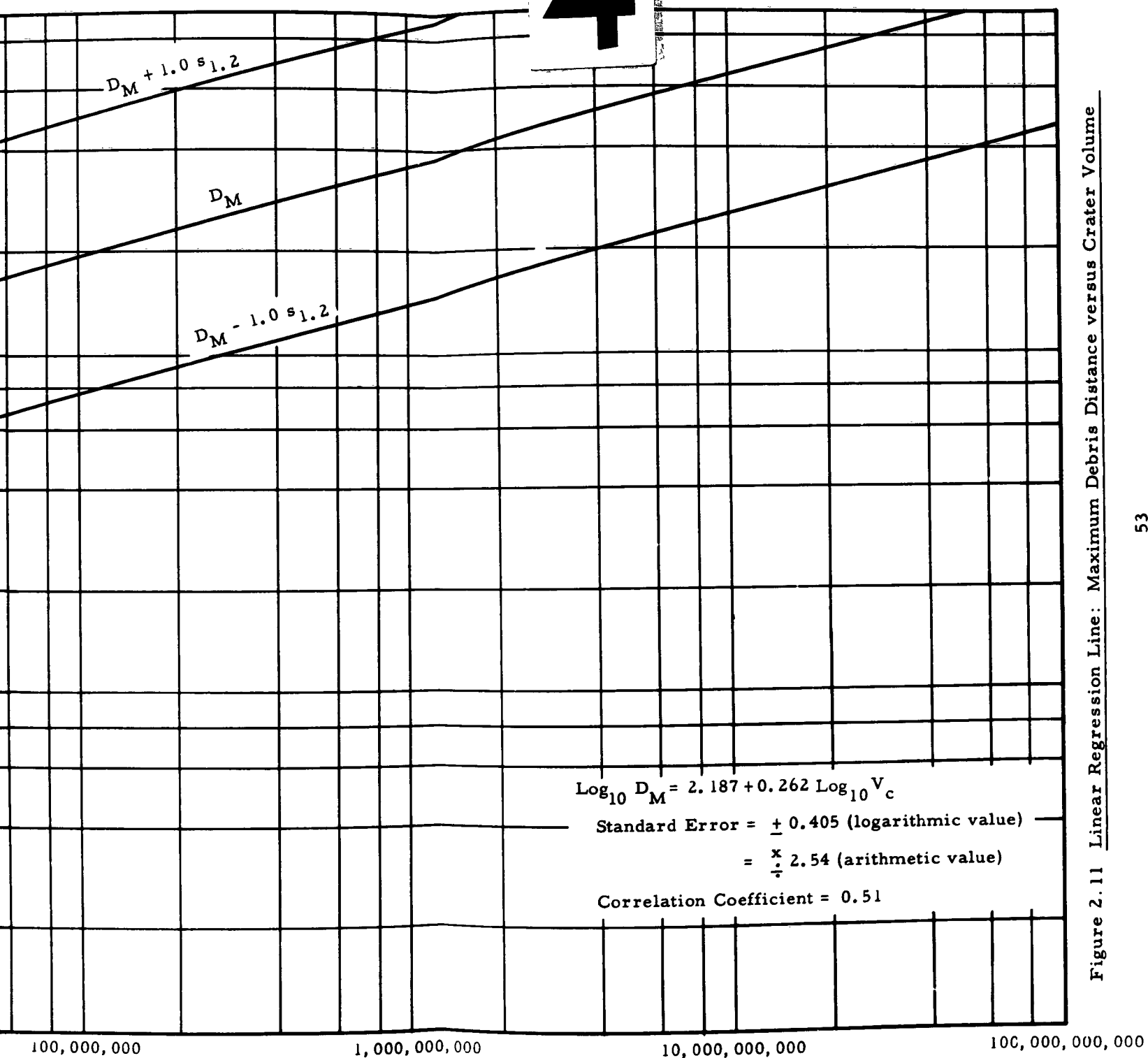


Figure 2.11 Linear Regression Line: Maximum Debris Distance versus Crater Volume

SECRET

2. 2. 3 Correlation of Maximum Debris Distance with Crater Dimensions

Maximum debris distance was correlated with crater dimensions using data from the series of thirty-six explosions tabulated in Appendix C (Ref. 6). Results of the regression study are tabulated in Table 2. 2. Linear and quadratic plots of maximum missile distance in terms of crater dimensions are presented in Fig. 2. 11 through 2. 16, while $W^{1/3}$ -scaled relationships are presented in Fig. 2. 17 through 2. 22. JANGLE U AND DANNY BOY results are also plotted on these figures. Again the considerable depth of burial in the DANNY BOY event accounts for the position of these points well below the lower one-standard-error band.

2. 3 Debris Dispersion Patterns

Theoretical models for distribution of debris about line charges are developed and compared with actual results from semi-contained explosions. Measured debris dispersion from HE detonations is studied. Comparisons of dispersion patterns for a series of six HE events of different magnitudes are made. Dispersion patterns for a single HE event are also studied in considerable detail.

2. 3. 1 Theoretical Models

Debris Dispersion for Line-Source Explosions

Theoretical models of the dispersion of structural fragments in terms of the maximum missile distance were derived for flat roots, walls, and arches. These models were prepared for the purpose of comparing theoretical distributions with those from experimental and accidental explosions.

Models developed to explain the dispersion of structural fragments, in terms of terminal ground range, are based on the following assumptions:

Complete fragmentation of the structure
into equal-sized fragments occurs

Fragments follow ballistic trajectories, and
air resistance can be neglected

SECRET

SECRET

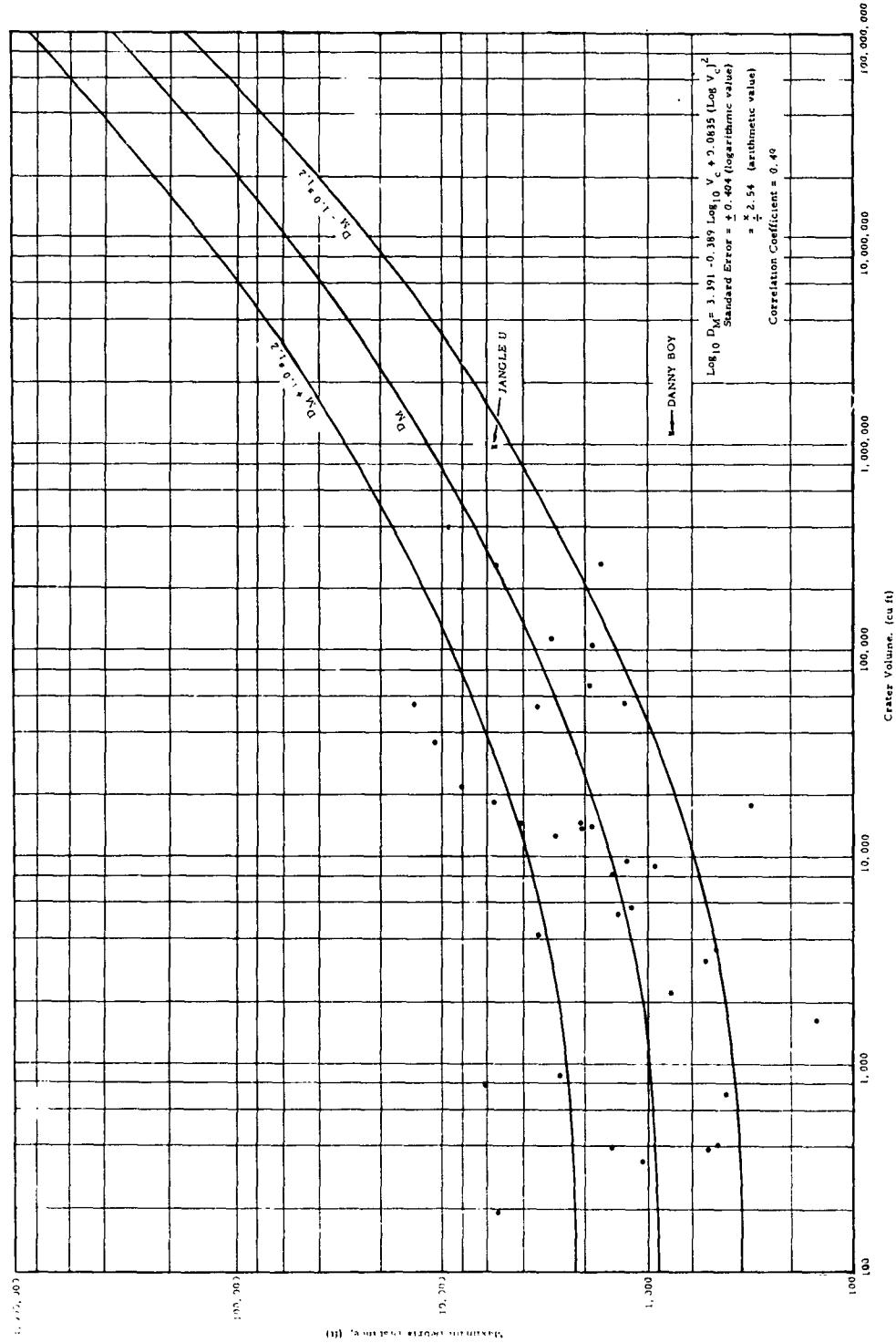


Figure 2.12 Quadratic Regression Line: Maximum Debris Distance versus Crater Volume

SECRET

SECRET

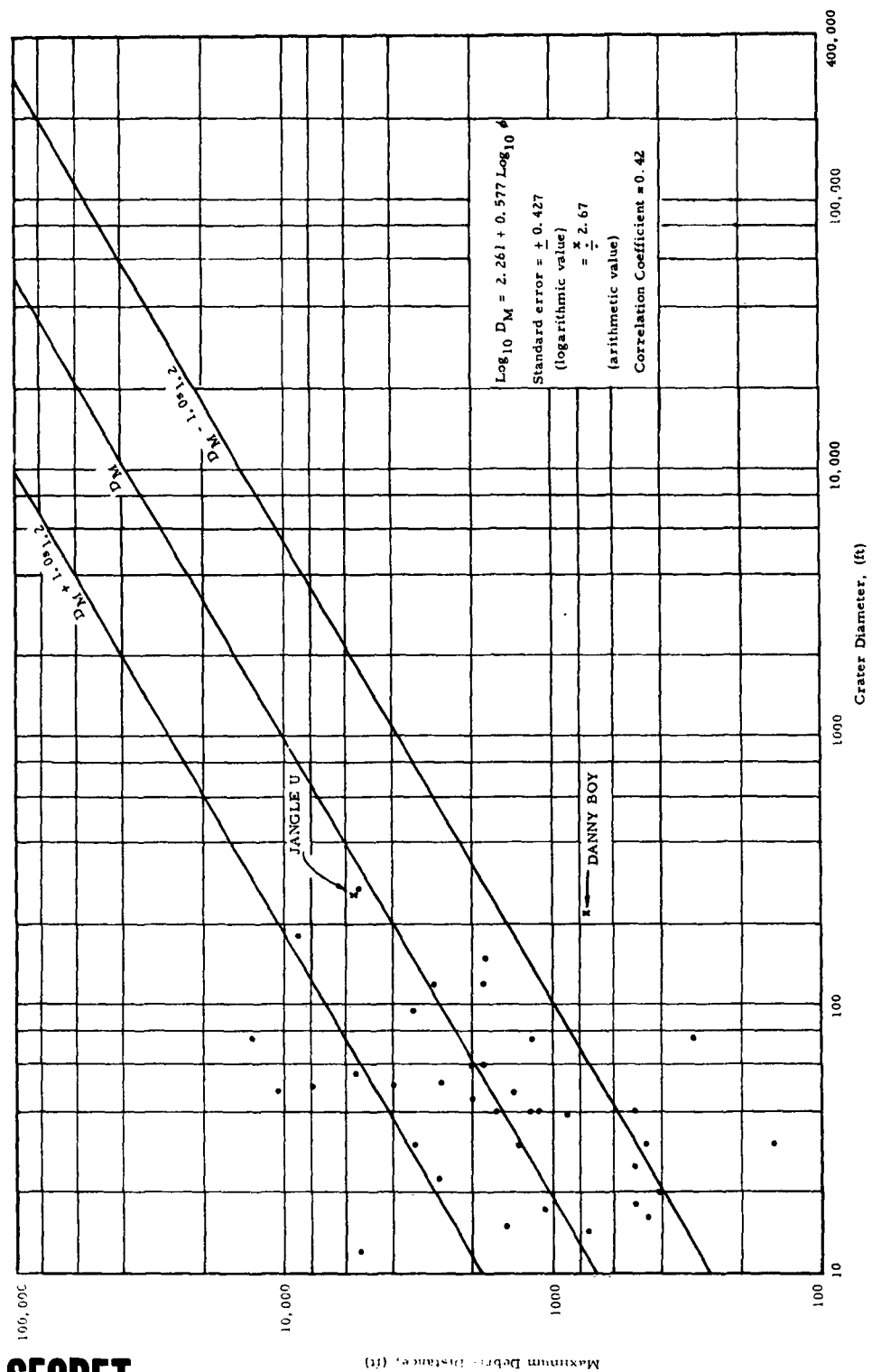


Figure 2.13 Linear Regression Line: Maximum Debris Distance versus Crater Diameter

SECRET

SECRET

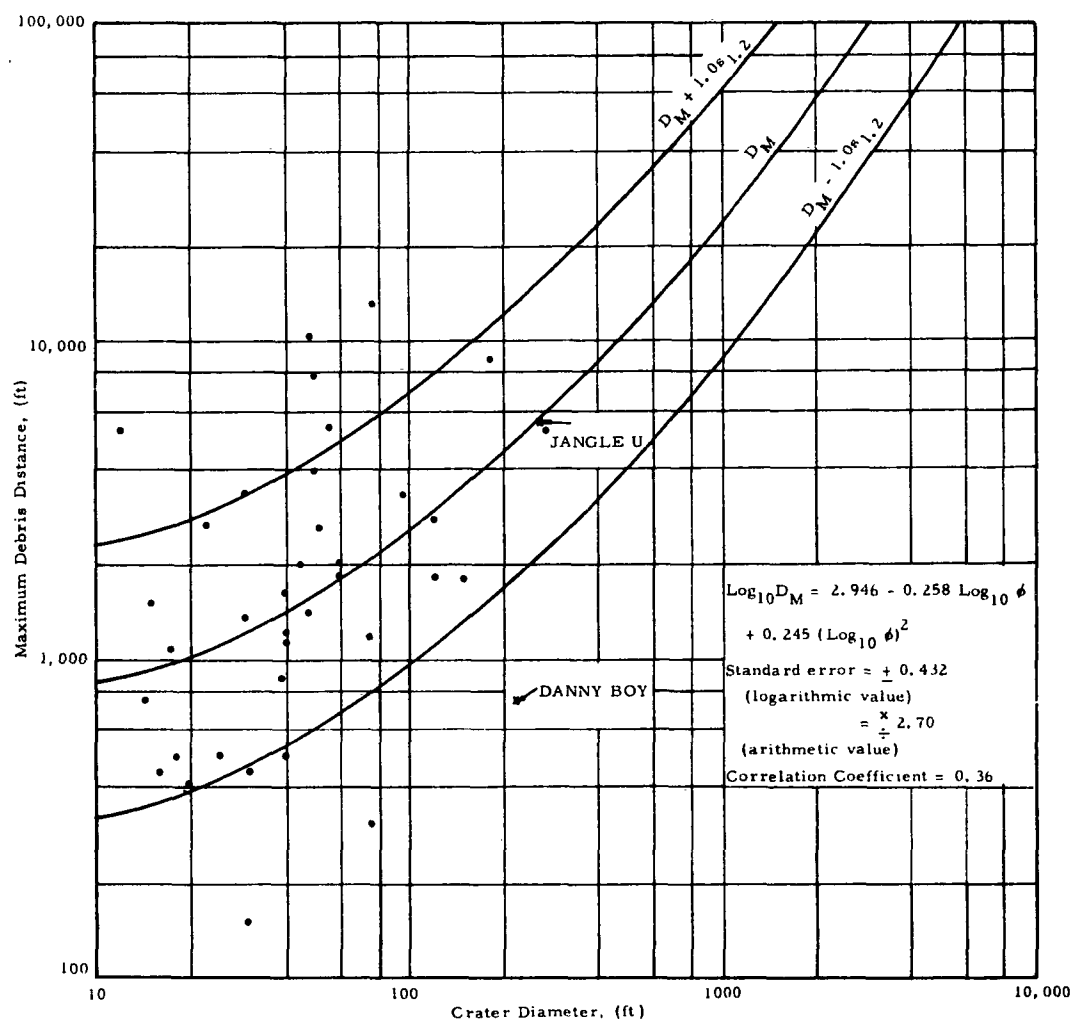


Figure 2.14 Quadratic Regression Line: Maximum Debris Distance
versus Crater Diameter

SECRET

SECRET

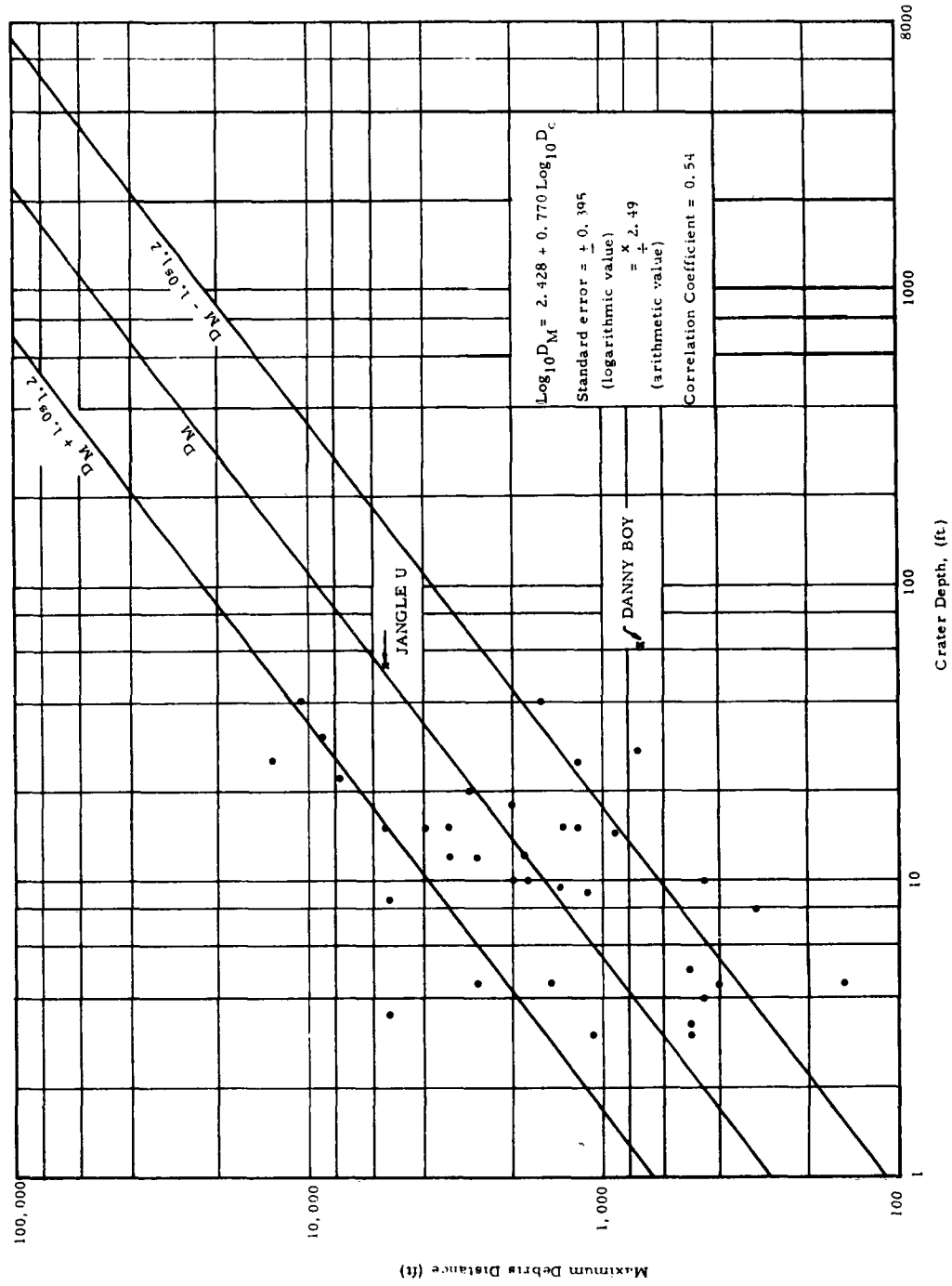


Figure 2.15 Linear Regression Line: Maximum Debris Distance versus Crater Depth

SECRET

SECRET

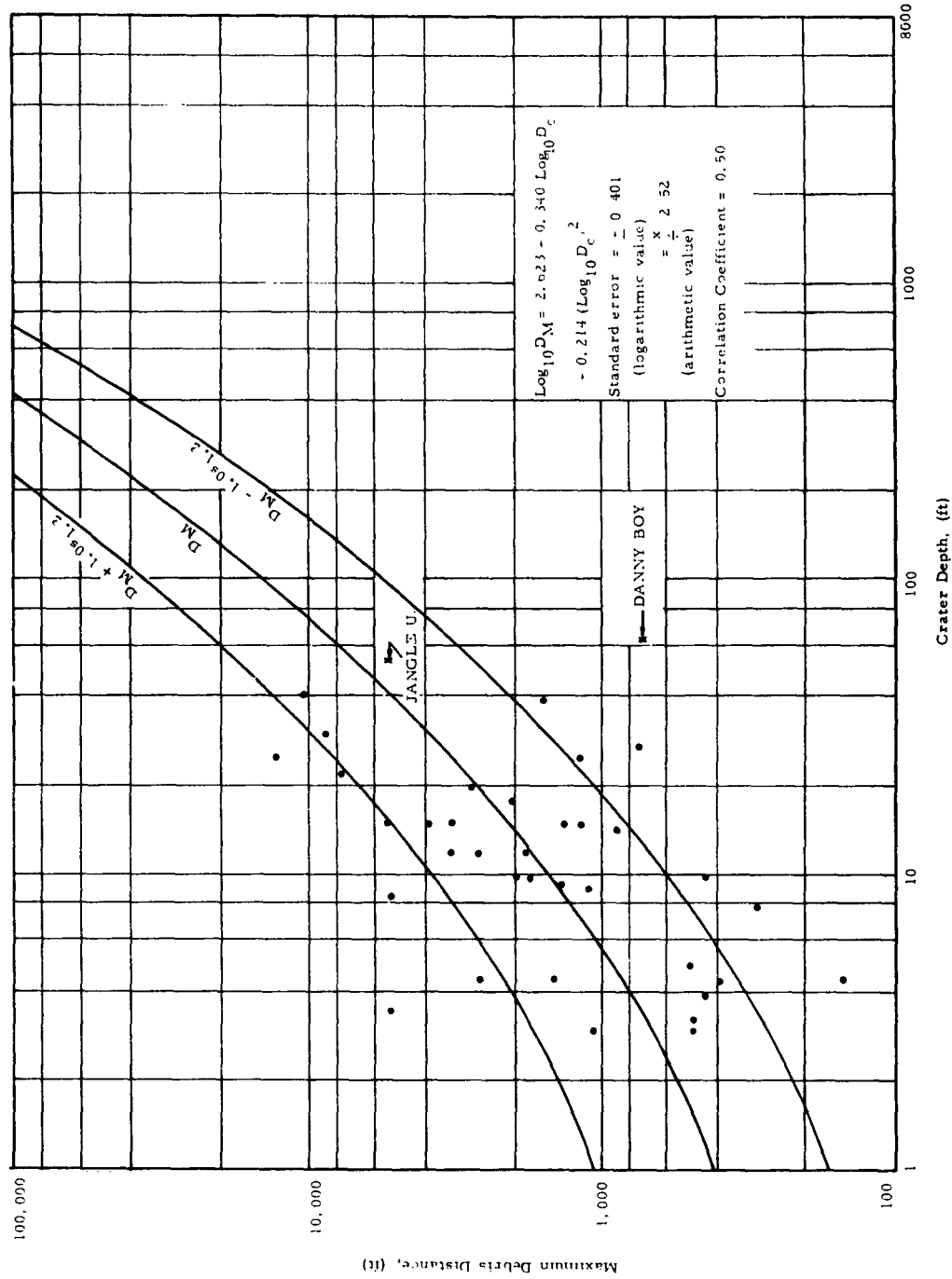


Figure 2.16 Quadratic Regression Line: Maximum Debris Distance versus Crater Depth

SECRET

Table 2.2

REGRESSION LINES FOR MAXIMUM DEBRIS DISTANCE

1

Factors Correlated	Type of Correlation	Logarithmic Form	
		Regression Line	Standard Error
Log ₁₀ Maximum Debris Distance (ft) Versus Log ₁₀ Crater Volume (ft ³)	Linear	$\text{Log}_{10} D_M = 2.187 + 0.262 \text{Log}_{10} V_c$	± 0
	Quadratic	$\text{Log}_{10} D_M = 3.391 - 0.389 \text{Log}_{10} V_c + 0.0835 (\text{Log}_{10} V_c)^2$	± 0
Log ₁₀ Maximum Debris Distance (ft) Versus Log ₁₀ Crater Diameter (ft)	Linear	$\text{Log}_{10} D_M = 2.261 + 0.577 \text{Log}_{10} \phi$	± 0
	Quadratic	$\text{Log}_{10} D_M = 2.946 - 0.258 \text{Log}_{10} \phi + 0.245 (\text{Log}_{10} \phi)^2$	± 0
Log ₁₀ Maximum Debris Distance (ft) Versus Log ₁₀ Crater Depth (ft)	Linear	$\text{Log}_{10} D_M = 2.428 + 0.770 \text{Log}_{10} D_c$	± 0
	Quadratic	$\text{Log}_{10} D_M = 2.623 + 0.340 \text{Log}_{10} D_c + 0.214 (\text{Log}_{10} D_c)^2$	± 0
Log ₁₀ $W^{1/3}$ - Scaled Maximum Debris Distance $\left(\frac{\text{ft}}{\text{tons}_{\text{TNT}}^{2/3}}\right)$ Versus Log ₁₀ Crater Volume (ft ³)	Linear	$\text{Log}_{10} \left(\frac{D_M}{W^{1/3}}\right) = 2.822 + 0.0467 \text{Log}_{10} V_c$	± 0
	Quadratic	$\text{Log}_{10} \left(\frac{D_M}{W^{1/3}}\right) = 3.867 - 0.518 \text{Log}_{10} V_c + 0.0724 (\text{Log}_{10} V_c)^2$	± 0
Log ₁₀ $W^{1/3}$ - Scaled Maximum Debris Distance $\left(\frac{\text{ft}}{\text{tons}_{\text{TNT}}^{1/3}}\right)$ Versus Log ₁₀ Crater Diameter (ft)	Linear	$\text{Log}_{10} \left(\frac{D_M}{W^{1/3}}\right) = 3.026 - 0.0122 \text{Log}_{10} \phi$	± 0
	Quadratic	$\text{Log}_{10} \left(\frac{D_M}{W^{1/3}}\right) = 3.526 - 0.640 (\text{Log}_{10} \phi) + 0.179 (\text{Log}_{10} \phi)^2$	± 0
Log ₁₀ $W^{1/3}$ - Scaled Maximum Debris Distance $\left(\frac{\text{ft}}{\text{tons}_{\text{TNT}}^{1/3}}\right)$ Versus Log ₁₀ Crater Depth (ft)	Linear	$\text{Log}_{10} \left(\frac{D_M}{W^{1/3}}\right) = 2.615 + 0.382 \text{Log}_{10} D_c$	± 0
	Quadratic	$\text{Log}_{10} \left(\frac{D_M}{W^{1/3}}\right) = 3.273 - 1.077 \text{Log}_{10} D_c + 0.727 (\text{Log}_{10} D_c)^2$	± 0
Log ₁₀ $W^{1/3}$ - Scaled Maximum Debris Distance $\left(\frac{\text{ft}}{\text{tons}_{\text{TNT}}^{1/3}}\right)$ Versus Log ₁₀ $W^{1/3}$ - Scaled Crater Volume $\left(\frac{\text{ft}^3}{\text{tons}_{\text{TNT}}^{1/3}}\right)$	Linear	$\text{Log}_{10} \left(\frac{D_M}{W^{1/3}}\right) = 2.569 + 0.110 \text{Log}_{10} \left(\frac{V_c}{W^{1/3}}\right)$	± 0
	Quadratic	$\text{Log}_{10} \left(\frac{D_M}{W^{1/3}}\right) = 3.379 - 0.339 \text{Log}_{10} \left(\frac{V_c}{W^{1/3}}\right) + 0.0618 \left[\text{Log}_{10} \left(\frac{V_c}{W^{1/3}}\right)\right]^2$	± 0
Log ₁₀ $W^{1/3}$ - Scaled Maximum Debris Distance $\left(\frac{\text{ft}}{\text{tons}_{\text{TNT}}^{1/3}}\right)$ Versus Log ₁₀ $W^{1/3}$ - Scaled Crater Diameter $\left(\frac{\text{ft}}{\text{tons}_{\text{TNT}}^{1/3}}\right)$	Linear	$\text{Log}_{10} \left(\frac{D_M}{W^{1/3}}\right) = 2.450 + 0.385 \text{Log}_{10} \left(\frac{\phi}{W^{1/3}}\right)$	± 0
	Quadratic	$\text{Log}_{10} \left(\frac{D_M}{W^{1/3}}\right) = 0.866 + 2.644 \text{Log}_{10} \left(\frac{\phi}{W^{1/3}}\right) - 0.781 \left[\text{Log}_{10} \left(\frac{\phi}{W^{1/3}}\right)\right]^2$	± 0
Log ₁₀ $W^{1/3}$ - Scaled Maximum Debris Distance $\left(\frac{\text{ft}}{\text{tons}_{\text{TNT}}^{1/3}}\right)$ Versus Log ₁₀ $W^{1/3}$ - Scaled Crater Depth $\left(\frac{\text{ft}}{\text{tons}_{\text{TNT}}^{1/3}}\right)$	Linear	$\text{Log}_{10} \left(\frac{D_M}{W^{1/3}}\right) = 2.506 + 0.616 \text{Log}_{10} \left(\frac{D_c}{W^{1/3}}\right)$	± 0
	Quadratic	$\text{Log}_{10} \left(\frac{D_M}{W^{1/3}}\right) = 2.299 + 1.164 \text{Log}_{10} \left(\frac{D_c}{W^{1/3}}\right) - 0.313 \left[\text{Log}_{10} \left(\frac{D_c}{W^{1/3}}\right)\right]^2$	± 0

SECRET

SECRET

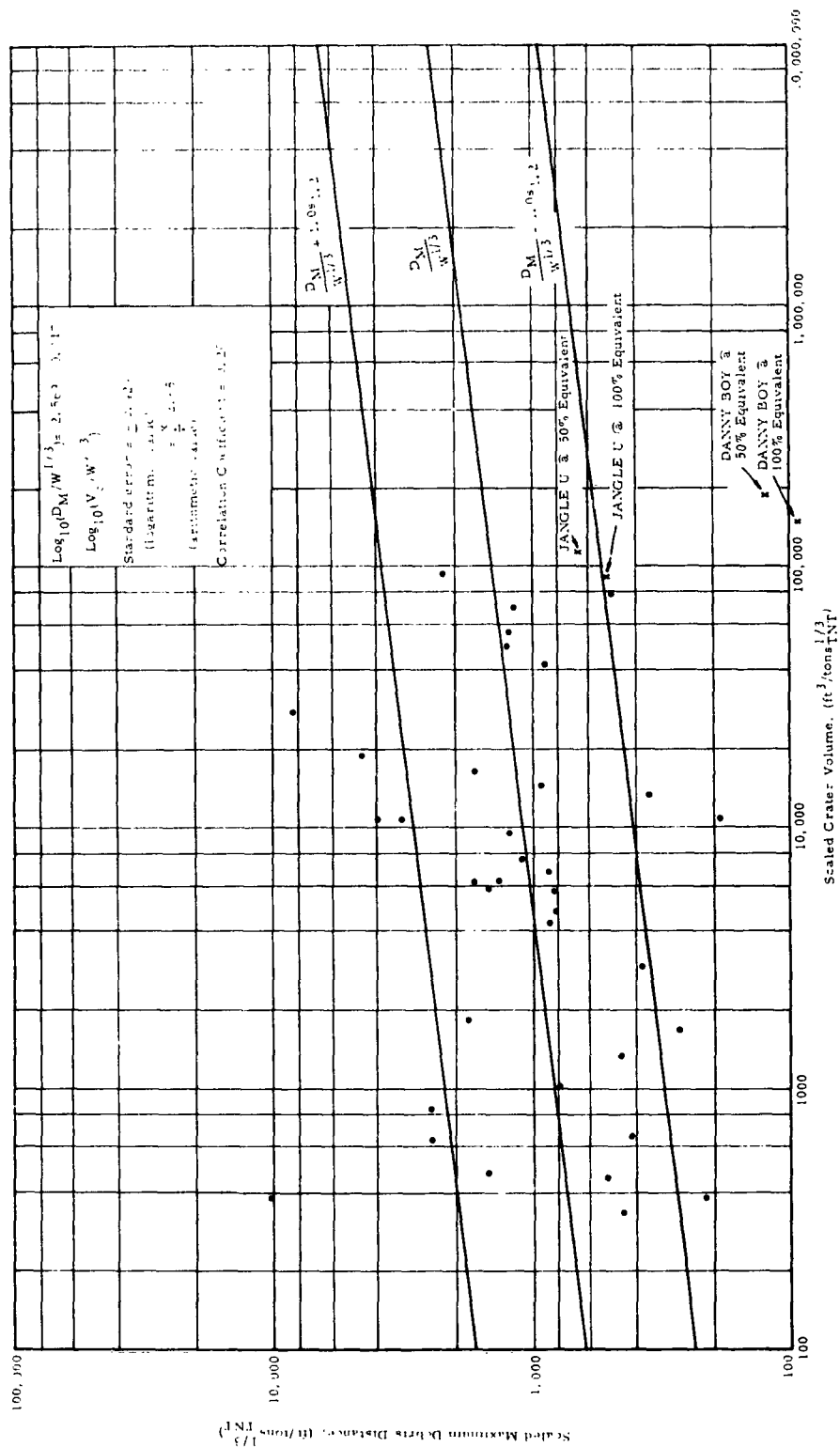
2

Table 2.2

OR MAXIMUM DEBRIS DISTANCE IN TERMS OF CRATER DIMENSIONS

Logarithmic Form		Exponential Form		Correlation Coefficient	Figure Number
Regression Line	Standard Error	Regression Line	Standard Error		
$2.187 + 0.262 \log_{10} V_c$	± 0.405	$D_M = 154 V_c^{0.262}$	$\frac{x}{\pm} 2.54$	0.51	2.11
$3.391 - 0.389 \log_{10} V_c + 0.0835 (\log_{10} V_c)^2$	± 0.404	$D_M = 2460 V_c^{-0.389} (10)^{0.0835 (\log_{10} V_c)^2}$	$\frac{x}{\pm} 2.54$	0.49	2.12
$2.261 + 0.577 \log_{10} \phi$	± 0.427	$D_M = 182 \phi^{0.577}$	$\frac{x}{\pm} 2.67$	0.42	2.13
$2.946 - 0.258 \log_{10} \phi + 0.245 (\log_{10} \phi)^2$	± 0.432	$D_M = 884 \phi^{-0.258} (10)^{0.245 (\log_{10} \phi)^2}$	$\frac{x}{\pm} 2.70$	0.36	2.14
$2.428 + 0.770 \log_{10} D_c$	± 0.395	$D_M = 268 D_c^{0.770}$	$\frac{x}{\pm} 2.49$	0.54	2.15
$2.623 + 0.340 \log_{10} D_c + 0.214 (\log_{10} D_c)^2$	± 0.401	$D_M = 419 D_c^{0.340} (10)^{0.214 (\log_{10} D_c)^2}$	$\frac{x}{\pm} 2.52$	0.50	2.16
$\frac{D_M}{W^{1/3}} = 2.822 + 0.0467 \log_{10} V$	± 0.431	$\frac{D_M}{W^{1/3}} = 664 V_c^{0.0467}$	$\frac{x}{\pm} 2.70$	0.098	
$\frac{D_M}{W^{1/3}} = 3.867 - 0.518 \log_{10} V_c + 0.072 (\log_{10} V_c)^2$	± 0.433	$\frac{D_M}{W^{1/3}} = 7370 V_c^{-0.518} (10)^{0.072 (\log_{10} V_c)^2}$	$\frac{x}{\pm} 2.71$	0.17	
$\frac{D_M}{W^{1/3}} = 3.026 - 0.0122 \log_{10} \phi$	± 0.433	$\frac{D_M}{W^{1/3}} = 1062 \phi^{-0.0122}$	$\frac{x}{\pm} 2.71$	0.010	
$\frac{D_M}{W^{1/3}} = 3.526 - 0.622 (\log_{10} \phi) + 0.179 (\log_{10} \phi)^2$	± 0.439	$\frac{D_M}{W^{1/3}} = 3560 \phi^{-0.622} (10)^{0.179 (\log_{10} \phi)^2}$	$\frac{x}{\pm} 2.75$	0.24	
$\frac{D_M}{W^{1/3}} = 2.615 + 0.382 \log_{10} D_c$	± 0.414	$\frac{D_M}{W^{1/3}} = 412 D_c^{0.382}$	$\frac{x}{\pm} 2.60$	0.29	
$\frac{D_M}{W^{1/3}} = 3.273 - 1.077 \log_{10} D_c + 0.727 (\log_{10} D_c)^2$	± 0.413	$\frac{D_M}{W^{1/3}} = 1876 D_c^{-1.077} (10)^{0.727 (\log_{10} D_c)^2}$	$\frac{x}{\pm} 2.59$	0.25	
$\frac{D_M}{W^{1/3}} = 2.569 + 0.117 \log_{10} \left(\frac{V_c}{W^{1/3}} \right)$	± 0.424	$\frac{D_M}{W^{1/3}} = 371 \left(\frac{V_c}{W^{1/3}} \right)^{0.117}$	$\frac{x}{\pm} 2.65$	0.20	2.17
$\frac{D_M}{W^{1/3}} = 3.379 - 0.339 \log_{10} \left(\frac{V_c}{W^{1/3}} \right) + 0.0618 \left[\log_{10} \left(\frac{V_c}{W^{1/3}} \right) \right]^2$	± 0.429	$\frac{D_M}{W^{1/3}} = 2400 \left(\frac{V_c}{W^{1/3}} \right)^{-0.339} (10)^{0.0618 \left[\log_{10} \left(\frac{V_c}{W^{1/3}} \right) \right]^2}$	$\frac{x}{\pm} 2.69$	0.11	2.18
$\frac{D_M}{W^{1/3}} = 2.450 + 0.385 \log_{10} \left(\frac{\phi}{W^{1/3}} \right)$	± 0.422	$\frac{D_M}{W^{1/3}} = 282 \left(\frac{\phi}{W^{1/3}} \right)^{0.385}$	$\frac{x}{\pm} 2.64$	0.23	2.19
$\frac{D_M}{W^{1/3}} = 0.866 + 2.644 \log_{10} \left(\frac{\phi}{W^{1/3}} \right) - 0.781 \left[\log_{10} \left(\frac{\phi}{W^{1/3}} \right) \right]^2$	± 0.421	$\frac{D_M}{W^{1/3}} = 7.34 \left(\frac{\phi}{W^{1/3}} \right)^{2.644} (10)^{-0.781 \left[\log_{10} \left(\frac{\phi}{W^{1/3}} \right) \right]^2}$	$\frac{x}{\pm} 2.64$	0.16	2.20
$\frac{D_M}{W^{1/3}} = 2.506 + 0.616 \log_{10} \left(\frac{D_c}{W^{1/3}} \right)$	± 0.382	$\frac{D_M}{W^{1/3}} = 320 \left(\frac{D_c}{W^{1/3}} \right)^{0.616}$	$\frac{x}{\pm} 2.41$	0.47	2.21
$\frac{D_M}{W^{1/3}} = 2.299 + 1.164 \log_{10} \left(\frac{D_c}{W^{1/3}} \right) - 0.313 \left[\log_{10} \left(\frac{D_c}{W^{1/3}} \right) \right]^2$	± 0.385	$\frac{D_M}{W^{1/3}} = 199 \left(\frac{D_c}{W^{1/3}} \right)^{1.164} (10)^{-0.313 \left[\log_{10} \left(\frac{D_c}{W^{1/3}} \right) \right]^2}$	$\frac{x}{\pm} 2.43$	0.43	2.22

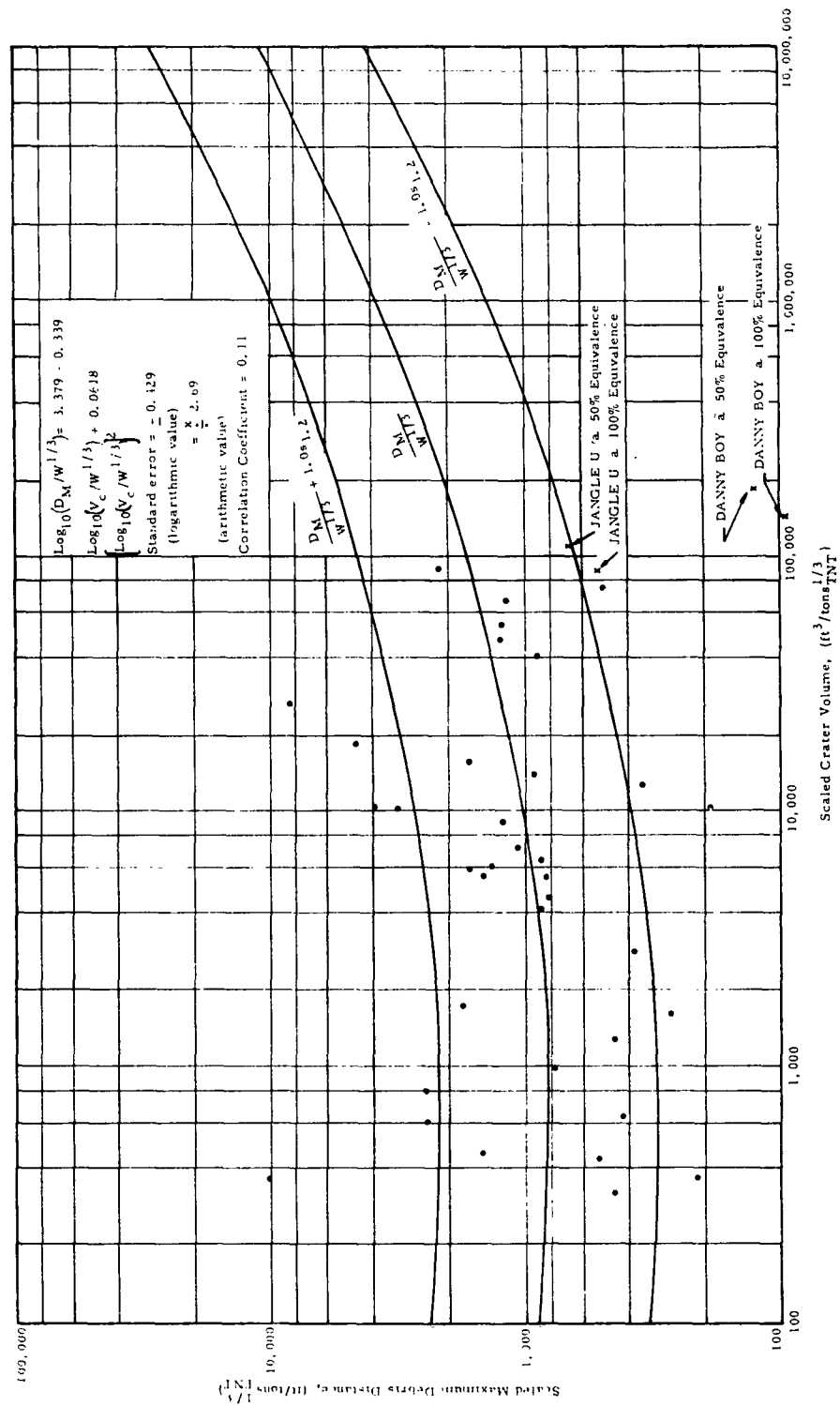
SECRET



SECRET

Figure 2.17 Linear Regression Line:
 $W^{1/3}$ - Scaled Maximum Debris Distance versus $W^{1/3}$ - Scaled Crater Volume

SECRET



SECRET

Figure 2.18 Quadratic Regression Line: $W^{1/3}$ -Scaled Maximum Debris Distance versus $W^{1/3}$ -Scaled Crater Volume

SECRET

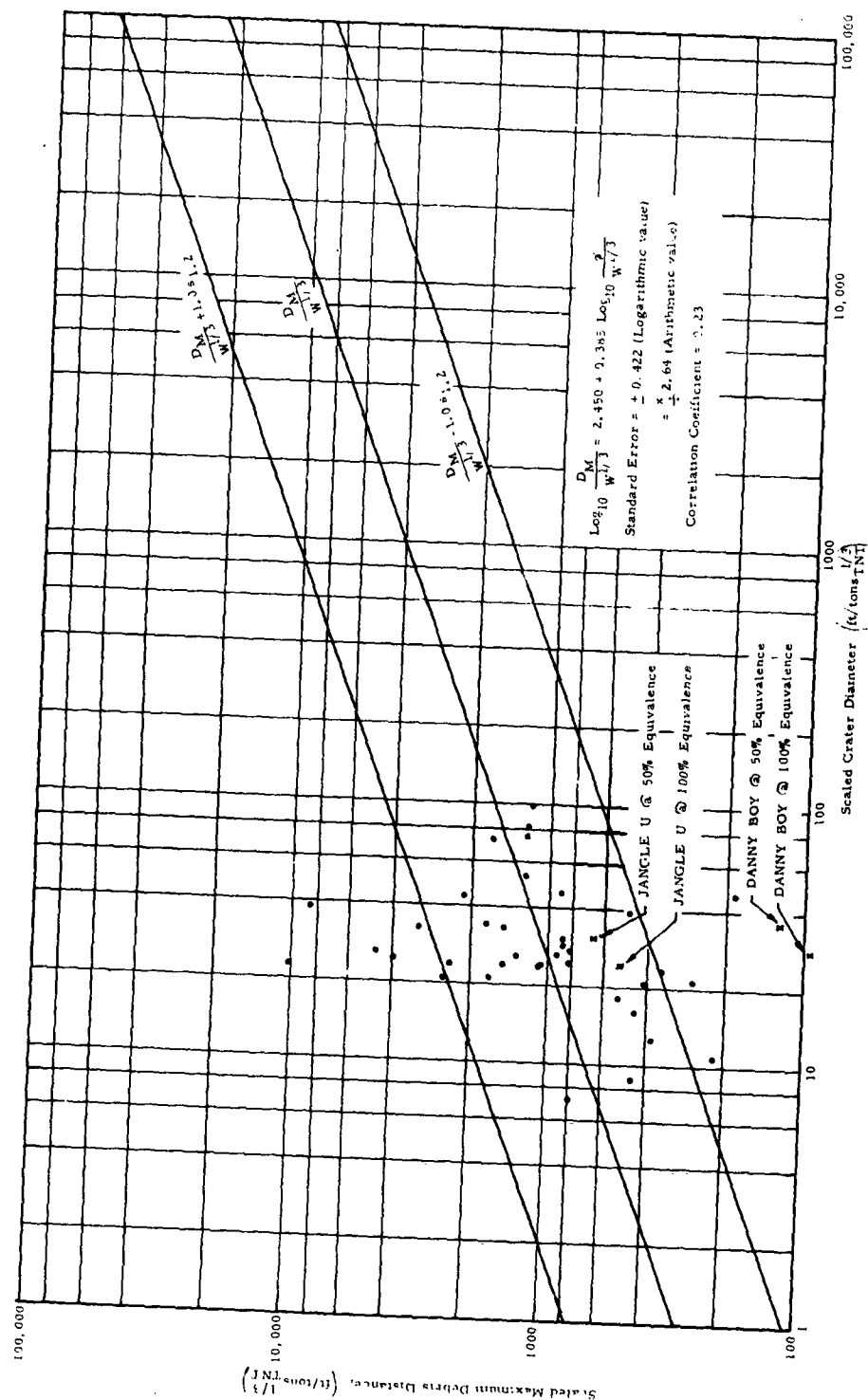


Figure 2.19 Linear Regression Line: $W^{1/3}$ -Scaled Maximum Debris Distance
versus $W^{1/3}$ -Scaled Crater Diameter

SECRET

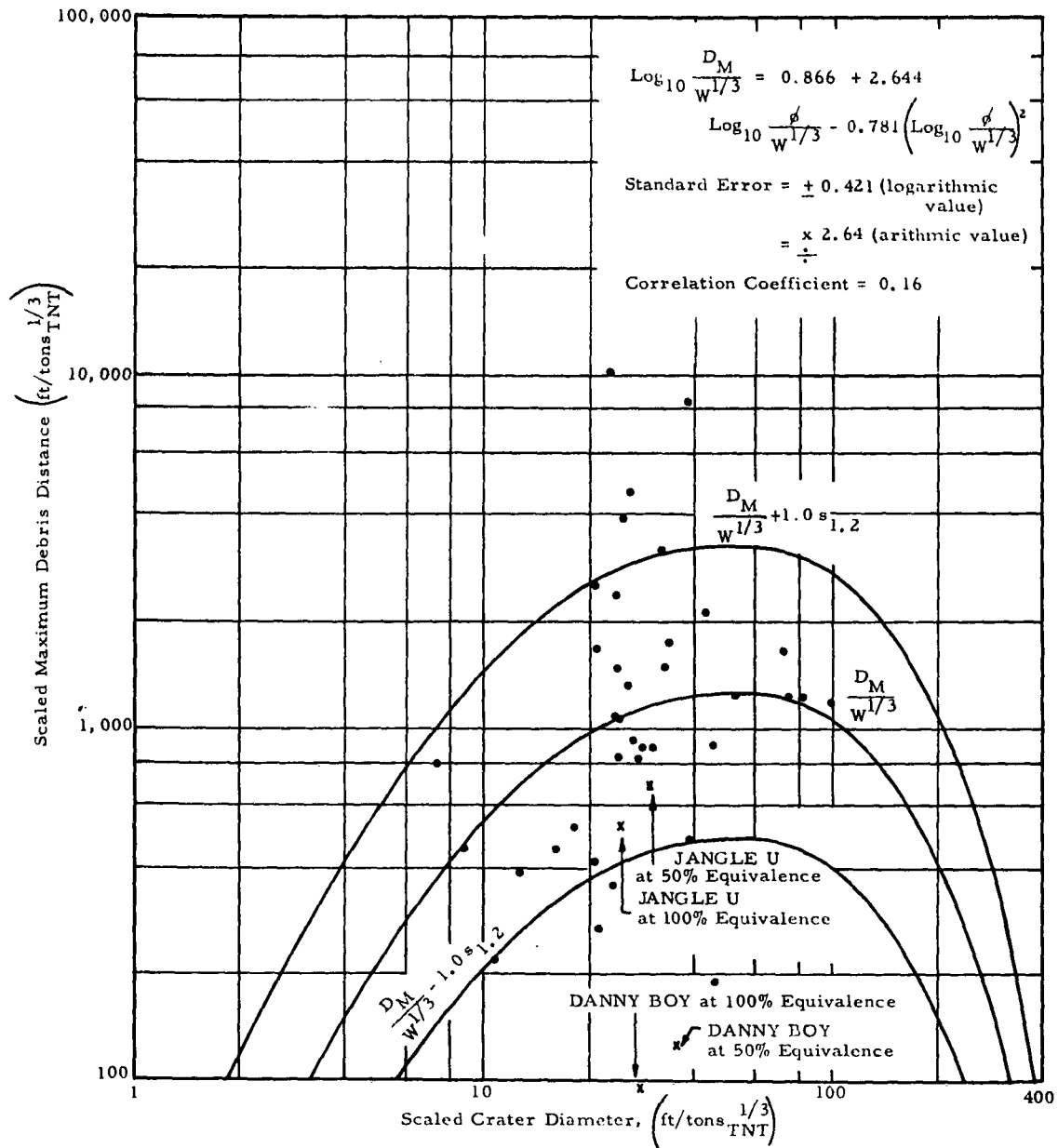


Figure 2.20 Quadratic Regression Line, $W^{1/3}$ -Scaled Maximum Debris Distance versus $W^{1/3}$ -Scaled Crater Diameter

SECRET

SECRET

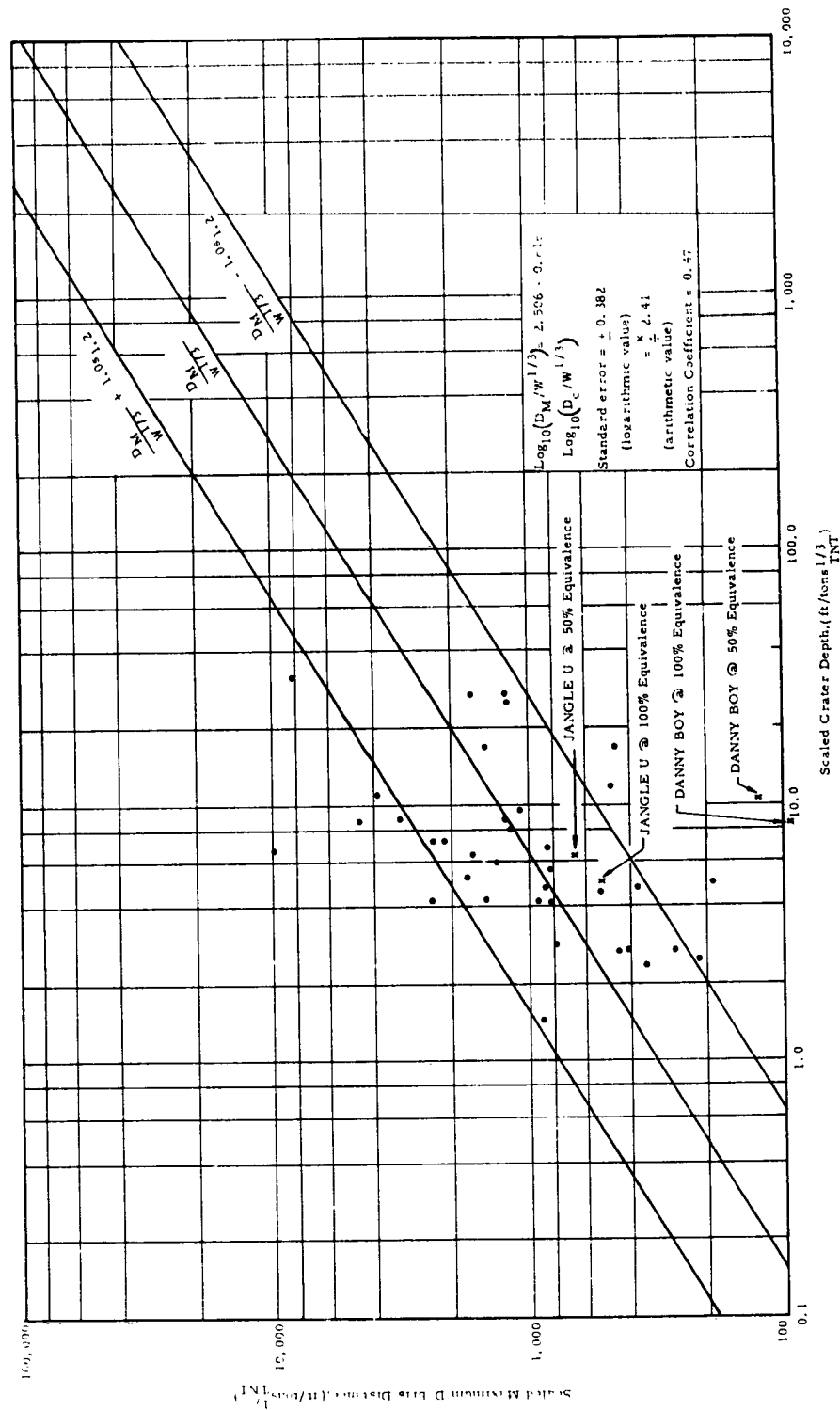
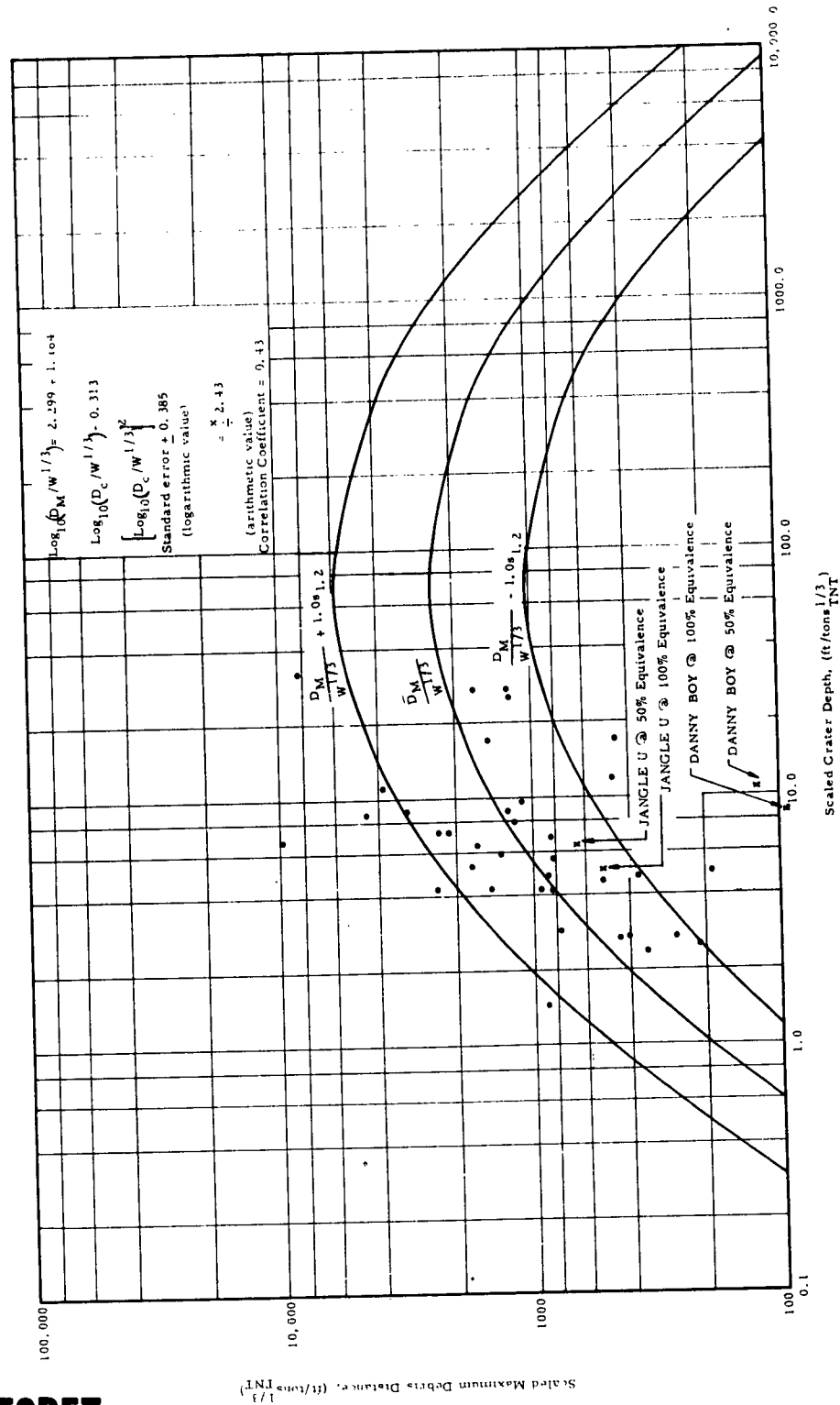


Figure 2-21 Linear Regression Line: $W^{1/3}$ -Scaled Maximum Debris Distance versus $W^{1/3}$ -Scaled Crater Depth

SECRET

SECRET



SECRET

Figure 2.22 Quadratic Regression Line: $W^{1/3}$ - Scaled Maximum Debris Distance versus $W^{1/3}$ - Scaled Crater Depth

SECRET

All fragments have equal initial velocities, though other assumptions as to the initial velocity field may be made.

These assumptions are obviously not true, but refined expressions either cannot be obtained for the general case or would unduly complicate the model. These assumptions are justified in development of a model for order-of-magnitude estimates of the relative densities of debris at various ground ranges.

Figure 2. 23 represents a wall subjected to an explosive impulse from a line-source charge.

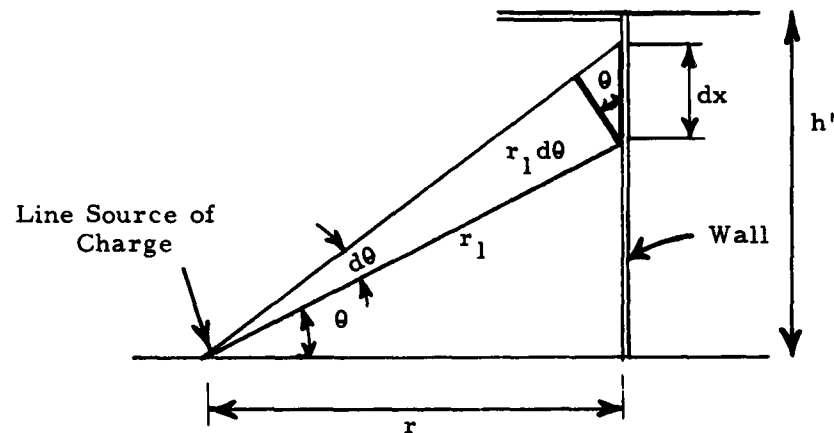


Figure 2. 23 Wall Panel under Explosive Impulse from Line Source Charge

SECRET

SECRET

In this figure,

$$\left. \begin{aligned} r_1 &= \frac{r}{\cos \theta} \\ dx &= \frac{r_1 d\theta}{\cos \theta} = \frac{r d\theta}{\cos^2 \theta} \\ \frac{dx}{d\theta} &= \frac{r}{\cos^2 \theta} \quad \text{in which the limit on } \theta \leq \tan^{-1} \frac{h'}{r}, \end{aligned} \right\} \quad (2.3)$$

and the fragment distribution in the wall becomes:

$$\frac{\text{Number of fragments}}{\text{Unit elevation angle}} \propto \frac{1}{\cos^2 \theta} \quad \text{with limit } \theta \leq \tan^{-1} \frac{h'}{r}.$$

Similarly, the geometry of the roof is shown in Fig. 2.24.

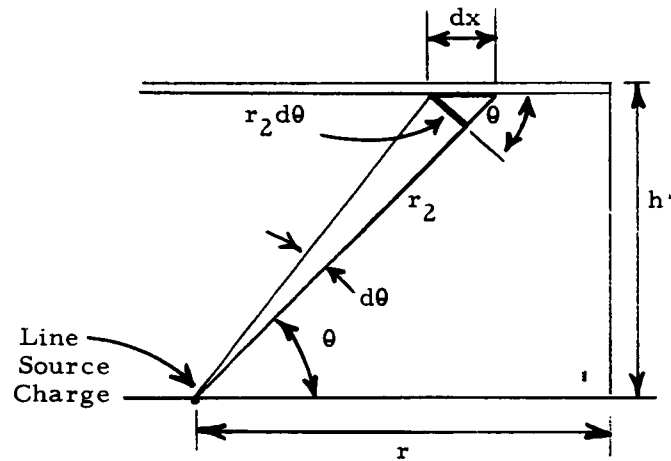


Figure 2.24 Roof Panel Fragmented by Line-Source Charge

SECRET

SECRET

Here,

$$\left. \begin{aligned} dx &= \frac{r_2 d\theta}{\cos \theta} \\ r_2 &= \frac{h'}{\sin \theta} \\ \frac{dx}{d\theta} &= \frac{h'}{\sin \theta \cos \theta} \text{ in which the limit on } \theta \geq \tan^{-1} \frac{h'}{r} \end{aligned} \right\} (2.4)$$

and the fragment distribution in the roof becomes

$$\frac{\text{Number of fragments}}{\text{Unit elevation angle}} \propto \frac{1}{\sin \theta \cos \theta} \text{ with limit } \theta \geq \tan^{-1} \frac{h'}{r}.$$

For the circular arch, shown in Fig. 2.25,

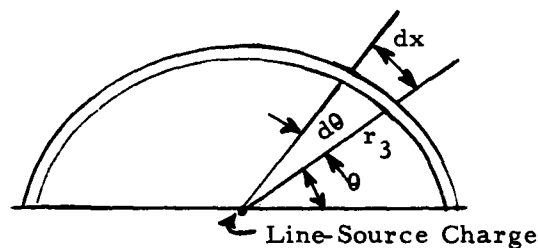


Fig. 2.25 Structural Arch Subject to Impulse Load From Line-Source Charge

the distribution of fragment quantities becomes a constant.

$$\frac{\text{Number of fragments}}{\text{Unit elevation angle}} = \frac{dx}{d\theta} = r_3 = \text{constant}$$

The distance traveled by the individual fragments is represented in Fig. 2.26,

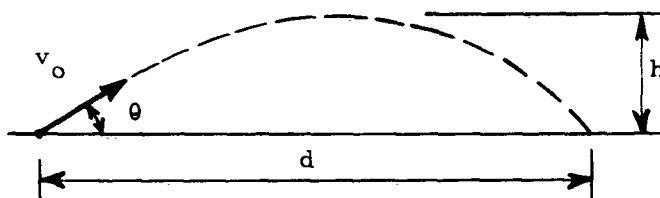


Figure 2.26 Trajectory of Individual Fragment

SECRET

SECRET

in which,

$$\begin{aligned}v_v &= v_o \sin \theta \\h &= v_o \sin \theta t - \frac{1}{2} g t^2\end{aligned}$$

and

$$h = \frac{1}{2} g t^2$$

Therefore,

$$\begin{aligned}v_o \sin \theta t &= g t^2 \\t &= \frac{v_o \sin \theta}{g}\end{aligned}$$

Also,

$$v_h = v_o \cos \theta$$

Therefore

$$\begin{aligned}d &= v_o \cos \theta t \\&= \frac{v_o^2 \sin \theta \cos \theta}{g},\end{aligned}$$

and the trajectory distance parameter becomes

$$d \propto \sin \theta \cos \theta.$$

The fragment quantity parameters, $\frac{1}{\cos^2 \theta}$ and $\frac{1}{\sin \theta \cos \theta}$, are plotted

against the fragment distance parameter $\sin \theta \cos \theta$ in Fig. 2.27 for values of θ from 0° to 90° . The relative quantity of fragments landing within any circumferential sector can be found by integrating these functions over the appropriate limits of the function $\sin \theta \cos \theta$.

This integration is carried out as follows for walls:

In Fig. 2.27 let

$$y = \frac{1}{\cos^2 \theta}$$

$$x = \sin \theta \cos \theta$$

SECRET

SECRET

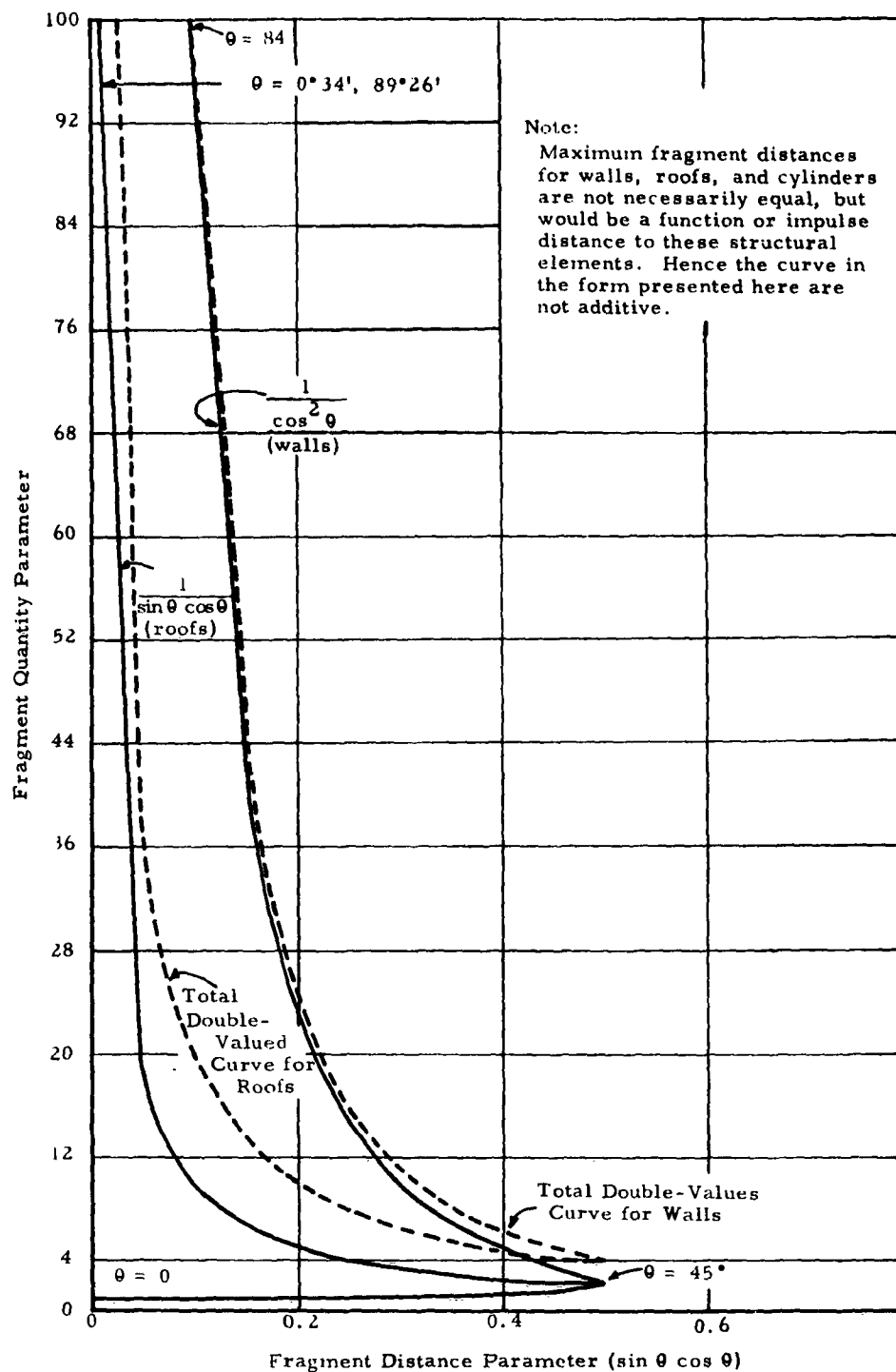


Figure 2.27 Theoretical Fragment Distribution Functions

SECRET

SECRET

Then

$$\begin{aligned} dx &= \frac{dx}{d\theta} d\theta \\ &= (-\sin^2 \theta + \cos^2 \theta) d\theta \\ &= (1 - 2 \sin^2 \theta) d\theta. \end{aligned}$$

The relative quantity of fragments in strips centered about the line charge, (or circumferential strips centered about ground zero), then becomes:

$$\begin{aligned} Q_w &= \int y dx \\ &= \int_{\theta_1}^{\theta_2} \frac{(1 - 2 \sin^2 \theta)}{\cos^2 \theta} d\theta \\ &= \left[\tan \theta - 2 (\tan \theta - \theta) \right]_{\theta_1}^{\theta_2} \\ &= \left[2\theta - \tan \theta \right]_{\theta_1}^{\theta_2} \quad \text{with limit on } \theta \leq \tan^{-1} \frac{h'}{r}. \end{aligned}$$

Similarly, for roofs, let

$$\begin{aligned} y &= \frac{1}{\sin \theta \cos \theta} \\ x &= \sin \theta \cos \theta \\ \frac{dx}{d\theta} &= (1 - 2 \sin^2 \theta) d\theta, \end{aligned}$$

thus

$$\begin{aligned} \theta_R &= \int y dx \\ &= \int_{\theta_1}^{\theta_2} \frac{(1 - 2 \sin^2 \theta)}{\sin \theta \cos \theta} d\theta \\ &= \left[\log_e \tan \theta - 2 (-\log_e \cos \theta) \right]_{\theta_1}^{\theta_2} \\ &= \left[\log_e \tan \theta + 2 \log_e \cos \theta \right]_{\theta_1}^{\theta_2} \quad \text{in which limit } \theta \geq \tan^{-1} \frac{h'}{r}. \end{aligned}$$

SECRET

SECRET

For arches:

$$y = \text{constant} = k$$

$$x = \sin \theta \cos \theta$$

$$\frac{dx}{d\theta} = (1 - 2 \sin^2 \theta) d\theta,$$

thus integration for arches yields a fragment quantity function as follows:

$$\begin{aligned} Q_A &= \int k (1 - 2 \sin^2 \theta) d\theta \\ &= \left[k\theta - 2k \left(\frac{\theta}{2} - \frac{\sin 2\theta}{4} \right) \right]_{\theta_1}^{\theta_2} \\ &= \left[\frac{k \sin 2\theta}{2} \right]_{\theta_1}^{\theta_2} . \end{aligned}$$

Relative fragment quantities for circumferential bands about the point of burst, (assumed here to be at zero elevation at the center of the containing structure), are obtained by equating Q over the appropriate values of θ_1 and θ_2 . For wall panels θ_1 is 0° and θ_2 the angle included between surface zero and the plane through the line charge and the wall-roof intersection. For actual structures Q must be corrected to account for the different material quantities in wall and roof panels, and for differentials between normal distances between the line charge and the wall and roof panels. Thus, for the structure pictured in Fig. 2.28, the relative number of fragments falling within any band $R_j - R_i$ about the structure would be

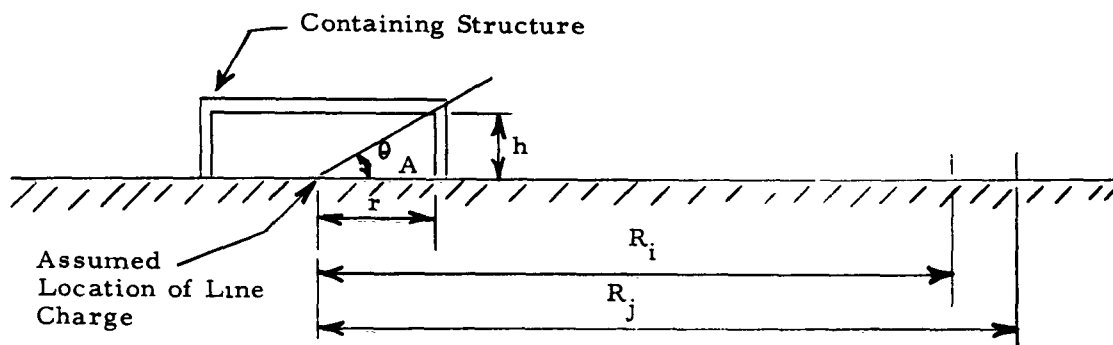


Figure 2.28 Typical Structure Subjected to Fragmentation by Internal Detonation

SECRET

SECRET

$$\begin{aligned} Q_T &= t_w r Q_w + t_R h Q_R \\ &= t_w r \left[2\theta - \tan \theta \right]_{0^\circ}^{\theta_A} + t_R h \left[\log_e \tan \theta + 2 \log_e \cos \theta \right]_{\theta_A}^{90^\circ} \end{aligned}$$

where

t_w = wall thickness
 t_r = roof panel thickness

Comparison of Ideal and Actual Debris Distribution from Semi-Contained Explosions

A comparison of the ideal fragment dispersion functions with three actual HE explosions is made in Fig. 2. 29. In making this comparison the quantities t_w , s , t_r , and h were dropped because of lack of data fully describing the containing structures. Furthermore, the functions Q_r and Q_w in Fig. 2. 29 are plotted for all values from 0° to 90° , since the actual value of θ_A was not known. Actually, this means that Q_r and Q_w are plotted for panels of infinite length. The theoretical curves Q_r and Q_w were plotted by equating $(\sin \theta \cos \theta)_{\max} = 1.0$, computing Q_r and Q_w for 10 percent increments of $(\sin \theta \cos \theta)_{\max}$, and plotting values of Q_r and Q_w at the midpoints of these sectors. Curves for the actual explosions were established by equating the maximum debris distance to 1.0, and plotting actual reported fragment counts for 10 percent increments of the maximum reported distance at the midpoints of the circumferential bands. The following explosions are included in this analysis.

Wolf Creek 1944: (Ref. 10)

Accidental Explosion.

4,800 lb of ammonium nitrate exploded in a building.
305 fragments were recorded within a maximum
range of one mile.

Kankakee, 1943: (Ref. 10)

Accidental Explosion.

5,300 lb of Bi-Oil exploded in a building.
160 fragments were recorded within a maximum
range of 3,750 ft.

SECRET

SECRET

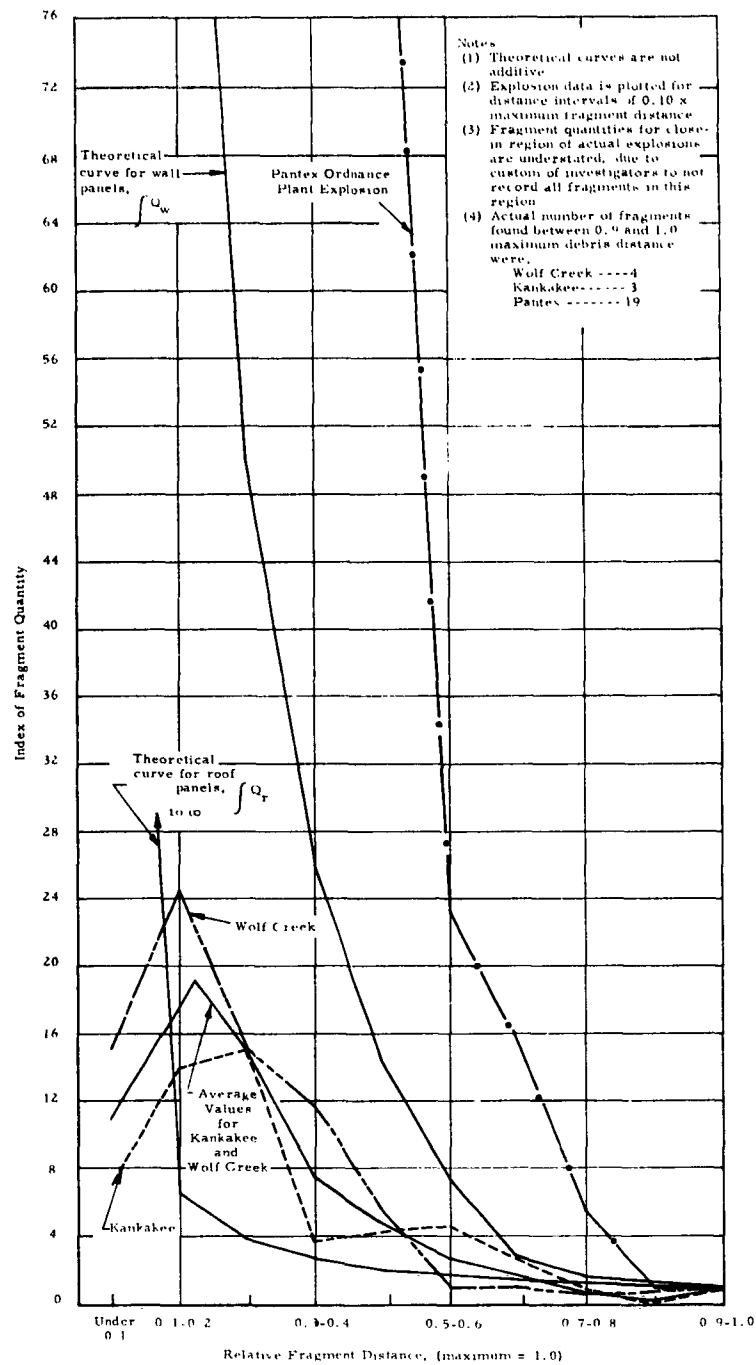


Figure 2.29 Comparison of Theoretical and Actual Fragment Dispersion Patterns

SECRET

SECRET

Pantex Ordnance Plant, 1960: (Ref. 11)

Experimental explosion.

2,000 lb of HE in encased warheads detonated
inside U-shaped bay of reinforced concrete
ordnance structure having one-foot thick walls.

About 31,000 concrete fragments, with a total
weight of about 85,000 lb, were recorded within
a maximum range of about 1,450 feet.

The plotting of data from these explosions assumed that the furthest-thrown fragments were found and recorded. This is generally a reasonable assumption in reports on accidental explosions since the furthest-thrown fragments are generally of sufficient size to be observed and found, and since, in the thickly strewn close-in region, only large fragments or fragments considered significant in determining the cause of the explosion are recorded.

On the general shapes of the actual and theoretical curves are similar; this similarity is quite pronounced for the Pantex explosion. The average curve of fragment distribution for the Wolf Creek and Kankakee explosions is observed to fall between the theoretical and actual curves for walls and roofs -- a reasonable expectation. The steeper rise of the Pantex curve below a range of 0.8-0.9 times maximum may result from the nature of the structure.

It would be desirable to use these curves along with the maximum debris distance curves presented earlier to develop areal density patterns or probability of hit. To do so would require that both (1) the number of fragments in the outermost circumferential sector and (2) the nature of the curve in the region where it starts rising rapidly, be defined better. These factors may be related to the size and strength of the structure and their determination would thus require extensive experimental investigation. The currently available data, considered above, could be used for this purpose although it should be recognized that they are far from well defined experimental input.

SECRET

SECRET

2.3.2 Debris Dispersion Patterns of HE Explosions

Several prior studies of debris dispersion about accidental and experimental explosions have been made. One was performed by Colonel Clark S. Robinson who studied the results of six ordnance explosions, then compiled and compared their results (Ref. 12). This study is reviewed here along with additional plots of the recorded data which were prepared in an effort to find greater consistency of the plotted patterns. The second study was made at the Pantex Ordnance Plant at Amarillo, Texas, where about 31,000 fragments totaling 85,000 lb from a reinforced concrete structure were located and weighed after a planned interior explosion of 2,000 lb of high explosives (Ref. 11). The raw data available from this study were used in making a detailed study of the debris dispersion pattern from this explosion.

Army-Navy Explosives Safety Board Investigation of Debris Dispersion

Colonel Robinson plotted the specific area per missile against ground range. Specifically, the following explosions were studied:

Badger Ordnance Works, 1945:

7,500 lb of nitroglycerine exploded accidentally in a barricaded storehouse building of light frame construction. Data on about 600 fragments from building and contents were recorded.

Cornhusker, Nebraska, 1945:

10,000 lb of explosives detonated accidentally in a loading plant manufacturing bombs. Chief interest in the investigation centered about fragments of machinery and contents and few building fragments were included.

Portage, Ohio, 1943:

Bombs amounting to 40,000 lb of HE detonated accidentally in an arch-type, earth-covered, igloo magazine. Data on whole bombs and bomb fragments constituted the bulk of recorded debris.

SECRET

SECRET

Umatilla, Oregon, 1944:

64,000 lb of HE in bombs exploded accidentally in an Army-type igloo. Debris described consisted chiefly of pieces of concrete and fragments of machinery stored in the igloo.

Hastings, Nebraska, 1944:

100,000 lb of HE ignited in a building where bombs were being loaded. Interest lay chiefly in large concrete fragments from the building itself, and only information on those weighing over 25 lb was included.

Arco, Idaho, 1945:

250,000 lb of explosive in bombs was detonated in a planned explosion in an igloo-type magazine. Data on over 13,000 fragments were recorded.

Specific area is plotted against ground range for these six explosions in Fig. 2.30. Several limitations of these plots, stemming from existent debris recording practices, must be recognized. First, the investigators made no attempt to record all fragments, especially in the first five explosions listed above; this tends to give higher values for specific area than actual, perhaps by several orders of magnitude. Secondly, in the thickly strewn close-in region, explosion investigators tend to record the exceptional fragments only; hence the reversal of several curves at short ground ranges in Fig. 2.30 is unrealistic. It is stated in the ASESB report, however, that at the greater ground ranges, it was customary for investigators to record all missiles of sizes that would damage structures or kill personnel -- that is, all fragments weighing one pound or more. It was observed that in these explosions the far-flying fragments were usually large and most were discovered and recorded.

The individual curves of specific area in Fig. 2.30 do exhibit a consistent and characteristic shape. The relative positions and crossing over of the four intermediate explosions (10,000-lb, 40,000-lb, 65,000-lb and 100,000-lb curves) make it difficult to derive a general expression for the functional relationship between specific area and ground range for contained explosions. This stems from the fact that the curves are based

SECRET

SECRET

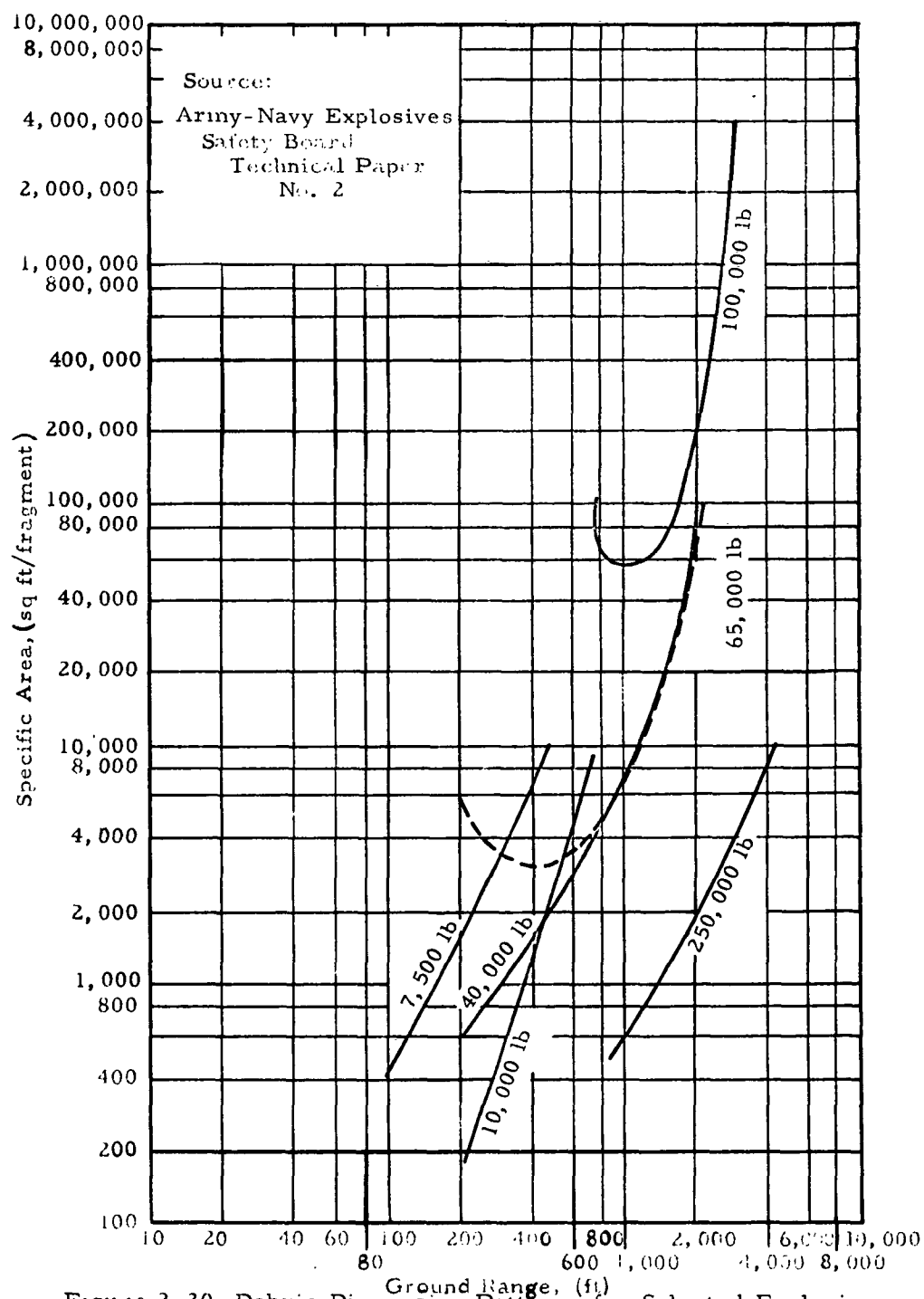


Figure 2 30 Debris Dispersion Patterns for Selected Explosions

SECRET

SECRET

on incomplete fragment counts, and that the actual specific area is a function of the nature of the structure itself, as well as the explosive weight and ground range.

Several additional plots of the data from Fig. 2. 30 have been prepared in an effort to find general curves for these functions with a better fit. These additional plots, shown in Fig. 2. 31 through 2. 36, were derived by selecting five points on each of the explosion curves of Fig. 2. 30 and computing new expressions as follows:

Fig. 2. 31 First-Order Logarithmic Curves of Debris Dispersion for Selected Explosions.

Log-log curves were fitted through the five selected points by the least-squares method, producing a series of curves of the form:

$$\log_{10} A_D = k [\log_{10} D]^n$$

No consistent relationship between either the slopes (n) or the intercepts (k) and the equivalent yield are apparent from these plots.

Fig. 2. 32 Second-Order Logarithmic Curves of Debris Dispersion for Selected Explosions.

Log-log second-order curves were fitted through the same five points as above for each curve. Distinct separations between the curves for the various yields are absent, and the negative slopes near ground zero are questionable.

Fig. 2. 33 Modified Second-Order Logarithmic Curves of Debris Dispersion for Selected Explosions.

Log-log second-order curves were fitted, again by the least-squares method, through six points for each curve -- the five used previously and the arbitrary addition of point (1, 1) as a data point. The resulting curves exhibit some separation at the shorter ground ranges, but the crossing-over of curves and their relative positions cannot be explained.

SECRET

SECRET

SECRET

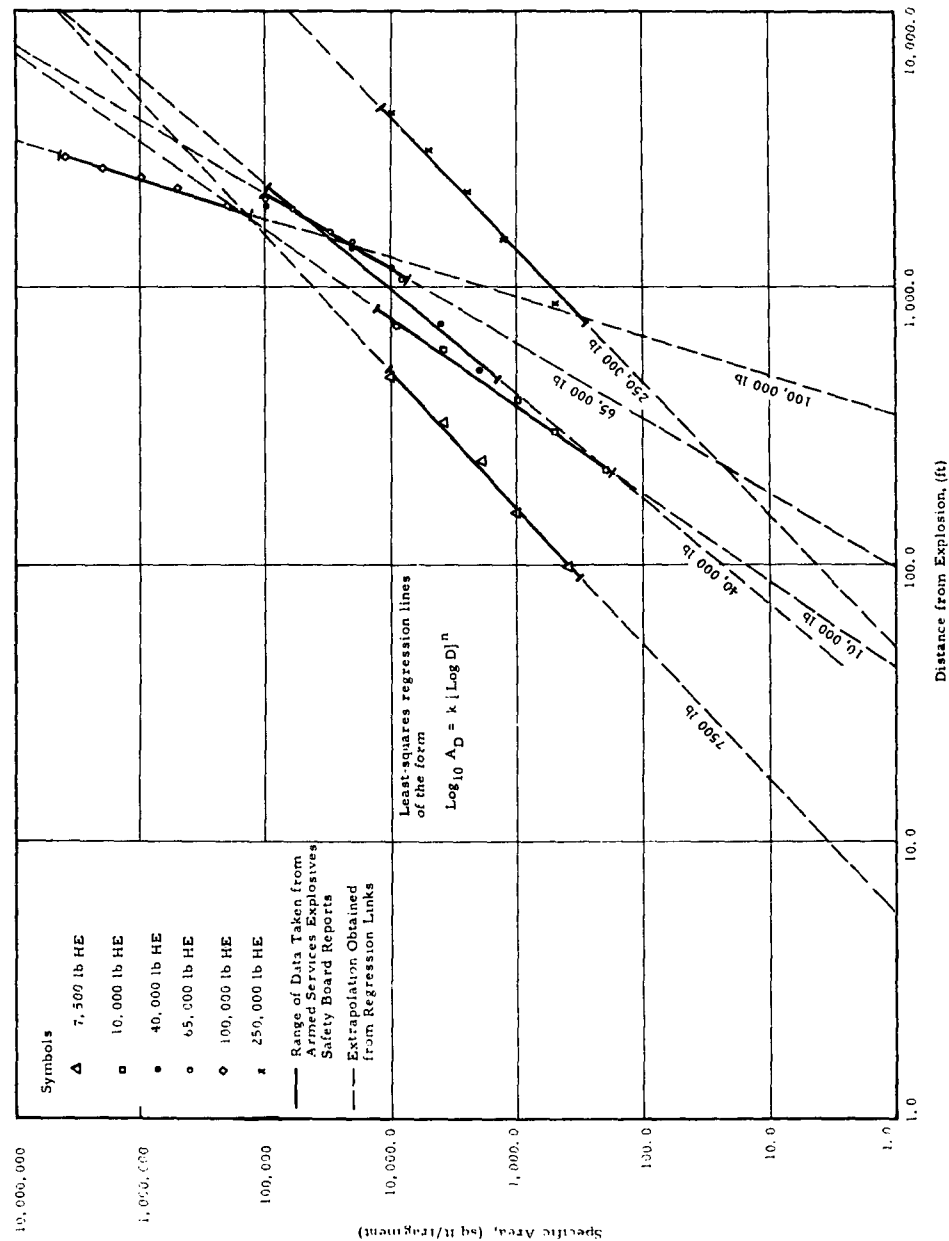
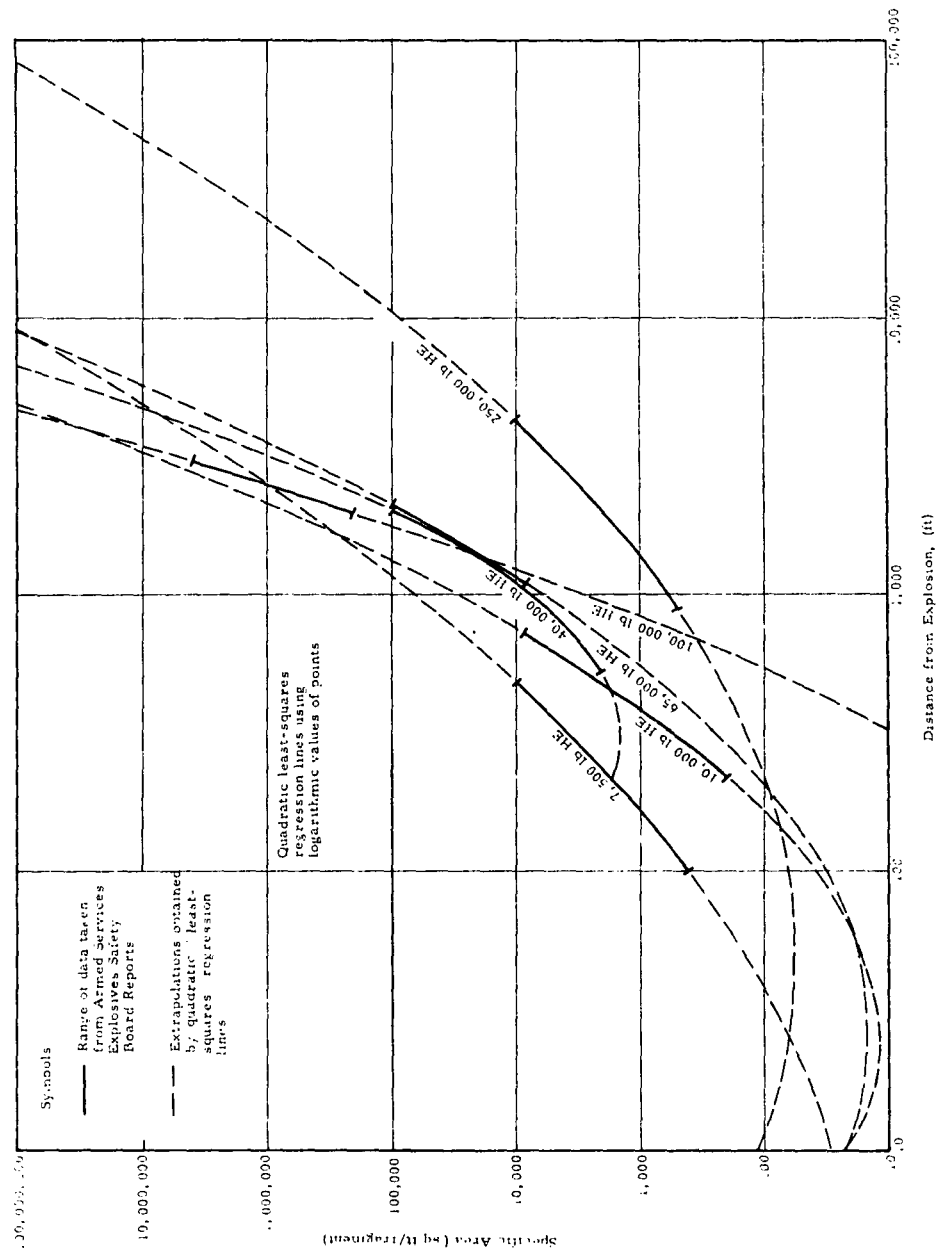


Figure 2.31 First-Order Logarithmic Curves of Debris Dispersion for Selected Explosions

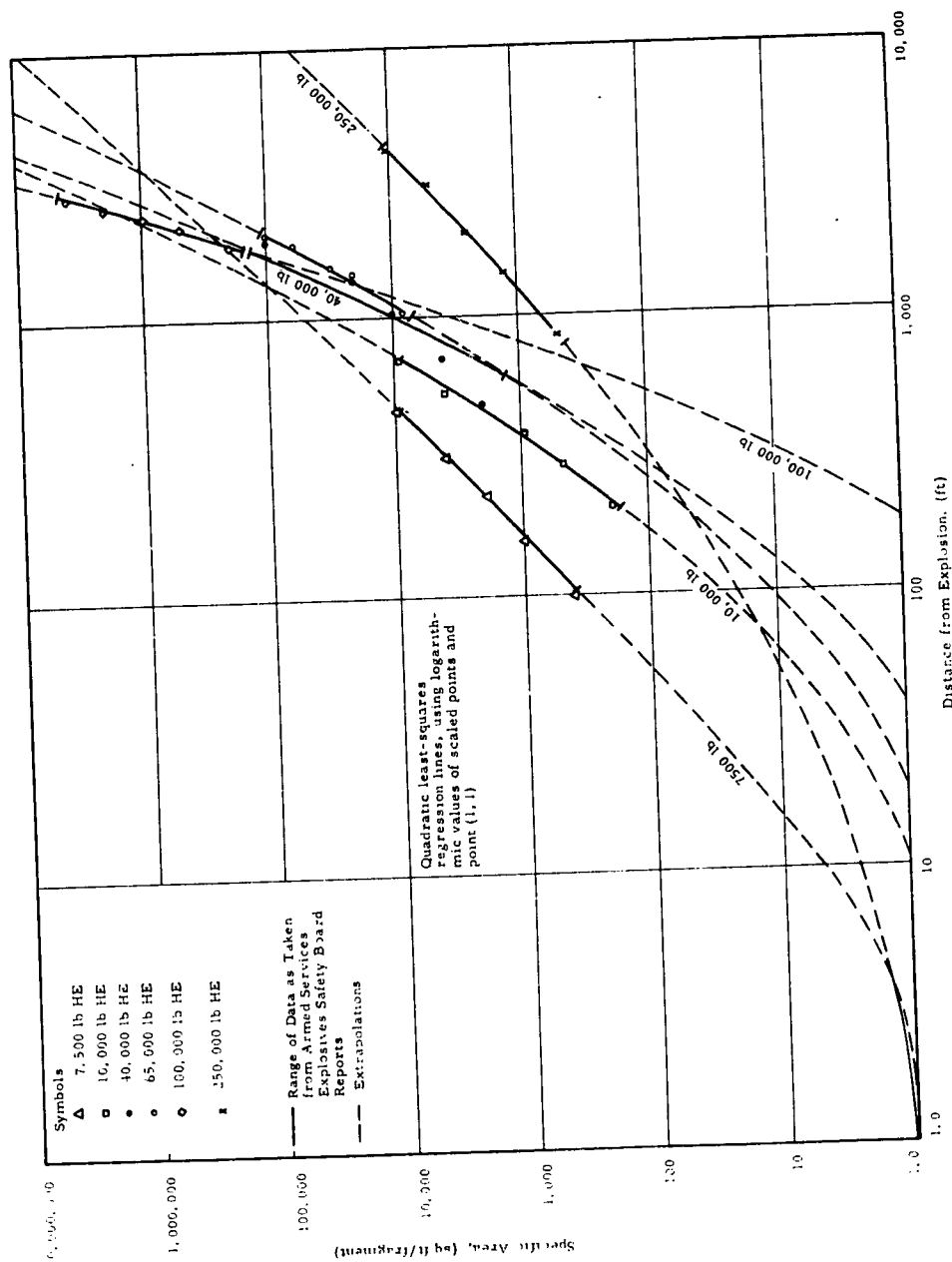
SECRET



SECRET

Figure 2 32 Second-Order Logarithmic Curves of Debris Dispersion for Selected Explosions

SECRET



SECRET

Figure 2.33 Modified Second-Order Logarithmic Curves of Debris Dispersion for Selected Explosions

SECRET

Fig. 2. 34 Parabolic Curves of Debris Dispersion for Selected Explosions.

These curves are parabolas of the form

$$A_D = k D^2$$

where, for each curve, k is the average value for a series of parabolas through point $(0, 0)$ and each of the five selected data points. The slope appears adequate for some curves (notably the 7, 500-lb and 250, 000-lb explosions), but the relative positions of the curves cannot be explained in terms of equivalent yield alone. Total quantity of available material for fragmentation probably is involved.

Fig. 2. 35 Logarithmic Parabolas of Debris Dispersion for Selected Explosions.

These curves are of the form

$$\text{Log}_{10} A_D = k (\text{log}_{10} D)^2$$

where, for each curve, k is the average value for a series of parabolas through point $(1, 1)$ and each of the five points on the curves.

Fig. 2. 36 Second-Order Semi-Logarithmic Curves of Debris Dispersion for Selected Explosions.

These curves are of the form

$$\text{Log}_{10} A_D = a + bD + cD^2$$

where the coefficients a , b , and c are determined by the least-squares method.

Of the six sets of curves, the logarithmic parabolas appear to provide the best fit. Relative positions of the curves cannot be explained, i. e., why they should not be consecutive in the order of yield. As stated earlier this may be a function of the amount of material available for fragmentation and the degree of fragmentation, which can be expected to vary with the quantity of explosives or the impulse. Because of the lack of consistency in these results, no further analysis was made of these results.

SECRET

SECRET

SECRET

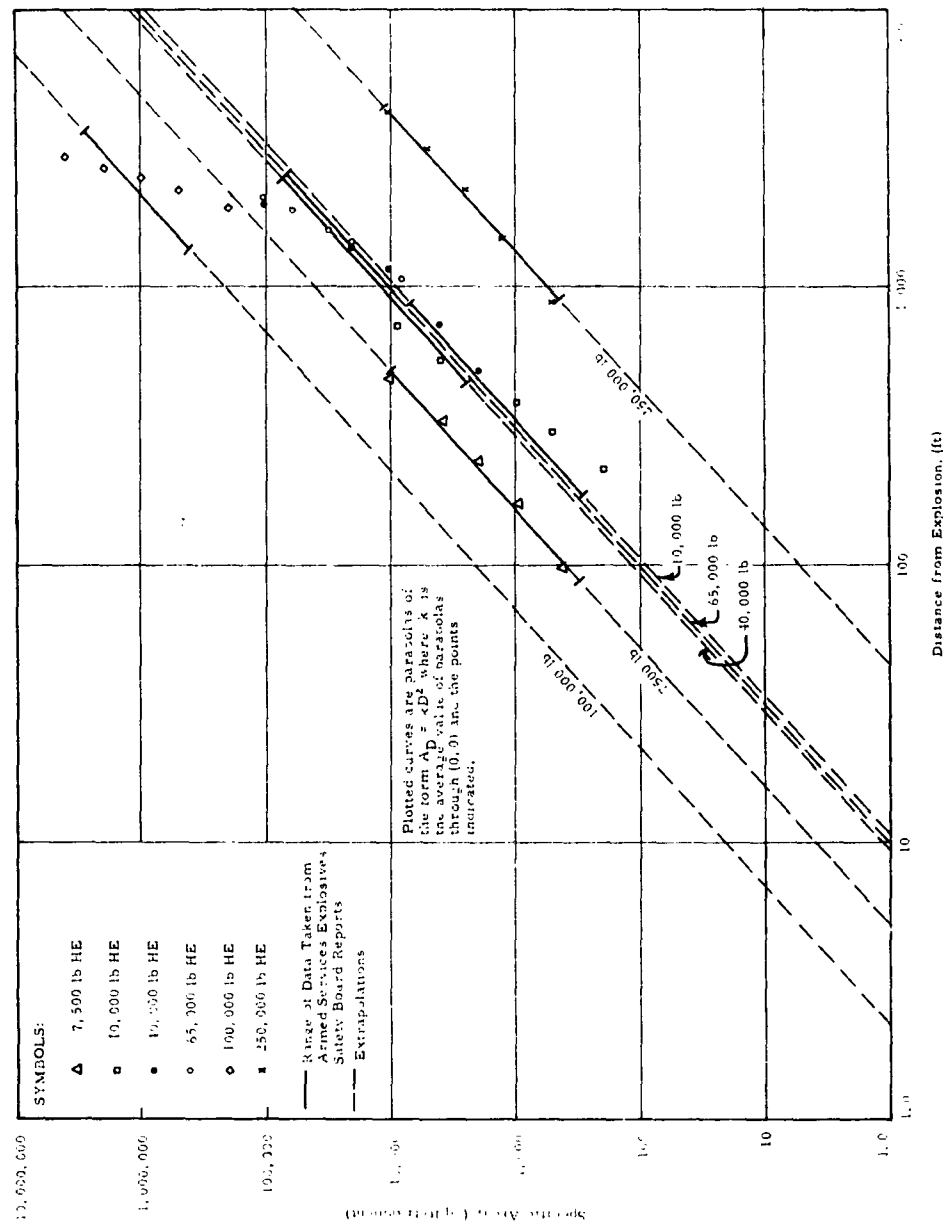


Figure 2.34 Parabolic Curves of Debris Dispersion for Selected Explosions

SECRET

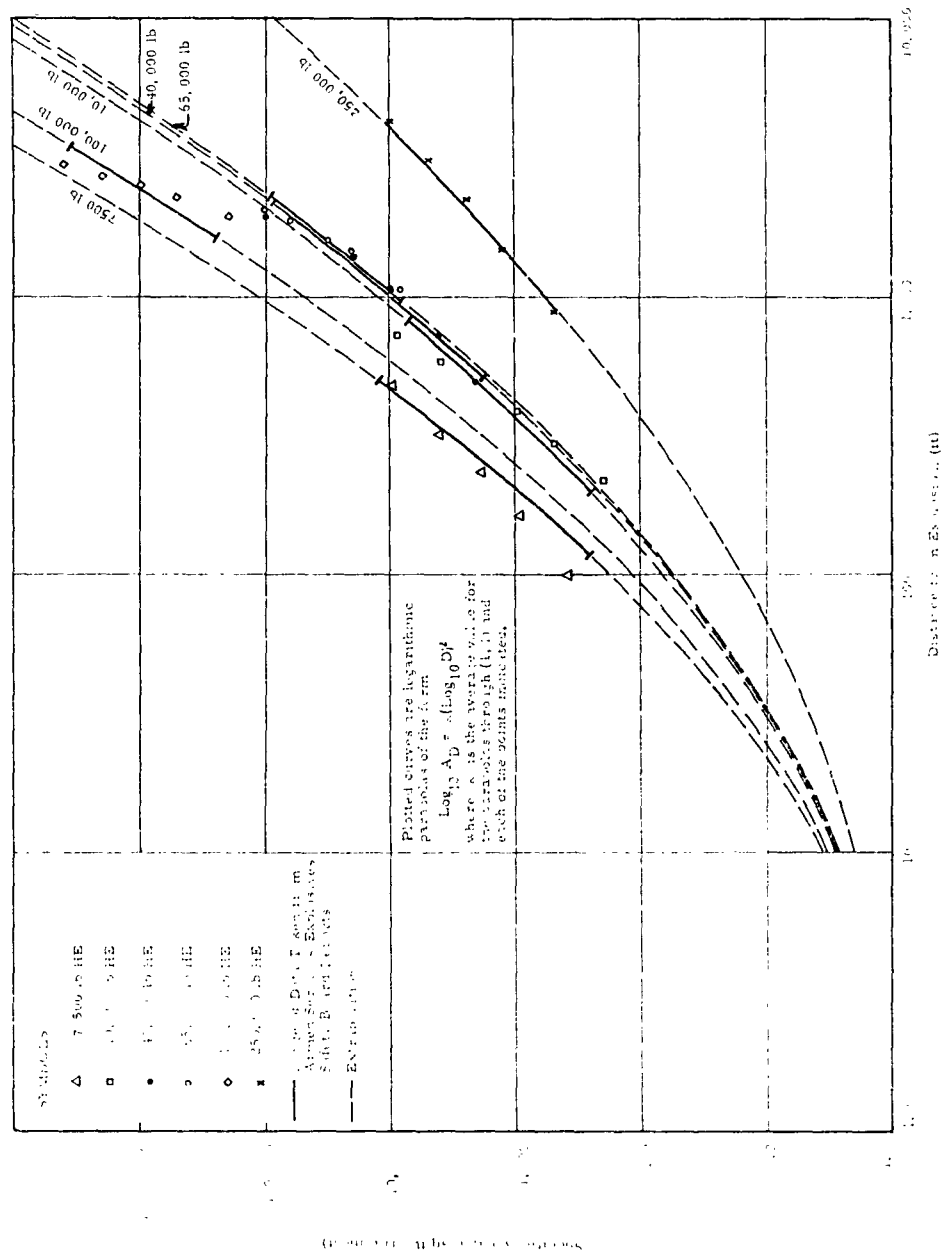


Figure 2.35 Logarithmic Parabolas of Debris Dispersion for Selected Explosions

SECRET

SECRET

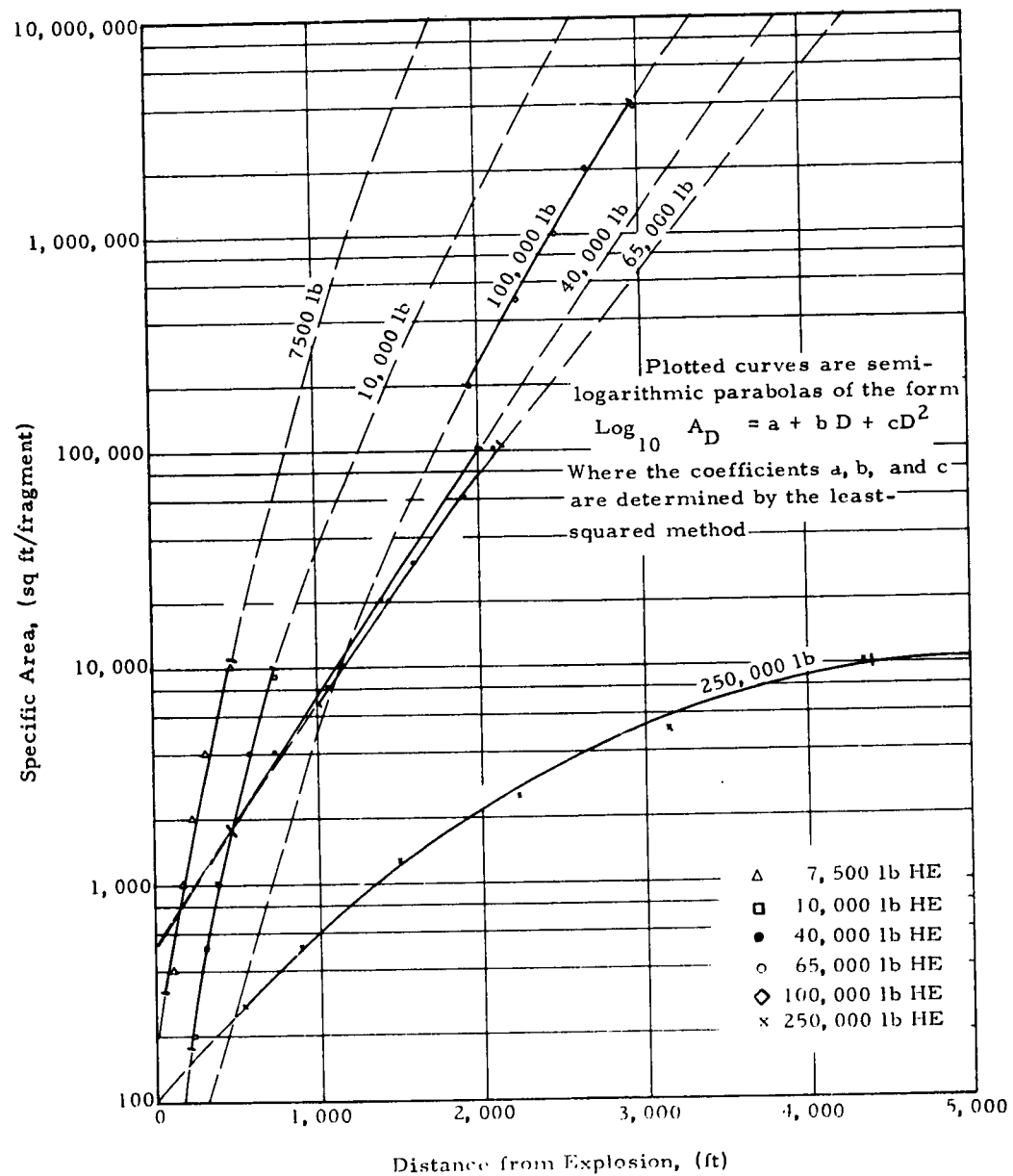


Figure 2.36 Second-Order Semi-Logarithmic Curves of Debris Dispersion for Selected Explosions

SECRET

SECRET

It will be recalled that investigators of accidental explosions tend to make incomplete counts of the smaller fragments in the thickly strewn close-in region about the source. Since plotted points in the foregoing study were all taken at equal value, this would result in curves which are too shallow, and thus tend to overestimate the debris problem when extrapolations are made beyond the limits of the data.

One measure of the fit of the fragment dispersion function can be obtained visually from data on the 1945 Badger Ordnance Works explosion of 7,500 lb of nitroglycerine from the plot of data points as shown in Fig. 2.37. Plotted points in Fig. 2.37 show debris dispersion expressed as specific area for each 10-ft interval in ground range from the point of burst. The average line drawn through these points was not originally computed by the least-squares method, but was an average based on the four central curves of Fig. 2.30 plotted at one-half the ground range. Though this original method of plotting was used merely because the Badger explosion was a barricaded structure, the line does appear to be a fair representation of this particular set of data.

The two curves denoting the one-standard-error limits have been plotted visually to include two-thirds of all plotted data points between them. The log value of the standard error is thus measured as ± 0.328 , giving a standard error of $\frac{x}{\bar{x}} = 2.13$ about the central line, assuming it were a true average and the distribution were normal.

Debris Dispersion from a Reinforced Concrete Structure

The 1960 planned explosion at Pantex Ordnance Plant provided extensive debris dispersion data (Ref. 11). This explosion involved the detonation of 2,000 lb of HE in the form of encased warheads placed inside the standard one-foot-thick reinforced concrete walls of a U-shaped bay. Two views of the structure are shown in Fig. 2.38 and 2.39. The structure was completely destroyed. Debris was dispersed over a large area, the maximum debris distance being about 1,500 ft from the point of burst. Figure 2.40 is a post-shot view of the close-in region. The area was canvassed and all fragments found were listed by terminal location. About 31,000 concrete fragments with a total weight of about 85,000 lb were

SECRET

SECRET

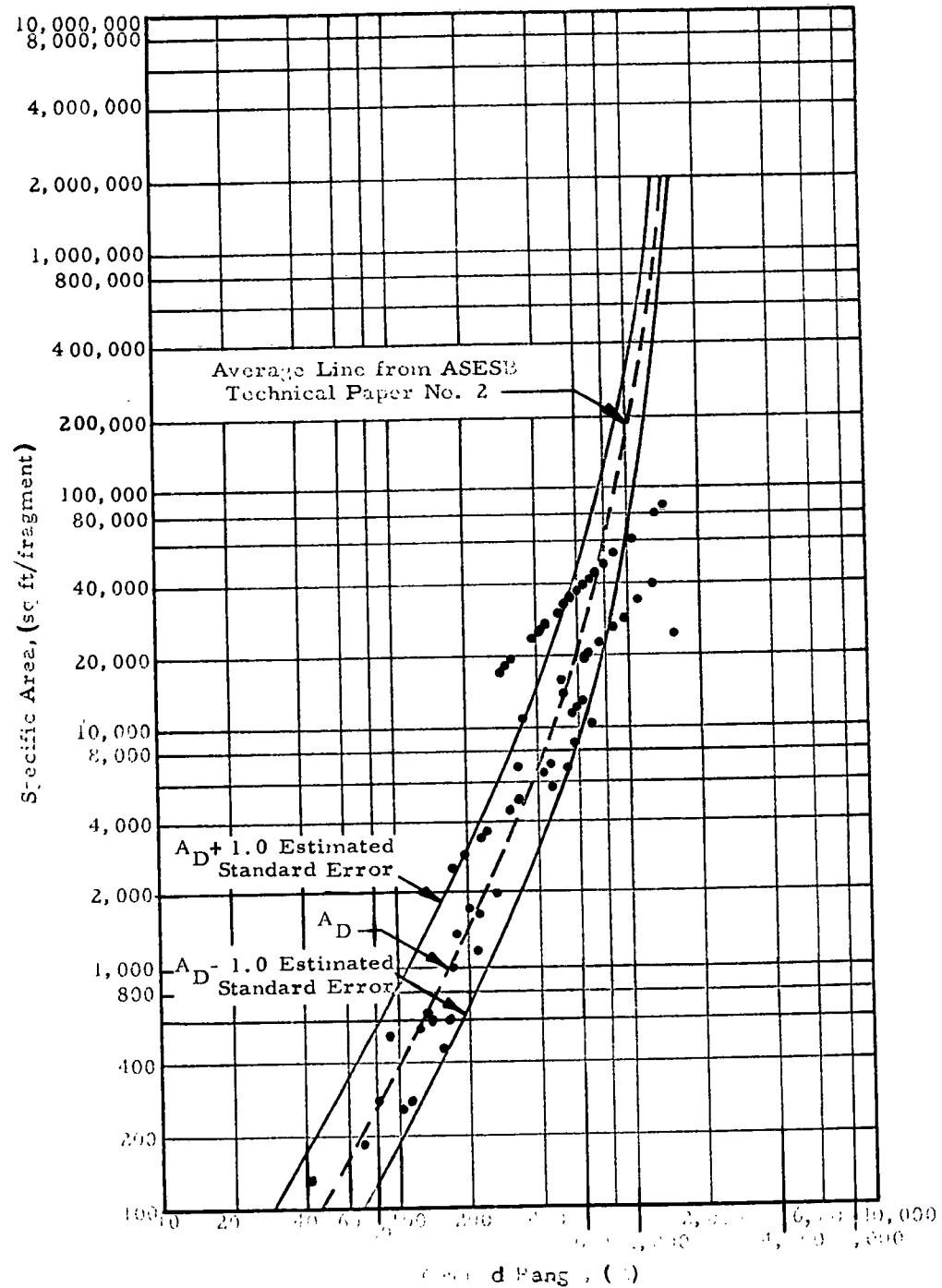


Figure 2.37 Debris Dispersion and Standard Error
for 1945 Badger Ordnance Works Explosion

SECRET

SECRET

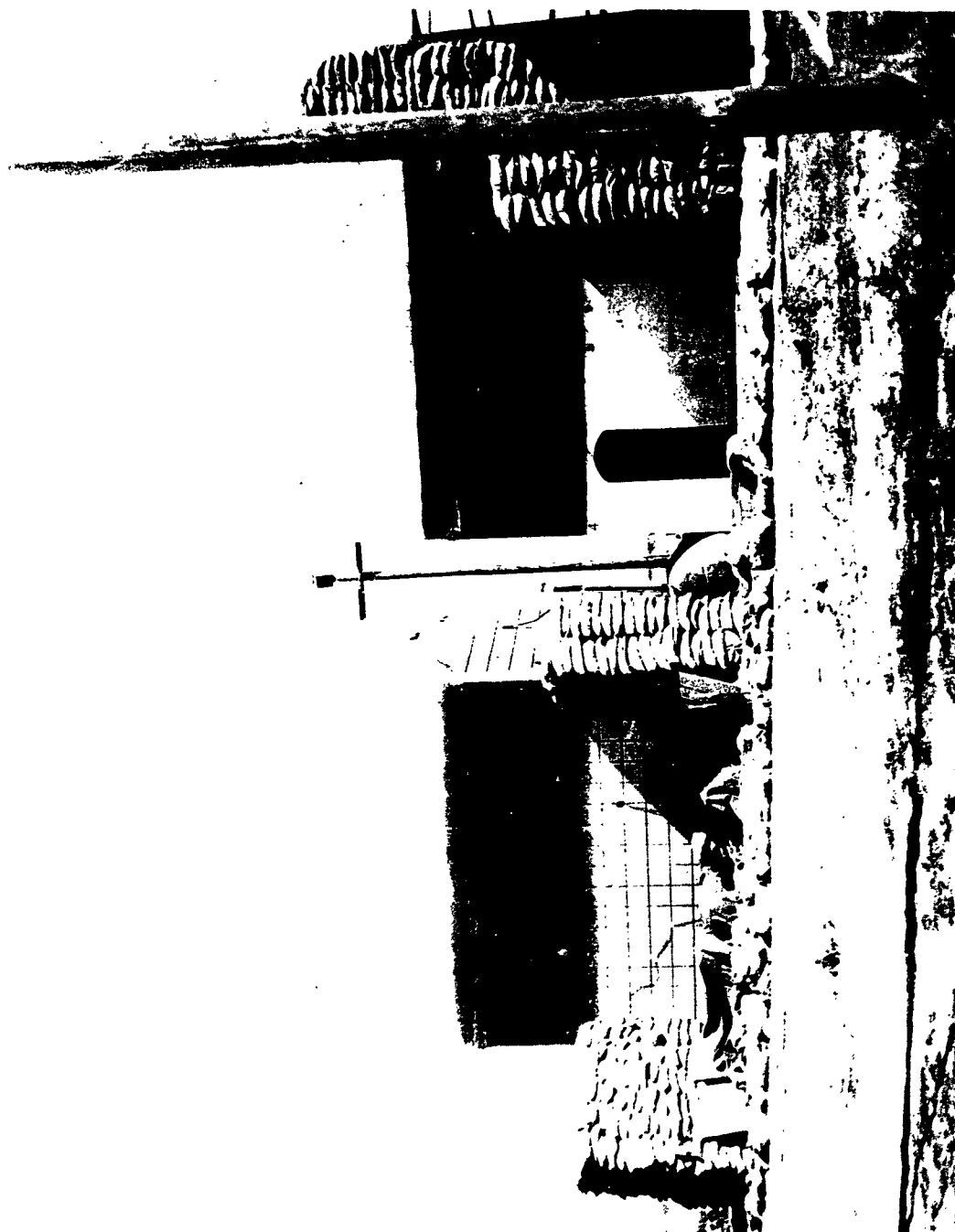


Figure 2.38
Pre-Shot View of Pantex Ordnance Plant Test Structure From Southeast

SECRET

SECRET



Figure 2.39
Pre-Shot View of Pantex Ordnance Plant Test Structure From Northwest

SECRET

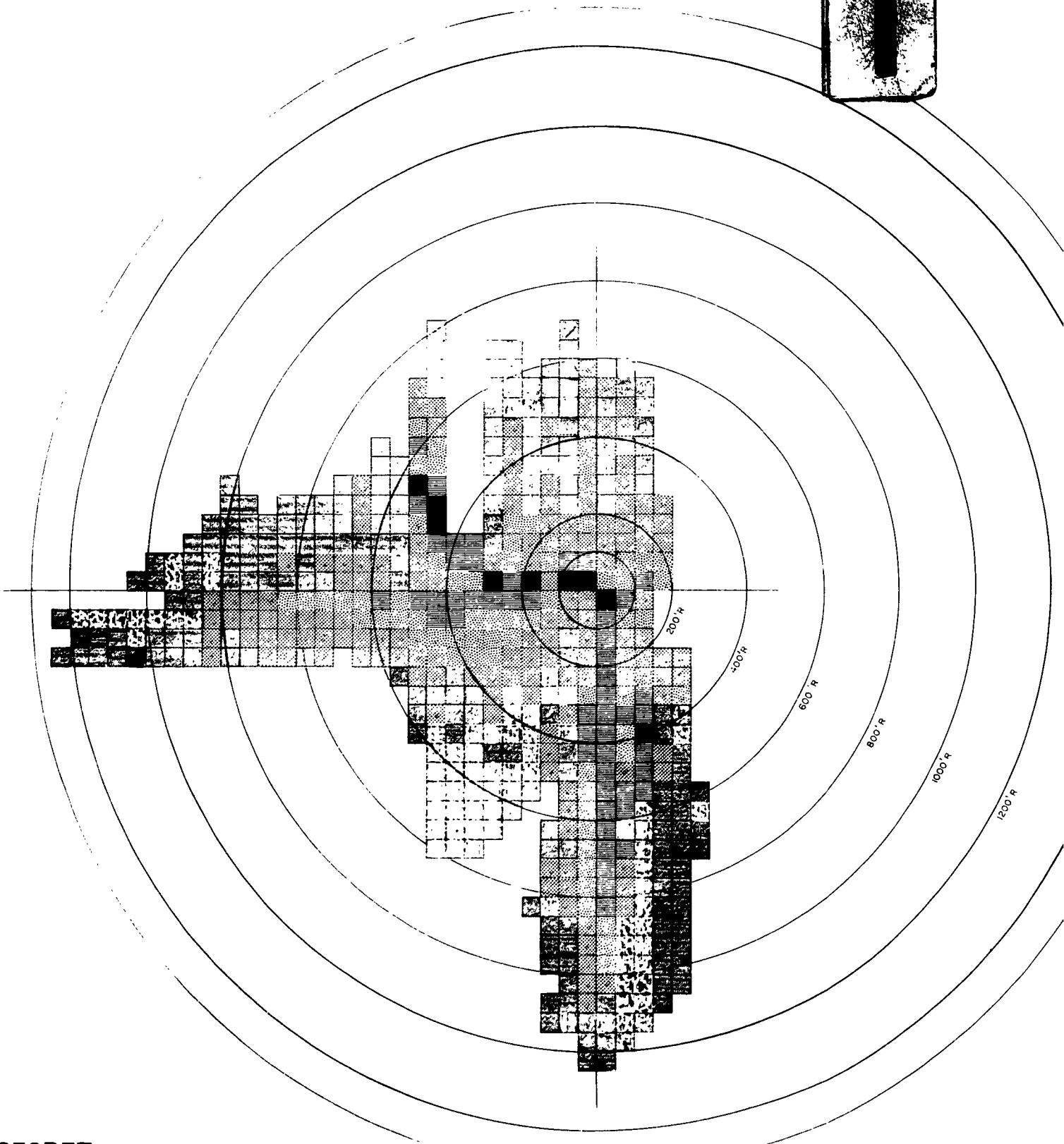
SECRET



Figure 2.40
Post-Shot View of Pantex Ordnance Plant Test Structure

SECRET

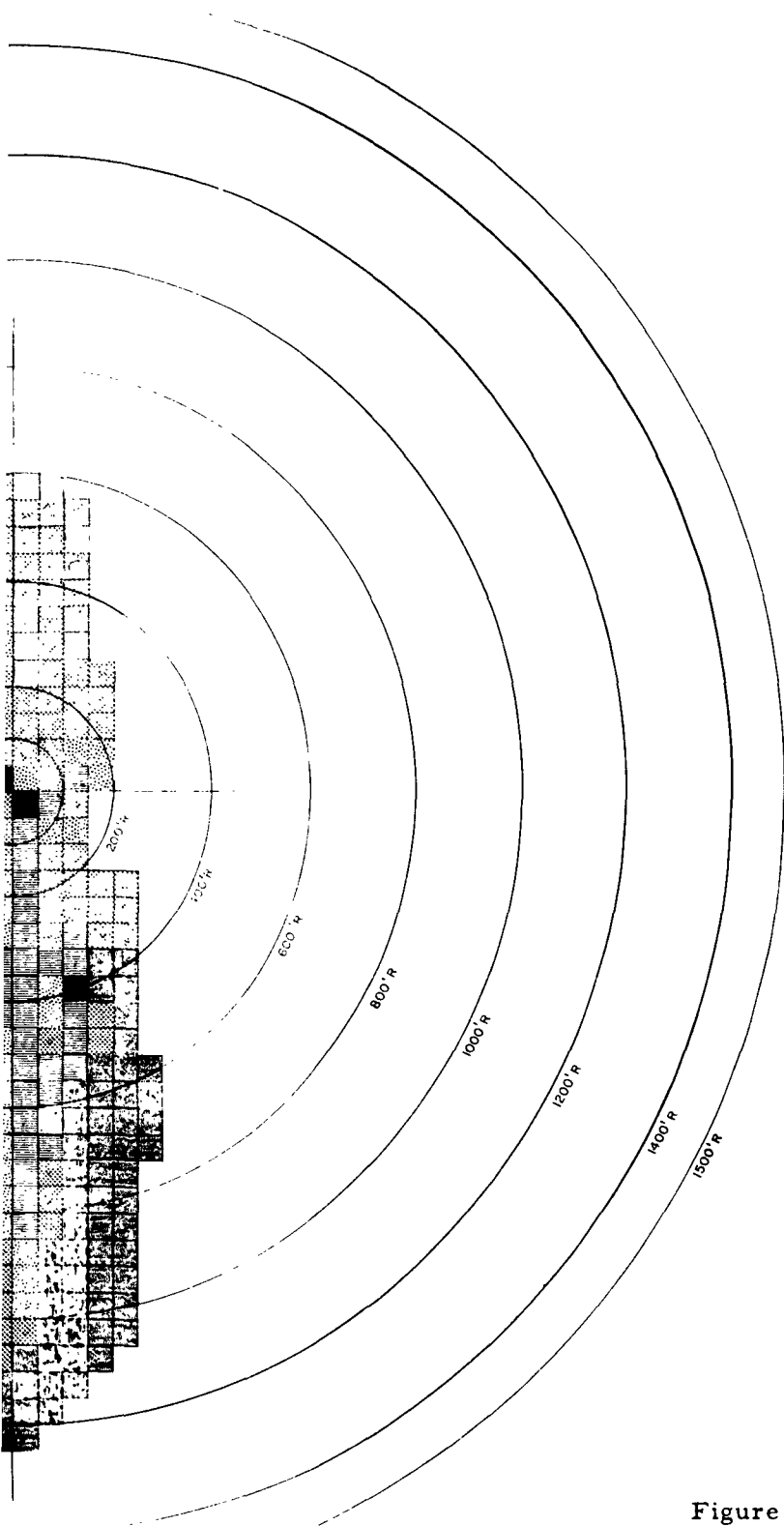
1



SECRET

2

SECRET



- Under 4.00 sq ft/fragment
- ▨ 4.01 to 20.00 sq ft/fragment
- ▤ 20.01 to 100.0 sq ft/fragment
- ▥ 100.1 to 500.0 sq ft/fragment
- ▧ 500.1 to 2500.0 sq ft/fragment
- ✱ Over 2500.0 sq ft/fragment

Figure 2.41 Area of Fragment Distribution
from Pantex Ordnance Plant Test Structure

SECRET

recorded along with their individual weights and terminal locations. Terminal locations were noted according to the serialized 50-ft square zones shown in the missile map, Fig. 2.41. As the missile map indicates, debris dispersion was non-uniform with the greatest concentration being to the south -- the direction of the front wall from the point of burst. Debris data were not analyzed in the original explosion report.

Since the fragment list reported for the Pantex Ordnance Plant event constituted the most extensive compilation of data found on dispersion of fragments, these results were studied extensively to obtain data on fragment-size distributions and fragment dispersion.

Over-all dispersion of fragments from the Pantex event is tabulated in Appendix D and plotted in Fig. 2.42 through 2.47. Two measures of dispersion are included here, specific area in sq ft per fragment, and areal dispersion in sq ft per lb of debris. The following plots have been prepared as alternate means of describing the dispersion function:

- Fig. 2.42 Log-Log Plot of Specific Area Vs Ground Range, with Second-Order Least-Squares Regression Line
- Fig. 2.43 Semi-Log Plot of Specific Area Vs Ground Range, with First-Order Least-Squares Regression Line
- Fig. 2.44 Semi-Log Plot of Specific Area Vs Ground Range, with Second-Order Least-Squares Regression Line
- Fig. 2.45 Log-Log Plot of Areal Dispersion Vs Ground Range, with Second-Order Least-Squares Regression Line
- Fig. 2.46 Semi-Log Plot of Areal Dispersion Vs Ground Range, with First-Order Least-Squares Regression Line
- Fig. 2.47 Semi-Log Plot of Areal Dispersion Vs Ground Range, with Second-Order Least-Squares Regression Line

In each case the dispersion measures, (Specific Area or Areal Dispersion), have been computed for 50-ft and 100-ft wide concentric circular bands about the point of detonation. Computed points were plotted at the midpoints of the circular bands. Since the original debris data from this event were collected for 50-ft squares from coordinates near the point of burst, the approximation of the actual dispersion function is based on considering the debris within any 50-ft square to be within the circular band containing its center. Regression lines are computed on the basis of all

SECRET

SECRET

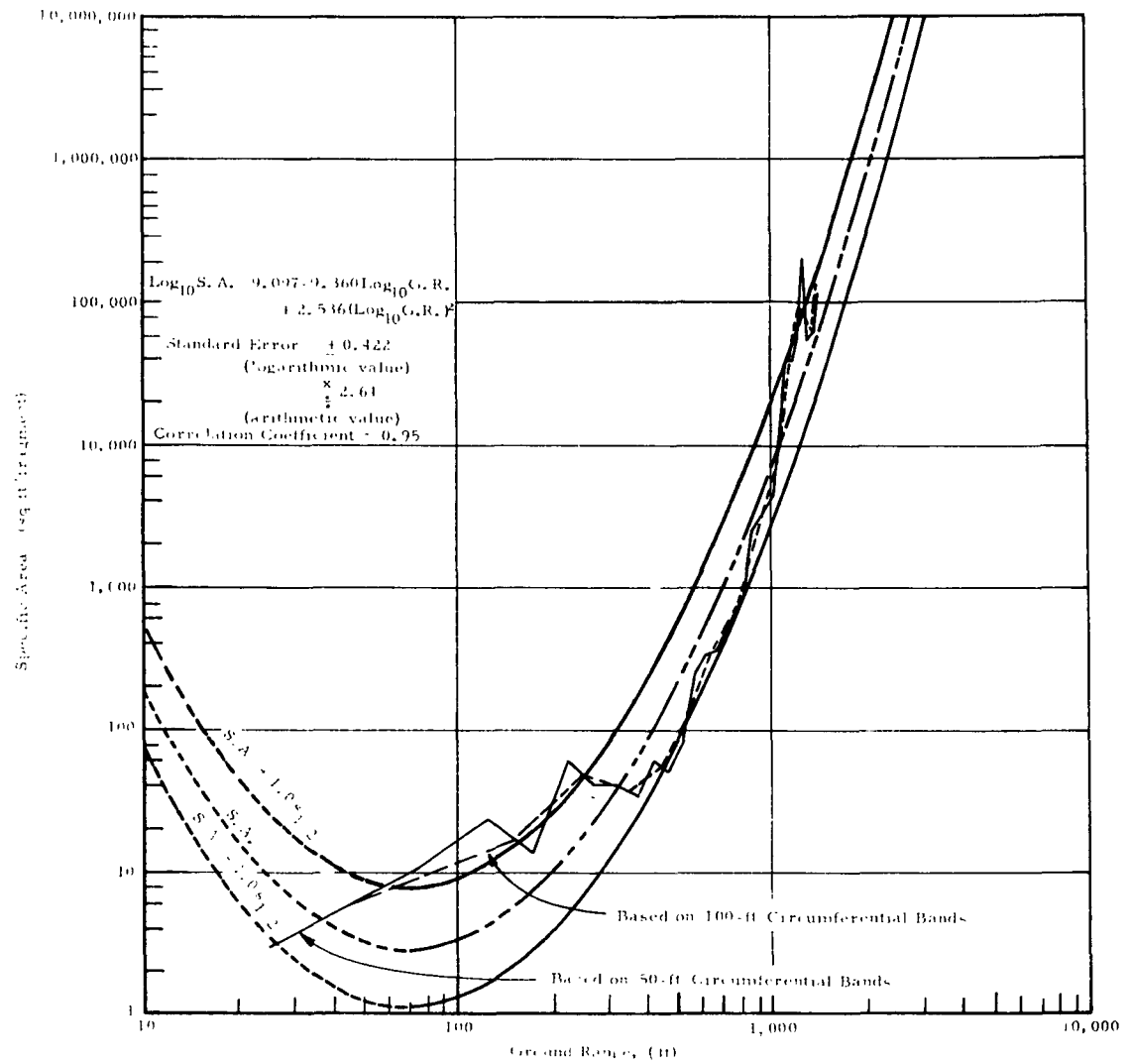


Figure 2.42 Debris Dispersion for Reinforced Concrete Structure
Logarithmic Plot with Second-Order Regression Line

SECRET

SECRET

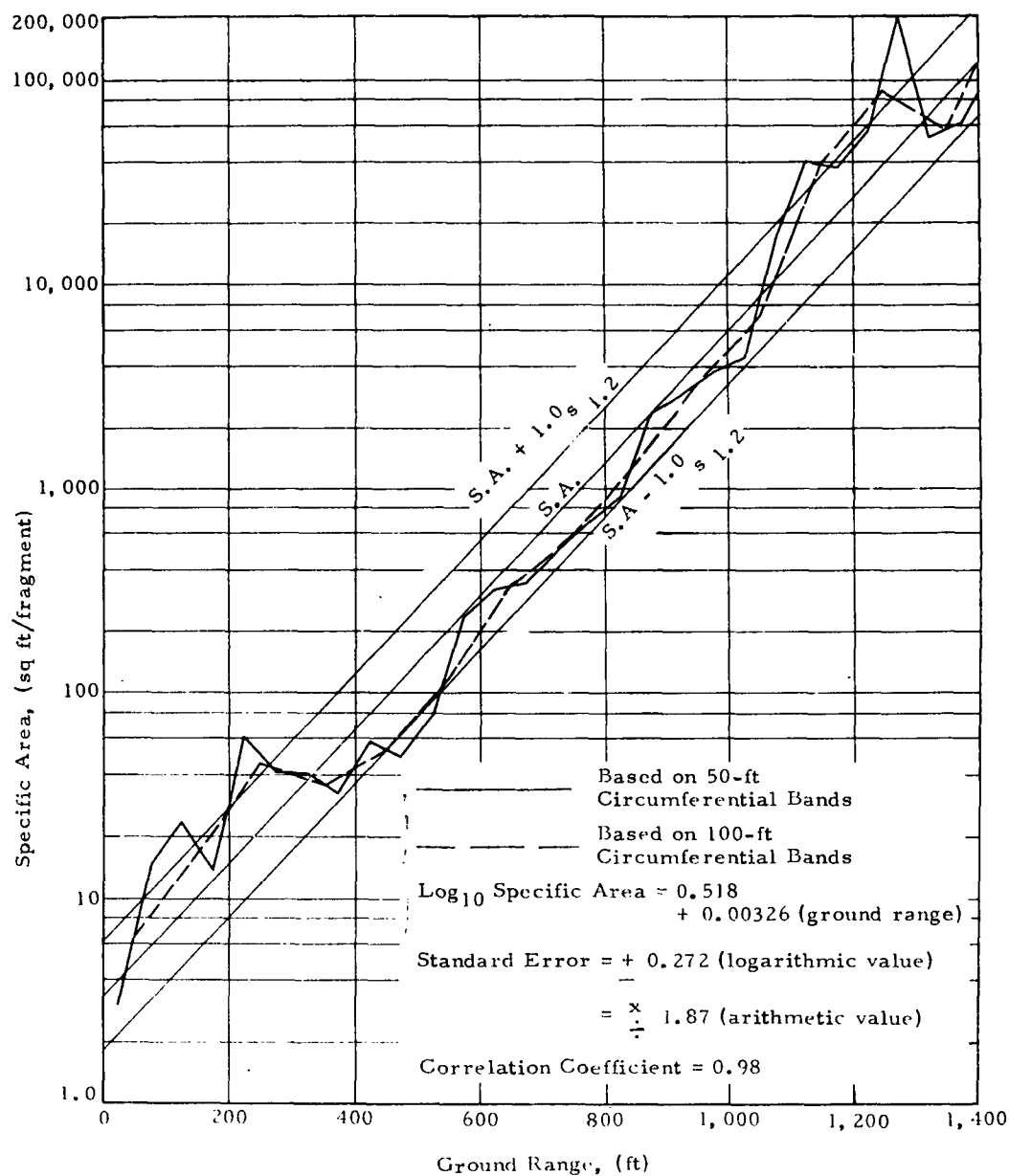


Figure 2.43 Debris Dispersion for Reinforced Concrete Structure
Semilog Plot with First Order Regression Line

SECRET

SECRET

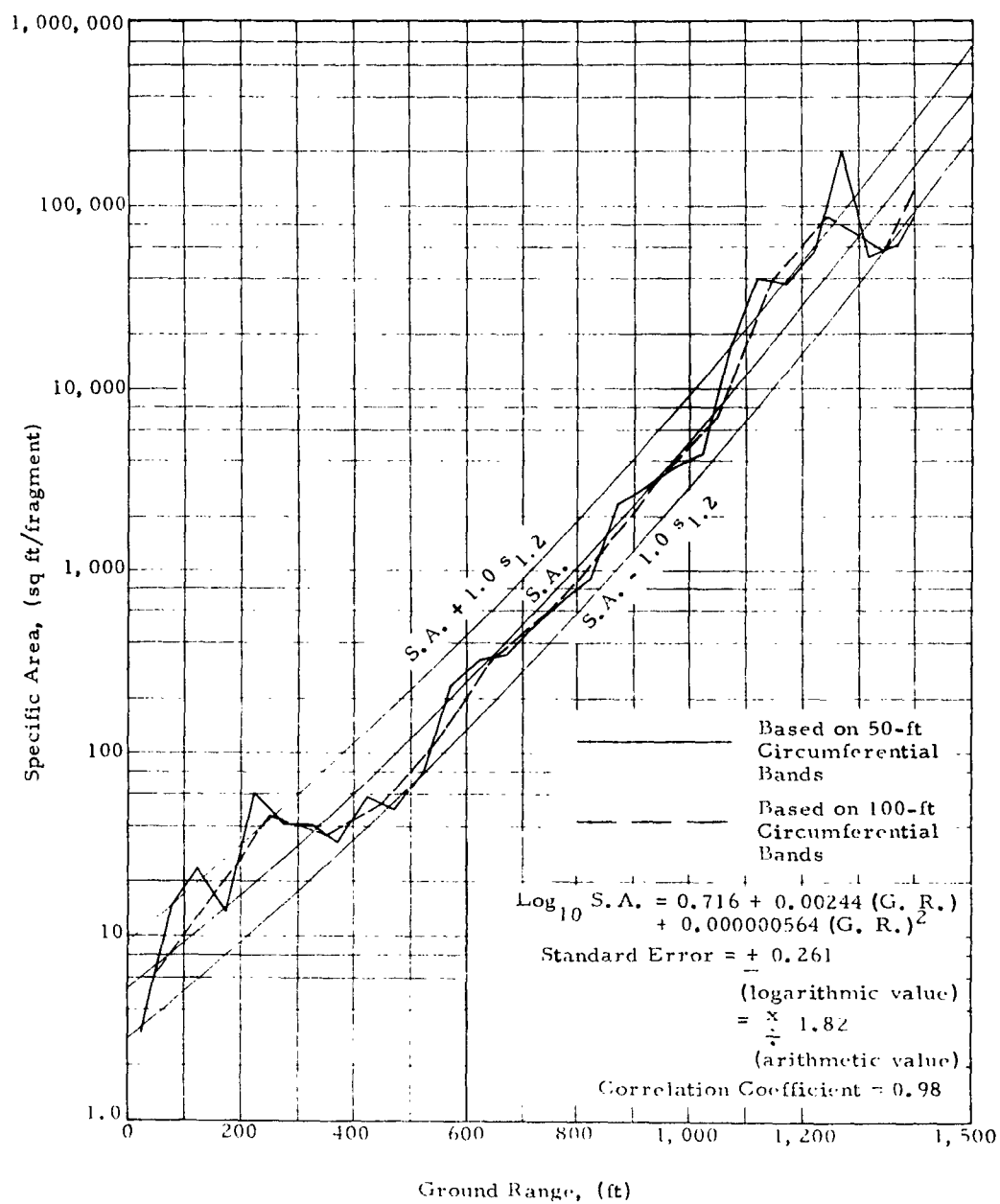


Figure 2.44 Debris Dispersion for Reinforced Concrete Structure
Semilog Plot with Second-Order Regression Line

SECRET

SECRET

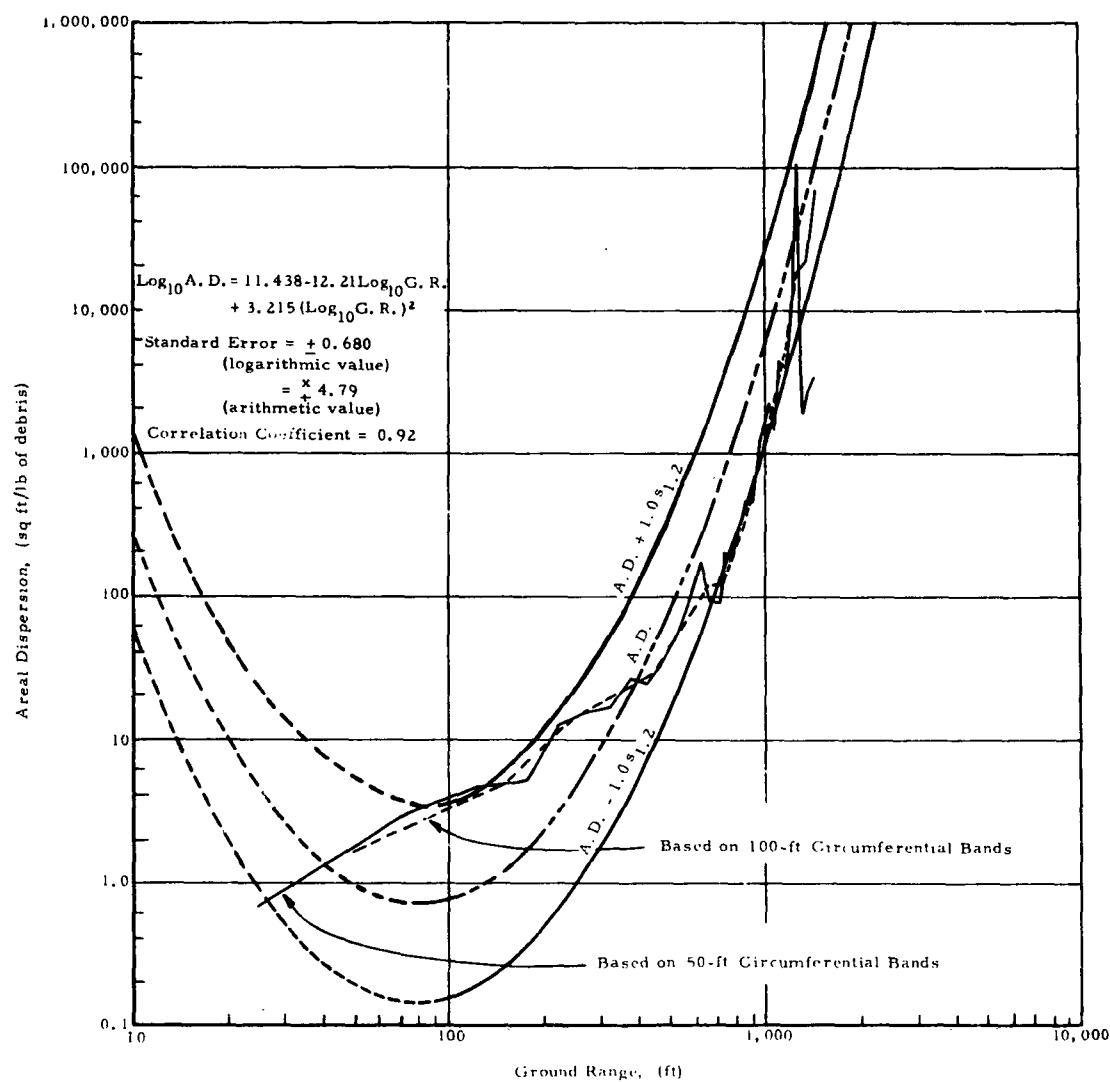


Figure 2.45 Areal Dispersion for Reinforced Concrete Structure
Logarithmic Plot with Second-Order Regression Line

SECRET

SECRET

points for the 50-ft circumferential bands as listed in Table D-2.

Variation in average fragment weight with ground range is plotted in Fig. 2.48. Again, these values were computed for concentric circular bands of 50-ft and 100-ft widths. Though the largest fragment recorded weighed about 4,000 lb, it is seen from this chart that the average weight of fragments at virtually all ground ranges was less than 12 lb. The bimodal nature of this curve is unexplained, and since this computation includes concrete fragments only, it does not stem from a two-phase nature of material. Relative distances from explosive sources to the various structural panels and the shielding effects of adjacent bays to the east of the bay containing the charge may have influenced this.

Fragment-size distribution for the 50-ft and 100-ft debris zones is plotted in Fig. 2.49 and 2.50. Figure 2.49 shows the total number of fragments above any indicated weight which were found at various ground ranges. This figure shows that relatively few fragments above three pounds were found at any ground range. An improved indication of variation in fragment-size distribution is obtained by plotting the cumulative percentage of fragments above indicated weights, as shown in Fig. 2.50. There is little separation between the cumulative-percentage curves over much of the range of fragment sizes in this figure. The pronounced "flattening-out" of these curves at the 3-lb fragment weight suggests that an optimum design point for debris hazards may exist, providing of course that these curves are truly characteristic. At all ground ranges, less than 6 percent of total fragments was above three pounds in size. It is interesting to note that at the greatest ground ranges (1200-1500 ft) no fragments above one pound were found; but at the intermediate ground ranges (600-1200 ft) the percentage of fragments over three pounds in size was greater than at the shorter ground ranges (0-600 ft). The largest sized fragments (over 100 lb) were found only at the shorter ground ranges. The tendency of making incomplete counts of the smallest fragments in the close-in region would actually result in the cumulative percentage curves of Fig. 2.50 being overstated for the greater fragment sizes.

SECRET

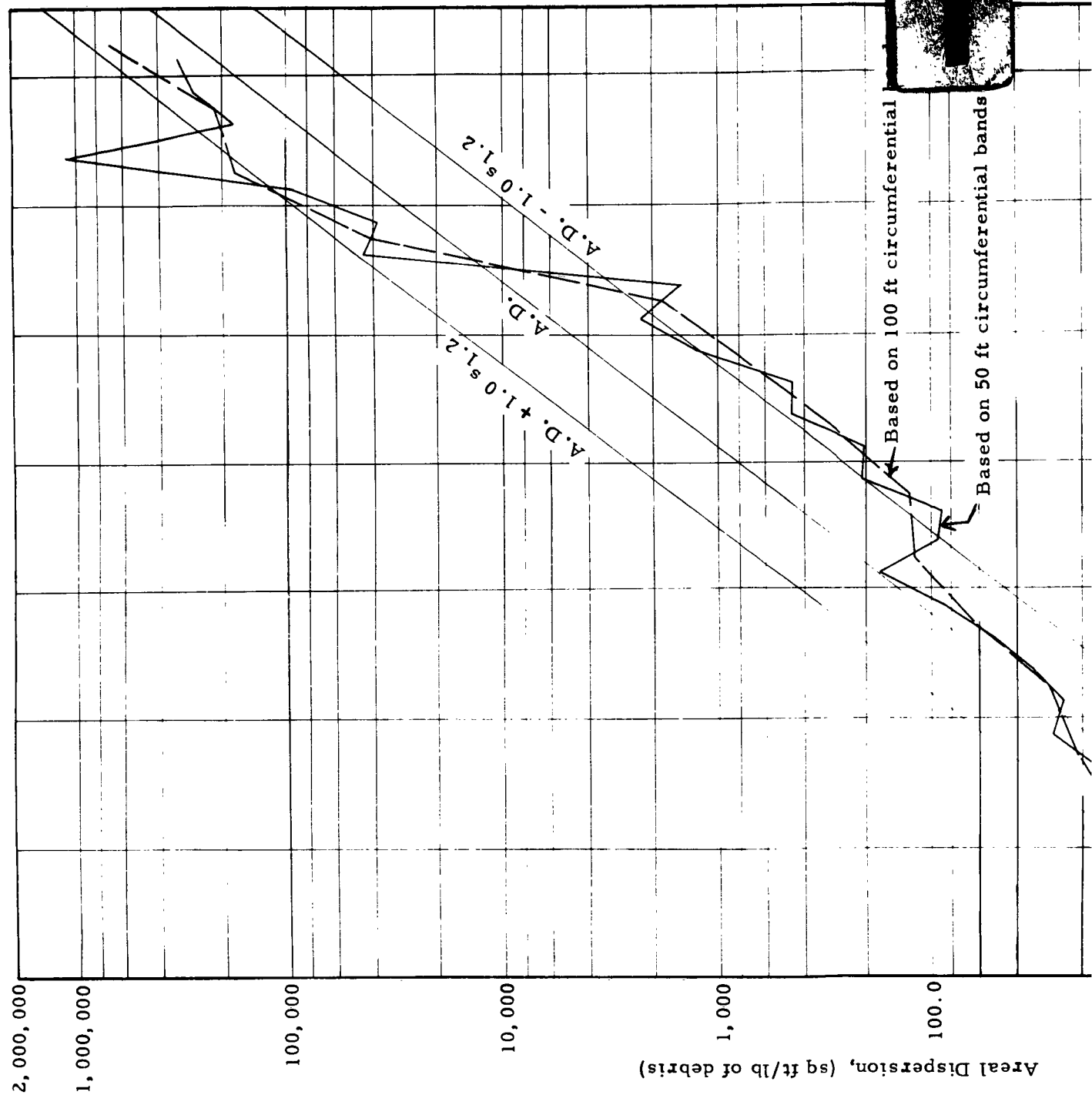
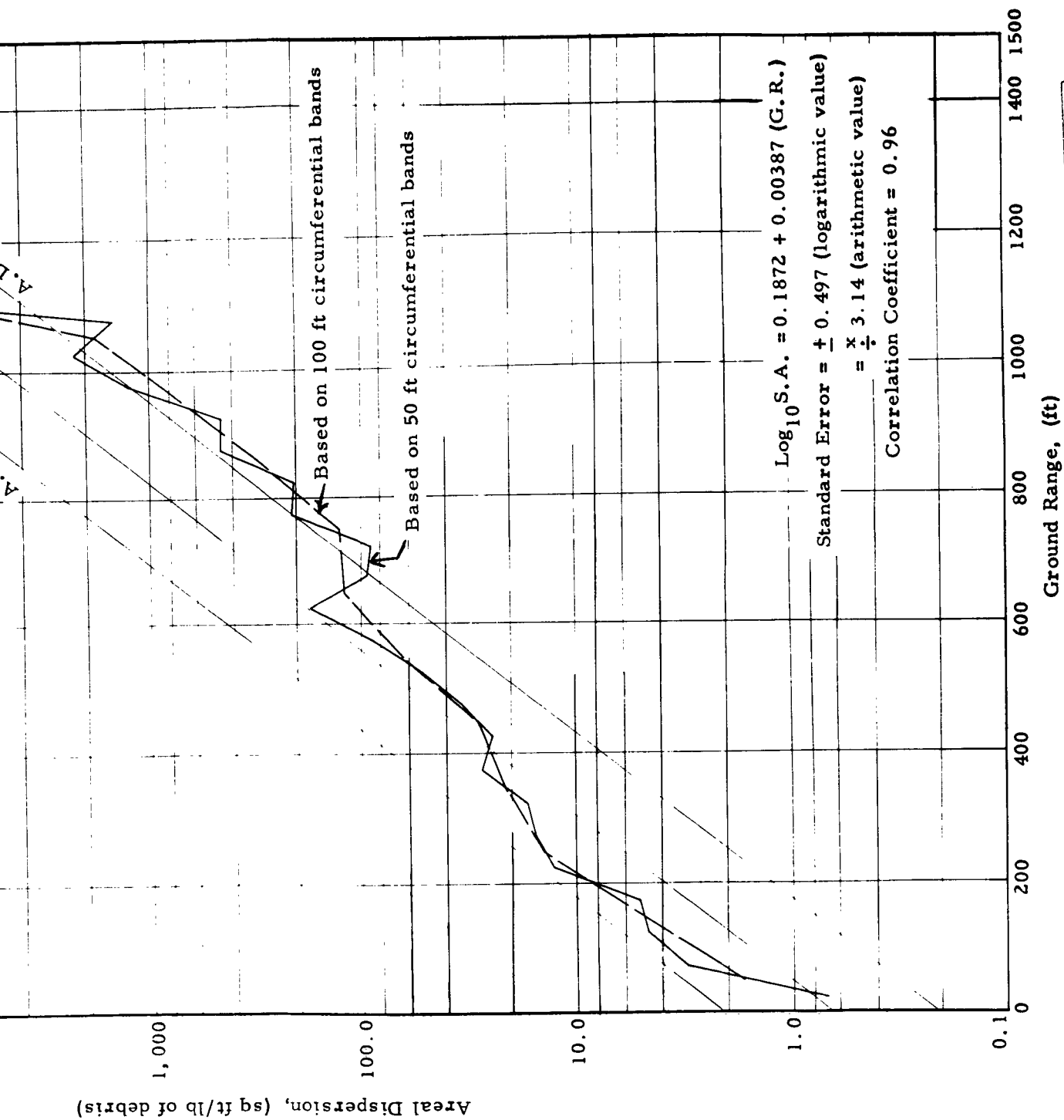


Figure 2.46 Areal Dispersion for Reinforced Concrete Structure
Semilog Plot with First-Order Regression Line

SECRET

Structure
Line


$$\text{Log}_{10} \text{S.A.} = 0.1872 + 0.00387 (\text{G.R.})$$

Standard Error = ± 0.497 (logarithmic value)

$$= \frac{x}{3.14} \text{ (arithmetic value)}$$

Correlation Coefficient = 0.96

SECRET

2

1

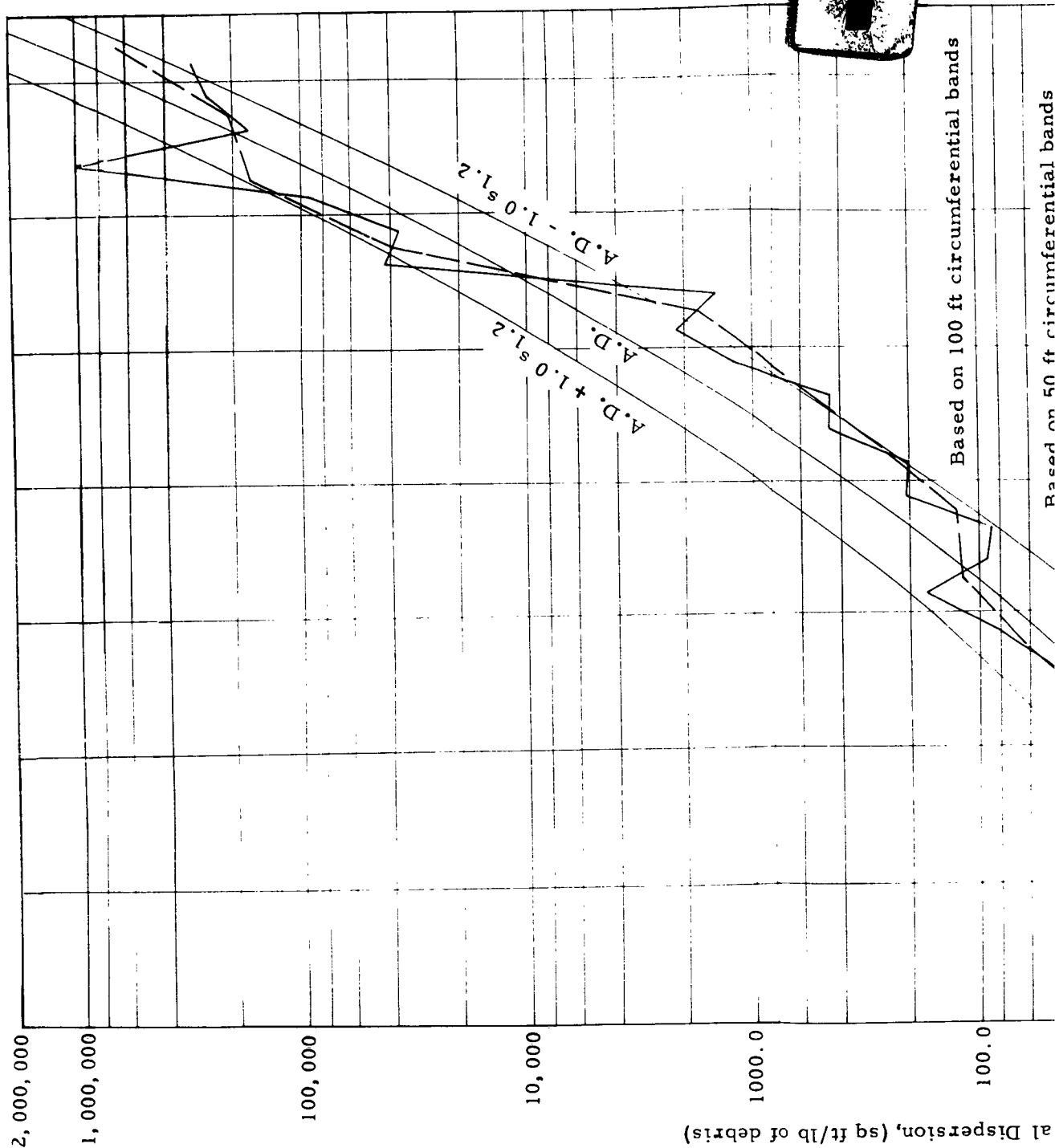
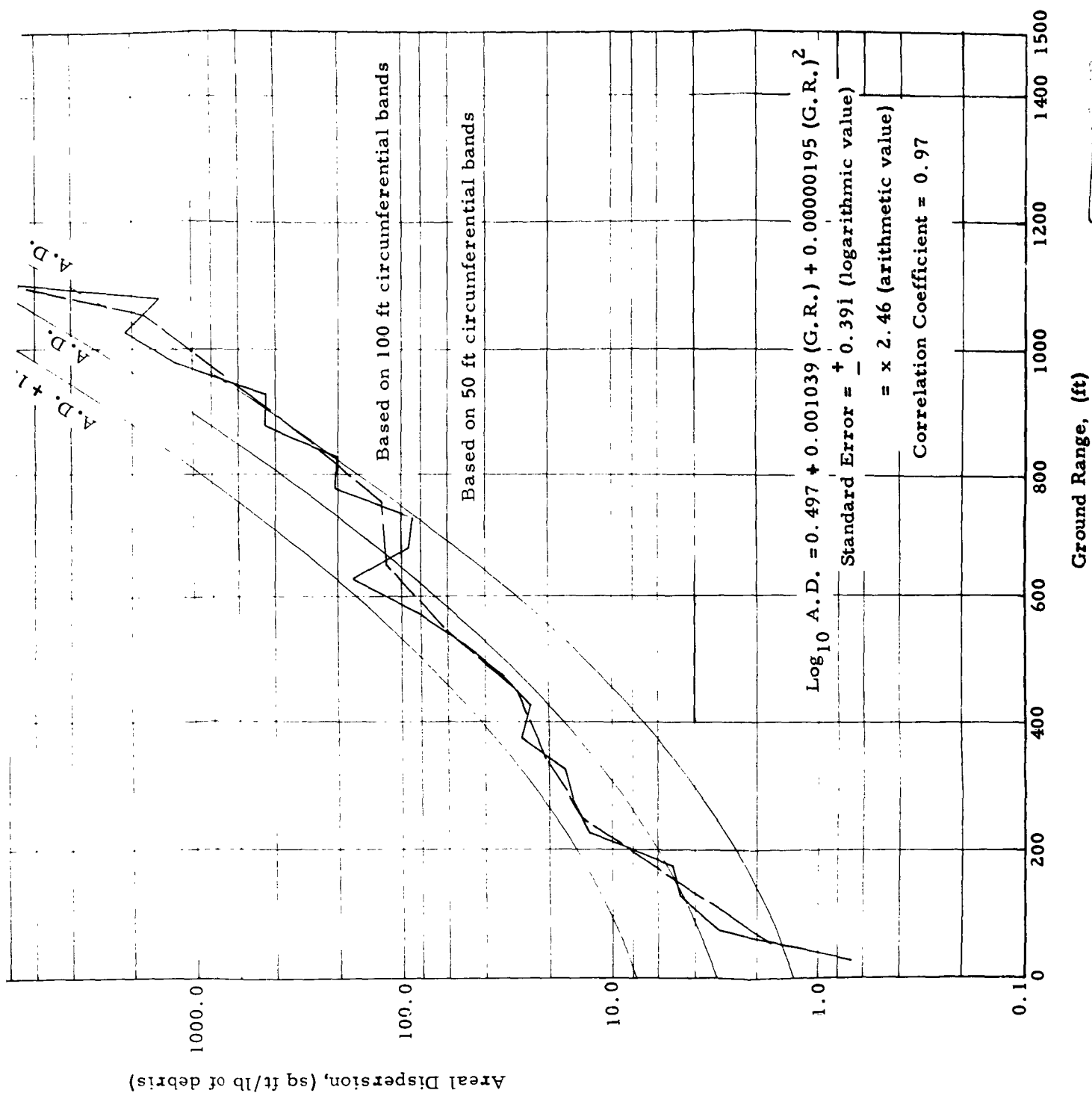


Figure 2.47 Areal Dispersion for Reinforced Concrete Structure
Semilog Plot with Second-Order Regression Line

SECRET

SECRET

2



SECRET

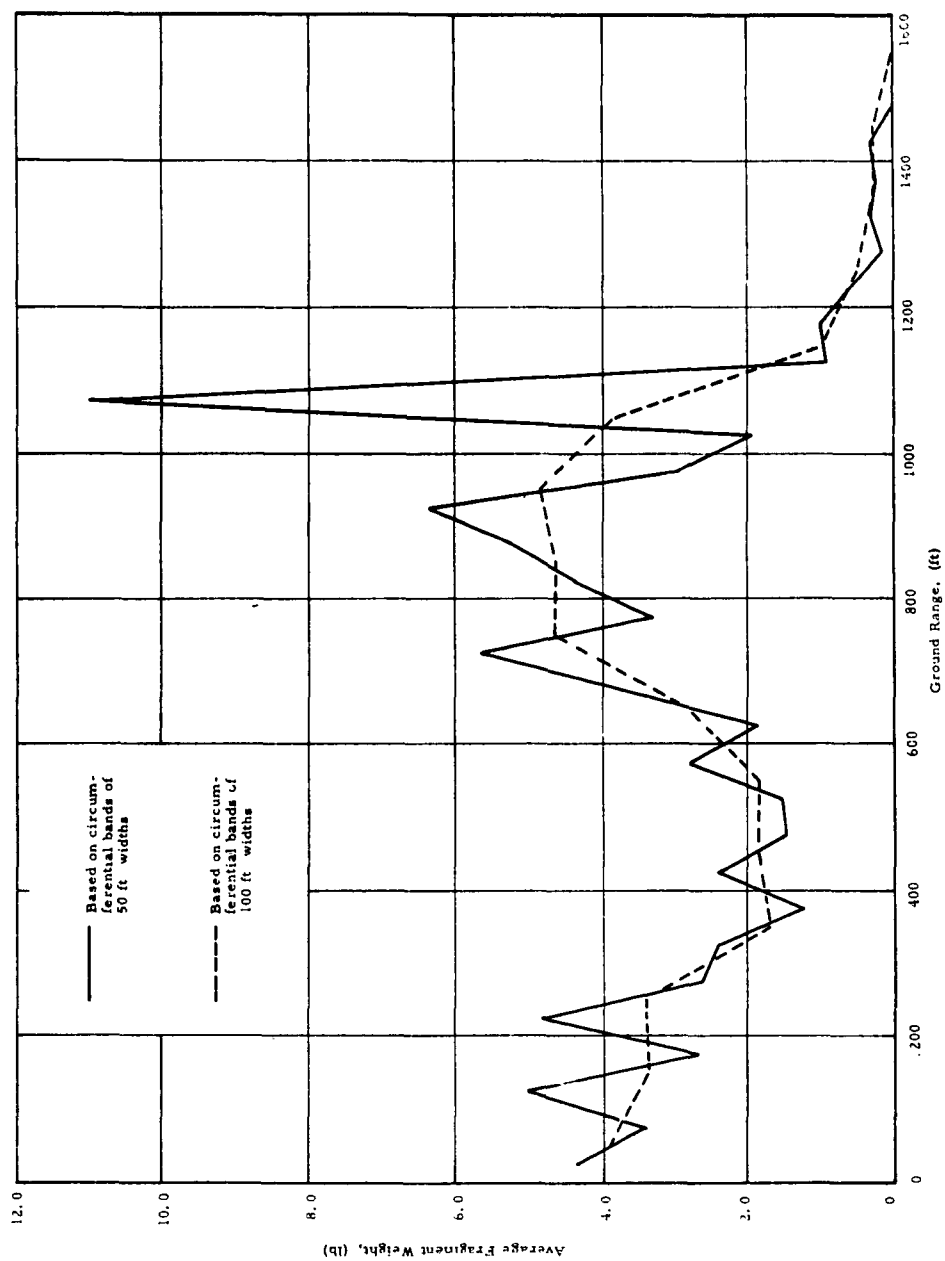


Figure 2.48 Average Fragment Weight versus Ground Range for a Reinforced Concrete Structure

SECRET

SECRET

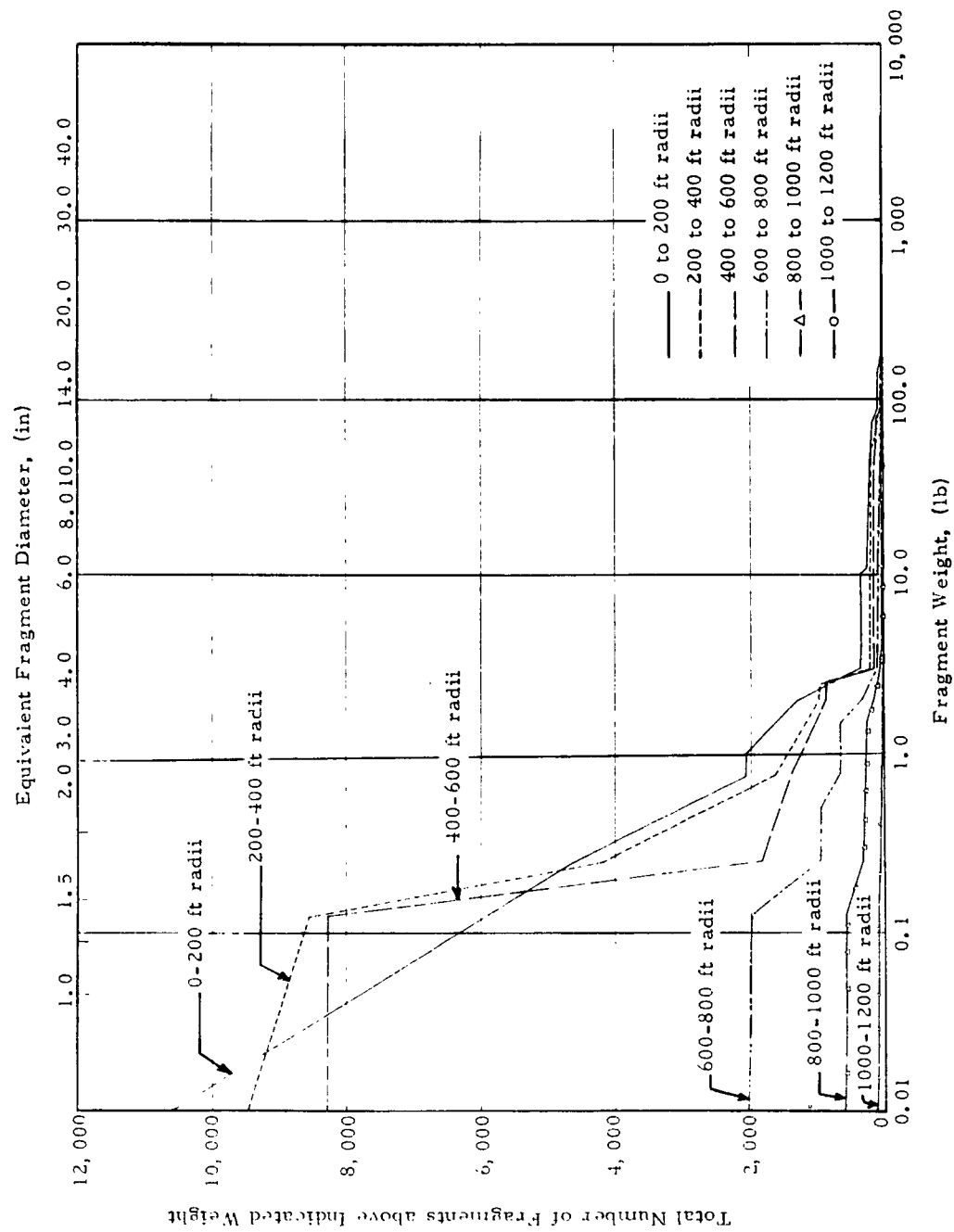
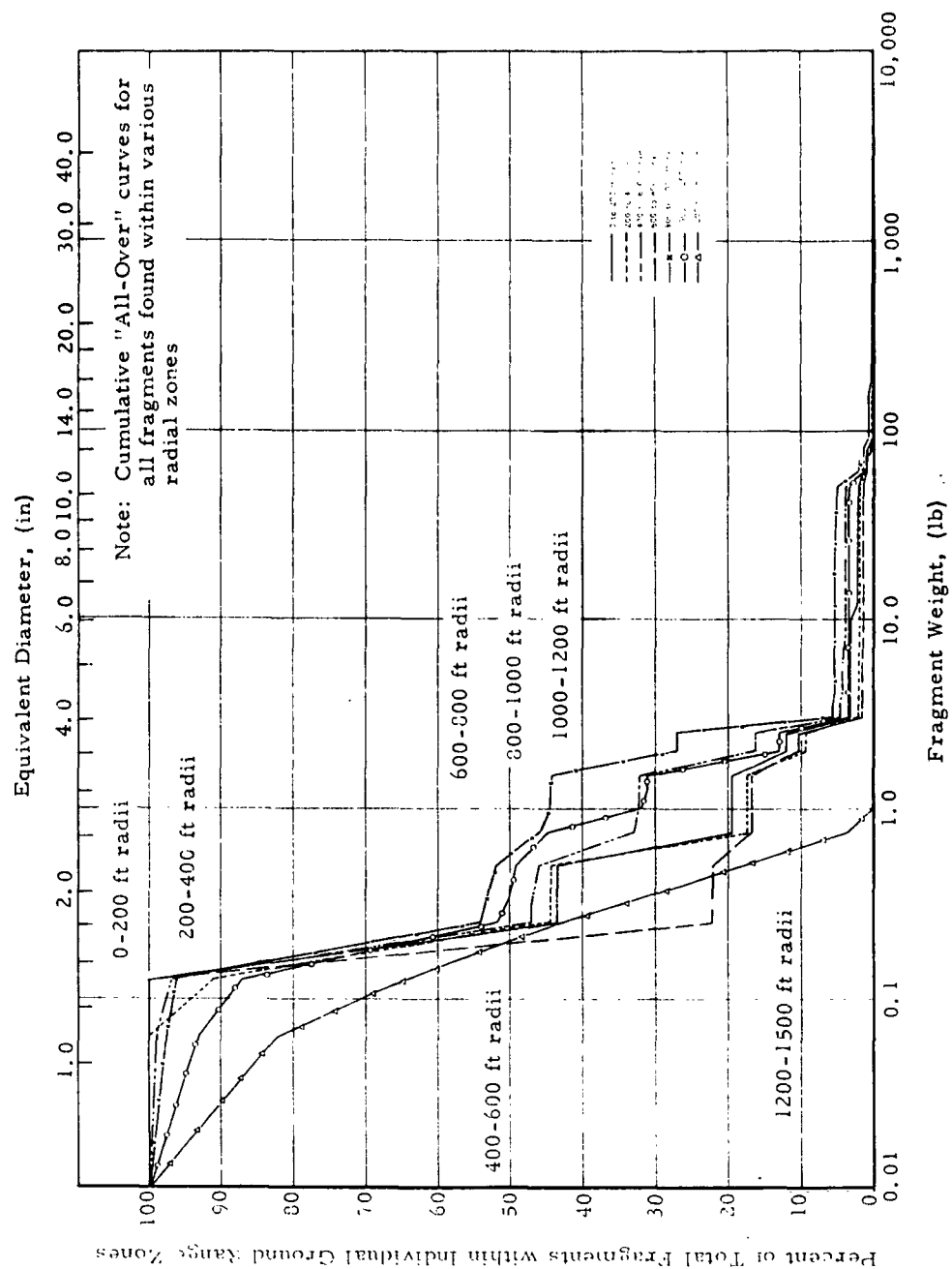


Figure 2.49 Fragment Quantities at Various Ground Ranges for a Reinforced Concrete Structure

SECRET

SECRET



SECRET

Figure 2.50 Fragment-Size Distribution at Various Ground Ranges for a Reinforced Concrete Structure

SECRET

Fragment dispersion for various weight classes is plotted in Fig. 2. 51 and 2. 52. Actual counts of fragments are presented in Fig. 2. 51. It is seen here that the heaviest fragments did not travel to the extreme ranges. Fragments of 1,000 lb and heavier were found only within 200 ft, those of 100 lb or more were found only within 600 ft, and those of 10 lb or more were not found beyond 1200 ft. This is contrary to what would normally be expected on consideration of air drag as shown in Chapter Five. The comparison is not altogether appropriate, however, since in this actual structure, the fragments which are subject to forces of sufficient magnitude to cause large motion are also likely to be broken up to a greater extent. Proportionate distribution of fragments of various size classes, among the various ground ranges, is shown in Fig. 2. 52. Other than for the extremely heavy fragments (over 100 lb) the proportionate distribution did not change much for the different fragment weights.

SECRET

SECRET

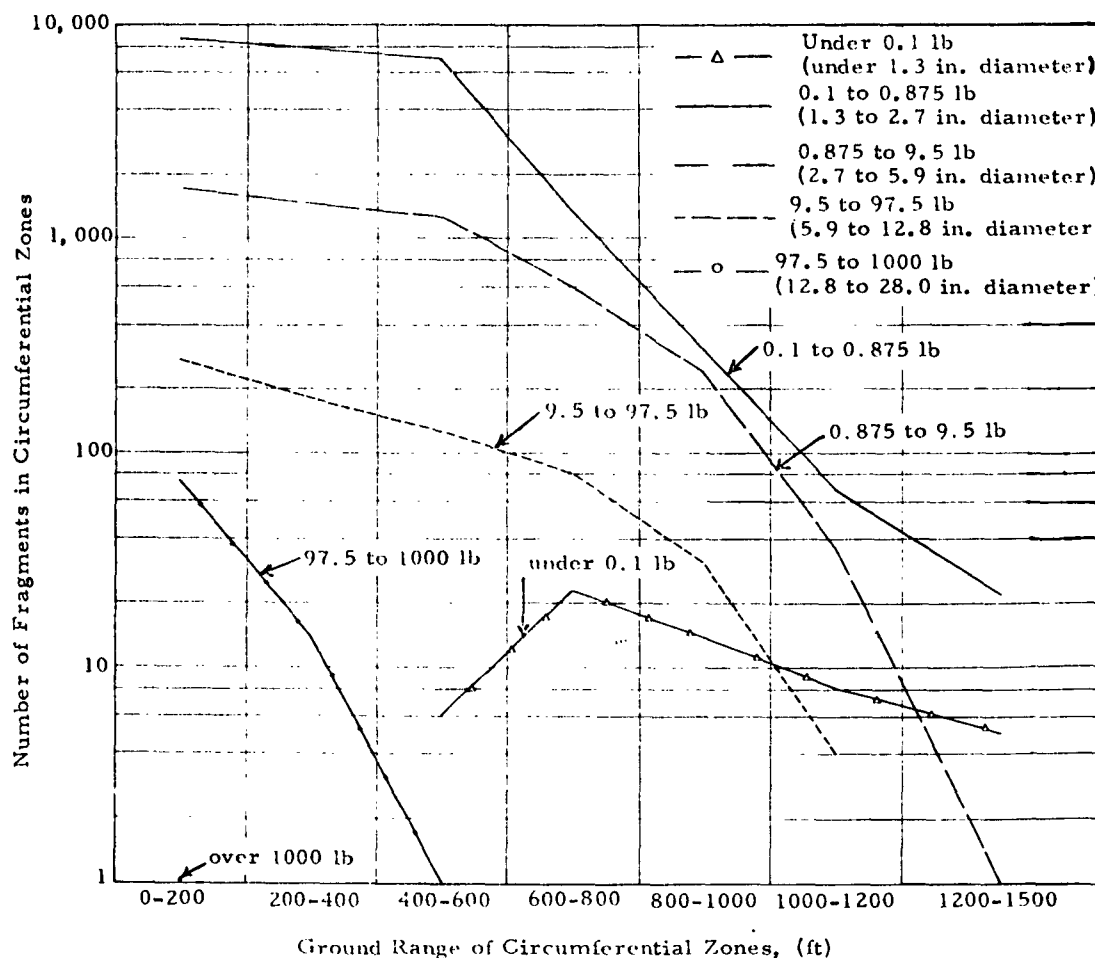


Figure 2.51 Fragment Distances for Various Weight Classes
for a Reinforced Concrete Structure

SECRET

SECRET

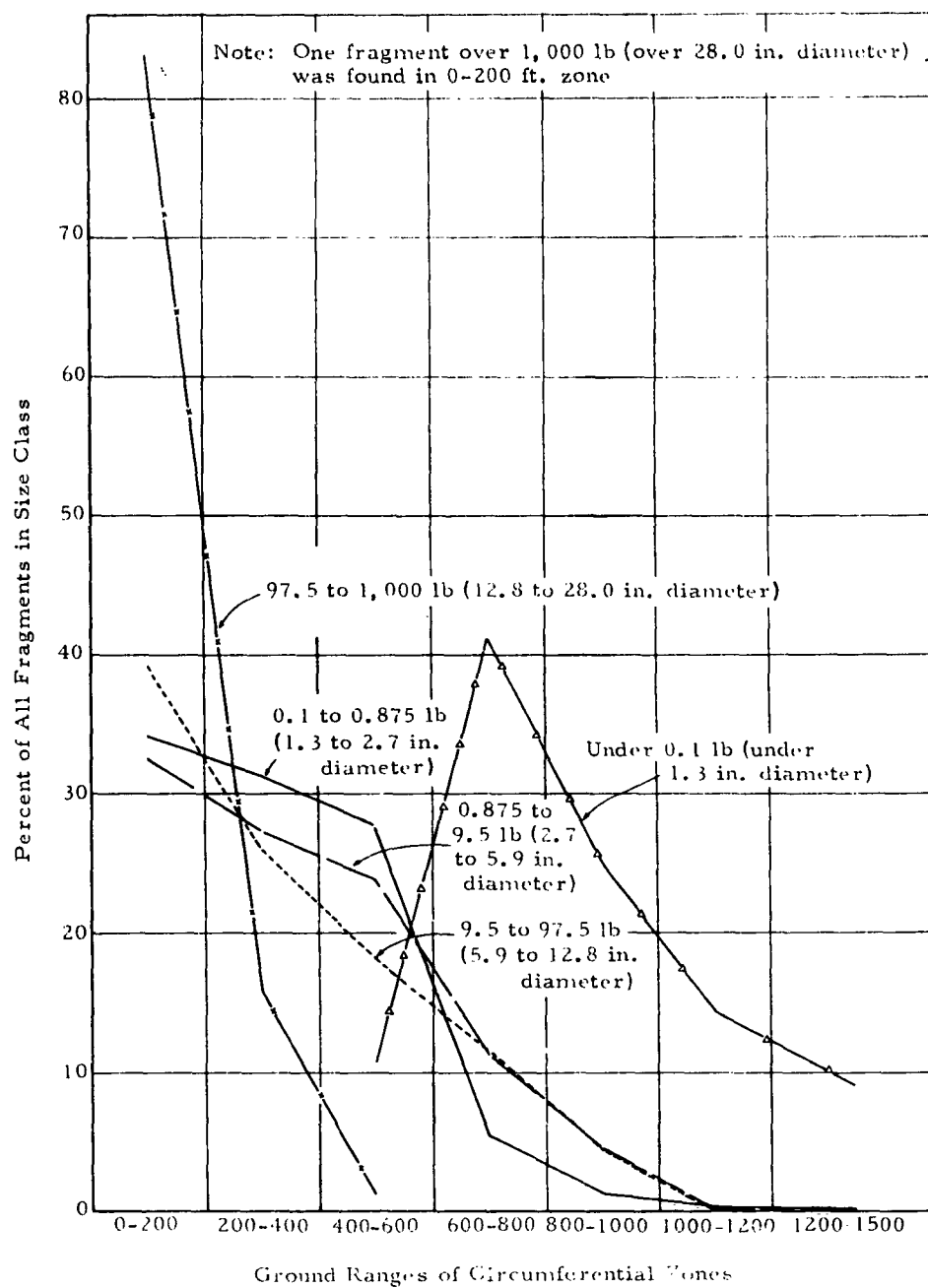


Figure 2.52 Fragment-Distance Distribution for Various Weight Classes for a Reinforced Concrete Structure

SECRET

SECRET

CHAPTER THREE
FRAGMENTATION, EXPERIMENTAL OBSERVATIONS

To predict the hazards of debris from nuclear explosions, in addition to defining the maximum range of debris and the distribution of debris within this limit, it is well to define the nature (i. e. , size or weight) of the expected missiles. Fragment weight combined with fragment velocity determines energy level of the fragment, and thus the loading upon equipment of personnel struck by the fragment. No definitive experimental investigation of structural fragmentation, relating fragment-size distribution to structural strength and loading parameters has yet been made. Recourse was made to collecting and summarizing past experimental investigations in fragmentation and to describing such general behavior and characteristic patterns as have been developed. Five such investigations are described in this chapter; research of the British Coal Utilization Research Association on coal breakage from random forces, research of the Safety in Mines Research Establishment of Great Britain on explosively detonated stone blocks, Stanford Research Institute model tests of containment structures fractured by internal explosions, an extensive study of fragments from a planned explosion of an ordnance structure at Pantex Ordnance Plant and findings of Project 4. 5 of Operation JANGLE.

The fragmentation of materials produced by mine charges or ore crushers has been the subject of considerable study. Many attempts have been made to analyze the fractions produced by these processes. It has been shown experimentally that the higher the loading on the source material, the smaller the fragments produced, and that a wide range of fragment sizes are produced at any loading. An "Ideal Law of Breakage" which shows excellent fit to experimental data has been developed from coal-crushing investigations.

The extensive collection of data on the sizes of more than 30,000 concrete fragments from the Pantex Ordnance Plant event afforded the opportunity for a detailed analysis of fragment-size distribution. An interesting result of this particular study is that only about 3 percent of

SECRET

SECRET

all the fragments produced weighed more than three pounds and that these fragments accounted for nearly 75 percent of total weight of all fragments recovered. Thus, as structures or equipment are built with increased resistance to fragments, the probability of being hit by a fragment sufficient to cause damage declines substantially.

The only structural fragmentation study conducted on full-scale nuclear tests was limited work performed on reinforced-concrete wall panels erected over the crater zone in Project 4.5 of Operation JANGLE (Ref. 5). Size distributions of the larger fractions were plotted as part of this project and it was noted that the JANGLE data did not preclude the possibility that the fragment-size distribution of concrete source material caused by the underground nuclear shot followed the same pattern as coal in a mine or ore in a crusher.

3.1 Fragmentation of Coal

A number of experimental investigations of coal fragmentation characteristics have been made. The mining industry, interested in minimizing dust formation and in producing fragments of an appropriate size for handling, has conducted numerous investigations of fragmentation from blasting and crushing operations. Assuming a brittle material with a random distribution of internal weaknesses, it has been deduced that when a single lump is fragmented by forces sufficiently violent to make breakage equally likely at any point, the broken product should have a fragment-size distribution obeying the exponential law (Ref. 13):

$$M(x) = 1 - e^{-x/\bar{x}}$$

where

$M(x)$ = percentage of material smaller in size than x
 x/\bar{x} = dimensionless measure of fragment size, such as
ratio of a characteristic length to a mean length.

This has been called the Ideal Law of Breakage. Experiments with large lumps of coal broken under conditions approximating random fracture tend to conform to the exponential law, at least for the smaller fragment sizes (under about 1/2-in. equivalent spherical diameter). Fitting data to the

SECRET

SECRET

equations

$$M(x) = c(1 - e^{-x/\bar{x}})$$

and

$$M(x) = 1 - e^{-x/\bar{x}},$$

researchers of the British Coal Utilization Board plotted experimental fragmentation data on broken coal of various types as shown in Fig. 3.1 (Ref. 13).

3.2 Fragmentation of Explosively Detonated Stone Blocks

In research conducted by personnel of the Safety in Mines Research Establishment, stemmed charges of 1-oz and 2-oz of coal-mining explosive were fired in stone blocks 18-in. in diameter by 30-in. long contained in a steel chamber (Ref. 14). Weights of the full-size-distribution fractions, including all dust, were measured.

Weights of the various fractions have been recomputed in terms of cumulative fragment quantities in Appendix E and are plotted in Fig. 3.2. The cumulative curves all follow the same general trend, which is nearly linear on logarithmic coordinates. Slopes of the lines vary with the quantity of charge, and seemingly with the diameter of the shothole, both of which would be determinants of the impulse impinging on the stone blocks. Average slopes of the cumulative size-distribution curves for 2-oz charges were all significantly greater than those for 1-oz charges and showed from only one-fifth to one-tenth the proportion of larger fractions. Thus, the larger quantities and smaller sizes of fragments were produced by detonations of the larger charges providing greater impulses -- certainly not an unexpected result. This tends to lend support to theories, that, in impulsive fragmentation, new surface area produced through fragmentation may be quantitatively related to explosive impulse or energy.

3.3 Fragmentation of Concrete Shielding of Reactor Models

The Stanford Research Institute conducted experimentation on model concrete biological shielding poured directly in contact with model

SECRET

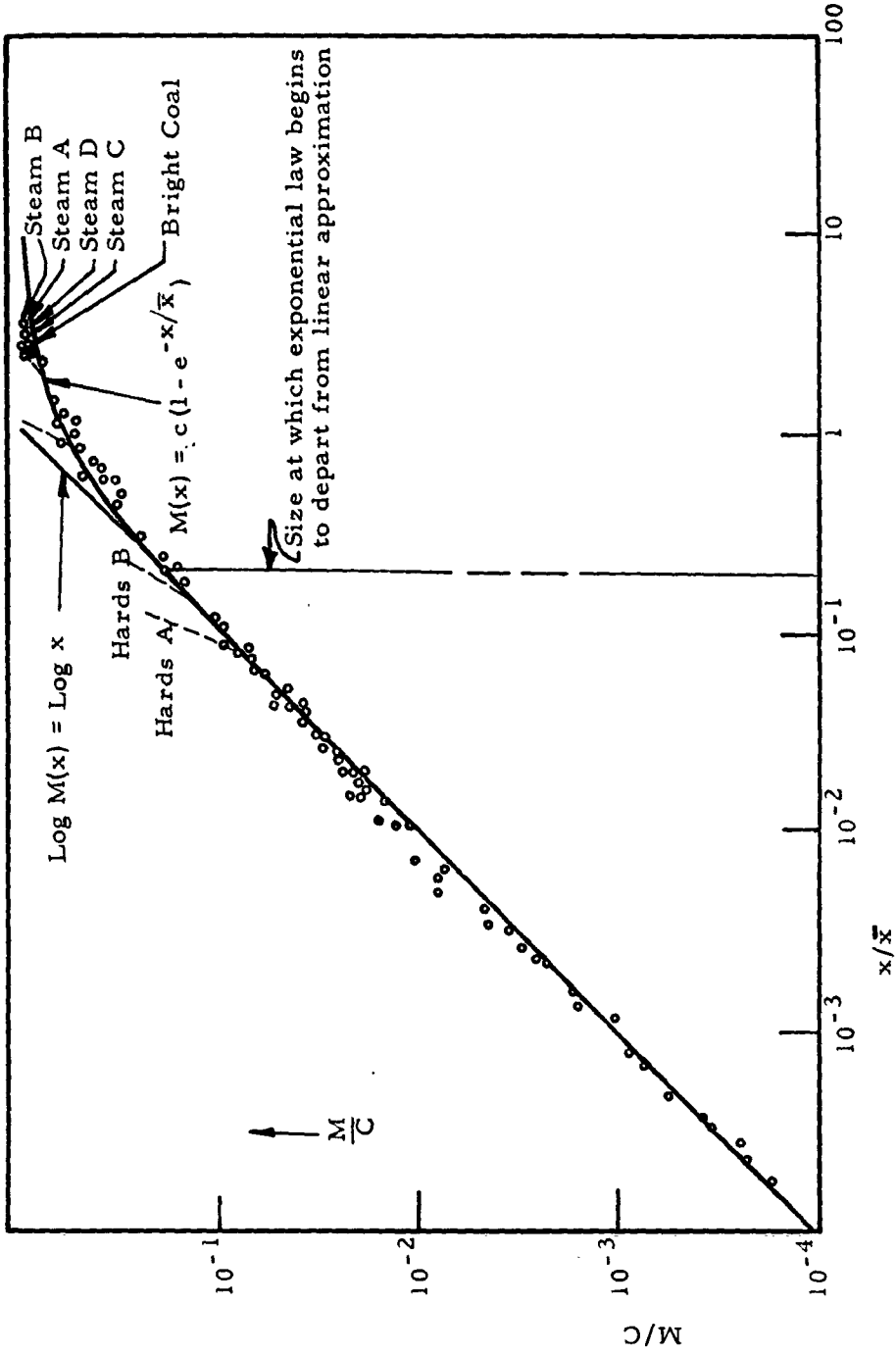


Figure 3.1 The Ideal Law of Breakage

SECRET

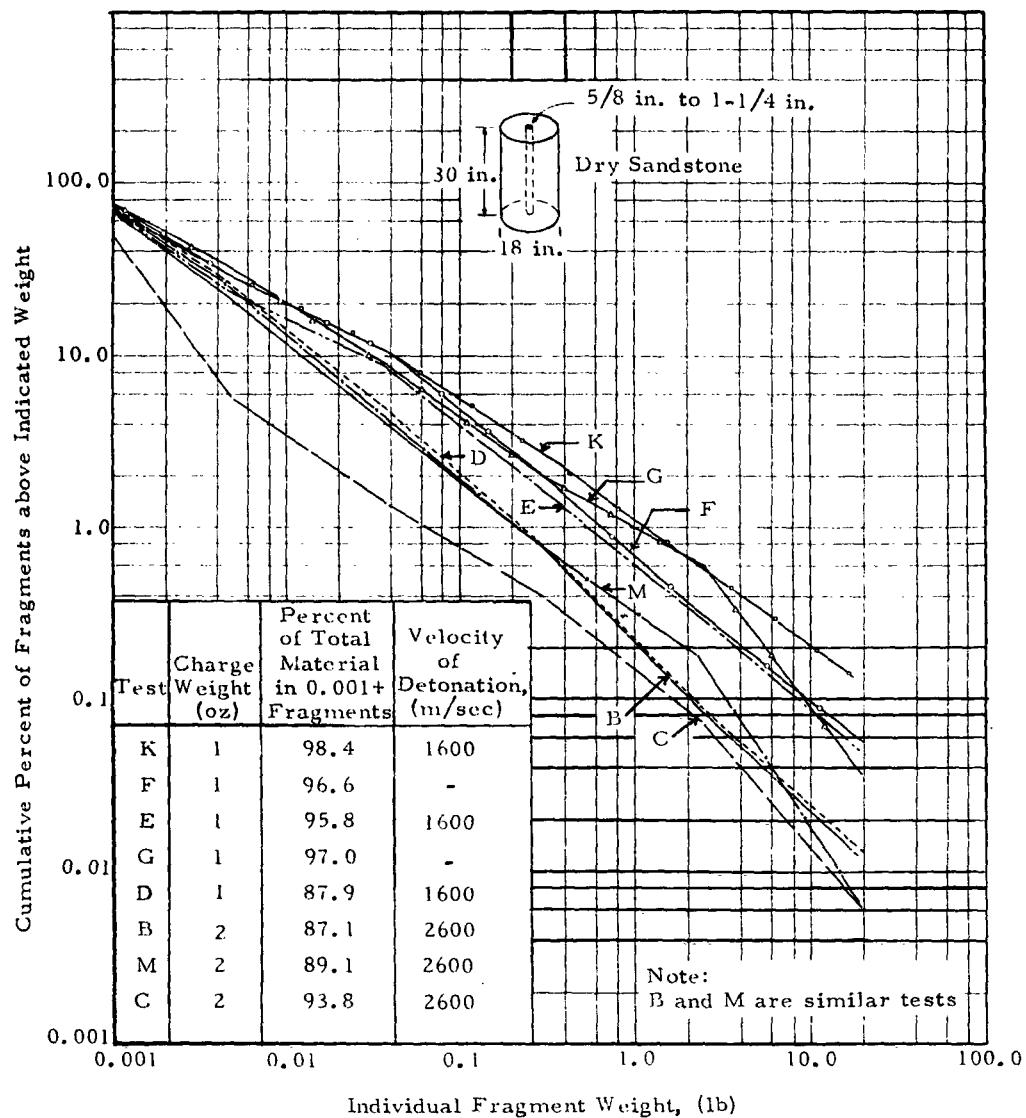


Figure 3.2 Cumulative Fragment Size Distribution
for Exploded Dry Sandstone Blocks

SECRET

SECRET

pressure vessels (Ref. 15). The models, shown in Fig. 3.3, consisted of a reactor vessel, the concrete biological shield, and a stepped plug filling the access opening at the top of the vessel. Vessels were filled with varying amounts of water (75 and 100 percent) and subjected to the detonation of scaled energy sources centered radially and axially in the pressure vessel. The following model tests were selected for detailed plotting in this study, since individual fragment weights were available for these events. Original source data from these tests are included in Appendix F.

Table 3.1

MODEL TESTS SELECTED FOR PLOTTING

Model Test No.	Event Simulated		Energy Source Material	Period, (msec)	Water in Vessels, (%)	Number of Fragments	
	Pounds of TNT	Megawatt-seconds				Above 0.1 lb	Total Recorded
15	150	280	Pyracore	1	75	14	24
17	160	300	Pyracore	1	100	7	9
14	160	300	Pyracore	1	75	2	2
16	210	400	MDF	1	100	41	373
19	210	400	MDF	1	75	55	287
5	510	960	Pyracore	1	100	23	63
3	730	1,360	Pyracore	1	75	45	96

The cumulative total number of fragments above the indicated size is plotted in Fig. 3.4 and 3.5. Figure 3.4 includes all recorded fragments, while Fig. 3.5 includes only those fragments weighing more than 0.1 lb. Three explosion factors in the test setup which influence the loading are the percent of water in the vessel, the quantity of explosive (as indicated by the magnitudes of the simulated event), and the equivalence of the explosive source material. Tests, numbered 16 and 19, in which MDF was used as the explosive source material produced the most

SECRET

SECRET

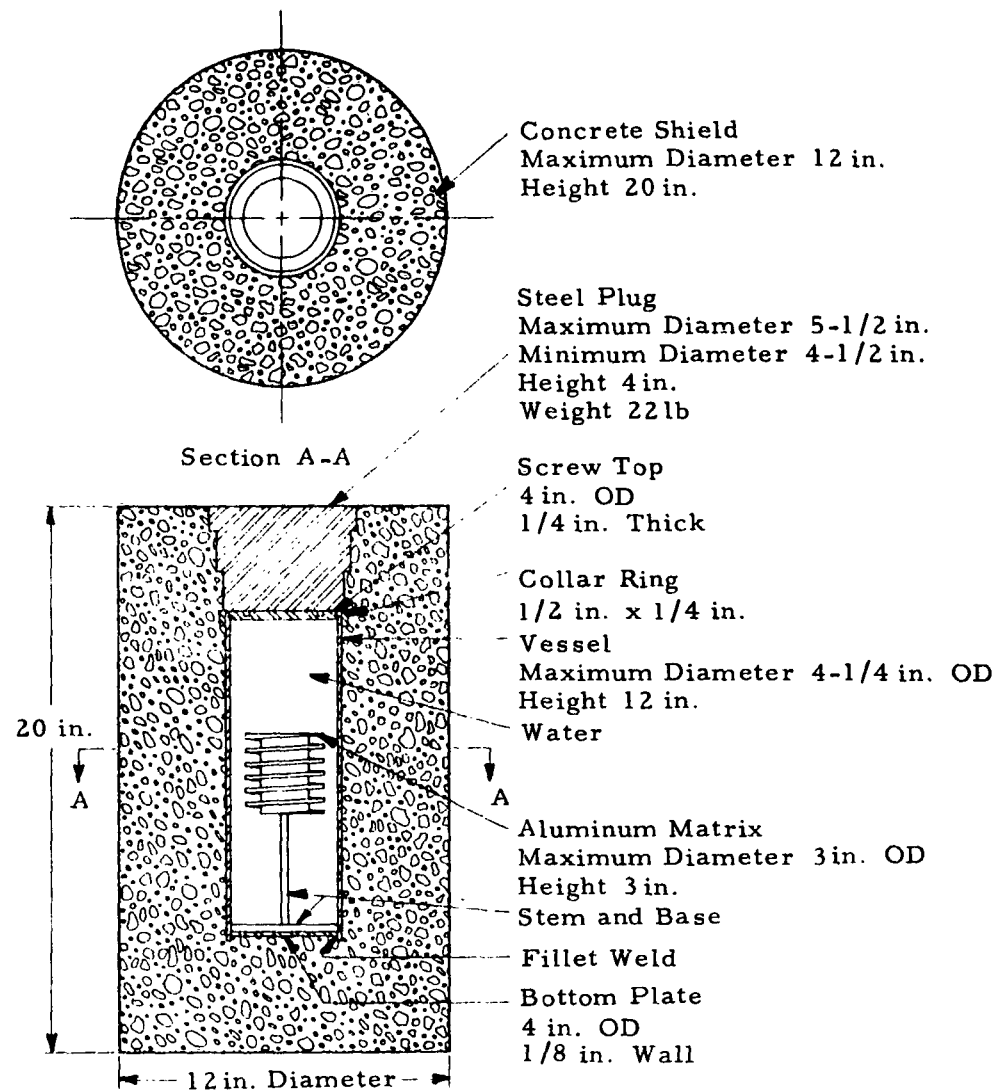


Figure 3.3 Model Reactor with Concrete Shielding

SECRET

SECRET

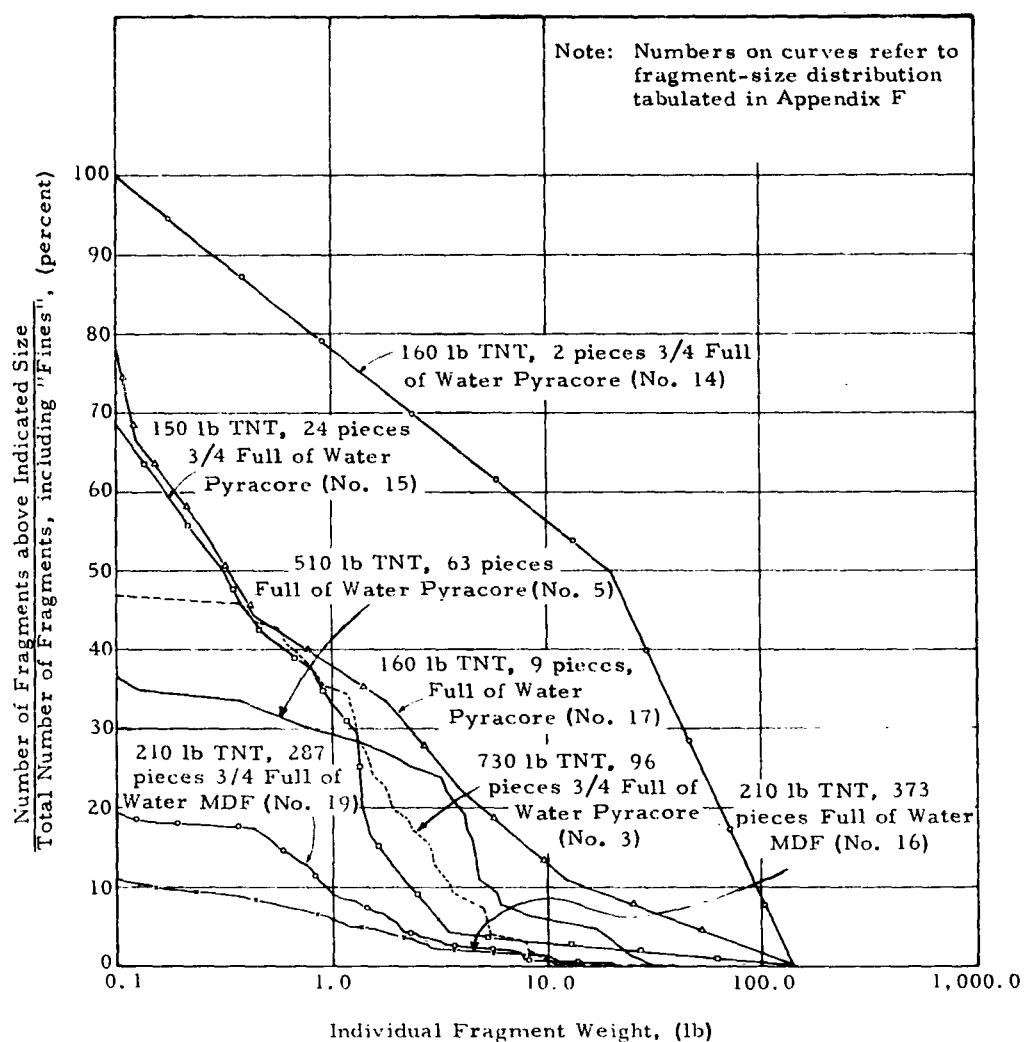


Figure 3.4 Cumulative Fragment Distributions for 1/24-Scale Shielded Reactor Vessels (includes all recorded fragments)

SECRET

SECRET

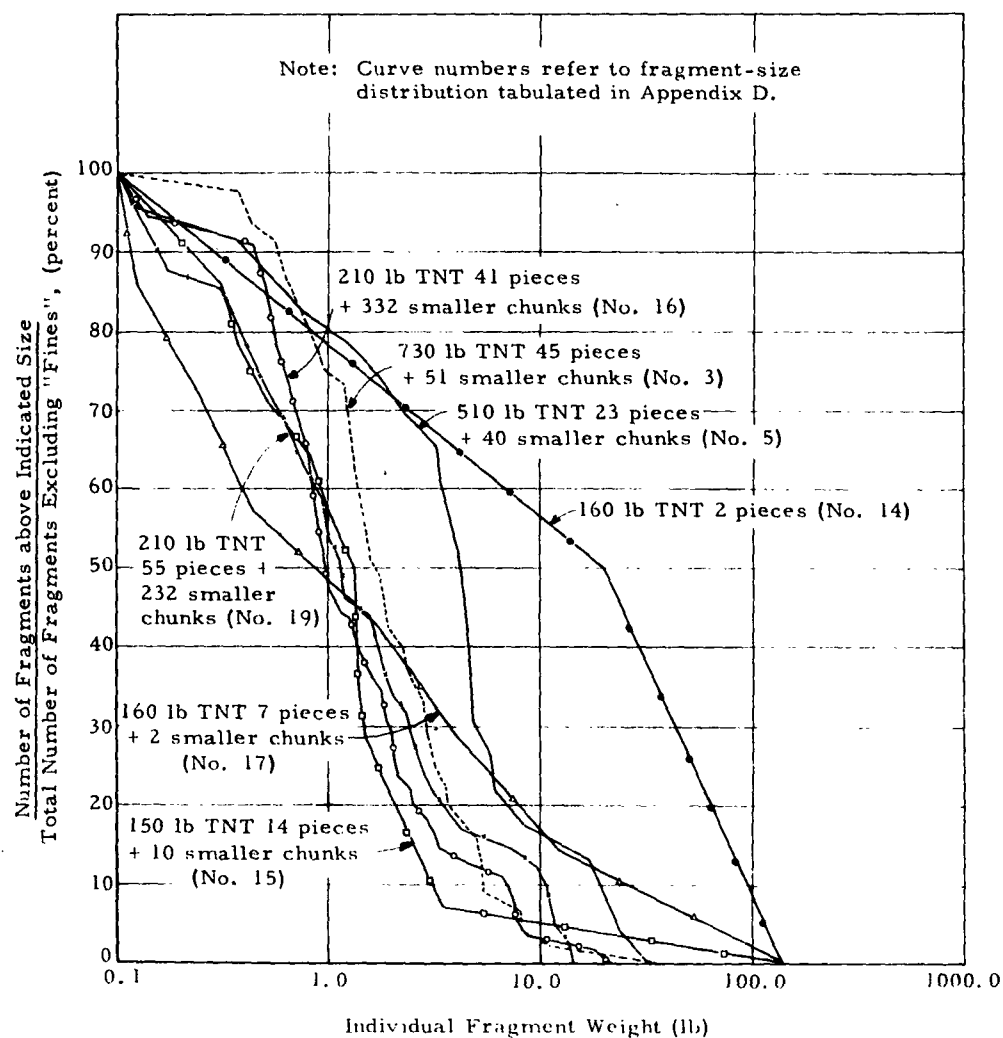


Figure 3.5 Cumulative Fragment Distributions for 1/24-Scale Shielded
Reactor Vessels (includes all fragments over 0.1 lb)

SECRET

SECRET

complete fragmentation. This certainly appears to be a function of the impulsive loading (or energy input) since the amount of gaseous reaction produce in the energy source is five times as high for MDF as for Pyracore (100% vs. 20%).

Other than for Test 15, it was observed that fragmentation became more complete with increasing magnitude of the simulated event, higher water level in the vessel, and increased quantity of gaseous combustion products from the charge. These are all factors which would increase the loading on the concrete shielding. In Test No. 15, 24 fragments were produced and 85 percent of the total concrete weight was in the largest fragment.

A highly favorable result of this series of tests is the consistency in the shape of the cumulative curves of Fig. 3.4 and 3.5. Crossing-over of curves exists in these plots, but the general shape of the curves is consistent and the relative position of the successive curves appears to bear some relation to the impulsive loading.

Similar results were observed in a series of 1/12-scale shielded reactor model tests (Ref. 16). Only the magnitude of the event simulated was varied in this series of tests, (data are tabulated in Appendix G and plotted in Fig. 3.6). As Fig. 3.6 shows, separation between the cumulative distribution curves for different events is decidedly pronounced, and the general shape of the curves is quite consistent. This series of tests appears to support contentions that fragmentation becomes more complete with increased loading and implies that the relationship between fragmentation and loading may be quantified, at least for simple ideal structures.

Stanford Research Institute selected three criteria to assess the fragmentation and fragment dispersion in the reactor shielding model tests. The quantity of new surface area created in the fragmentation process was regarded as an indicator of the energy absorbed in breaking the concrete shielding. It can be shown that this newly created surface area (termed fragmentation in the SRI reports) can be approximated from the individual fragment weights:

SECRET

SECRET

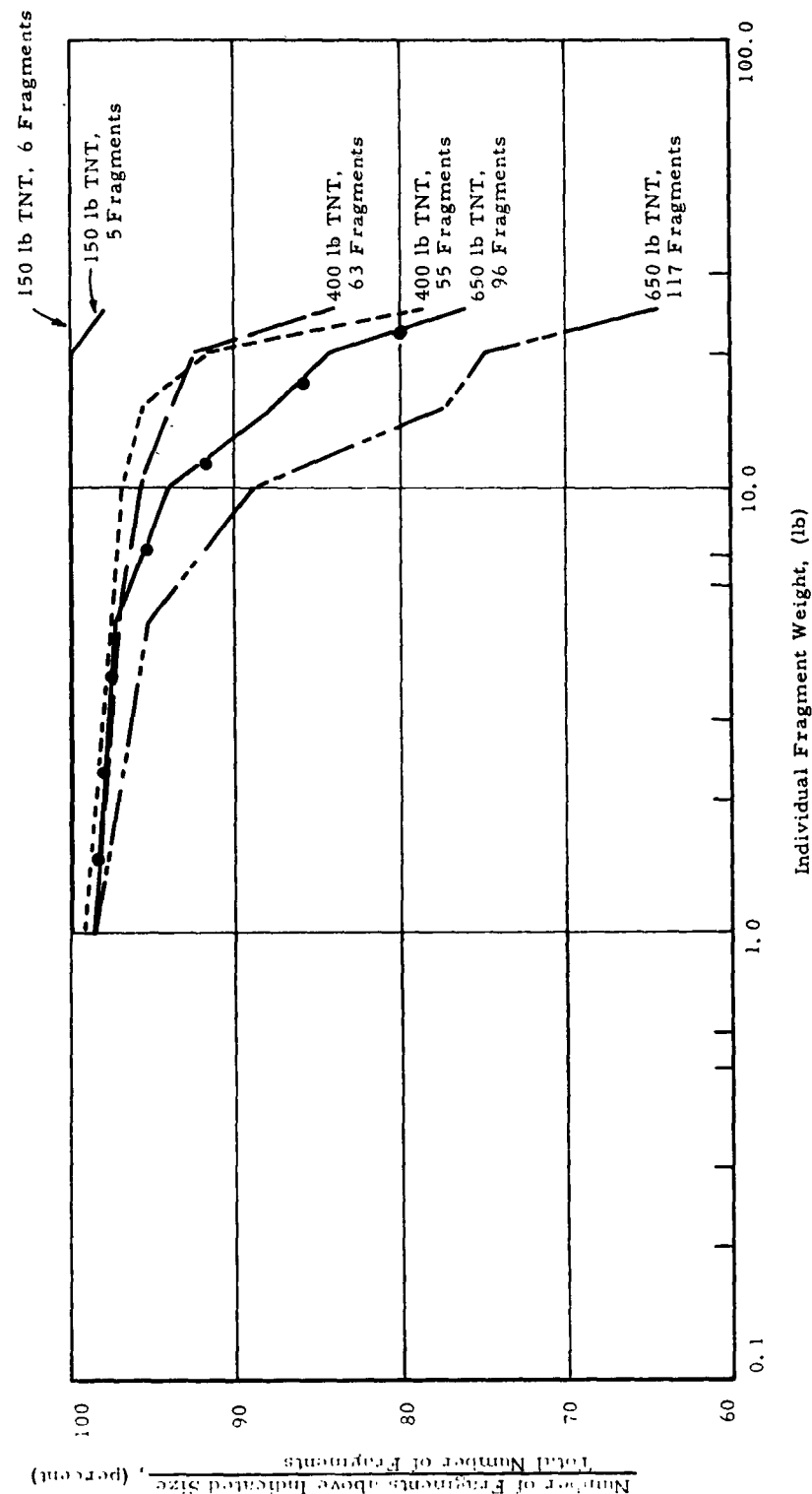


Figure 3.6 Cumulative Fragment Distributions for 1/12-Scale Shielded Reactor Vessels

SECRET

SECRET

Fragmentation \propto New Surface Area

$$\propto \sum W_f^{2/3}$$

where W_f is the individual fragment weight.

Similarly, the throw, defined as the summation of the products of weight times distance thrown for individual fragments, was taken as an indicator of the total amount of input energy diverted into transport of fragments;

$$\text{Throw} \propto \sum W_f D_f$$

where D_f is distance thrown for the individual fragment.

A measure of structural integrity representative of the degree to which concrete shielding remained intact was defined as the ratio of the sum of the squares of individual fragment weights to the square of the total shielding weight;

$$I \propto \frac{W_f^2}{(\sum W)^2}$$

The inverse of this integrity ratio was considered to be a measure of the total damage to the shielding structure.

The measures of fragmentation, throw, and integrity were computed for the various reactor shielding models by SRI. Plots of these values are included in Fig. 3.7 through 3.10. For the various series of models, the selected debris parameters (fragmentation, throw, and the inverse of the integrity ratio) show varying degrees of consistency in the shape of the plotted relationships. Some of the more pronounced deviations between plotted points and the curves as drawn are perhaps explainable in terms of the considerable scatter customarily experienced in explosion testing.

Figure 3.7 shows results of 1/12- and 1/24-scale model tests for the debris criteria. In this figure the fragmentation and throw for the 1/12-scale models are reduced by the reciprocal of appropriate scale factors:

SECRET

SECRET

SECRET

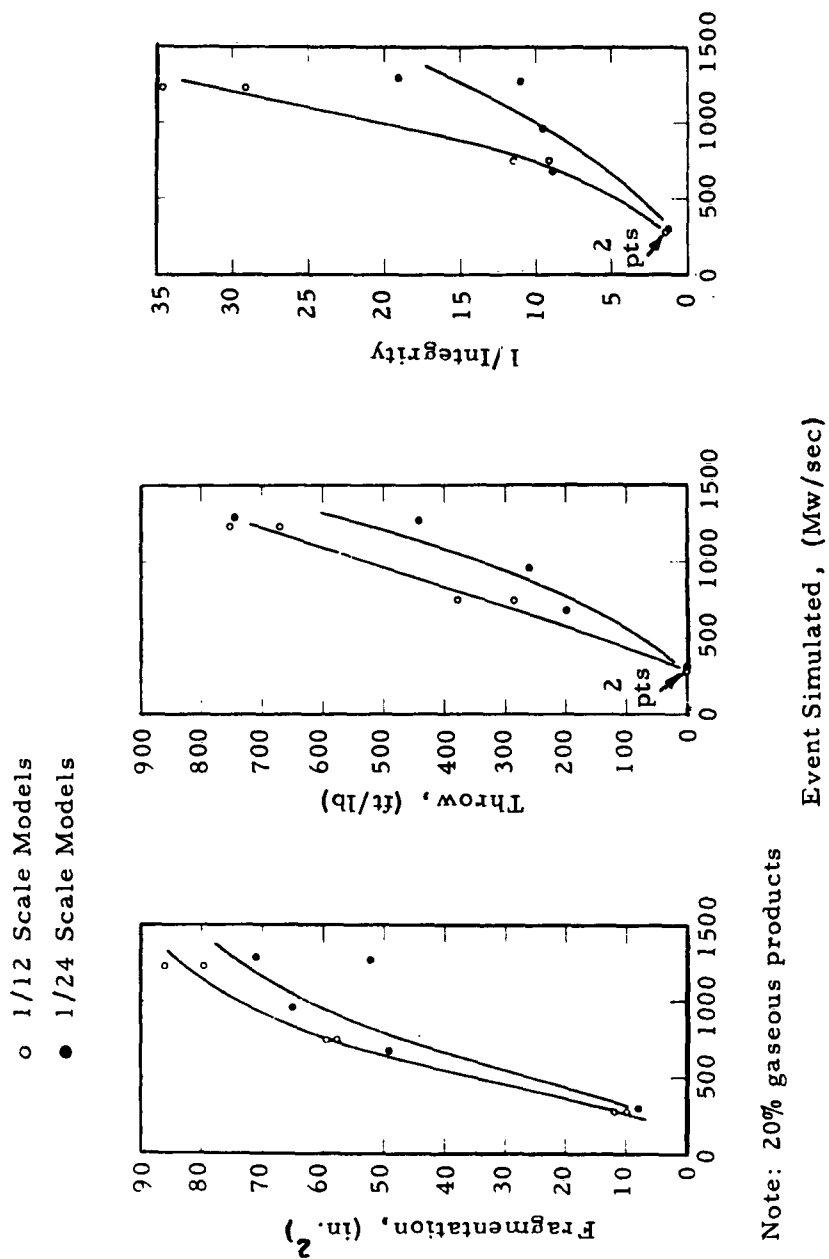
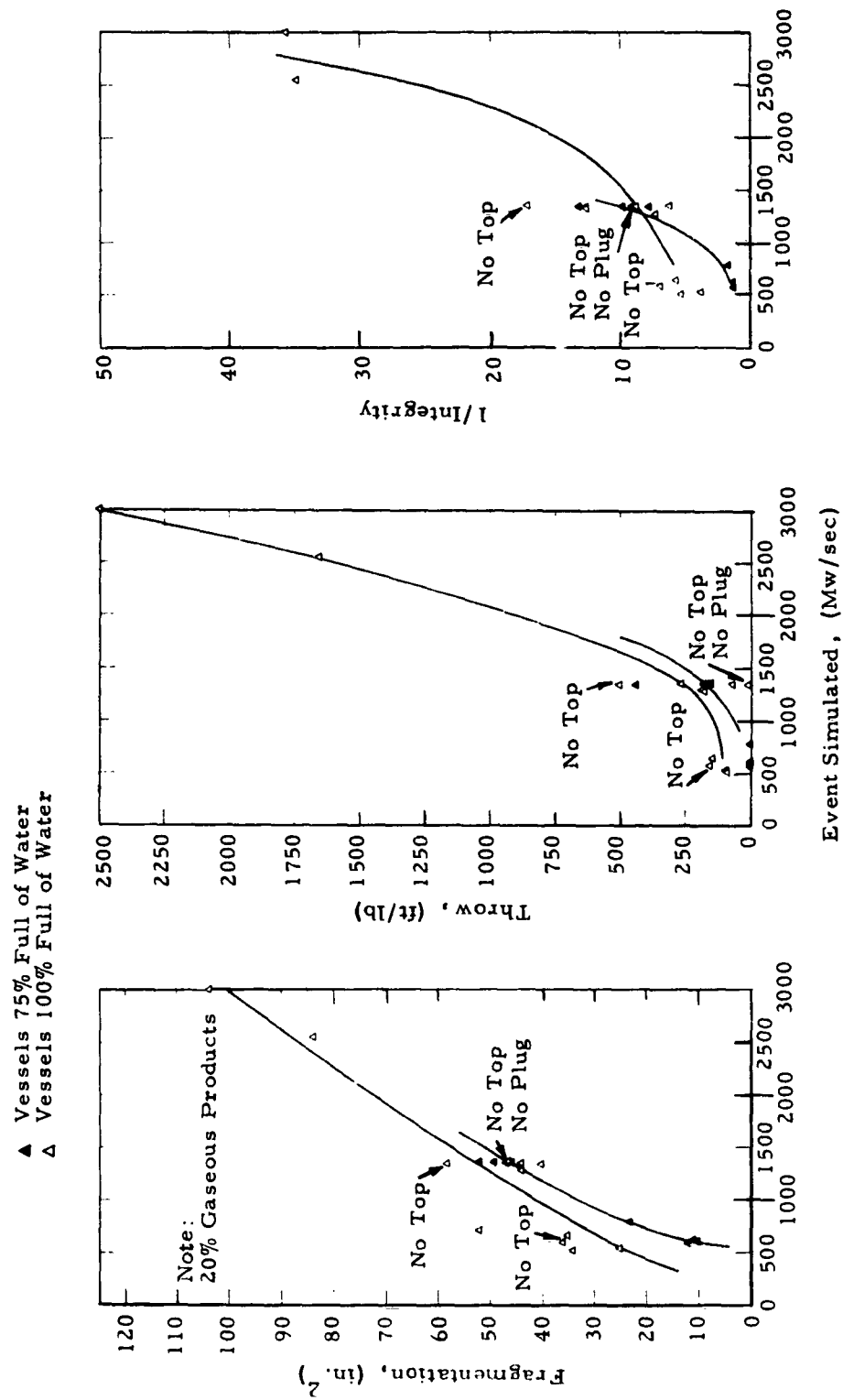


Figure 3.7 Fragmentation Measures for 1/12- and 1/24-Scale Shielded Reactor Model Tests

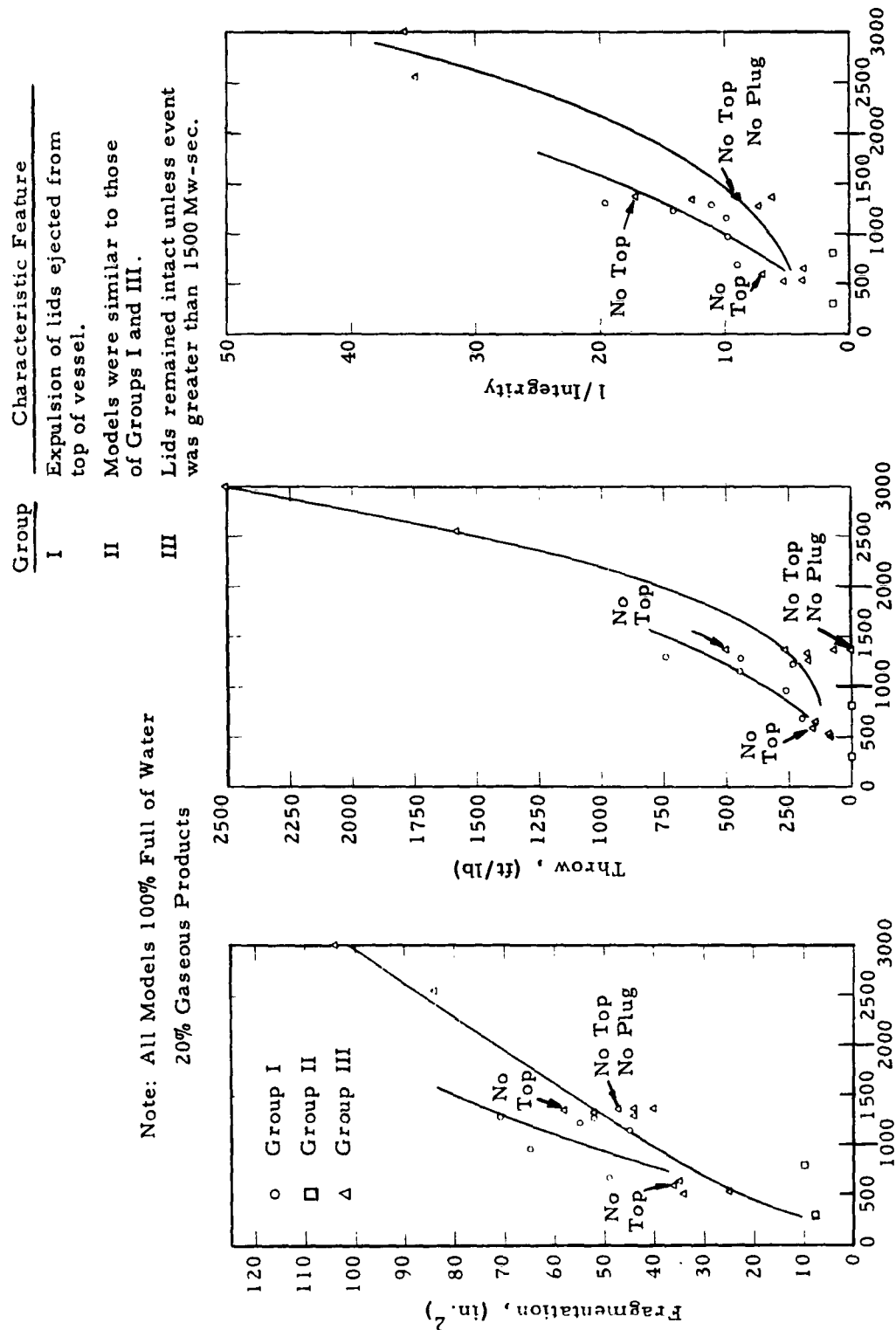
SECRET



SECRET

Figure 3.8 Fragmentation Measures for 1/24-Scale Shielded Reactor Models Full and 3/4-Full of Water

SECRET



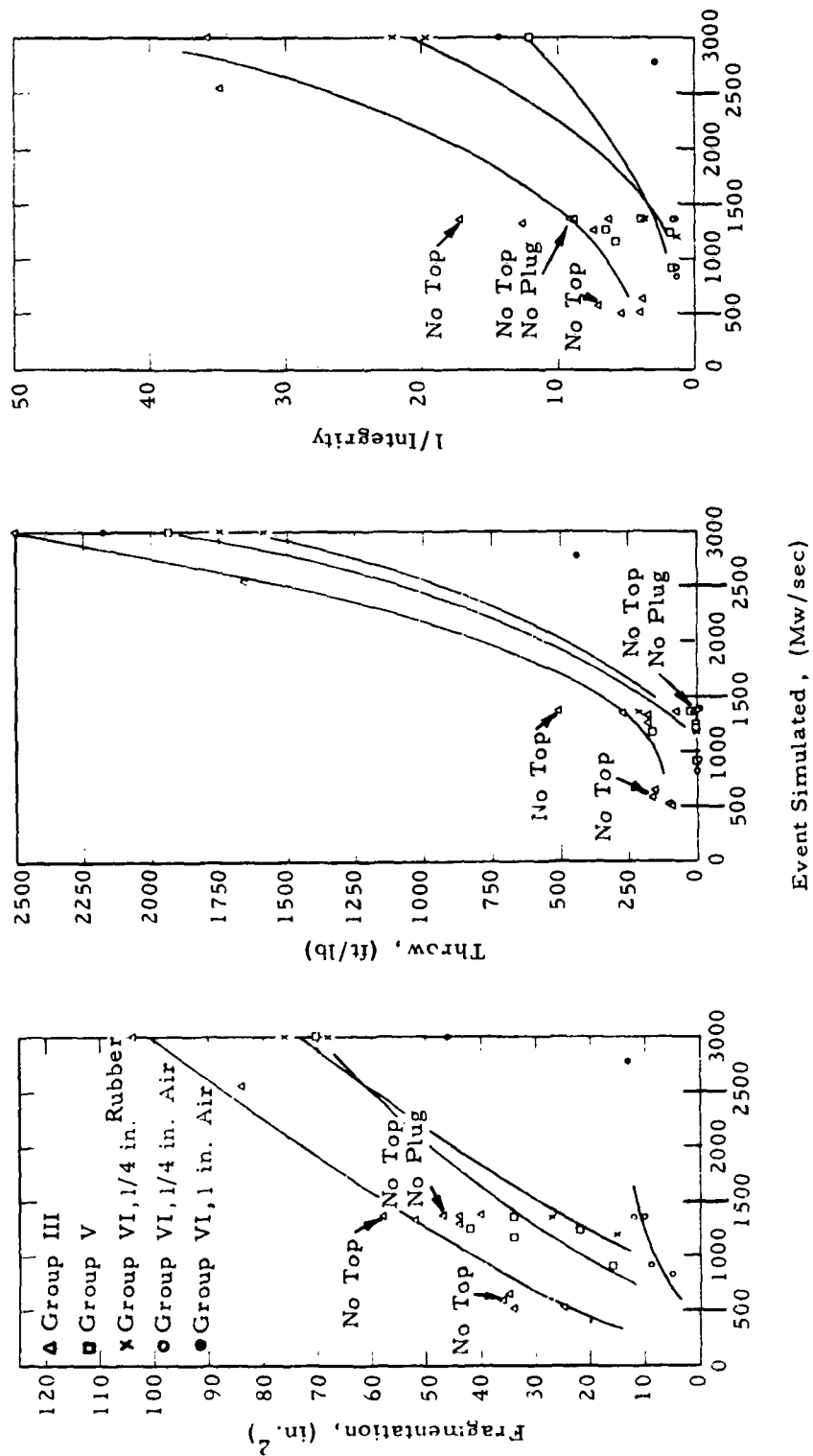
Event Simulated, (Mw/sec)

Figure 3.9 Fragmentation Measures for Selected 1/24-Scale Shielded Reactor Model Tests

SECRET

SECRET

Note: All Models 100% Full of Water
20% Gaseous Products



Note:

Group V - Reinforcing bars included in models.

Group VI - Insulated models.

Figure 3.10 Fragmentation Measures for Selected 1/24-Scale Shielded Reactor Model Tests

SECRET

SECRET

Fragmentation: $A_1 \sim \lambda^2 A_2$, by 4

Throw: $W_f D_f \sim \lambda^3 \lambda^{1/2} W_f' D_f'$, by $8\sqrt{2}$

where λ is the ratio of scale factors.

Comparison of debris parameters for model reactor shielding with different quantities of contained water are shown in Fig. 3.8. Some, but not complete, separation of data points is apparent in the series of model tests in Fig. 3.9 and 3.10. With further tests, more conclusive definition of these functions might evolve.

No relationships can be established between the results of these reactor shielding model tests, fragmented by the impulsive loading of an internal explosion, and the fragmentation behavior of other structures under nuclear blast loading. Under the longer duration nuclear loading, it is likely that peak overpressure may exert a greater significance than impulse on the fragmentation process. It is significantly demonstrated, however, that fragmentation patterns can be measured and related to loading, and that, for a uniform model structure consistent relationships are obtained. This suggests the feasibility of experimenting with suitable ideal structural elements, on a full-scale or model basis, to develop basic input data for debris hazard estimating purposes.

3.4 Fragmentation of a Reinforced Concrete Ordnance Structure

Fragment counts from the Pantex Ordnance Plant event described previously provided data on the individual weights of more than 31,000 recovered concrete fragments with a total weight of more than 85,000 lb (Ref. 11). Individual fragment weights recorded ranged from 1/16 lb to 4,000 lb.

The fragment-size distribution of the recorded fragments is shown in Fig. 3.11. Fragment classes in this figure are in a geometric progression, each class being twice as large as the preceding class. From this chart it appears that the greatest portion of fragments were in the weight range of 0.250 to 0.499 lb, with equivalent diameters of

SECRET

SECRET

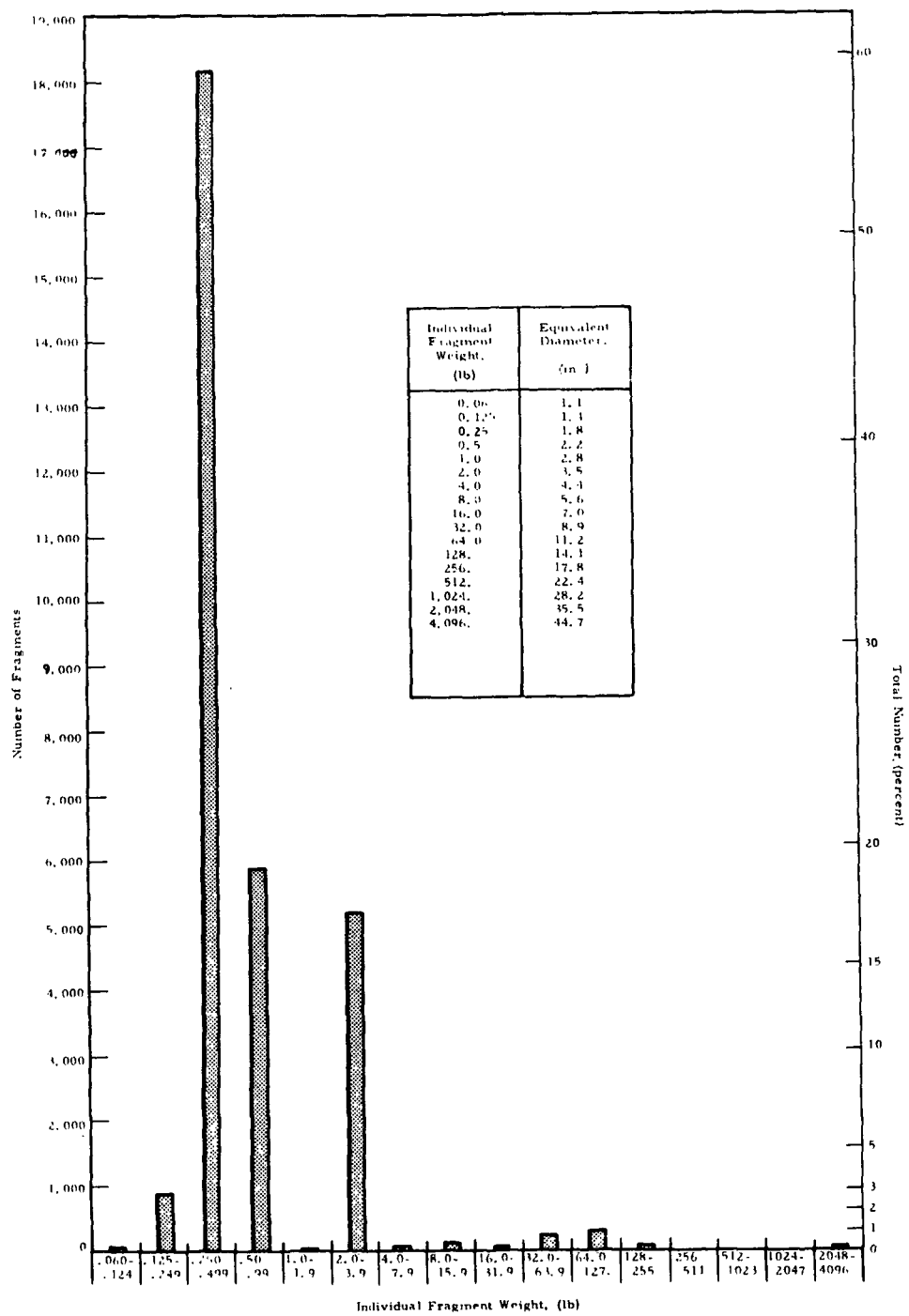


Figure 3.11 Fragment-Size Distribution For a Reinforced Concrete Ordnance Structure

SECRET

SECRET

1.8 to 2.2 in. The expected preponderance of relatively small fragments, under 4 lb or 4.4-in. diameter, is apparent. The relatively few fragments in the 0.060-0.249 lb range is questionable and could result from the tendency to not record all the smallest items at close-in ranges (see Fig. 2.51).

Though the smaller fragments are produced in the greatest quantities, the amount of material involved is relatively small. The distribution of total weight of fragments, pictured in Fig. 3.12, shows more than 65 percent of the total material fragmented into pieces weighing between 32 and 255 lb, that is, with equivalent diameters from 8.9 to 17.8 in.

Cumulative distributions of fragment sizes are approximated in Fig. 3.13. The median fragment weight is found to be about 0.22 lb, and more significantly -- more than 95 percent of all fragments weigh about 3 lb or less, i. e., have equivalent diameters of 4 in. or less. Less than 1 percent of all fragments weigh 90 lb or had equivalent diameters greater than about 1.1 ft. In general, fragments above one pound in size are considered potentially lethal to personnel. Only about 20 percent of all recorded fragments from this test were above this size.

Cumulative weight distribution for fragments is presented in Fig. 3.14. Whereas the greatest number of fragments produced in this event were about 3 lb or less in size, Fig. 3.14 shows that somewhat over 50 percent of the total weight of fragments was in boulders weighing greater than 70 lb or having equivalent diameter of about 11.5 in. or more. Over 70 percent of total fragment weight was in pieces above 3 lb in size. Thus, although substantial quantities of concrete fragmented into large pieces, the number of these was small. The probability of being hit by small pieces is much higher than that of being hit by large boulders.

3.5 Fragmentation of Concrete Walls

The only fragmentation study of structural elements under nuclear loading was conducted as part of Project 4.5 of Operation JANGLE. For this event a series of six reinforced concrete wall panels was

SECRET

SECRET

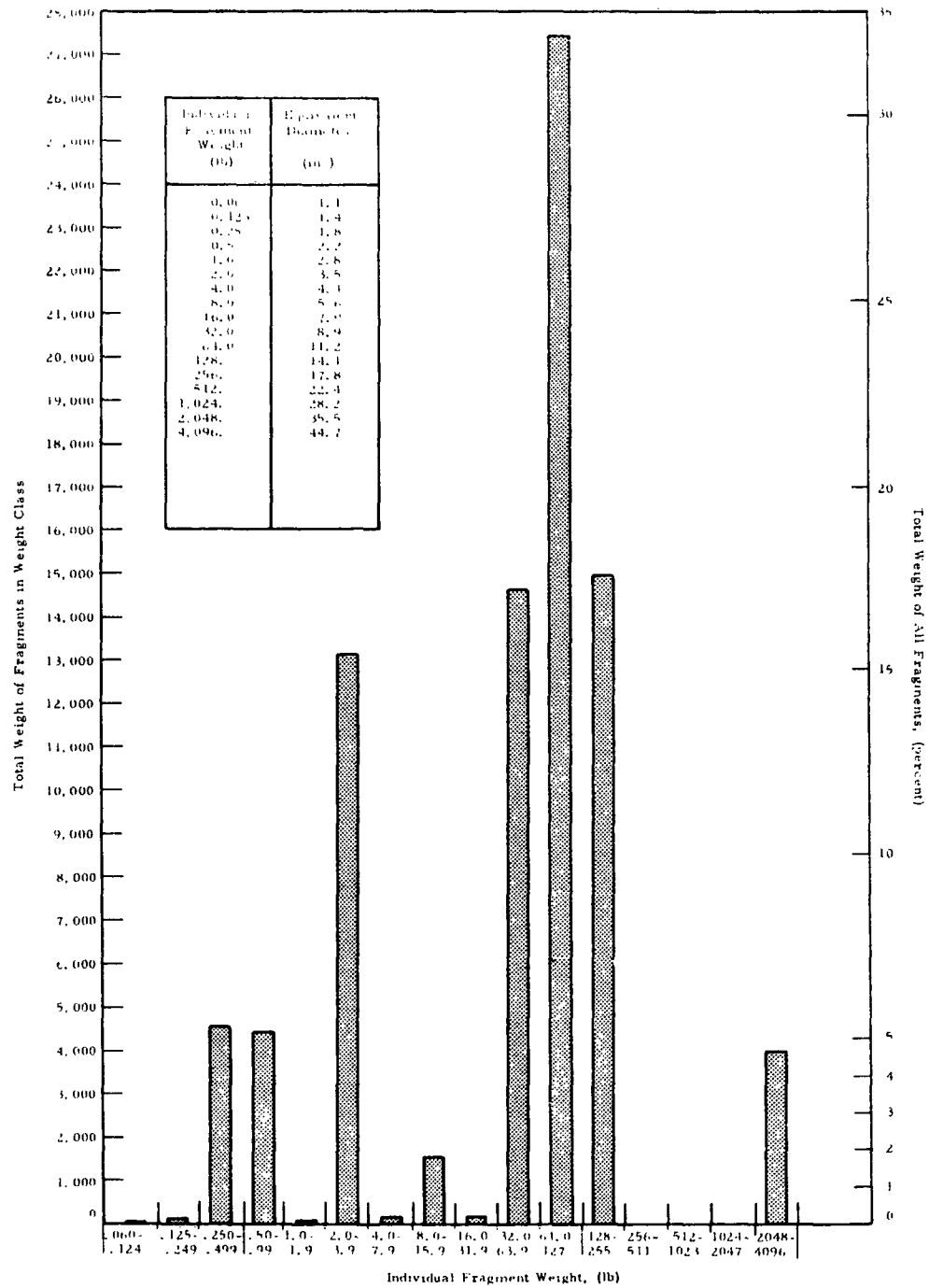


Figure 3 12 Distribution of Total Fragment Weight by Fragment-Size Classes For a Reinforced Concrete Structure

SECRET

SECRET

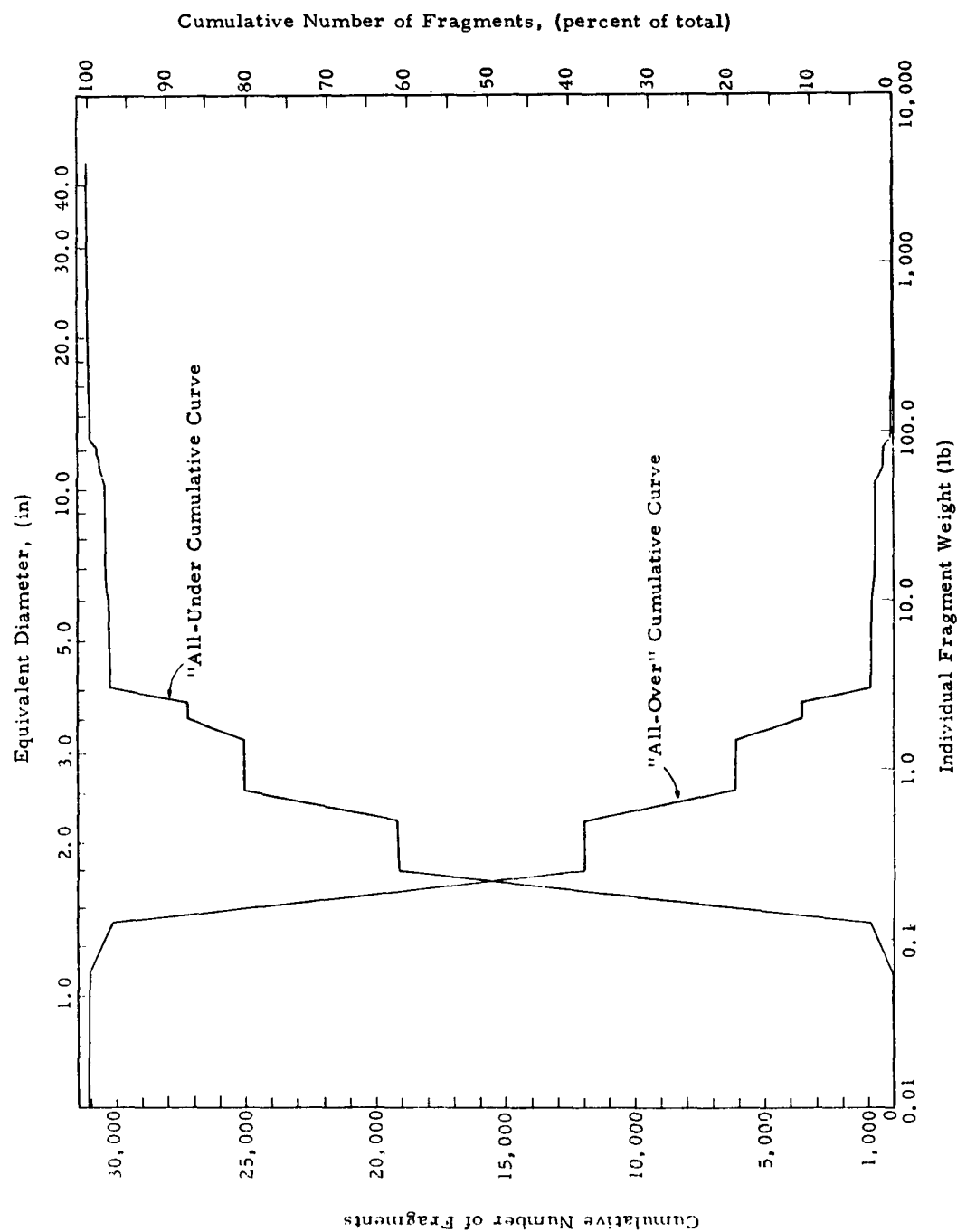


Figure 3.13 Cumulative Fragment Size Distribution for a Reinforced Concrete Ordnance Structure

SECRET

SECRET

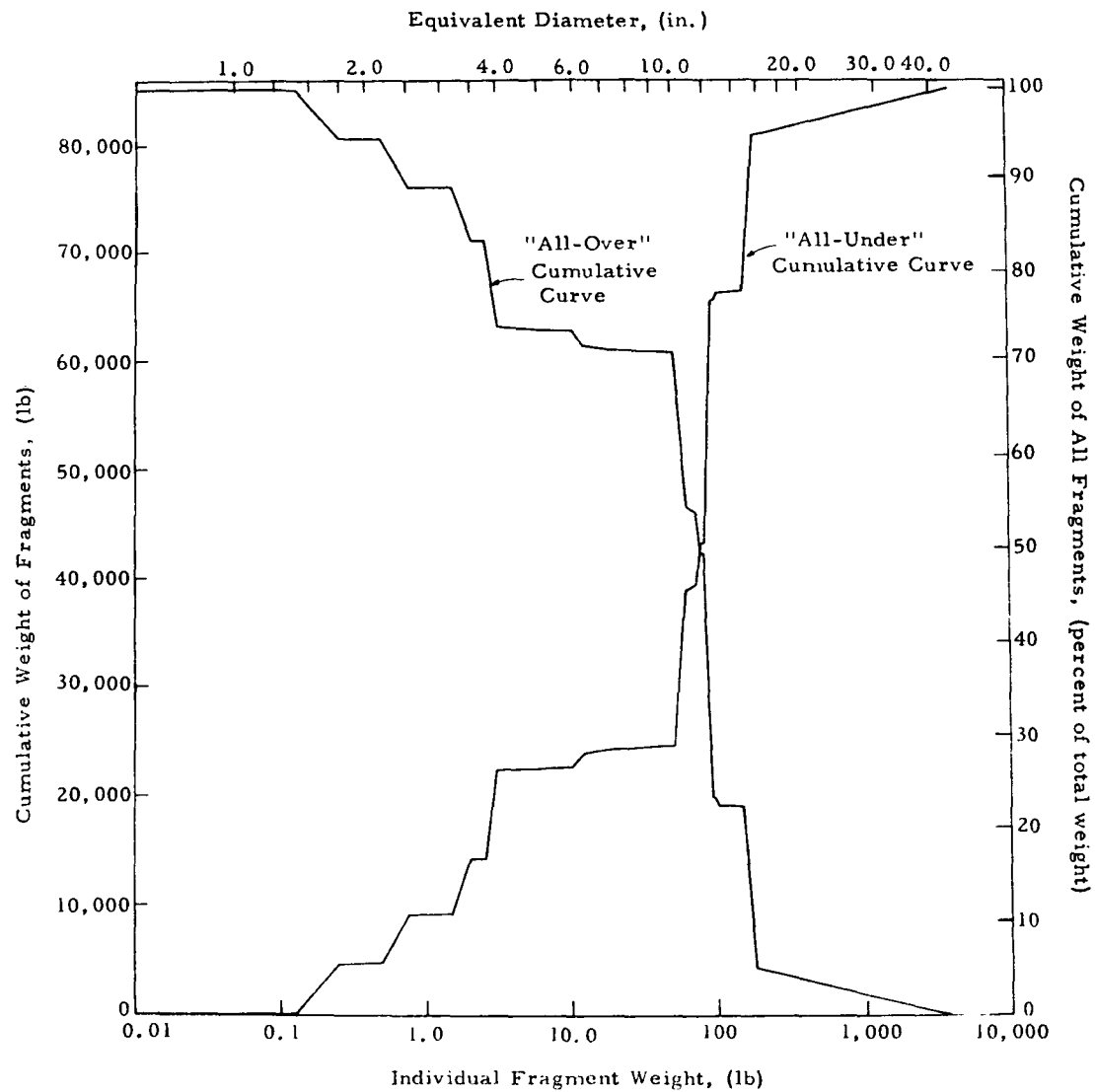


Figure 3.14 Cumulative Distribution of Total Fragment Weight
for a Reinforced Concrete Ordnance Structure

SECRET

SECRET

erected over the crater zone of the underground shot as shown in Fig. 3.15. This event involved a 1.2-KT device emplaced at a depth of burst of 17 ft; the apparent crater diameter was about 260 ft. The wall panels were thus placed fairly close-in relative to the total crater -- i. e., at ground ranges from 14 percent to 40 percent of apparent crater radius.

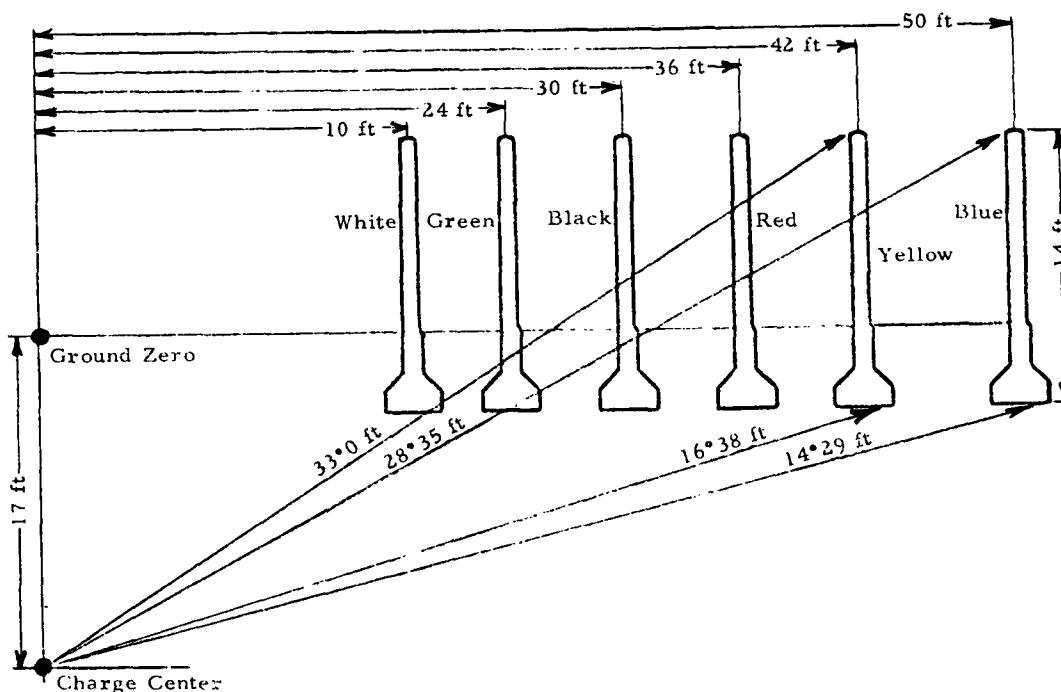


Figure 3.15 Placement of Wall Targets in JANGLE U Event

The fragment-size distribution of wall fragments reported from this test is presented in Fig. 3.16. These curves are plotted through the data points at a slope of 0.5 (the slope predicted on the basis of the Ideal Breakage Law). The JANGLE report pointed out that only the larger fragments were collected and that these would normally be expected to deviate from the ideal fragment-size distribution when a limited amount of material is available. It was concluded that the JANGLE data did not preclude the possibility that the breakup of concrete source material caused by a nuclear detonation follows the same pattern as coal in a mine or ore in a crusher.

SECRET

SECRET

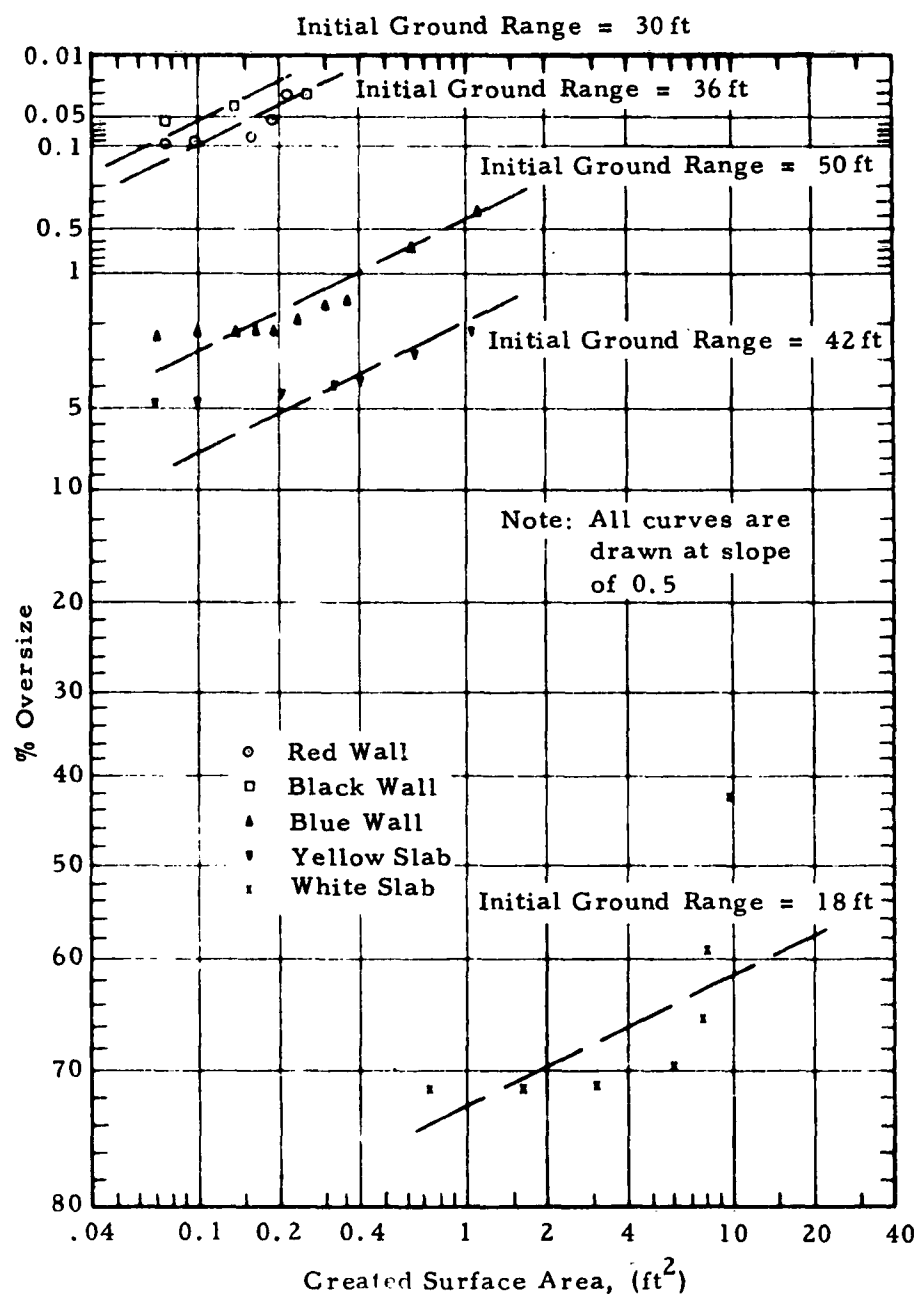


Figure 3.16 Size Distribution of Fragments from Wall Targets in JANGLE U Event

SECRET

SECRET

It is noted that the relative positions on the curves (and their associated data points) are not arrayed in the same sequence as the initial ground ranges of the walls. The lowest curve, representing the largest fragments, corresponds to the wall closest to surface zero, where vertical components of the load may be expected to be higher. However the two topmost curves, representing the smallest fragment sizes, correspond to the middle two walls rather than the farthest-out.

SECRET

SECRET

CHAPTER FOUR

FRAGMENTATION, ANALYTICAL CONSIDERATIONS

4.1 State of Knowledge of Fracture Mechanics

Analytical consideration of debris resulting from the fracture of concrete or masonry structures poses two fundamental questions: 1) What is the fracture strength, i. e., the ultimate load which the structure can sustain? and 2) What is the number and size of the resulting fragments? The first question is by far the easier to answer and it is discussed briefly from the point of view of existing fracture theory.

The theoretical strength of materials is of the order of 100 to 1000 times the observed strength. Griffith (Ref. 17) proposed that this difference can be rationalized in terms of pre-existing flaws contained in the solid. This model of a solid containing an array of flaws is the basis of the "fracture mechanics" approach to the problem. Treatment of this problem is concerned with the growth of pre-existing flaws contained in the solid. This model of a solid containing an array of flaws is the basis of the "fracture mechanics" approach to the problem. Treatment of this problem is concerned with the growth of pre-existing flaws and conditions of instability which can change the crack propagation from a slow process to that characteristic of a fast-running crack.

Griffith formulated the condition of stability, under load, of a body containing a certain type flaw upon two theorems. The theorem of minimum energy states that the equilibrium state of an elastic body, deformed by specific surface forces, is such that the potential energy of the whole system is a minimum. He obtained his new criterion of rupture by adding to the theorem of minimum energy the statement that the equilibrium position, if equilibrium is possible, must be one in which rupture of the solid has occurred, if the system can pass from the unbroken to the broken condition by a process involving a continuous decrease in potential energy. Thus, in the propagation of a crack, stored potential energy is released, but the potential energy of the system is increased by the creation of new surfaces (surface energy). Griffith's condition for

SECRET

SECRET

continuing propagation of a crack is that the resultant potential energy of the system is decreasing. Likewise, the equilibrium crack size is one in which the decrease in potential energy just equals the increase in surface energy. The theory predicts strength reasonably well for bodies such as glass and ceramic which behave in a brittle fashion. Using the Griffith theory, we can reason that there will be a distribution of strengths in a given specimen in the sense that a different amount of force will be needed to fracture a specimen at one point than at another. If one assumes that the flaws are distributed at random with a certain density per unit volume, then the statistical formulation of the strength problem becomes apparent. The strength of a specimen is determined by the weakest point in the specimen or by the smallest value to be found in a sample of size n where n is the number of flaws. Clearly, n increases as the volume increases and, therefore, the problem of finding out how the strength depends on the volume of the specimen is equivalent statistically to studying the distribution of the smallest value as a function of n , the sample size. This statistical problem is an important one on which much theoretical work has been done. For breaking strength the major contributions have been made by Weibull (Ref. 18).

Essentially, Weibull assumes that the probability of failure of a unit volume of material can be represented by a distribution function of the form

$$F(\sigma) = \begin{cases} 1 - \exp \left[- \int_V \left(\frac{\sigma - \sigma_y}{\sigma_o} \right)^m dV \right] & \sigma \geq \sigma_y \\ 0 & \sigma < \sigma_y \end{cases} \quad (4.1)$$

where

$F(\sigma)$ = failure probability for stress σ
 σ_u, σ_o, m = constants of the material

SECRET

SECRET

Once the unit probability of failure $F(\sigma)$ is known, it is a reasonably straightforward procedure to find the probability of failure of any structure under any known system of stresses. Note, however, that the failure mode is not unique since the location of the weakest link is a statistical quantity. Since the likelihood of failure is greatest in regions of high stress, it is certainly possible to anticipate the origin of failure. This predicability is relied upon when brittle test specimens are designed to break in the gage length. But even here it is quite common to get fractures outside of this region.

The applicability of the weakest link theories, and especially the Weibull theory, to the prediction of fracture strength in masonry and ceramics is a problem which is currently undergoing the most intensive investigation. Since the theories, at best, only treat the static load problem, their use in the exceedingly complex debris formation problem is simply too much to expect.

4.2 Mathematical Model

Since a sophisticated treatment of fragmentation involves application of fracture mechanics to an extent that is well beyond the current state-of-the-art, our objective here is to formulate a relatively simple mathematical model which can be used to predict debris formation and which can be adapted to include advances in fracture mechanics.

The response of structures to nuclear blast loading is calculated by considering the response of an equivalent single-degree-of-freedom system (equivalent to neglecting all but the fundamental mode of vibration of the structure). The stiffness of this equivalent system is assumed to be elastic - perfectly plastic so that the structure's response into the plastic range can be considered.

Since this model has proved adequate for analyzing the response of structures up to failure, we propose a simple extension of the model to include fracture. The model is shown on Fig. 4.1. A structure is represented as an equivalent mass M_e and resistance $R(x)$. The

SECRET

SECRET

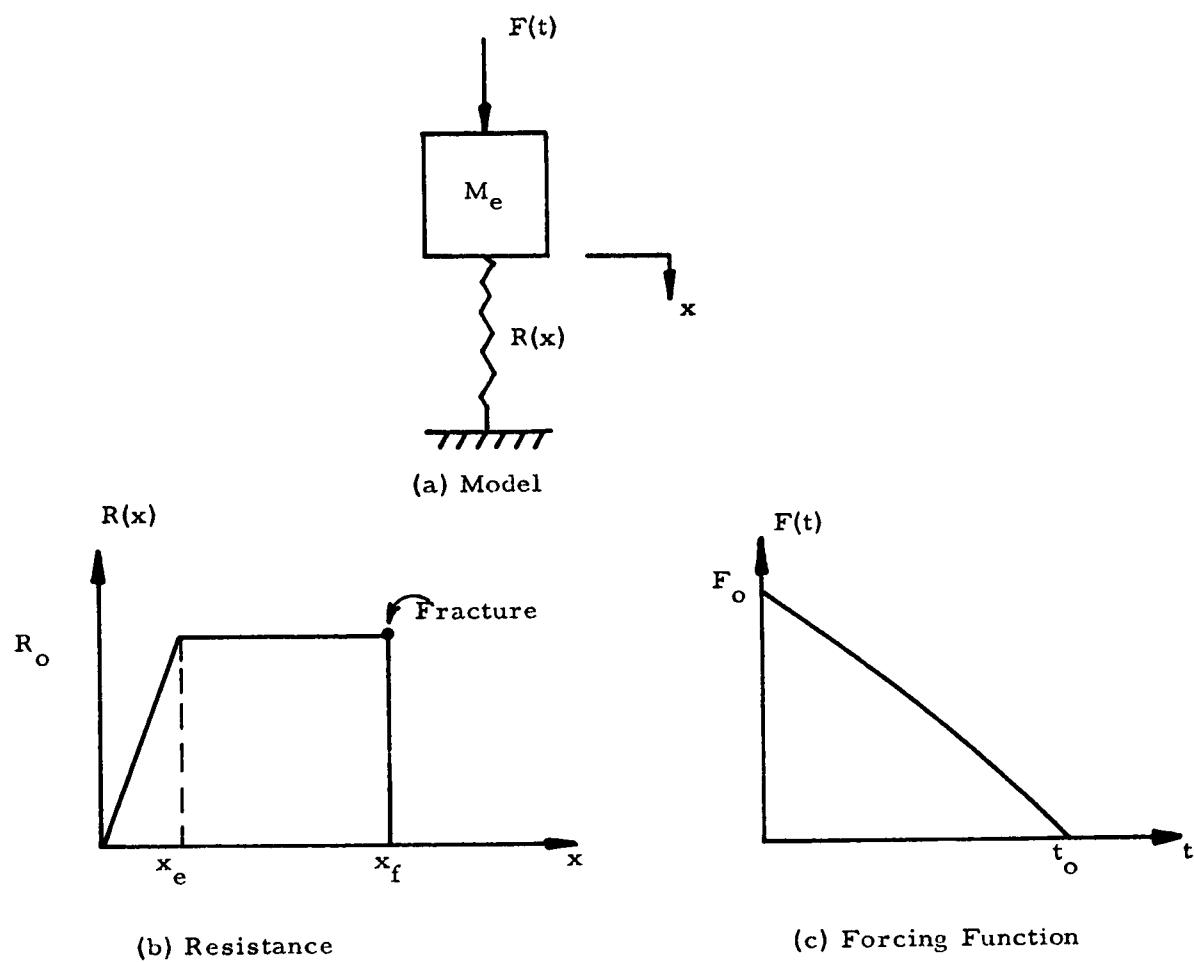


Figure 4.1 Fragmentation Model

SECRET

SECRET

resistance is taken to be elastic-perfectly plastic up to a displacement (x_f) at which the structure fractures. Such a model can be used to predict the velocity and time at which the equivalent mass reaches the fracture displacement.

Limitations to this model are obvious. First, the mass distribution of fragments from the structure will not be determined by this model. Secondly, it is somewhat presumptuous to assume that all fragments are formed at a single displacement. These are questions, however, which must be answered by advances (experimental and analytical) in fracture mechanics. Here, we say

$$M_f = \alpha M_e$$

where,

M_f = mass distribution of fragments

α = normalized mass distribution of fragments to be determined.

Similarly, there would be a statistical distribution about x_f which would result in a corresponding distribution in the time of fracture and velocity spectra of the fragments. Thus, refinements of the basic simple model would be statistical in nature. An experimental program could be undertaken to establish the nature of these distributions for particular types of structures (e. g. , brick walls, concrete structures, steel frames). Hence, it is feasible to obtain answers to these questions (at least insofar as required to modify our model) without waiting for a complete understanding of the fracture mechanics.

The equation of motion for the model of Fig. 4. 1(a) is,

$$M_e \frac{d^2 x}{dt^2} + Rx = F(t) \quad (4. 2)$$

SECRET

SECRET

For convenience, the following nondimensional parameters are defined:

$$\tau = t/t_o$$

$$\zeta = x/x_e$$

$$\beta^2 = \frac{R_o t_o^2}{M_e x_o} = (\omega t_o)^2$$

$$\omega = \text{circular frequency of elastic system}$$

$$\delta^2 = \frac{F_o}{R_o}$$

$$\rho = \frac{x_f}{x_e}$$

The equation of motion then becomes,

$$\zeta'' + \beta^2 \zeta = \beta^2 \delta^2 (1 - \tau)$$

$$\text{for } \zeta \leq 1 \quad (4.3)$$

and

$$\zeta'' + \beta^2 \zeta = \beta^2 \delta^2 (1 - \tau) \quad (4.4)$$

for

$$1 < \zeta \leq \rho$$

where the double prime denotes differentiation with respect to τ .

Equation 4.4 has a solution of the form (for zero initial conditions),

$$\zeta = \delta^2 \left[-\cos \beta \tau + \frac{\sin \beta \tau}{\beta} + 1 - \tau \right] \quad (4.5)$$

for

$$\zeta \leq 1,$$

SECRET

SECRET

and

$$\zeta = \frac{\beta^2 (\delta^2 - 1)}{2} (\tau - \tau_e)^2 - \frac{\beta^2 \delta^2}{6} \left[\tau^2 - 3\tau (\tau_e)^2 + 2\tau_e^3 \right] \quad (4.6)$$

$$+ \zeta'_e (\tau - \tau_e) + 1$$

for

$$1 < \zeta \leq \rho$$

where

τ_e = time at which $\zeta = 1$; determined from Eq. (4.5).

ζ'_e = nondimensional velocity at τ_e ; determined from Eq. (4.5).

Solutions for Eq. (4.5) and (4.6) were obtained for final velocity and the time of fracture. These solutions are presented graphically in Fig. 4.2 through 4.4. Thus, the velocity of fragments and time of fracture can be found from this analysis. These would then be inputs to the analysis of debris transport which would provide a complete displacement history of the fragment.

4.3 Example

As an example of the application of this analysis consider the wooden siding from a railroad car. The failure of such siding was observed during the UPSHOT-KNOTHOLE series of weapon effects tests (Ref. 19). The velocity at failure of siding located in the 10-psi overpressure region was observed to be 60 fps.

The ultimate elastic resistance of a simply supported rectangular beam is,

$$R_o = 2 \frac{bd^2}{L} \sigma_y = \frac{2 b (1.25)^2 \times 1400}{10 \times 12} = 37b$$

SECRET

SECRET

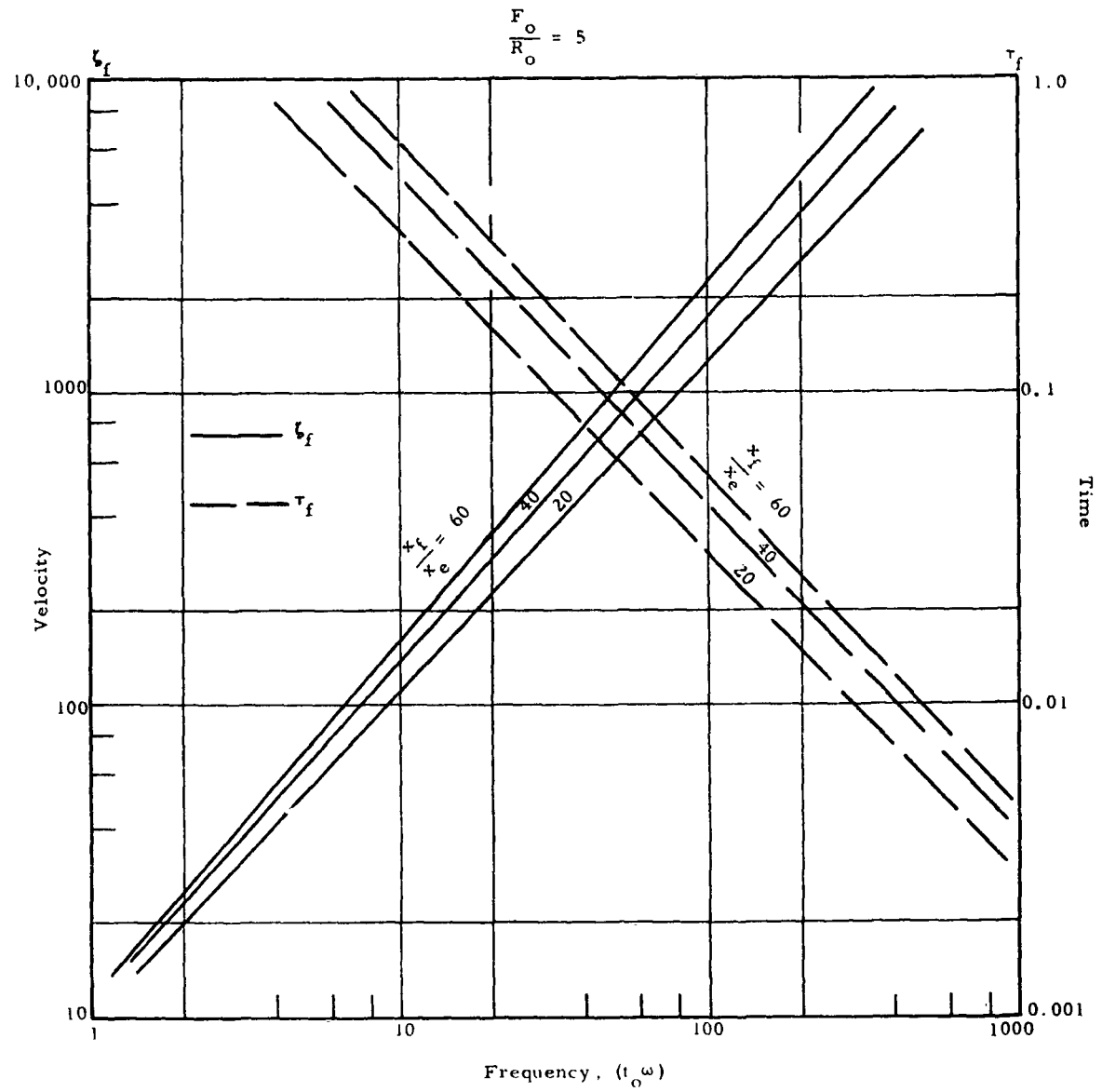


Figure 4.2 Motion of Mass At Failure ($\delta = 5$)

SECRET

SECRET

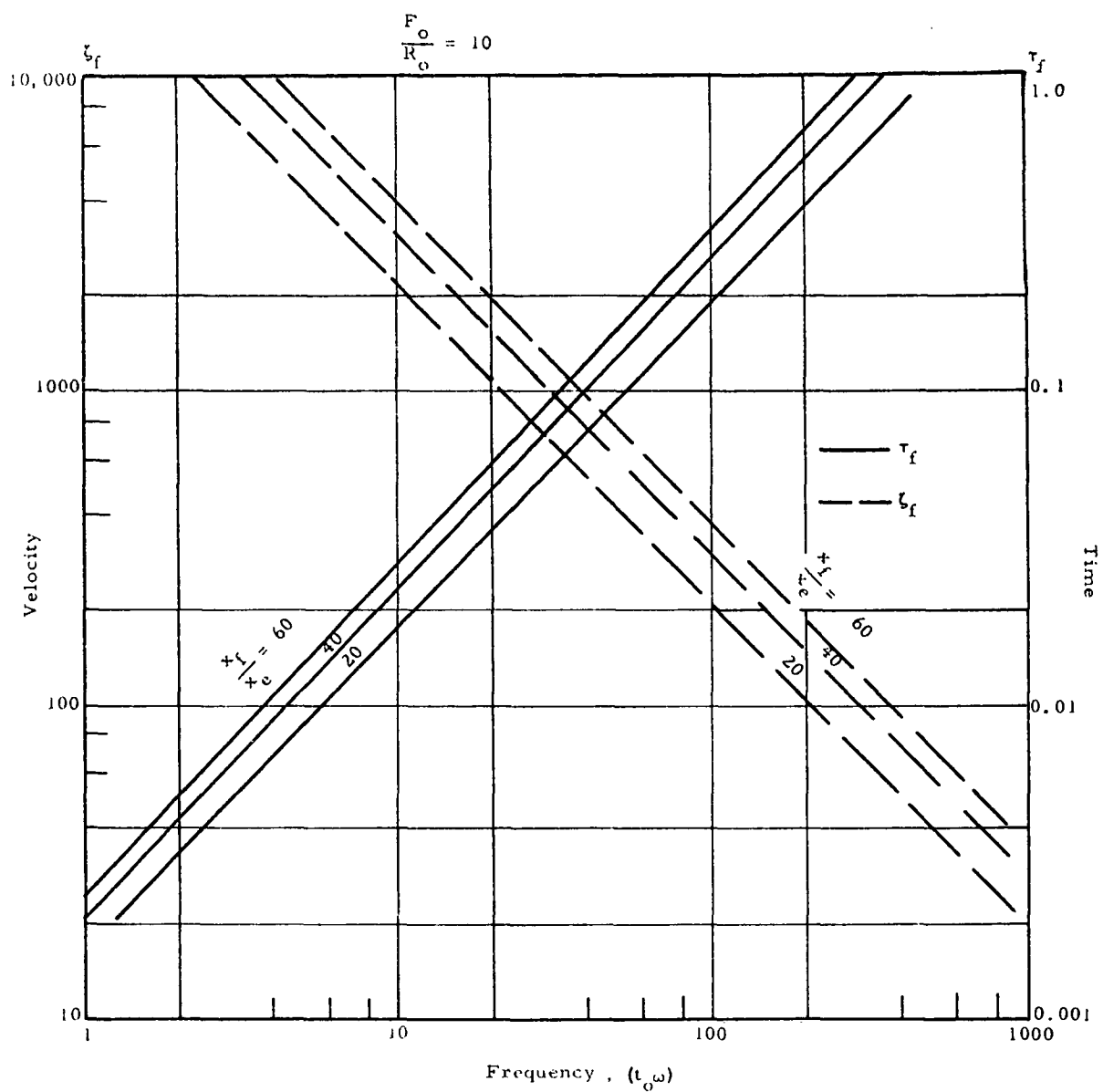


Figure 4.3 Motion of Mass At Failure ($\delta = 10$)

SECRET

SECRET

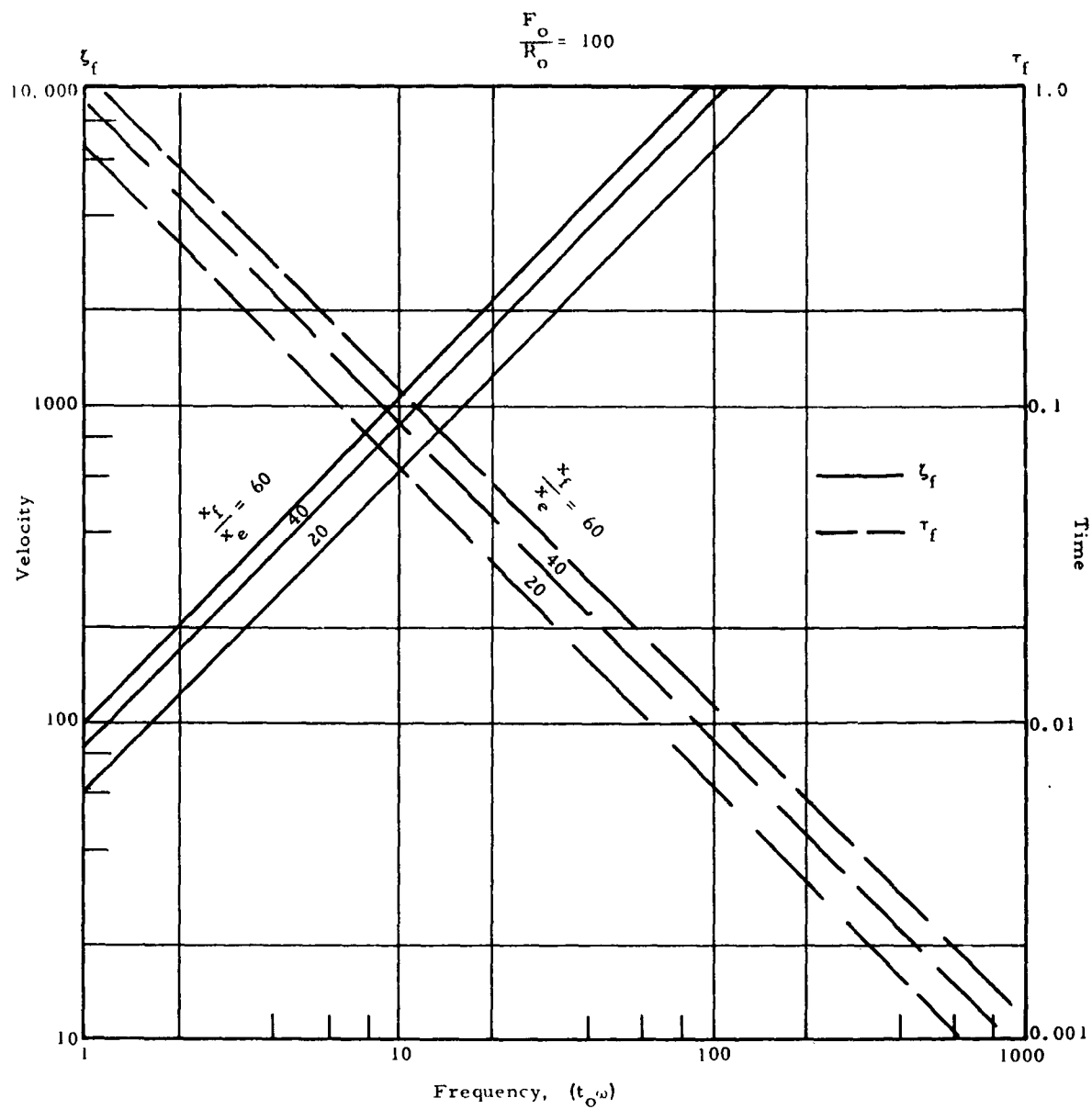


Figure 4.4 Motion of Mass At Failure ($\delta \approx 100$)

SECRET

SECRET

where

$$\begin{aligned} b &= \text{width of member,} & L &= \text{span, and} \\ d &= \text{depth of member} & R_o &= \text{total uniform load on beam.} \\ \sigma_y &= \text{yield strength of material,} \end{aligned}$$

The deflection of such a member is,

$$x_e = \frac{R_o L^3}{6.4 E b d^3} = \frac{37 \times 10^3 \times 1728}{64 \times 10^6 \times (1.25)^3} = 1.52 \text{ in.}$$

The circular frequency of a simply supported rectangular beam is

$$\begin{aligned} \omega &= \frac{\pi^2}{L^2} \sqrt{\frac{E}{12} \frac{d^2 g}{\gamma}} \\ &= \frac{\pi^2}{100} \sqrt{\frac{10^6 (1.25) (1.25) 32.2}{12 \times 40}} = 31.8 \text{ rad/sec} \end{aligned}$$

where

$$\begin{aligned} E &= \text{Young's Modulus} \\ g &= \text{gravitational constant} \\ \gamma &= \text{density of material} \end{aligned}$$

The 10-psi overpressure region corresponds (Ref. 20) to a 2-psi dynamic pressure and a positive phase duration of 0.7 sec. The drag loading acting on the siding is then

$$F_o = b L (2) c d = b \times 10 \times 12 \times 2 \times 1 = 240 b$$

Therefore

$$\delta^2 = \frac{F_o}{R_o} = \frac{240 b}{37 b} = 6.5$$

and,

$$\beta = \omega t_o = 31.8 \times 0.7 = 22.3$$

SECRET

SECRET

Then if we interpolate between Fig. 4.2 and 4.3 and assume a fracture displacement of $\rho = 20$,

$$\zeta'_f = 300$$

$$\tau_f = 0.125$$

or, in dimensional form,

$$\dot{x} = \frac{x_e}{t_o} \zeta'_f = \frac{1.52 \times 300}{12 \times 0.7} = 54 \text{ fps}$$

$$t_f = 0.125 \times 0.7 = 0.09 \text{ sec.}$$

Obviously, this fracture velocity is dependent on the value assigned to ρ . Therefore, the reasonably accurate prediction of this velocity does not establish the validity of our model. It does show, however, that reasonable values of ρ lead to an acceptable prediction.

The subsequent motion of the debris fragments is studied in Chapter Five. The significance of debris velocity at fragmentation x_f and time of fragmentation t_f are also considered in subsequent chapters.

SECRET

SECRET

CHAPTER FIVE
DEBRIS TRANSPORT BY BLAST WINDS

The motion of a particle acted on by the nuclear blast wind is considered with the fracture velocity and time of fracture forming the initial conditions of the transport problem. The model used here assumes that the force acting on the particle is proportional to the square of the relative velocity between the particle and air. The blast parameters are assumed to be constant over the range of travel of the debris, and it is further assumed that the effective lengthening of positive phase duration (i. e. , the so-called time correction) which is due to the debris motion in the direction of shock propagation can be handled by a simple adjustment of positive phase duration. These assumptions reduce the problem to the solution of a one-parameter nondimensional differential equation. Thus, much can be learned about the general behavior of flying debris. Without these two assumptions, it would be necessary to treat each weapon yield and placement as a separate problem and no general observations could be made.

The general equations are derived and numerical solutions for many problems of interest are obtained. The application of these results to specific debris problems is outlined and general observations regarding the behavior of flying debris are detailed.

5.1 General Treatment of Problem

The motion of a piece of debris of arbitrary shape is first considered and then the problem is reduced to the point where the vertical and horizontal motions are uncoupled.

Consider the motion of the body shown in Fig. 5.1. By equilibrium,

$$\begin{aligned} m\ddot{x} &= f_x \\ m\ddot{y} &= f_y \\ j\ddot{\phi} &= f_y (x_1 - x_0) + f_x (y_0 - y_1) \end{aligned} \tag{5.1}$$

SECRET

SECRET

where

m = mass of body

j = product of inertia of body.

ϕ = coordinate describing orientation of body with respect to x-y coordinate system

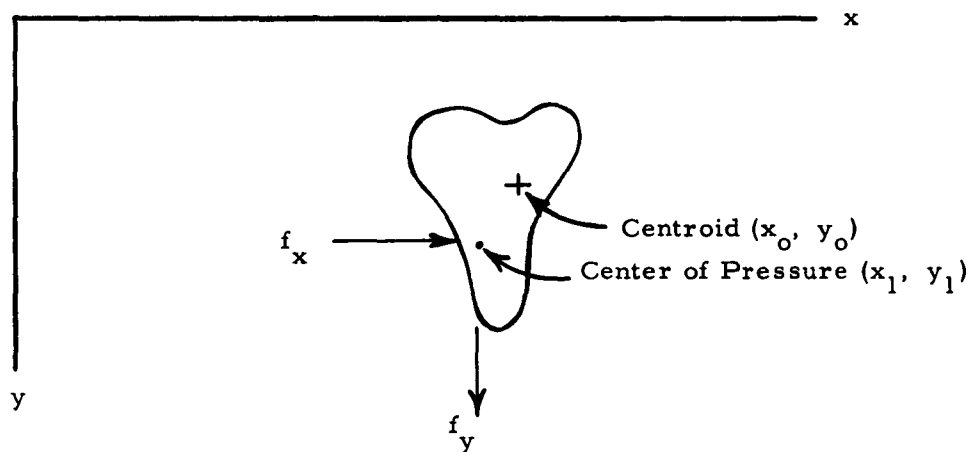


Figure 5.1 General Debris Particle

The forces (f_x, f_y) are given by

$$f_x = k \frac{a C_d(x)}{2} \rho (u - \dot{x})^2 \quad (5.2)$$

$$f_y = k' \frac{a C_d(y)}{2} \rho \dot{y}^2 + mg$$

SECRET

SECRET

where,

$a_{x,y}$ = projected area in x and y direction

$C_{d(x,y)}$ = drag coefficient in x and y direction

ρ = mass density of air

u = particle wind velocity

g = gravitational constant

$$k = \begin{cases} +1; & u \geq \dot{x} \\ -1; & u < \dot{x} \end{cases}$$

$$k' = \begin{cases} +1; & \dot{y} < 0 \\ -1; & \dot{y} > 0 \end{cases}$$

Equations (5.1) are coupled, in general, by the dependence of aC_d on ϕ . Consideration of this dependency on ϕ makes exact descriptions of debris particles necessary. We are, however, concerned with the gross behavior of groups of debris particles of many different sizes and shapes rather than a detailed treatment of specific shapes. Thus we restrict our attention to those particle shapes where aC_d does not depend on ϕ and, hence, the equations of motion Eq. (5.1) are uncoupled. The trajectory dispersion which is due to ϕ -variation of aC_d can be investigated separately, thereby leading to a dispersion function which can be superposed on the results determined for the simpler problem considered here. Thus we consider only the first of Eq. (5.1). The following nondimensional parameters are defined:

$$\tau = \frac{t}{t_o}$$

$$0 = U_o t_o \rho \frac{aC_d}{m}$$

$$\zeta = \rho \frac{aC_d}{m} x \quad (5.3)$$

SECRET

SECRET

where

U_0 = characteristic air particle velocity such that

$$U = U_0 h(t)$$

t_0 = characteristic time of air particle velocity-duration curve

Substituting Eq. (5.3) into Eq. (5.1) we have

$$\zeta'' = \frac{k}{2} \left[\theta h(\tau) - \zeta' \right]^2 \quad (5.4)$$

where the prime denotes differentiation with respect to τ .

Equation (5.4) is a Riccati-type nonlinear differential equation which can be linearized by the substitution,

$$\zeta' = -k \frac{s'}{s} \quad (5.5)$$

Equation (5.5) reduces Eq. (5.4) to

$$s'' + k \theta h s' + \theta^2 \frac{h^2 s}{2} = 0 \quad (5.6)$$

However, closed-form solutions can be obtained to Eq. (5.6) only for special classes of the forcing function $h(\tau)$ (e. g., $h(\tau) = \text{constant}$ leads to second-order differential equations with constant coefficients; $h(\tau) = h_0/\tau$ leads to a Cauchy-Euler equation). The blast-induced wind is unfortunately not one of these forms. Therefore, we are forced to integrate Eq. (5.4) numerically. The case of $h = 0$ is of interest and the solution for this case can be readily derived from Eq. (5.5) and (5.6) to be,

$$\zeta = -k \log(\tau + C_1) + C_2$$

and note that,

$$\zeta' = \frac{-k}{\tau + C_1} \quad (5.7)$$

SECRET

SECRET

where C_1 , C_2 are constants of integration to be determined from initial conditions.

Observe from Eq. (5.7) that the velocity only asymptotically goes to zero. This can be explained by recognizing that when the surrounding air is motionless the retarding force acting on the particle is proportional to the square of the particle velocity. Thus, solutions based on our model will predict infinite displacement at an infinite time. It will be necessary to place a maximum time limitation on the debris particles flight based on the time required for it to hit the ground.

Numerical solutions to Eq. (5.4) are obtained for a wide class of problems of interest. Specifically, results are obtained for a wide range of aerodynamic coefficients, various initial conditions, and a few possible negative phase representations of the blast induced winds.

We must consider first the form of the wind loading $h(\tau)$, however. The particle velocity can be related to the dynamic pressure q by,

$$q = \frac{1}{2} \rho u^2. \quad (5.8)$$

During the positive phase of the loading, the dynamic pressure is

$$q = q_0 e^{-2\tau} (1 - \tau)^2. \quad (5.9)$$

When Eq. (5.9) is substituted into (5.8)

$$u = \sqrt{\frac{2q_0}{\rho}} e^{-\tau} (1 - \tau). \quad (5.10)$$

Thus, in terms of Eq. (5.4),

$$u = u_0 h(\tau)$$

SECRET

SECRET

where, for $0 < \tau < 1$

$$u_o = \sqrt{\frac{2q_o}{\rho}} \quad (5.11)$$

$$h(\tau) = e^{-\tau} (1 - \tau).$$

Variation of $\sqrt{\frac{2q_o}{\rho}}$ and t_o with weapon yield and distance from ground zero is shown on Fig. 5.2 and 5.3.

Relatively little data are available regarding the negative phase dynamic pressure (i. e., wind blowing toward ground zero). We have taken the negative phase dynamic pressure to be of the form,

$$\bar{q} = \bar{q}_o \sin \pi \frac{(\tau - 1)}{k} \quad (5.12)$$

so that wind ceases at $\tau = 1 + k$.

It can be argued that, to have ambient conditions at ground zero some time after detonation of the weapon, the area under the positive phase dynamic pressure curve must equal the area under the negative phase curve. This results in,

$$K = 0.34 \frac{q_o}{\bar{q}_o} \quad (5.13)$$

The wave form descriptions apply to a fixed location with reference to ground zero. The debris particles, however, move with respect to ground zero. Note that u_o and t_o vary with distance from ground zero so that, to exactly represent the forcing function, the particle and pressure wave motion must be followed. As an example, consider a particle originally located at (x) and assume the pressure wave arrives at this location at time $t = 0$. The peak particle velocity and positive phase duration are $u_o(x)$ and $t_o(x)$. At some later time (Δt) the particle has moved to $(x + \Delta x)$; the pressure wave arrives at this location at some time less than (Δt) , say $(\Delta t')$. Thus, the particle velocity at this time and at the actual debris location is given by,

SECRET

SECRET

SECRET

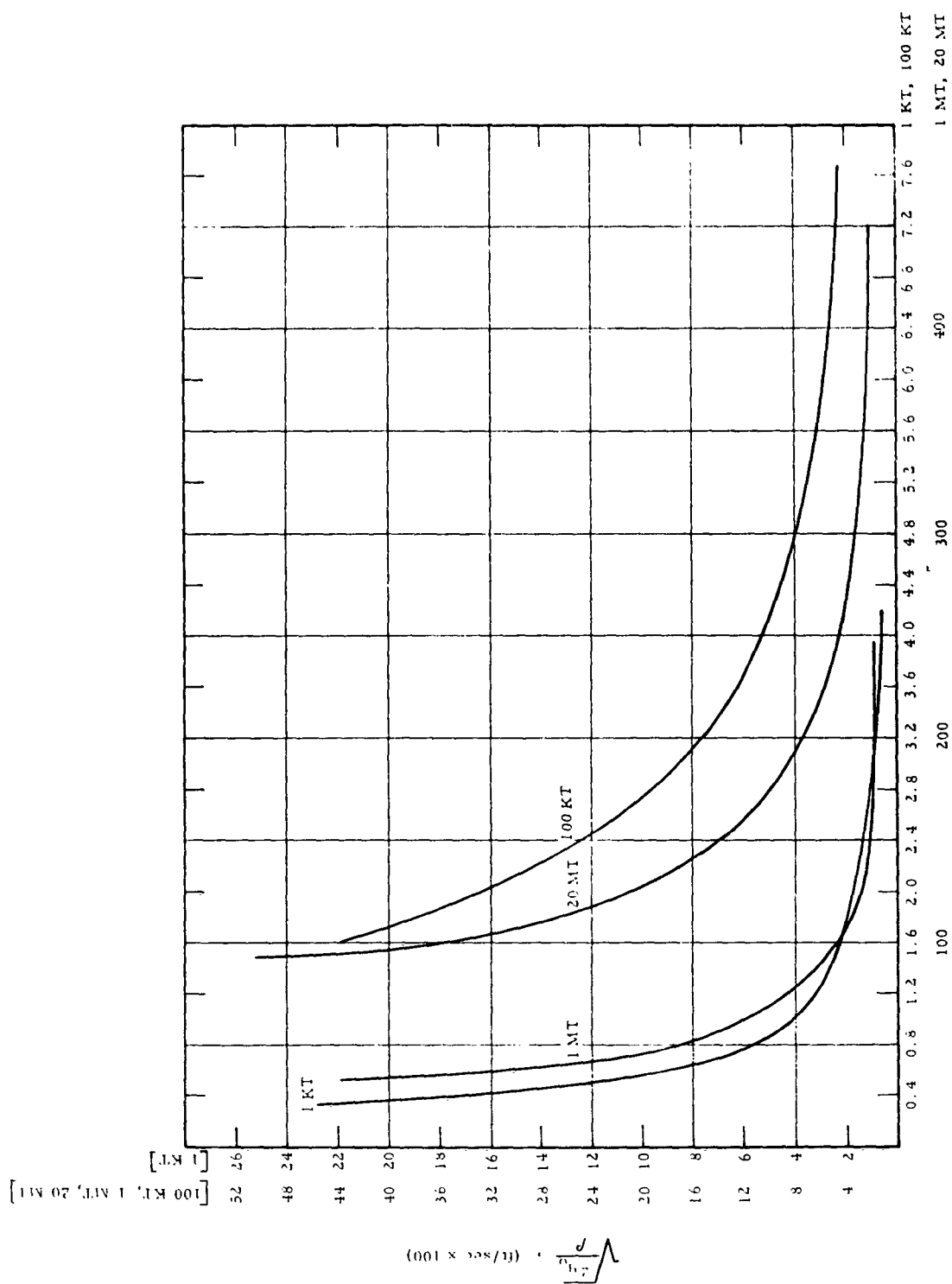


Figure 5.2 Dynamic Pressure Variation

SECRET

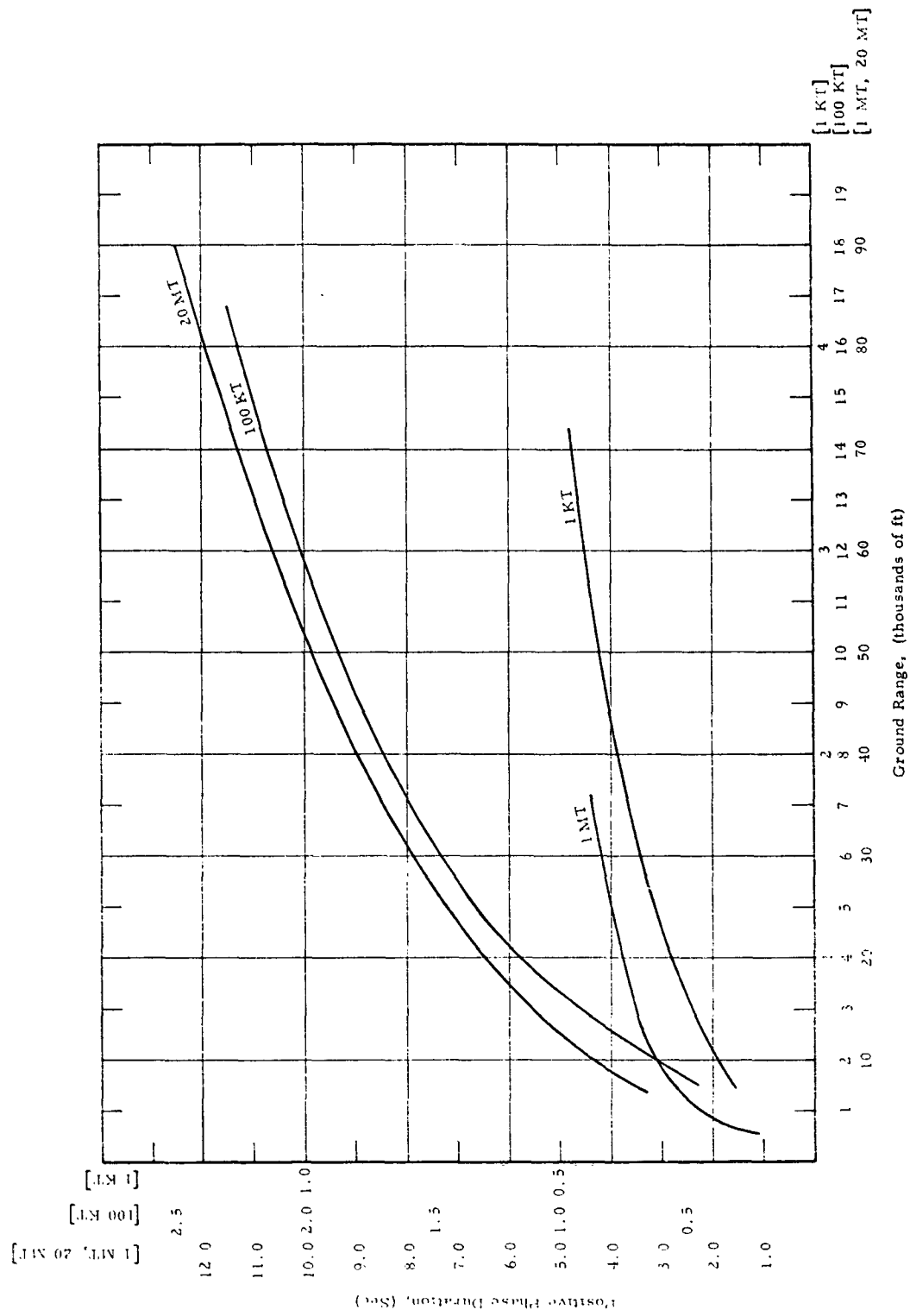


Figure 5.3 Positive Phase Duration

SECRET

SECRET

$$u = u_o \exp \left[- (\Delta t' - \Delta t) / t_o \right] \left[1 - \left(\frac{\Delta t' - \Delta t}{t_o} \right) \right] \quad (5.14)$$

where

u_o , t_o are evaluated at $(x + \Delta x)$.

Equations (5.14) cannot be used to represent the particle velocity unless attention is restricted to specific weapon yields. Thus, to retain generality in the study, this refinement is not considered here. Note, however, that the form of Eq. (5.14) is well suited for inclusion in a numerical integration routine such as will be used to integrate the equations of motion.

5.2 Numerical Results

A computer program was written for the UNIVAC 1105 digital computer to numerically integrate Eq. (5.4). The Runge-Kutte-Gill numerical integration procedure was used. Solutions were obtained for zero initial conditions of the debris particle, and a complete range of realistic aerodynamic coefficients. The effect of negative phase wind on particle motion is also considered. It was the objective of this numerical analysis to obtain results in a form such that mass-velocity curves can be constructed for a given attach condition and location from a source of debris.

5.2.1 Zero Initial Conditions Excluding a Negative Phase

We consider first the piece of debris that is free to move, acted upon only by the positive phase wind loading. Solutions are obtained for values of θ in the range $0.1 < \theta < 10$. These are presented in Fig. 5.4 and 5.5 in the form of curves of nondimensional velocity versus nondimensional distance from original debris source. Time is included as a parameter on these curves.

As stated, attention has been limited to the horizontal motion of a particle. These solutions are invalid if the particle hits the ground. Therefore, the time parameter on the curves of Fig. 5.4 and 5.5 can be used to establish the range of validity of the results based on initial height

SECRET

SECRET

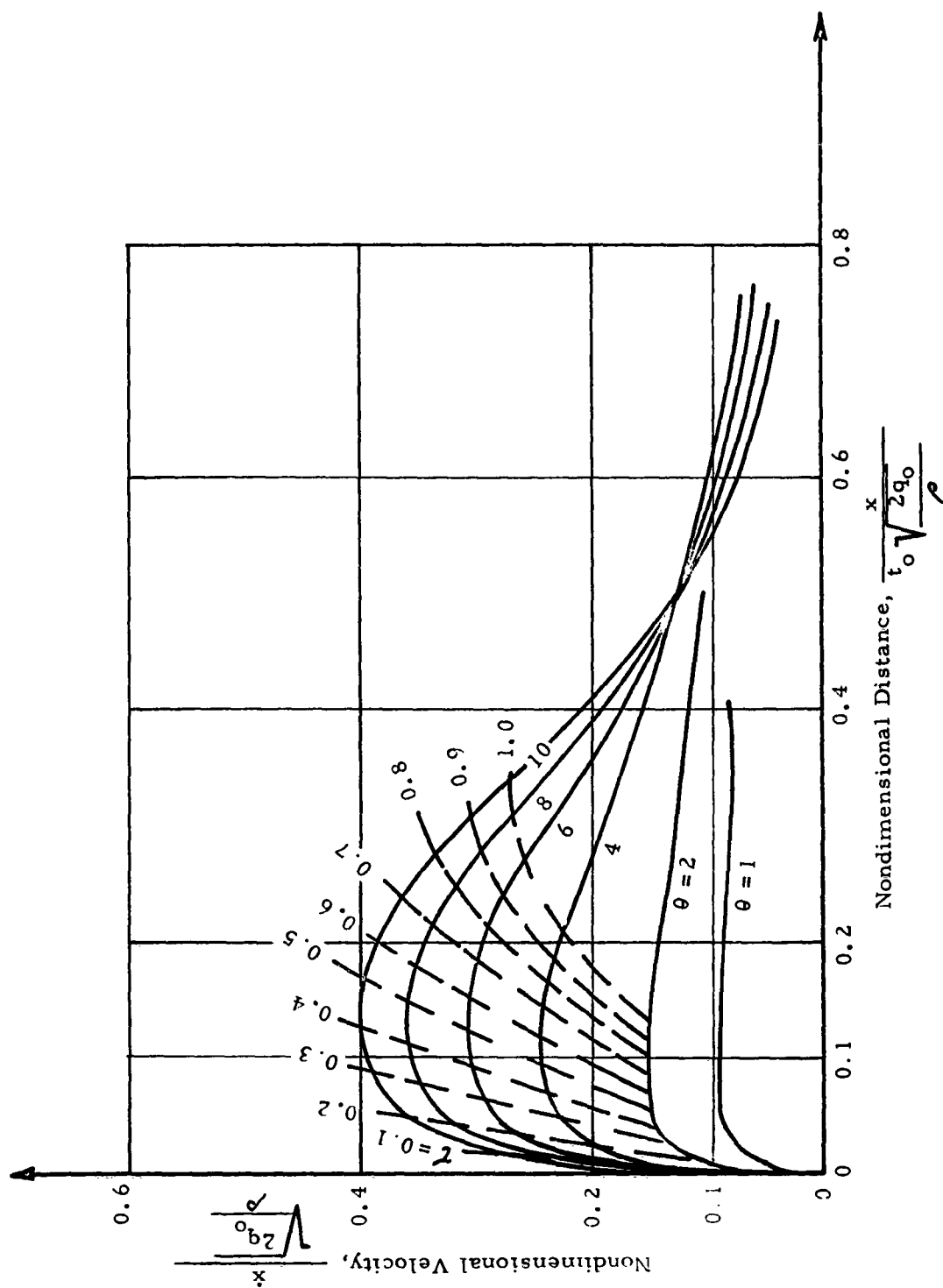


Figure 5.4 Velocity-Distance Plot For $2 < \theta < 10$

SECRET

SECRET

h of the debris and any vertical component of velocity v_o imparted to the particle. Based on elementary kinematics the particle will hit the ground at

$$t = \frac{v_o}{g} \left[1 + \sqrt{\frac{2hg}{v_o^2} + 1} \right]. \quad (5.15)$$

An interesting observation regarding the size and shape of particle that will travel the furthest can be drawn from these data. To this end, the parameter θ is plotted as a function of distance for various times on Fig. 5.6. Note that the results of this analysis predict that the size and shape (i. e., aerodynamic coefficient) of the piece of debris that travels furthest depends on the length of time required for the debris to hit the ground surface. The longer this time, the larger the piece of debris that travels furthest. This could explain the apparent randomness in high-explosive debris data.

5.2.2 Zero Initial Conditions Including a Negative Phase

As has been mentioned, little data which quantitatively describes the negative phase wind are available. A sine wave is assumed for the wave shape of the negative phase wind, and the area under the sine wave is made to equal the area under the positive phase wind. In this study, the peak negative phase wind velocity was taken to be 0.02 times the peak positive phase wind velocity.

Velocity-distance curves for this negative phase wind are given in Fig. 5.7 and 5.8. The sharp departure of these results from those for zero negative phase is of considerable interest. Given sufficient time, all particles move toward ground zero. Of course, these required times of flight are sufficiently long that this reversal of velocity can probably not be realized for most practical cases. There have been instances, however, at the Nevada test site where pieces of structural debris were found closer to ground zero than the place they started. Of course, structural debris requires some time to be ripped from the structure so that a portion of the positive-phase wind impulse is not effective on the piece of debris. Thus the velocity reversal occurs sooner and can be realized with practical times of flight.

SECRET

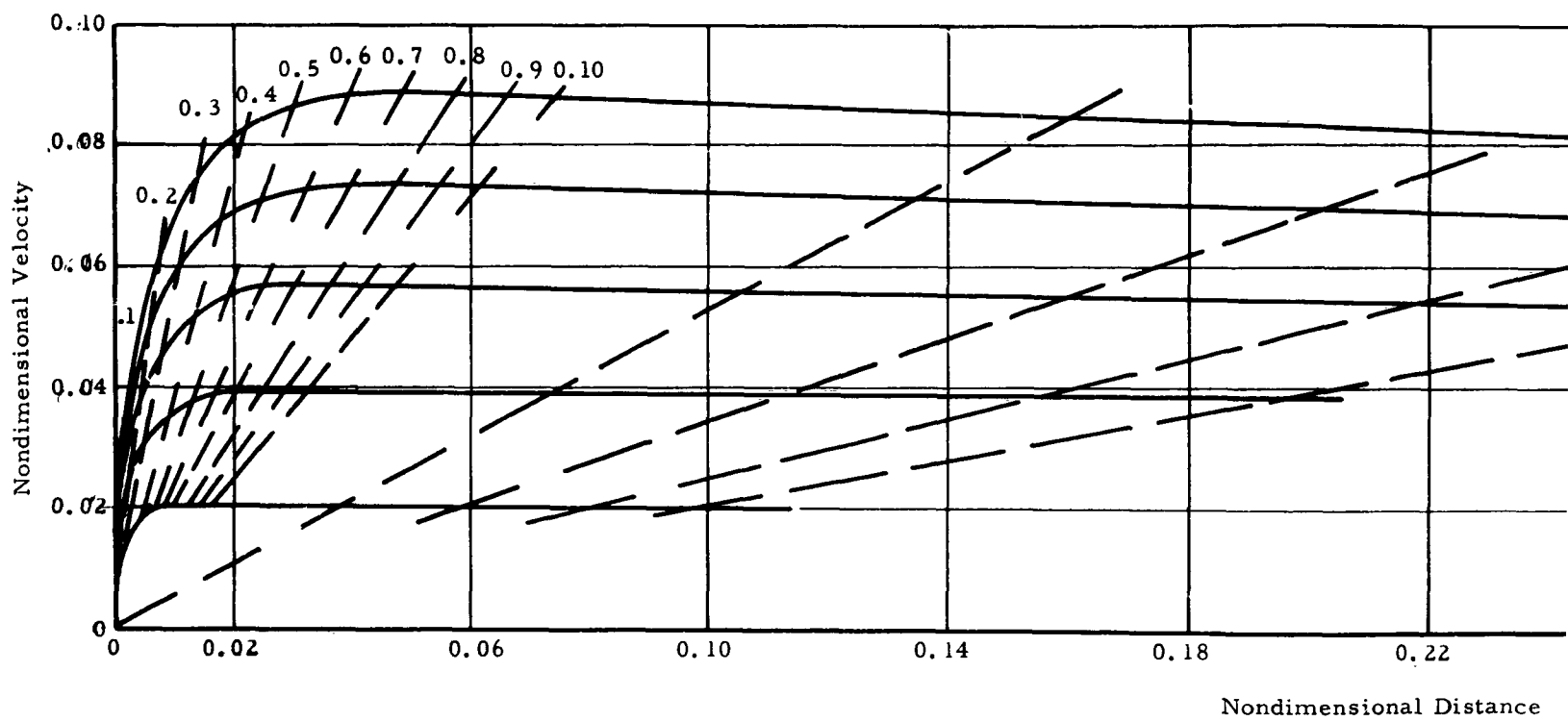
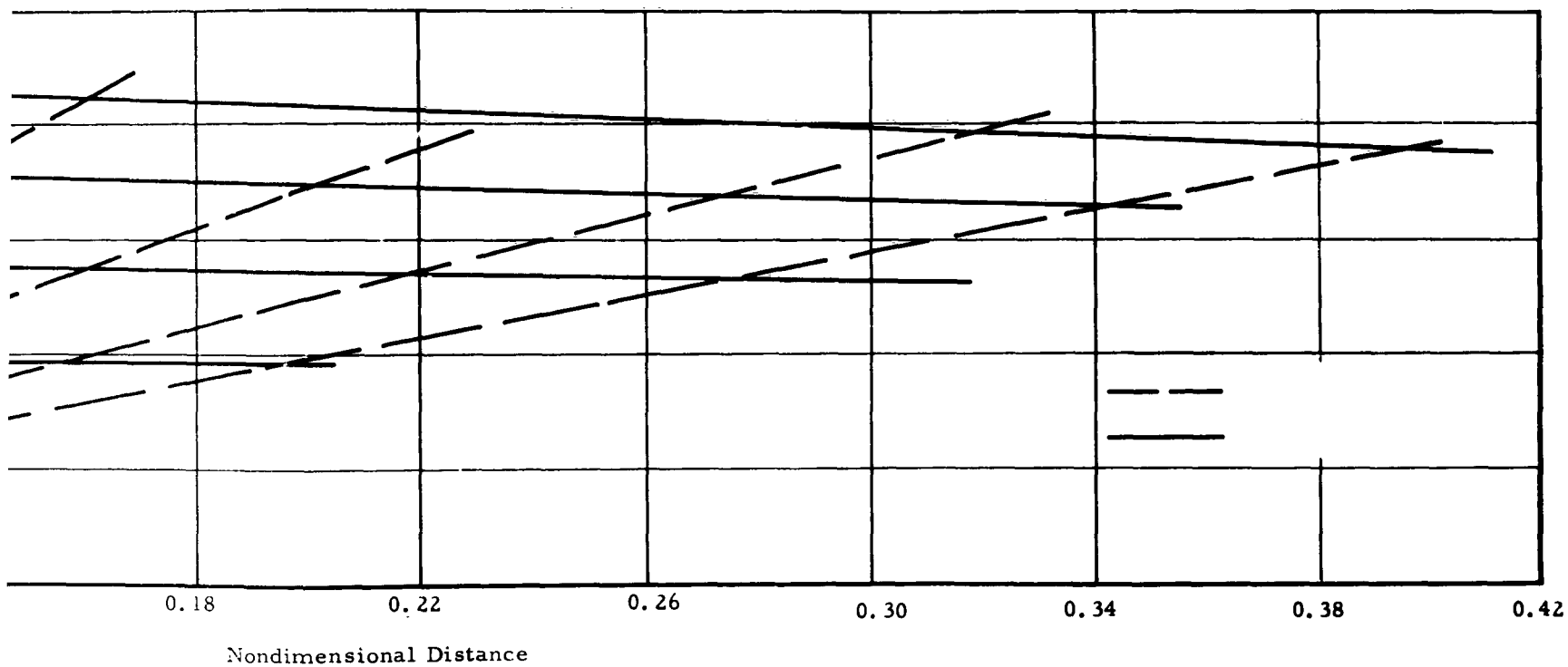


Figure 5.5 Velocity-Distance Plot for $0.2 < \theta \leq 1$

SECRET

SECRET

2



SECRET

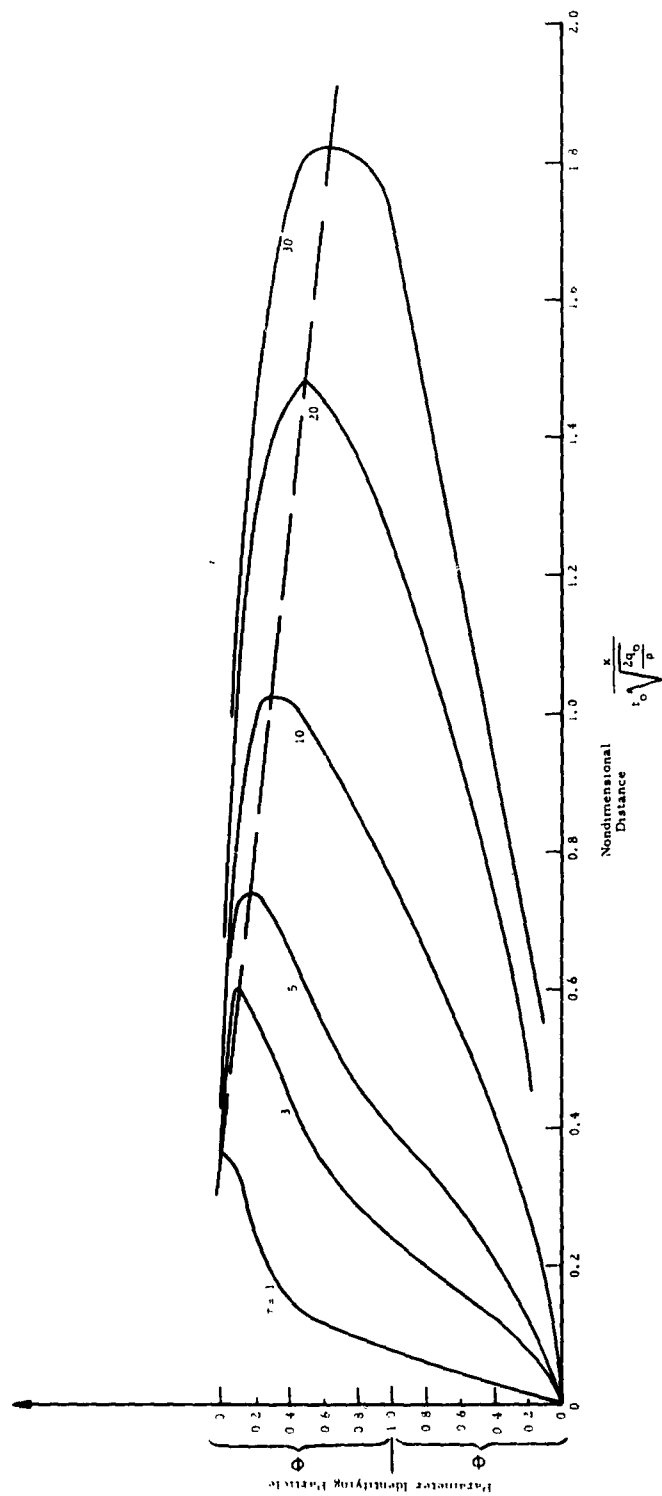


Figure 5.6 Comparison of Distance Traveled by Different Size Particles

SECRET

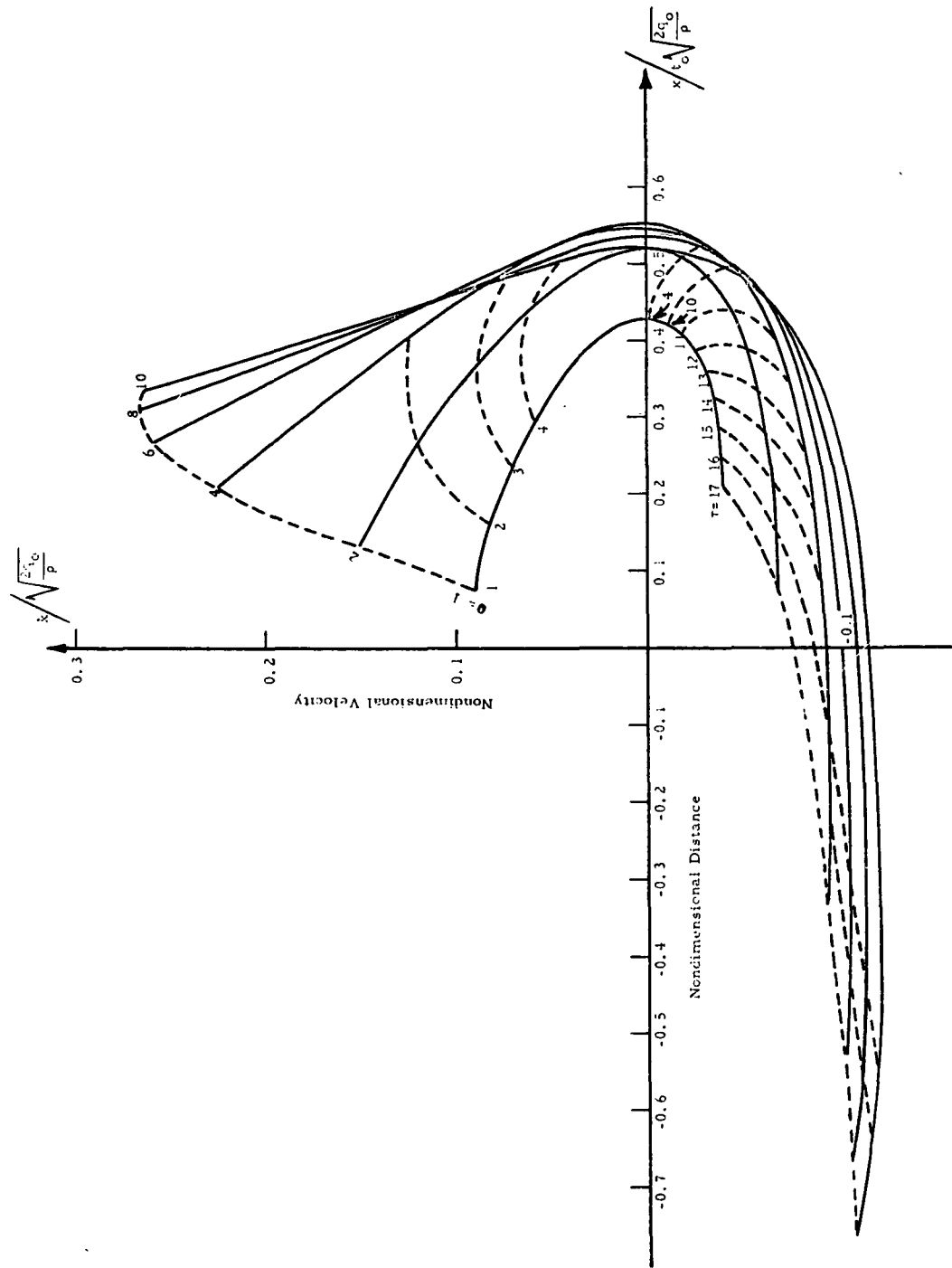


Figure 5.7 Velocity-Distance Plot Including Negative Phase For $1 < \theta < 10$

SECRET

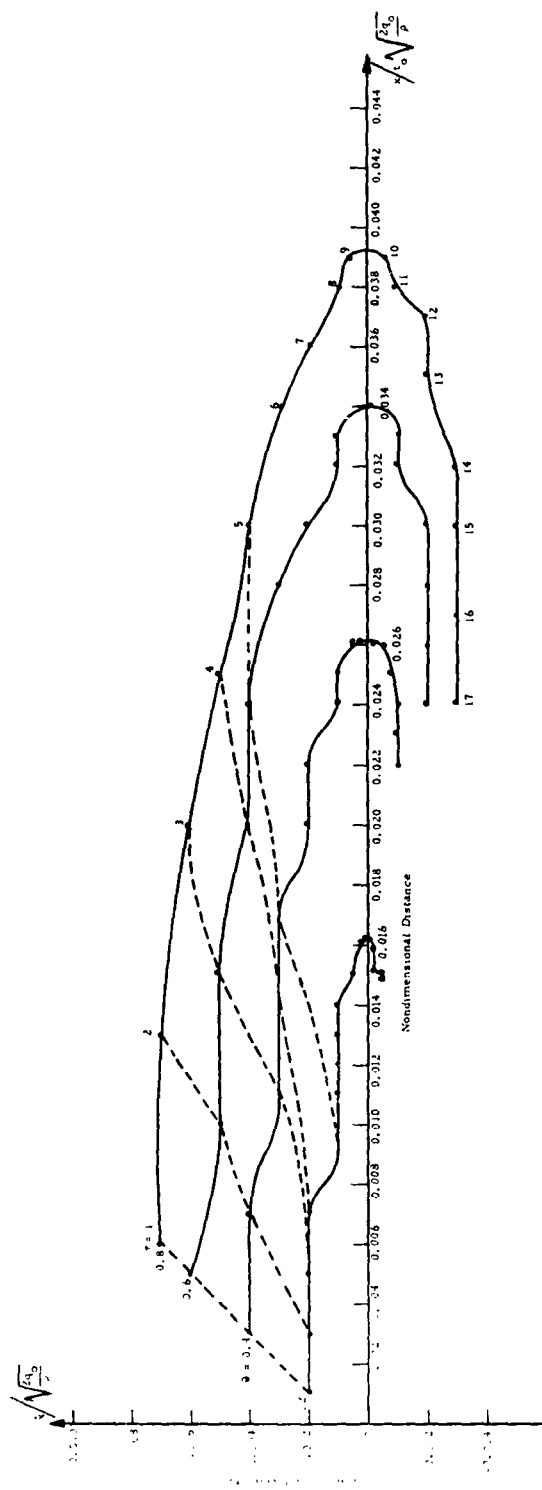


Figure 5.8 Velocity-Distance Plots Including Negative Phase For $0.2 < \theta < 1$

SECRET

SECRET

5. 2. 3 Effect of Initial Conditions

The results described in the previous two sections must be modified to include the initial condition of failure time and velocity at failure. One could accomplish this modification by constructing velocity-distance curves (similar to Fig. 5. 4 and 5. 5) for all combinations of initial velocity and failure times of practical interest. Such an approach is impractical because of the number of combinations that would need to be considered. Rather, an approximate method of modifying the existing data (Fig. 5. 4 and 5. 5) to include the initial conditions must be found.

Two approximations are made in this regard, and the errors induced in practical problems are evaluated. First, the failure time condition is approximated by applying to the debris particle a negative impulse equal to the area under the dynamic pressure time curve from time $t = 0$ to time $t = t_f$. Mathematically then, the apparent initial impulse is given in nondimensional form as,

$$\zeta'_a = \zeta'(0) - \frac{\rho a^2 C_d^2 t_o^2 q_o}{m^2} \int_0^{\tau} e^{-2\tau} (1 - \tau)^2 d\tau$$

where

ζ'_a = apparent initial velocity

$\zeta(0)$ = actual initial velocity.

when this is carried out the apparent initial velocity becomes,

$$\zeta'_a = \zeta(0) - \frac{\theta^2}{4} \left[e^{-2\tau_f} \left(\tau_f^2 - \tau_f + \frac{1}{2} \right) - \frac{1}{2} \right].$$

The failure time τ_f is always small ($\tau_f < 1$) so that if $e^{-2\tau_f}$ is expanded in a power series and τ_f^2 is neglected in comparison to τ_f . Then,

$$\zeta'_a = \zeta(0) - \frac{\theta^2}{2} \tau_f \quad (5. 16)$$

results.

SECRET

SECRET

The second approximation made was to assume that the particle motion resulting from the apparent initial velocity acting alone can be superposed on the particle motion which is due to the blast wind, to give the resulting motion of the particle which is due to the combined effect of initial velocity and blast wind. By virtue of the general dependence of air friction on the square of the relative velocity, the two results are superposed by the square root of the sum of the squares. The motion which is due to the initial velocity can be determined from Eq. (5.7) subject to the initial conditions

$$\begin{aligned}\zeta(0) &= 0 \\ \zeta'(0) &= \zeta'_a\end{aligned}$$

The solution of Eq. (5.7) is then,

$$\begin{aligned}\zeta'_1 &= \frac{-k\zeta'_a}{\zeta'_a\tau - k} \\ \zeta_1 &= -k \log \left(\frac{\tau\zeta'_a - k}{-k} \right) .\end{aligned}\tag{5.17}$$

For the case of interest,

$$k = \begin{cases} -1 ; \zeta'_a \geq 0 \\ +1 ; \zeta'_a < 0 \end{cases}$$

In summary, the procedure for applying these results to a real problem is as follows:

- (1) Compute ζ'_a from Eq. (5.16)
- (2) Compute $\zeta'_1(\tau)$ and $\zeta_1(\tau)$ from Eq. (5.17) for the range of τ 's of interest.
- (3) Use Fig. 5.4 or 5.5 to determine $\zeta'_2(\tau)$ and $\zeta_2(\tau)$ for zero initial conditions for the same values of τ as above.

SECRET

SECRET

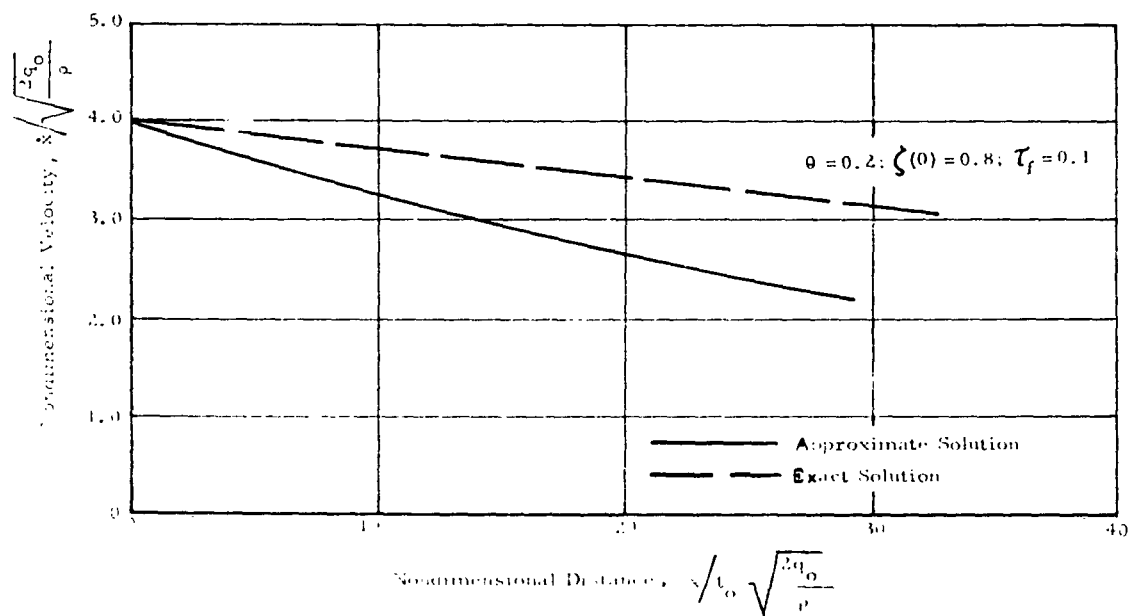
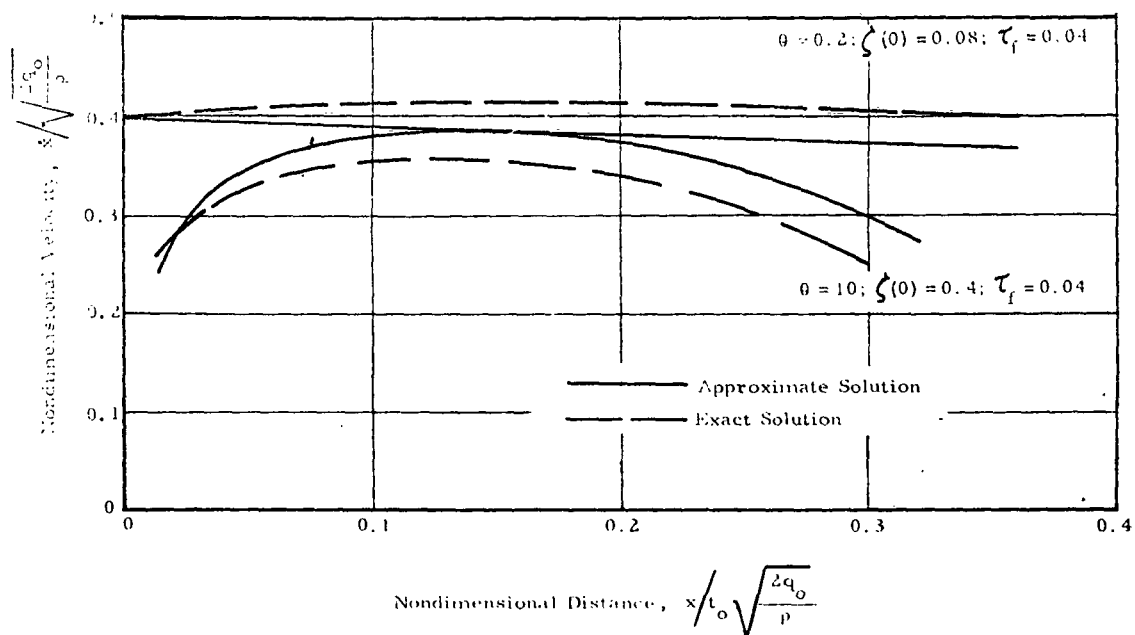


Figure 5.9 Comparison of Exact and Approximate Method of Handling Initial Conditions

SECRET

SECRET

(4) At each given (τ) compute the final results,

$$\zeta = \sqrt{-k(\zeta_1)^2 + (\zeta_2)^2}$$

$$\zeta' = \sqrt{-k(\zeta_1')^2 + (\zeta_2')^2}$$

The validity of these results was tested by comparing the approximate results obtained by the above procedure to "exact" solutions obtained by numerically integrating Eq. (5.4) subject to the initial conditions. These comparisons are presented on Fig. 5.9. It can be noted that the results are reasonably accurate in view of the over-all accuracy requirements of the debris prediction problem. For very high initial velocities (e. g. , velocity displacement curves convex downward with a high initial peak) the approximate analysis is not very good. However, this problem is probably not very important when considering the nuclear environment.

SECRET

SECRET

CHAPTER SIX
VULNERABILITY OF FIELD TROOPS TO TREE DEBRIS

A supplementary study involving vulnerability of field troops to casualties from tree debris caused by a nuclear explosion in the proximity of a forest, instituted upon recognition of needs by the Office of the Chief of Engineers for estimating the hazards to engineer and field troops, was undertaken. Making certain simplifying assumptions (i. e. , zero-strength tree limbs, plane blast wave loading, unobstructed trajectories, and that a hit upon personnel by a tree limb is a casualty), tree limbs are followed in their trajectories from the time of shock loading to their impact with the ground. The safe distance may fall either inside or outside the forest and both cases are treated.

Results of this analysis show that for the lower yields (1 KT, for example) a uniform horizontal translation of all branches is obtained since trajectories become vertical with an attendant small vertical drop, and the appearance of the area in front of the forest up to the "safe distance" would be similar to that of a forest floor after all of the branchwood were allowed to drop vertically. Basically similar behavior is observed for the higher yields where trajectories terminate before they become vertical (20 MT, for example), with the exception that the highest branches of the first few rows of trees pile up in a lower density than those following the closer-in trajectories.

6.1 Previous Studies

The results of previous studies on tree vulnerability which have influenced our assumptions concerning debris (Ref. 21, 22, and 23) are as follows:

- (1) Results of OPERATION UPSHOT-KNOTHOLE indicated that stands of 145 Ponderosa pines of heights 50 to 75 ft offered no attenuation of peak overpressure or dynamic pressure.

SECRET

SECRET

- (2) That low burst heights were found to cause more damage to trees than large burst heights when the peak dynamic pressure was the same.
- (3) OPERATION CASTLE indicated no pressure attenuation from the trees in natural tree stands. Damage predictions for two weapon yields compared favorably with the observed damage.
- (4) Damage to broadleaf stands is principally limb breakage and defoliation with occasional breakage of the main stem or uprooting.
- (5) The deflection and breakage of trees in the stand on UPSHOT-KNOTHOLE Shot 9 were approximately twice the values predicted on the basis of calculations of the first maximum deflection. By including the probability of breakage during the second maximum deflection under the negative phase, the predictions were brought into agreement with experimental values.
- (6) Trees are drag structures. The best parameter with which drag can be correlated is the dry weight of the crown.
- (7) In OPERATION SNAPPER, it was observed that when stem breakage occurred the stems broke at the tree base.
- (8) A considerable amount of data describing the mechanical and aerodynamic properties of tree stems and crowns is available. Almost none exist for the isolated branches.

6.2 Problem Approach

Consider first the case shown in Fig. 6.1 where the troops are dispersed outside of the forest.

SECRET

SECRET

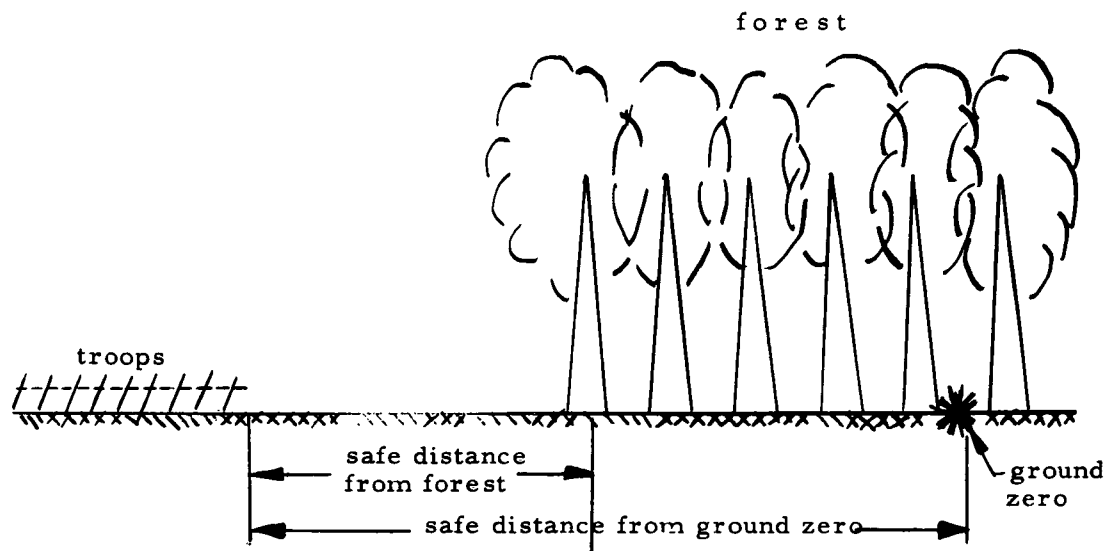


Figure 6.1 Relative Positions of Troops, Forest, and Ground Zero

Our objective is to determine a conservative or upper bound "safe distance" rather than tackle the enormous task of finding the "smallest safe distance". To accomplish this goal, we made the following assumptions:

- (1) Ground burst is assumed for all attack conditions since it produces the most severe tree damage.
- (2) Trees are assumed not to attenuate static or dynamic pressures.
- (3) The trajectories of the flying branches are considered to be unobstructed by the other branches and trees.
- (4) If any debris strikes an individual, he is assumed to be incapacitated.
- (5) The total "flight time" of a branch is considered to be equal to its free-fall time in a vacuum. This assumption turns out to be unimportant for yields no greater than 1 MT.

SECRET

SECRET

- (6) Positive wind phase is taken equal to the positive shock wave phase. They are approximately equal.
- (7) The branches travel the same horizontal distance as an air particle during the positive wind phase.

Assumption 7 is the most far-reaching and important on the list. Physically it corresponds to a branch which has zero strength, is completely diffraction insensitive, and which has an infinite acceleration coefficient. The acceleration coefficient is the product of projected area and drag coefficient divided by mass. Clearly, for tree branches this is a relatively large factor. Assuming the branches to be only drag sensitive is fairly good; assuming them to have zero strength is conservative but poor. The items tend to counteract one another.

If only drag forces were operative, it is quite clear that a particle of air would be transported further than a solid object. The questions arise when the solid object has an initial velocity; for example, particles originating as crater throwout. Such particles are not of concern here; however, it is conceivable that sufficient impulse is delivered to a branch to both sever it from the tree stem and give it an initial velocity greater than the peak particle velocity. In such a case the branch or any other particle would experience a deceleration resulting from a drag force opposing its motion. The high acceleration coefficient of a branch would quickly bring its velocity into coincidence with the particle or wind velocity behind the shock front.

During the negative phase, the reversed winds decelerate any airborne objects. Particles having sufficiently high acceleration coefficients have their forward motion reversed. In the spirit of conservatism, the negative phase is neglected.

At low pressure levels (2.4 psi), the stems of trees remain standing and offer considerable interference to the flight of branches. However, at pressures of interest (between 5 and 30 psi) the stems are all broken and probably create no interference to flying debris. Because the shock wave moves at a higher velocity than the winds behind it, there is a strong possibility that debris from remote trees travels ahead of debris

SECRET

SECRET

from trees closer in to ground zero.

The trajectories of the wind particles have been computed as described in Appendix H and the results are presented in Fig. 6.2. The following remarks are based on, or are concerned with, this figure.

- (1) Pressures over 30 psi are not included in trajectories since these pressures represent a greater hazard than the debris.
- (2) As the wind velocity drops to zero the trajectories become vertical. The curves for the 20-MT devices were terminated at about 255 ft of vertical drop since trees of greater height are not of interest.
- (3) The horizontal distance associated with the vertical tangent to the trajectories can be scaled approximately according to cube-root scaling; e. g. , $D/D_0 = (W/W_0)^{1/3}$ where D is the distance and W the yield.
- (4) In the cases where the trajectories become vertical with an attendant small vertical drop (e. g. , the case of the 1-KT device), a uniform horizontal translation of all the branches was obtained. This situation is illustrated in the sketch shown in Fig. 6.3. The appearance of the area in front of forest labeled "safe distance from forest" would be similar to that of a forest floor after all of the tree branchwood were allowed to drop vertically. This situation is illustrated in Fig. 6.4 and 6.5 for forests exposed to low pressure blasts.
- (5) In cases where the trajectories terminate before they become vertical (e. g. , the case of the 20-MT device), basically the same behavior as in the previous case was found, with the exception of the highest branches on the first few rows of trees. These branches pile up with a lower density than those following the closer-in trajectories. This situation is depicted in Fig. 6.6 where the final horizontal locations of branch centers

SECRET

SECRET

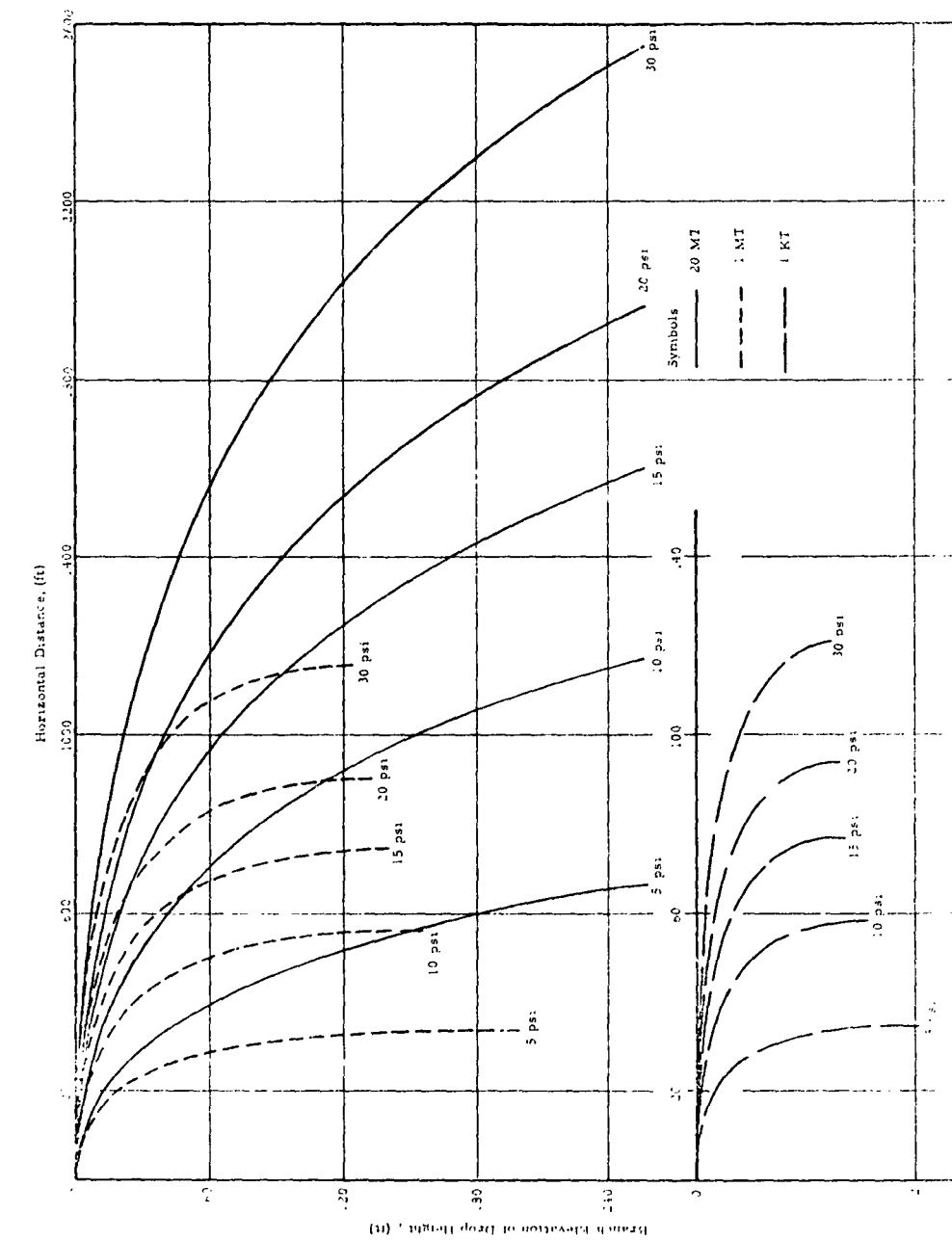


Figure 6.2 Wind Particle Trajectories During The Positive Phase of a Nuclear Blast

SECRET

SECRET

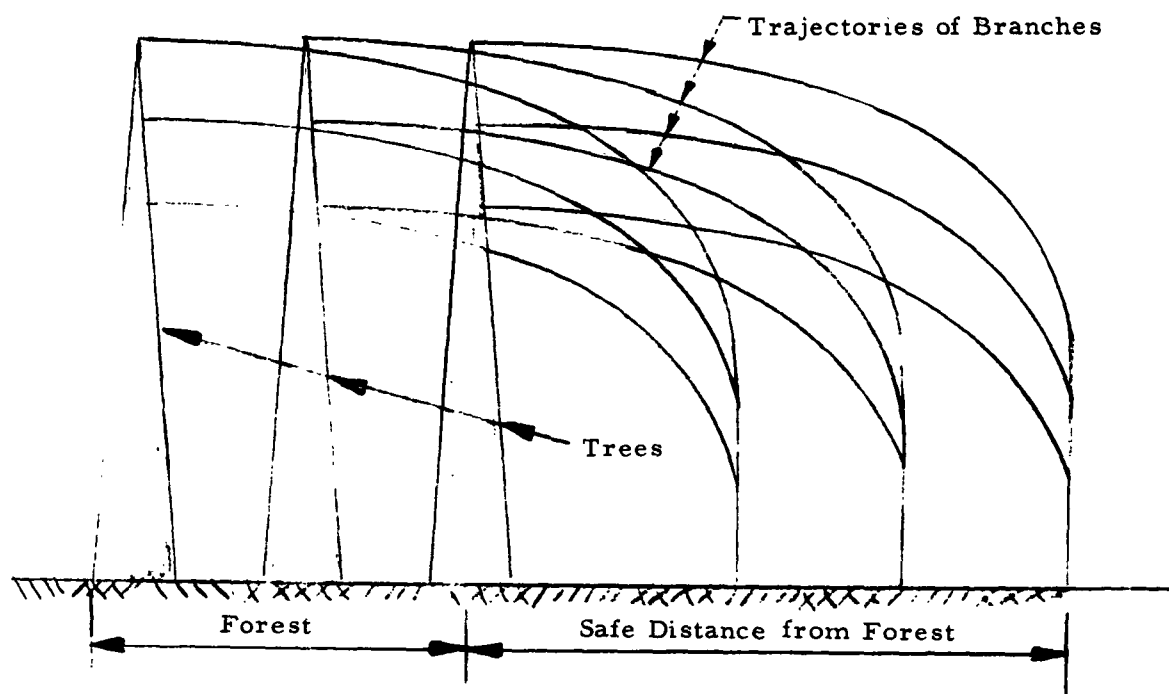


Figure 6.3 Trace of Branchwood for Low Yield Weapons

for various branch elevations in a typical forest are indicated. Each cross represents the branchwood in a 5-ft vertical distance along the tree stem. The most cursory examination of typical trees indicates that the limbs in the top 15 ft would completely cover the area surrounding the tree. Referring to Fig. 6.6, we find that "complete kill" is experienced for distances up to 1800 ft. Going from 1800 ft to 1880 ft, the density of limbs diminishes and 100 percent kill is not expected in this region. The precise determination of the kill probability in this 80-ft area is not warranted and in such case the safe distance from forest is set equal to the maximum trajectory (e. g. , 1880 ft).

SECRET

SECRET



Figure 6.4
Forest Stand After a Nuclear Explosion
(2.4 psi overpressure)



Figure 6.5
Forest Stand After a Nuclear Explosion
(3.8 psi overpressure)

SECRET

SECRET

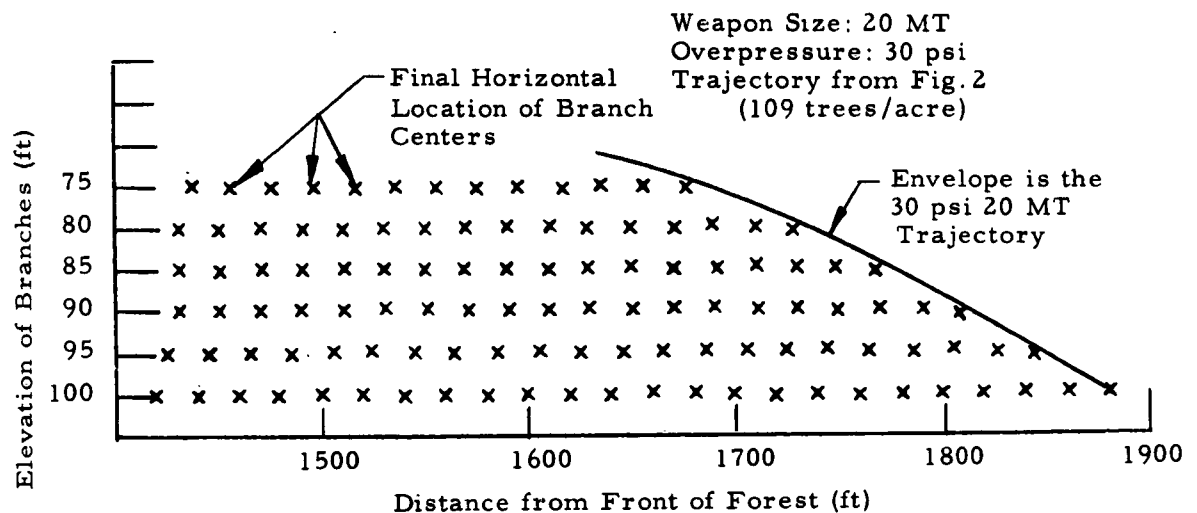


Figure 6.6 Horizontal Displacement of Tree Limbs

We now turn our attention to the very straightforward task of determining the safe distance from ground zero in a forest of infinite extent. In Table 6.1 we have reproduced a schedule of damage criteria for forests from the ART 6.24 of Reference 20. The damage level described in class D of this table represents the borderline condition for troop safety.

Table 6.1
DAMAGE CRITERIA FOR FORESTS

Damage Class	Nature of Damage	Equivalent Hurricane Wind Velocity, (mph)
A and B	Up to 90 percent of trees blown down; remainder denuded of branches and leaves. (Area impassable to vehicles and very difficult on foot.)	130-140
C	About 30 percent of trees blown down; remainder have some branches and leaves blown off. (Area passable to vehicles only after extensive clearing.)	90-100
D	Very few trees blown down; some leaves and branches blown off. (Area passable to vehicles.)	60-80

SECRET

SECRET

Table 6.2
SAFE DISTANCES TO PREVENT CASUALTIES FROM TREE DEBRIS

Yield of Weapon	Height of Tree, feet	Safe Distance Falls Inside of Forest	Safe Distance Falls Outside of Forest									
		Safe Distance from Ground Zero	Safe Distance from Ground Zero for Various Overpressures at the Front of the Forest, (yd)					Safe Distance from Forest for Various Overpressures at the Front of the Forest, (yd)				
			5 psi	10 psi	15 psi	20 psi	30 psi	5 psi	10 psi	15 psi	20 psi	30 psi
0.05 KT	20	311 - 376 yards	193	130	109	98	87	7	8	10	12	16
	40		200	136	113	100	87	14	14	14	14	15
	60		206	142	119	106	91	20	20	20	20	20
	80		213	149	126	113	98	27	27	27	27	27
	100		220	156	133	120	105	34	34	34	34	34
	120		226	162	139	126	111	40	40	40	40	40
	160		239	175	152	139	124	53	53	53	53	53
	200		253	189	166	153	138	67	67	67	67	67
0.1 KT	20	392 - 473 yards	241	164	137	123	108	7	10	12	15	19
	40		248	168	139	123	108	14	14	14	15	19
	60		254	174	145	128	109	20	20	20	20	20
	80		261	181	152	135	116	27	27	27	27	27
	100		268	188	159	142	123	34	34	34	34	34
	120		274	194	165	148	129	40	40	40	40	40
	160		287	207	178	161	142	53	53	53	53	53
	200		301	221	192	175	156	67	67	67	67	67
0.5 KT	20	670 - 809 yards	410	279	235	210	186	10	16	21	26	33
	40		414	279	235	210	186	14	16	21	26	33
	60		420	283	235	210	186	20	20	21	26	33
	80		427	290	241	211	186	27	27	27	27	33
	100		434	297	248	218	187	34	34	34	34	34
	120		440	303	254	224	193	40	40	40	40	40
	160		453	316	267	237	206	53	53	53	53	53
	200		467	330	281	251	220	67	67	67	67	67
1 KT	20	845 - 1021 yards	517	351	295	264	233	12	20	26	32	41
	40		519	351	295	264	233	14	20	26	32	41
	60		525	351	295	264	233	20	20	26	32	41
	80		532	358	296	264	233	27	27	27	32	41
	100		539	365	303	266	233	34	34	34	34	41
	120		545	371	309	272	233	40	40	40	40	41
	160		559	385	323	286	246	54	54	54	54	54
	200		572	398	336	299	259	67	67	67	67	67
1 MT	20	8,448 - 10,208 yards	5,119	3,430	2,856	2,526	2,182	68	121	165	203	265
	40		5,137	3,460	2,895	2,574	2,243	86	151	204	251	326
	60		5,147	3,475	2,916	2,599	2,273	96	166	225	276	356
	80		5,153	3,485	2,927	2,612	2,290	102	176	236	289	373
	100		5,157	3,490	2,934	2,620	2,299	106	181	243	297	382
	120		5,160	3,493	2,937	2,623	2,302	109	184	246	300	385
	160		5,163	3,495	2,938	2,623	2,302	112	186	247	300	385
	200		5,163	3,495	2,938	2,623	2,302	112	186	247	300	385
20 MT	20	22,932 - 27,709 yards	13,792	9,128	7,505	6,553	5,528	81	146	200	247	325
	40		13,821	9,179	7,575	6,639	5,640	110	197	270	333	437
	60		13,842	9,215	7,624	6,699	5,718	131	233	319	393	515
	80		13,858	9,243	7,662	6,746	5,779	147	261	357	440	576
	100		13,871	9,267	7,693	6,786	5,829	160	285	388	480	626
	120		13,882	9,287	7,720	6,818	5,872	171	305	415	512	669
	160		13,901	9,304	7,764	6,872	5,940	190	322	459	566	737
	200		13,916	9,345	7,799	6,914	5,994	205	363	494	608	791

SECRET

SECRET

The wind velocities 60-80 mph are associated with overpressures of 1.7 - 2.2 psi. The distance from ground zero for a surface burst at which these pressures are realized can be scaled from Fig. 3.94a in Reference 20.

6.3 Results

Based on the approaches described in this chapter, we have computed the safe distances to prevent casualties from tree debris for various conditions and presented them in Table 6.2. Whenever the safe distance from the forest, which was computed from the maximum trajectory range, fell below the associated tree height, the tree height was used as the safe distance from the forest. At the pressure levels considered the trees will be blown over; hence, the stems and not the branchwood represents the more severe hazard under these conditions.

SECRET

SECRET

CHAPTER SEVEN
VULNERABILITY OF FIELD TROOPS TO THROWOUT DEBRIS
FROM CRATERING AND STREAM-BED CHARGES

This study was undertaken to define a "safe line" for positioning engineer or field troops in the proximity of very-low yield nuclear cratering and stream-bed charges, based on debris criteria. Since no reliable analytical method of predicting crater throw out debris was available, the problem involved locating and utilizing experimental data on debris distribution under variations in the major controlling parameters - weapon yield, depth of burst, and soil characteristics. A number of sources were found to include data concerning crater throw out debris, some including variations in parameters (Ref. 2, 24, 25, 26, 27, 28, 29). Of these, two modes of measurement are used: the U.S. Geological Survey (Ref. 24) expresses debris distribution in terms of fragment sizes; the Suffield Experiment Station (Ref. 27) presents debris data in terms of a real density; and the Boeing Airplane Company (Ref. 25 and 26) presents data in both ways.

The procedure described here for estimating the throwout environment about cratering charges is based primarily on the U.S. Geological Survey reports of cratering tests in basalt in Area 18 at the Nevada test site (Ref. 24). Contours were plotted by USGS defining ground ranges for several average particle sizes. Average ranges for various fragment sizes were derived from these plotted contours and related to the yield and depth of burst. Nomographic methods are included whereby the average debris distance can be obtained for a wide range of weapon yields, depths of burst, and fragment size in basalt. A multiplication factor is introduced to convert the average ground range to maximum ground range, based on observations of the ray-like patterns noted in the USGS report on basalt craters. Data from the earlier Panama Canal series of tests were used to develop correction factors in converting the estimates for basalt to estimates for other soil media (Ref. 30). Likewise, debris measurements for cratering tests in marine muck, conducted as part of the Panama Canal series of experiments, were used to provide estimates of debris distance for streambed charges.

SECRET

SECRET

7.1 Method of Solution

In general, the debris beyond the crater lip has been observed to conform to the following two expressions;

$$\rho = \frac{C_1}{x^{n_1}} \quad (7.1)$$

and

$$D = \frac{C_2}{x^{n_2}} \quad (7.2)$$

where

ρ = areal density in weight of debris per unit area

D = fragment size

x = distance from ground zero

C_1, C_2 = constants

n_1, n_2 = exponents

Data which verify Eq. 7.1 are available (Ref. 2, 25, 26, and 27). Data which verify Eq. 7.2 are also available (Ref. 2 and 26).

Equations 7.1 and 7.2 comprise the basis for two different sets of relationships which can be used for determining safe line distances.

Certain question regarding the use and validity of Eq. 7.2 must remain. First, there is the greater tendency for fragments which travel greater distances to break into smaller fragments when they hit the ground. Therefore, even if all fragments are of equal size at takeoff, a decrease in particle size for increased distance would still be witnessed. Secondly, when air resistance is considered, it can be reasoned that, in general, large particles will travel further than small particles. Of course, there are other considerations such as the origin of different-sized particles relative to the point of burst, which lend reasonability to the observed distribution. It is not known which consideration is most important. In future tests, it would be desirable to consider the occurrence of impact breakage, since the criteria for safety involves the fragment characteristics before impact rather than after impact.

SECRET

SECRET

Let us now consider the criteria for the determination of a safe line ground range. The Armed Services Explosives Safety Board has used a 1-lb fragment as being capable of producing a fatal injury. If the safety criteria were established considering any injury less than fatal as safe, then if material density is known it is possible to use Eq. 7.2 to find the safe line ground range.

To apply the safety criteria to Eq. (7.1), consider the area covered by an average soldier laying flat on the ground. For a given areal density, the most severe situation is that in which all of the material landing in the area covered by the soldier were lumped into a single fragment. The distance at which the areal density is such that would require this fragment to be equal to the critical weight (e. g. , 1 lb) is the safe line ground range.

The one-pound fragment considered here is only an example. The actual size of fragment selected is a function of the probability of injury which is considered desirable. A much smaller fragment size might be selected if velocities were high.

When a criterion for determining the equipment damage capabilities of fragments is developed, it will also be possible to apply Eq. (7.1) and (7.2) to equipment.

Before any problems can be solved, we must find the functional relationship between the constants C and n , and the independent blast parameters. These parameters consist of yield, depth of burial, and soil characteristics. A fourth parameter, geological conditions, is also important (Ref. 24). It is very difficult, however, to evaluate geological factors, especially in military situations, and these will therefore not be considered as a parameter. Let us first attempt to develop relationships between the three blast parameters and the C and n constants for the distribution in fragment size.

7.2 Fragment Size Distribution Method

Ross B. Johnson (Ref. 24) has used maps to present data concerning throw out from a series of high explosion craters in basalt. Contour lines of equal average particle size for 1.0-ft and 0.5-ft diameter particles

SECRET

SECRET

are presented. (See Fig. 7.1, for example.) This information is used to obtain a first approximation of the relation between C , n , and the blast parameters. It must be emphasized at this point that the relations developed here are only first approximations.

Data from eight charges of 1000 lb TNT and three charges of 40,000 lb TNT exploded at various depths are tabulated in Table 7.11. The areas within the contour lines of each map were measured and the radii of circles of equivalent areas calculated. Each radius so calculated is termed the "area mean distance for particles of given size". Accepting the size distribution law,

$$x = \frac{C}{D^n} \quad (7.3)$$

where Eq. (7.3) is simply a modification of Eq. (7.2), the area mean distance was plotted as a straight line on a log-log plot (Fig. 7.2). The slopes of the curves n and the coefficients C were found and tabulated in Table 7.1. Table 7.1 expresses C in scaled form. The resulting data were then used in plotting Fig. 7.3 and 7.4. Figure 7.3 is a plot of the Distribution Law Exponent, n , vs scaled depth of burial, $d/W^{1/3.5}$, and Fig. 7.4 is a plot of scaled distribution law coefficient, $c/W^{1/3.5}$, vs scaled depth of burst, $d/W^{1/3.5}$.

A scaling factor of 3.5 was found to produce the best fit. Its use agrees with data presented by R. B. Vaile of Stanford Research Institute (Ref. 31). Figure 7.5 shows the Vaile curves of crater radius vs yield for different materials. The curve for sandstone yields a scaling exponent of 3.6. Since Johnson's data are for basalt it may be expected that they also have a scaling coefficient in the vicinity of 3.6, hence, 3.5.

Note that both curves of Fig. 7.3 and 7.4 have the general appearance of an inverted parabola, similar to the curves of scaled crater radius and scaled crater volume versus scaled depth of burial found in many references on cratering. Notice on Fig. 7.4 that not all points fit the curve closely. At first glance one might expect an ellipse. However, the results of the 1000-lb TNT shots are encouraging. Each data point for the 1000-lb shots represents two shots whereas each point for the 40,000-lb shots

SECRET

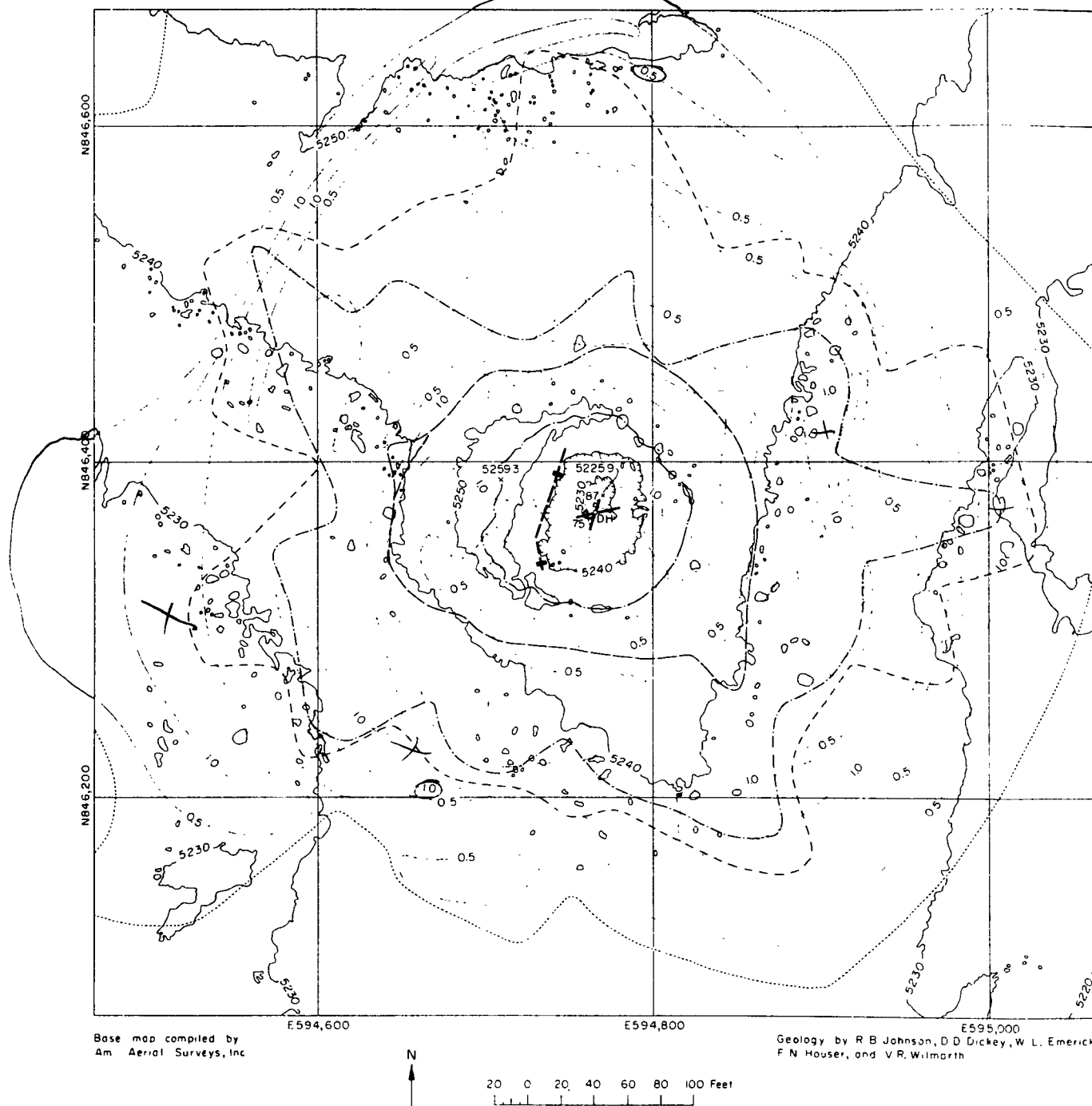


Figure 7.1

High Explosion Crater 13 (40,000 pounds), Buckboard Mesa,
Nevada Test Site, Nye County, Nevada

SECRET

SECRET

2

EXPLANATION



Strike and dip of joints
Pre-explosion joints mapped in drill hole



Strike and dip of surface joints
Joints activated by explosion-position inferred



Crest of crater rim



Outer edge of crater rim



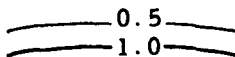
Outer limit of area entirely covered by
fragments of all sizes



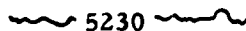
Outer limit of area one-half covered by
fragments of all sizes



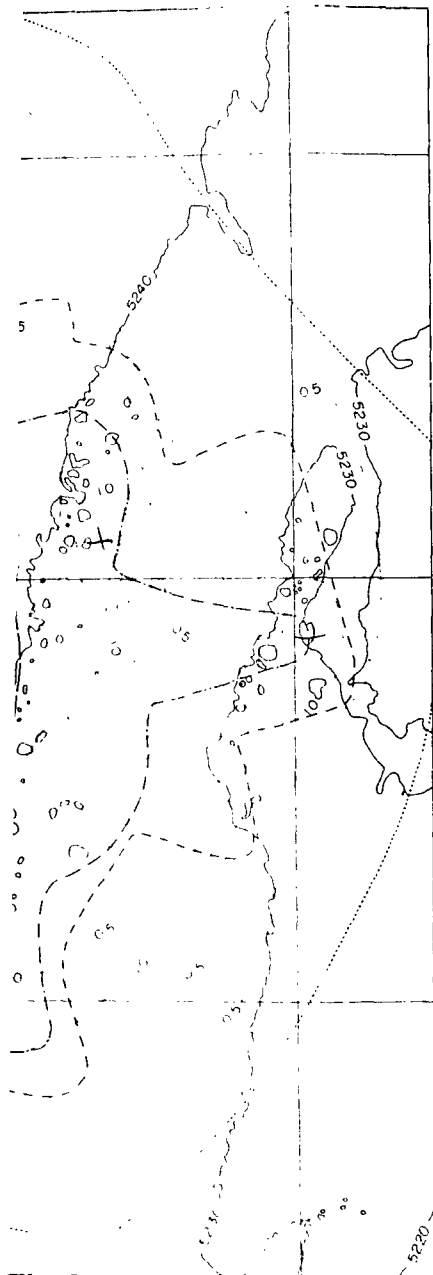
Outer limit of fragments of one-foot or
greater maximum dimension



Contour lines of equal average fragment size
Only contours for average size of 0.5 and
1.0 foot fragments are shown



Post-explosion topographic contours (by Am. Arial Surveys)
Interval 10 feet. Datum is sea level



E595700

Geology by R. H. Johnson, L. D. Ockey, W. L. Emerick,
F. N. Houser, and C. R. Wilmouth

SECRET

Table 7.1
DEBRIS DISTANCES FOR CRATERING TESTS IN BASALT

Crater Number	Charge Weight, W, (lb TNT)	Depth of Charge (ft)	Area Mean Distance of 0.5-ft Diam Fragments, (ft)	Area Mean Distance of 1.0-ft Diam Fragments, (ft)	Average of Mean Diam for 0.5-ft Fragments, (ft)	Average of Mean Diam for 1.0-ft Fragments, (ft)	Scaled Depth of Charge $d/3.5\sqrt{W}$	Scaled Coefficient $c/3.5\sqrt{W}$
2	1,000	20	32.1	18.2	34.8	17.2	2.0	2.39
7	1,000	20	37.4	17.5				
3	1,000	15	33.9	16.8	46.4	20.6	1.5	2.88
8	1,000	15	58.8	24.4				
4	1,000	10	45.6	18.2	41.6	16.0	1.0	2.22
9	1,000	10	37.5	13.8				
5	1,000	5	33.5	11.9	32.6	10.7	0.5	1.49
10	1,000	5	31.7	9.5				
11	40,000	25.6	33.9	15.1	33.9	15.1	.75	0.73
12	40,000	42.8	34.8	15.1	34.8	15.1	1.25	0.73
13	40,000	59.8	57.0	28.8	57.0	28.8	1.75	1.39

Note: x_{avg} = average mean distance

W = blast yield in lb TNT

d = depth of burial

SECRET

SECRET

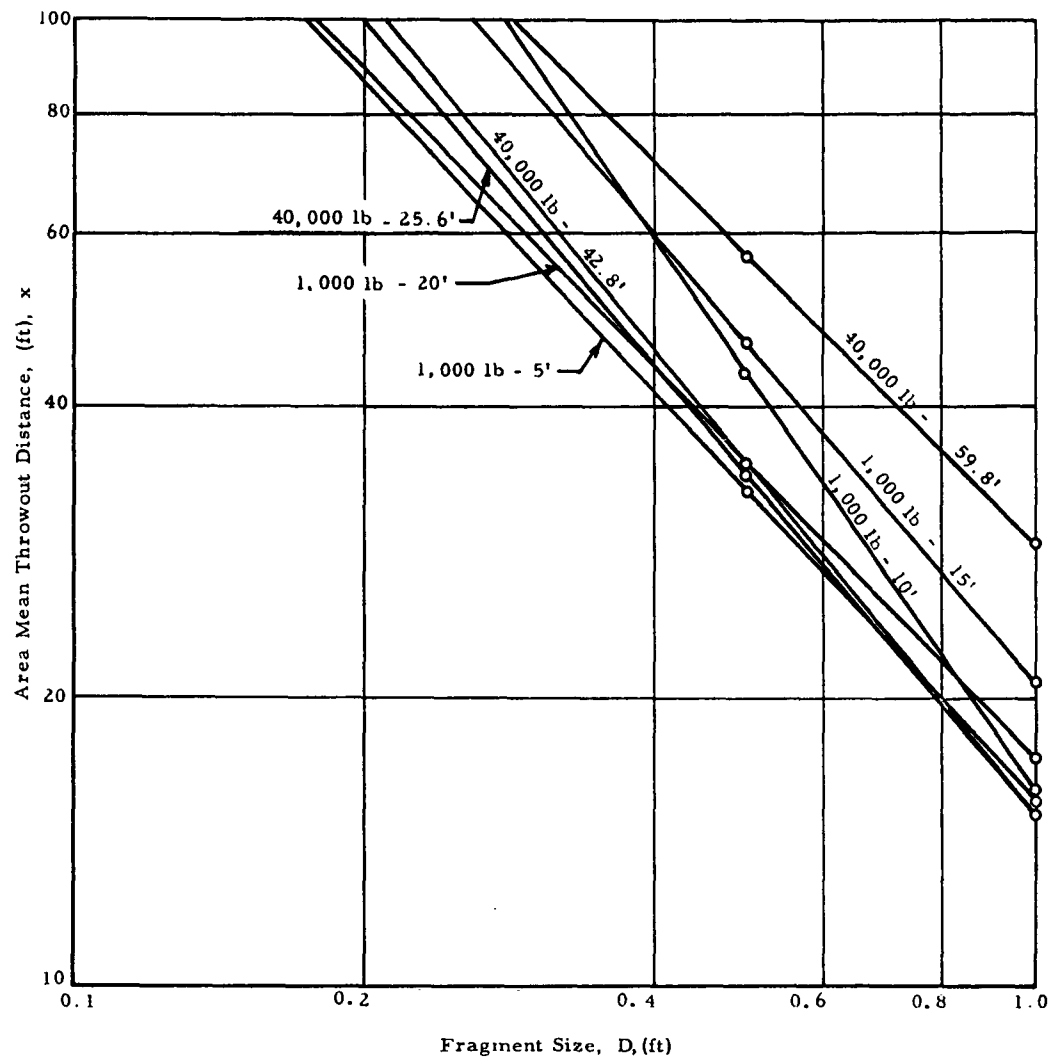
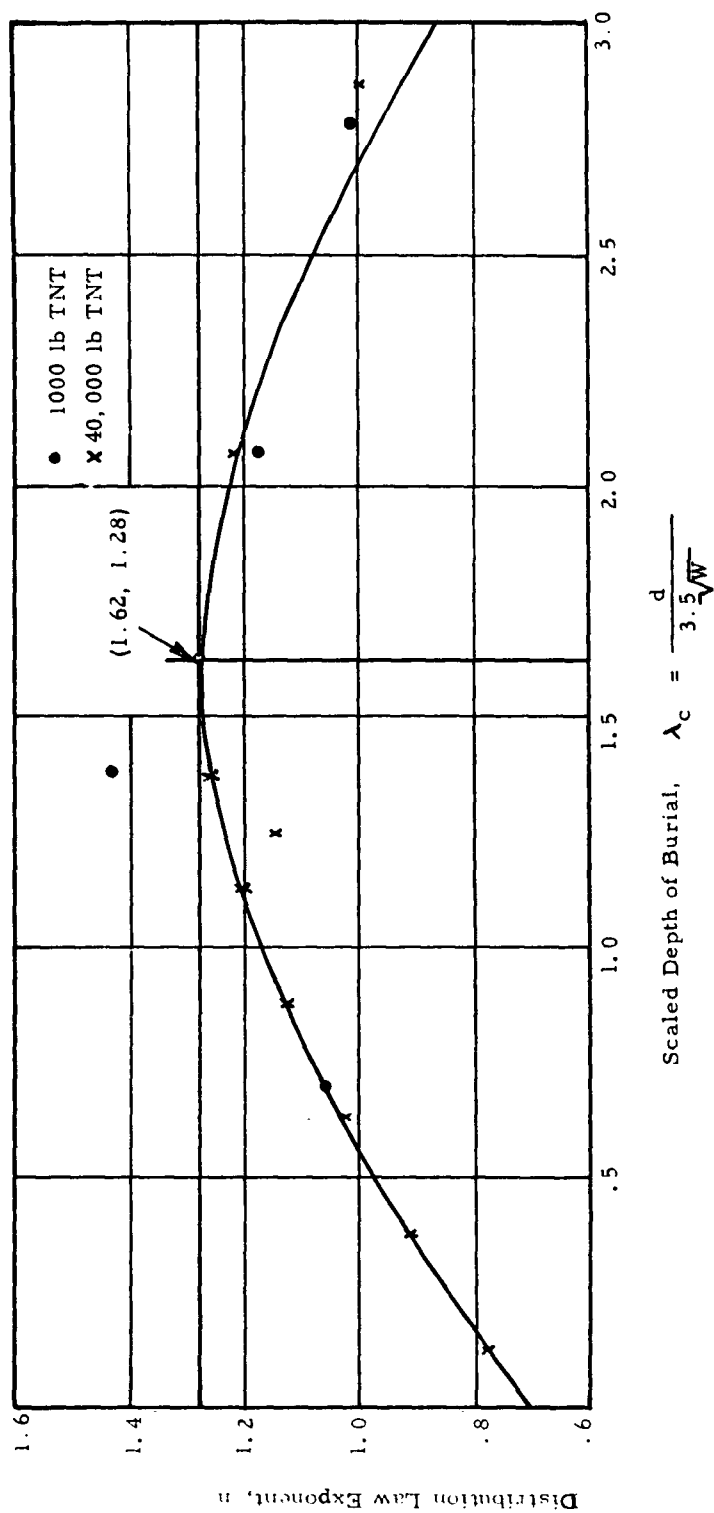


Figure 7.2 Area Mean Distance versus Fragment Size

SECRET

SECRET



SECRET

Figure 7.3 Distribution Law Exponent versus Scaled Depth of Burial

SECRET

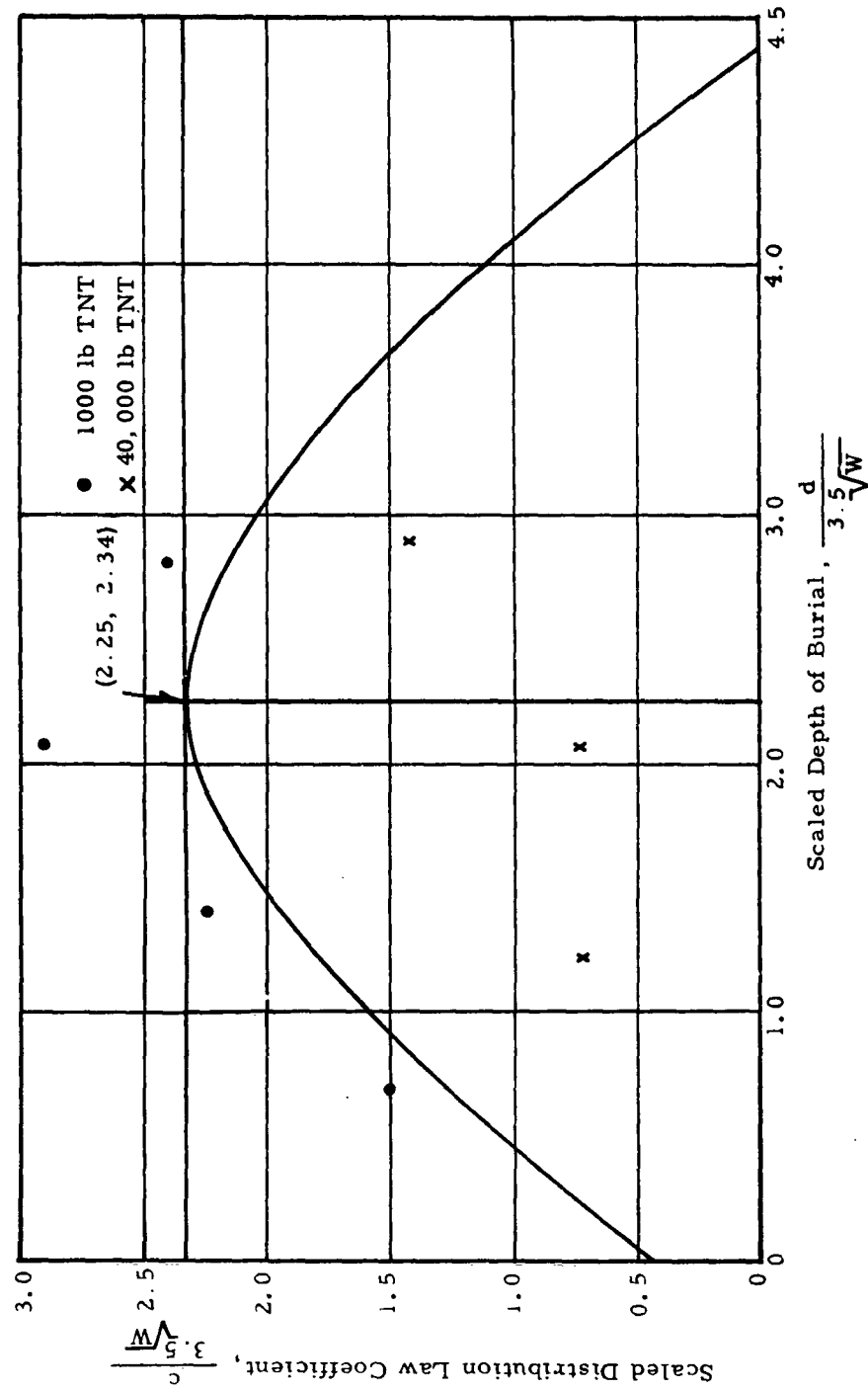


Figure 7.4 Scaled Distribution Law Coefficient versus Scaled Depth of Burial

SECRET

SECRET

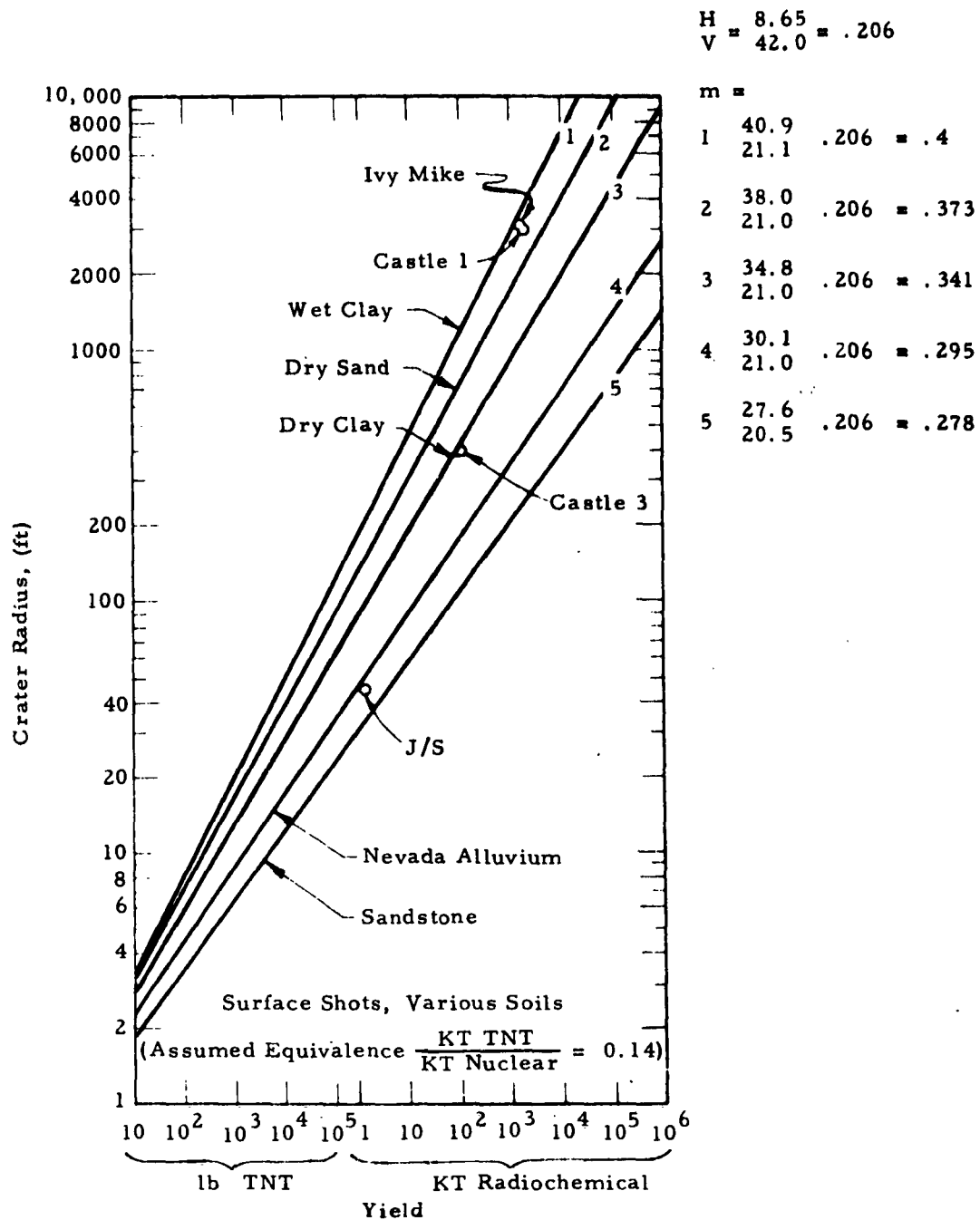


Figure 7.5 Crater Radius versus Yield, Surface Shots, Various Soils

SECRET

SECRET

represent only one shot. Data for the 1000-lb shots show in general, what would be expected, i. e., a curve similar to an inverted parabola. Especially encouraging is the fact that the vertex of the parabola lies very close to the optimum scaled depth of burial for basalt. The data for the 40,000-lb shots show a great deal of scatter.

Figure 7.6 is used to determine the equations for the curves of Fig. 7.3 and 7.4. Offsets from axes placed through the vertical were plotted in Fig. 7.6 to obtain coefficients and exponents. The resulting equations are:

$$n = 1.28 - 0.25 (\lambda_c - 1.62)^{1.8} \quad (7.4)$$

$$C = W^{3.5} \left[2.34 - 0.52 (\lambda_c - 2.25)^{1.73} \right] \quad (7.5)$$

where

n = distribution law exponent

C = distribution law coefficient

W = charge weight in lb of TNT

$\lambda_c = d/W^{1/3.5}$

d = depth of burial

Equations (7.3), (7.4), and (7.5) are the basis of the charts of Fig. 7.7 and 7.8. These charts can be used to predict safe line ground range. Let us reiterate that this represents only a first approximation. Instructions for the use of the charts follows. Two examples are presented on the charts.

7.2.1 Nomographic Calculation of Safe Distances Based on Size Distribution

Instructions for Use of Charts

Find n , and C as follows:

- (1) Select yield of device in Fig. 7.7 on horizontal axis.
- (2) Draw a vertical straight line upward to the diagonal line representing the desired depth of burst, d , (ft).

SECRET

SECRET

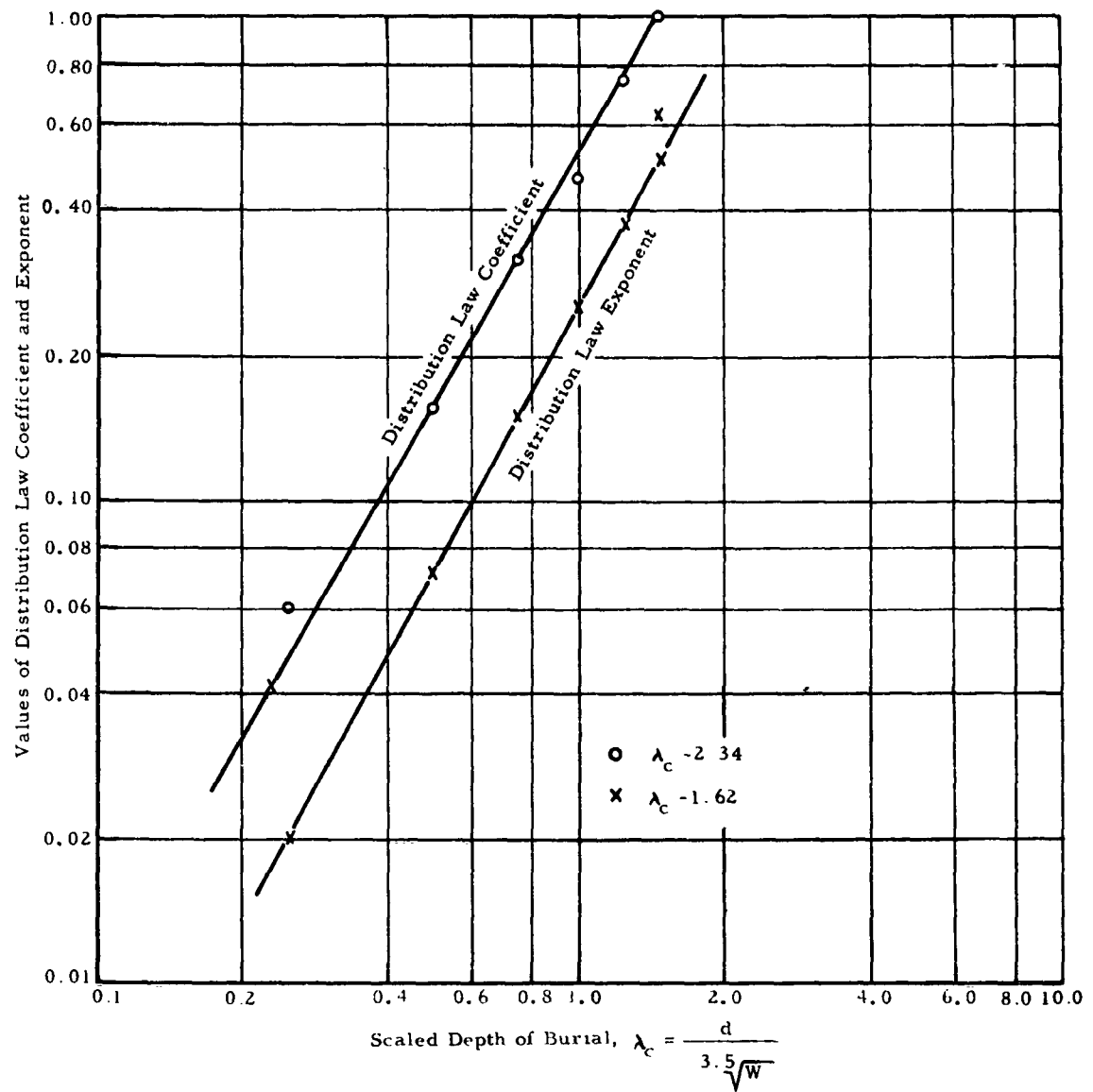


Figure 7.6 Distribution Law Exponent and Constant
versus Scaled Depth of Burial

SECRET

SECRET

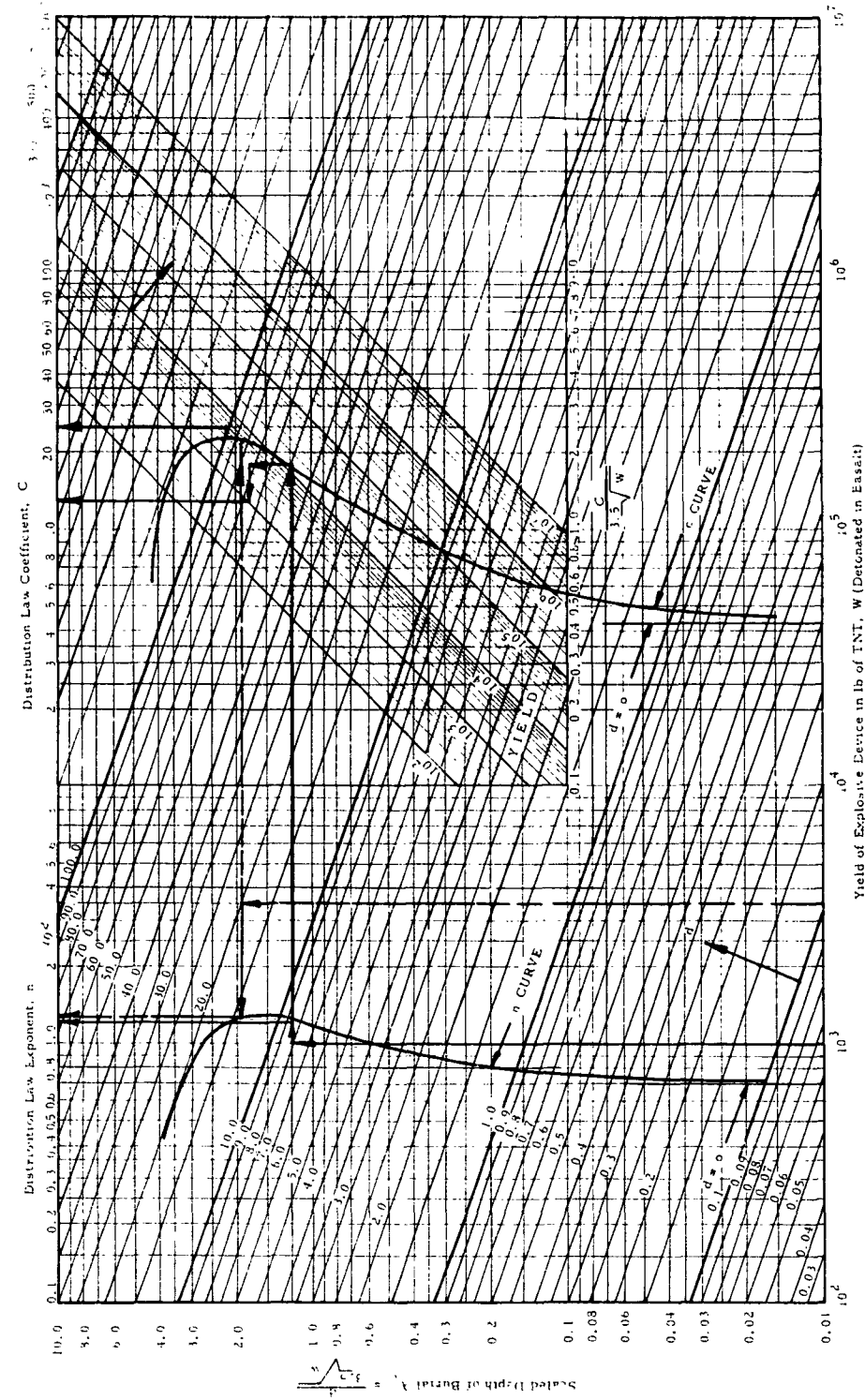


Figure 7.7 Nomographic Chart No. 1 for Computing Values of C and n

SECRET

SECRET

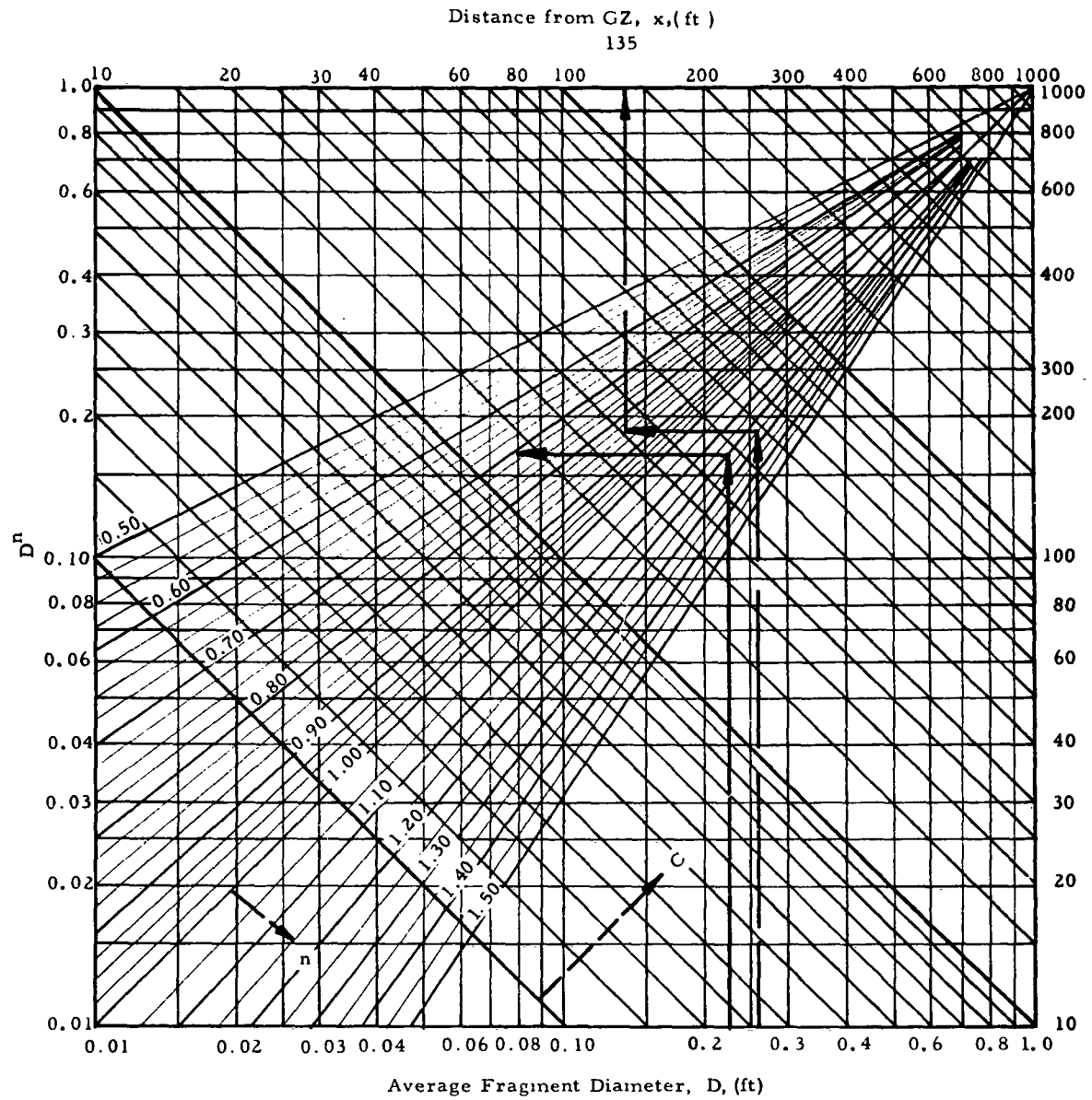


Figure 7.8 Nemographic Chart No. 2 for Computing Debris Distance

SECRET

SECRET

- (3) Draw a horizontal line from the resulting intersection with the diagonal to both the n and C curves.
- (4) Draw a line vertically upward from intersection on n curve to the top scale and find the value of the distribution law exponent n .
- (5) Draw a line vertically from the intersection with the C curve to the line A-A.
- (6) From the intersection with A-A, draw a horizontal line to intersection with the diagonal (parallel to A-A) line of constant device yield.
- (7) Draw a vertical line from the resulting intersection upward to the C scale and find the value of the distribution law coefficient, C .

Use values of n and C found above as input for Fig. 7. 8 and find maximum average distance of encounter with particle of diameter D .

- (1) Select diameter of particle on the lower horizontal axis.
- (2) Draw a vertical line upward to the diagonal representing the value of n found previously.
- (3) Draw a horizontal line from the resulting intersection to the diagonal line of constant value of the C found previously.
- (4) Draw a line vertically to the upper horizontal scale to find the maximum radial distance from ground zero at which the particle of diameter D may be expected.

Note now that distances found by this chart are average ground ranges at which a given average particle size will be found. In reference to Fig. 7. 1 it will be recognized that a large degree of variability can be attributed to the geological characteristics of the soil, such as discontinuities, non-homogeneity and anisotropy.

To estimate a safe line, it is necessary to take these factors into consideration. This can be done by considering the maximum variation about the average. Table 7. 2 tabulates the variations by showing the calculation of the ratio of maximum contour line distance and average contour

SECRET

Table 7.2
DEBRIS CONTOURS FOR CRATERING EXPLOSIONS IN BASALT

Crater Number	Maximum Contour Line Distance for 0.5-ft Diam Fragments (ft)	Maximum Contour Line for 1.0-ft Diam Fragments (ft)	Average Maximum for 0.5-ft Diam Fragments (ft)	Average Maximum for 1.0-ft Diam Fragments (ft)	1.0-ft Particles		0.5-ft Particles	
					$\frac{x_{\max}}{x_{\text{ave}}}$	Mean Value	$\frac{x_{\max}}{x_{\text{ave}}}$	Mean Value
2	62	65.5	86.5	73.9	4.3	2.49	1.55	1.96
7	111	82.3						
3	58.4	53.0	93.2	82.5	4.0	2.01	1.81	1.61
8	128	112						
4	81	69	64.7	37.8	4.05	3.48	2.57	1.23
9	49.5	31.2						
5	53.0	41.6	59.0	37.3	4.5	3.18	1.05	1.20
10	65.0	33.0						
11	87.0	68.0	87	68	4.0	2.57	1.23	1.61
12	57.6	48.0						
13	86.0	72.5	86	72.5	2.52	1.05		
DANNY BOY								

Note: x_{\max} = maximum contour line distance

SECRET

line distance. The resulting ratios were plotted on semilog paper versus yield in lb of TNT in Fig. 7.9.

Note the general decrease in x_{\max}/x_{avg} ratio for increasing yield. This is exactly what would be expected for the following reason. The soil will appear to be very nonhomogeneous, discontinuous, and anisotropic to a small blast. As the blast yield increases the appearance of the soil will become homogeneous, continuous, and isotropic. The randomness in throw out will therefore become less as blast yield is increased and consequently we can expect the asymmetry ratio-vs-yield curve will be asymptotic to the line

$$\frac{x_{\max}}{x_{\text{avg}}} = 1.$$

Data from DANNY BOY have been included in Fig. 7.9. However, compatibility with the other data is questionable since these values of asymmetry are based, at least in part, on elevation contours instead of particle size contours. The term asymmetry is used since it describes the throw out pattern. Figure 7.10 shows the DANNY BOY contours.

Figure 7.9 can be used to find an asymmetry factor. This factor should be multiplied by the average contour line distance found from Fig. 7.3. Since the results are still only a first approximation it is advisable to apply a safety factor of at least 1.5 to the results. Additional charts can be developed to take the asymmetry and safety factors into account automatically. The final result will be a safe line ground range for blast set off in basalt.

If it is desired to scale from basalt to the other materials, Fig. 7.11 will provide factors which can be applied to the final result obtained. However, in some cases such as Cucaracha and Culebra, and marine muck, this scaling may be questionable since it is so difficult to consider fragments when speaking of these soils. The scaling may possibly be good only for the materials capable of fragmentation. The curves of Fig. 7.11 were developed from the debris curves of Fig. 7.12 taken from the Panama Canal Studies (Ref. 29).

SECRET

SECRET

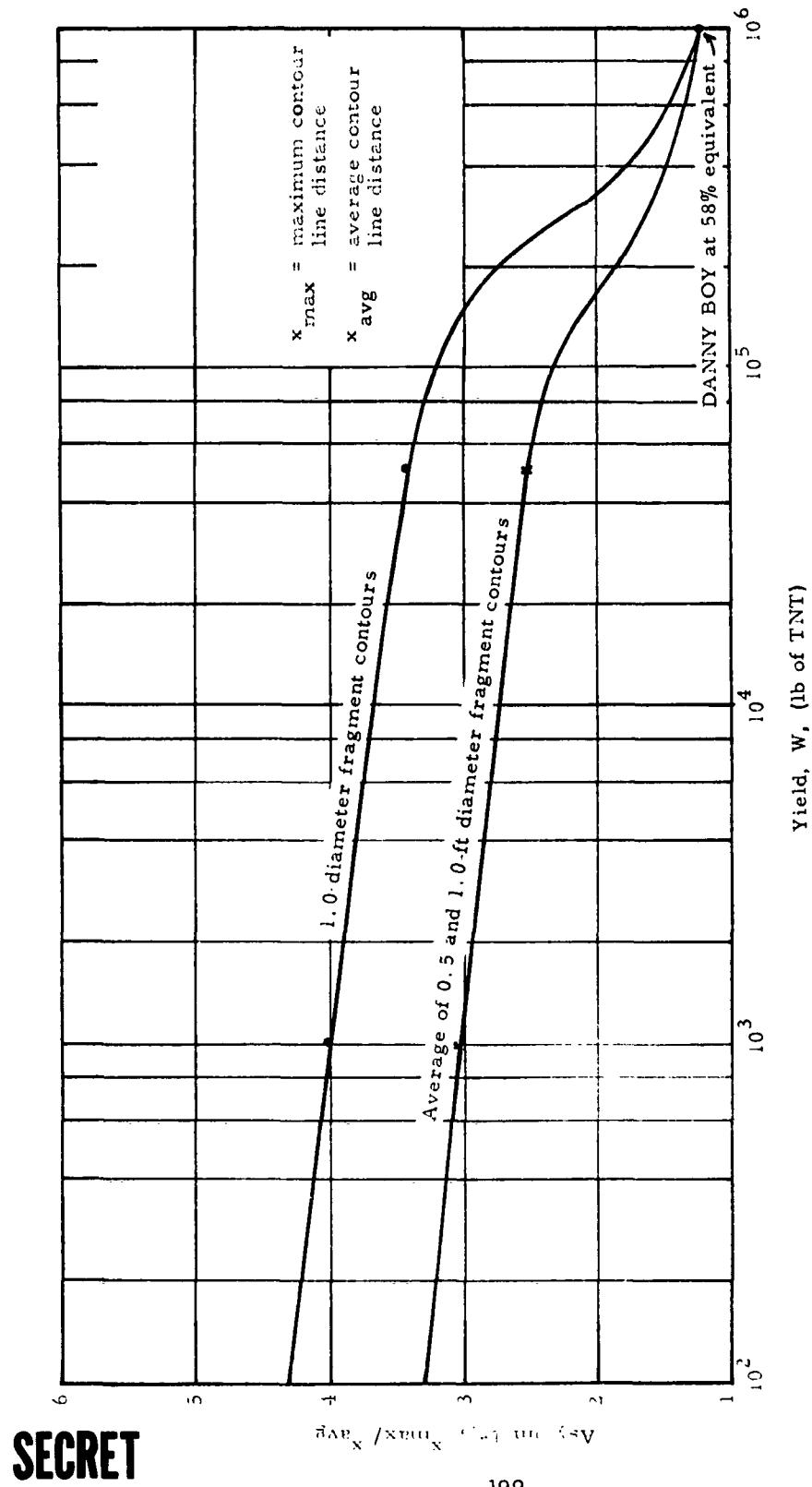


Figure 7.9 Asymmetry versus Yield

SECRET

SECRET

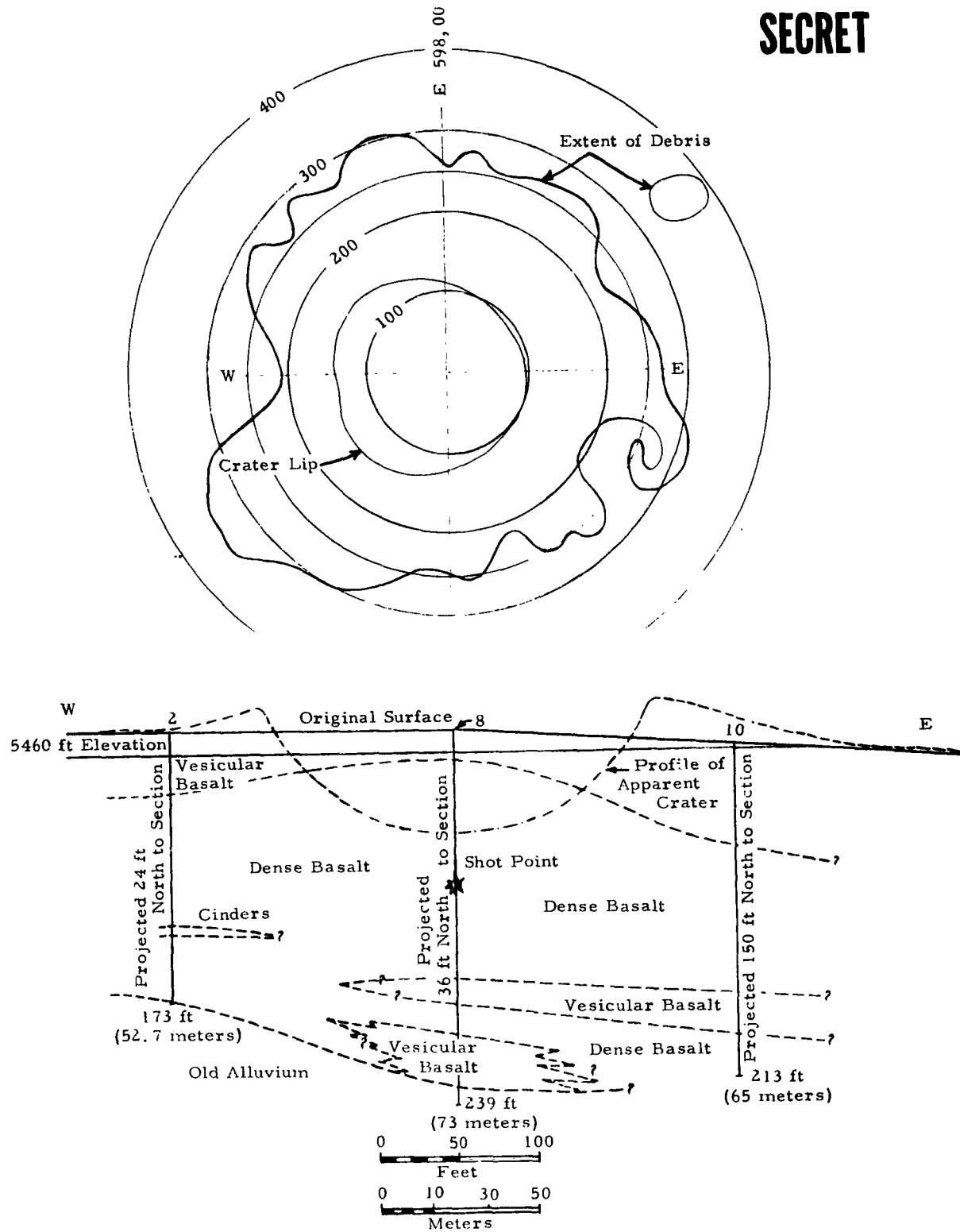


Figure 7-10 Plan and Section of the DANNY BOY Crater

SECRET

SECRET

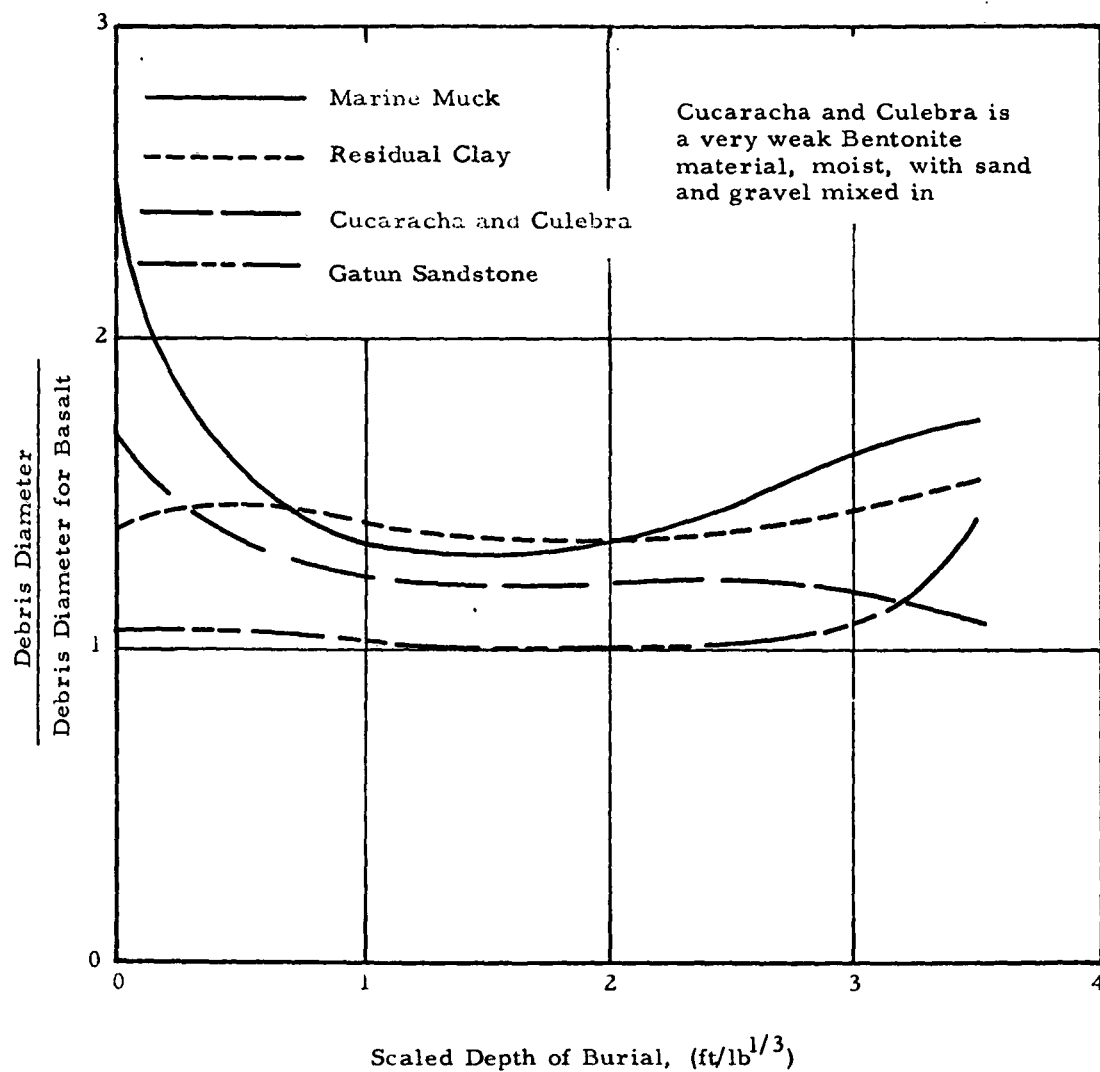


Figure 7.11 Debris Diameter Ratio versus Scaled Depth of Burial

SECRET

SECRET

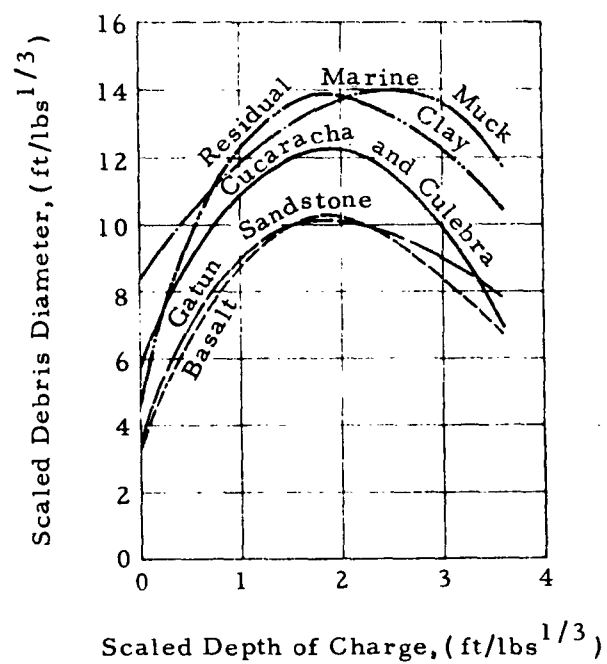


Figure 7-12 Debris Diameter for HE Charges in Various Soils

SECRET

SECRET

7.2.2 Explosive Equivalence

The data presented in Fig. 7.7 and 7.8 are for TNT charges. If nuclear charges are to be used, it is necessary to find an equivalence factor which would provide a means of finding the TNT equivalent of the nuclear device. The state-of-the-art concerning equivalence is uncertain at present. One can only hypothesize on the basis of the limited data that exist.

The first problem concerning equivalence is one of semantics. Depending upon the terminology used, almost any factor ranging from 2 percent to 120 percent is acceptable. First, let us here define equivalence. For this study, a TNT and a nuclear device would be equivalent when each produces the same amount of throw out debris distributed at the same distance.

One approach to equivalence is to hypothesize on the basis of the energy available in a nuclear blast. Effects of Nuclear Weapons (Ref. 20) states that energy of a nuclear blast is divided as follows*:

Blast and Shock	- 50 percent
Thermal Radiation	- 35 percent
Residual Nuclear Radiation	- 10 percent
Initial Nuclear Radiation	- 5 percent

On this basis it can be expected that at the ground surface a nuclear blast will be at least 50 percent efficient in terms of debris-producing capabilities. If the blast is set off underground a portion of the 35 percent thermal radiation will be transformed into mechanical effects as a result of the vaporization of material in the immediate vicinity of the device. Therefore, for buried bursts efficiencies between 50 percent and 85 percent are expected. The above does not take into account variation due to partition of energy between the air and soil - this could, in fact, result in a substantially lower efficiency. For our purposes the more conservative estimate has been selected.

* Taken in atmosphere.

SECRET

SECRET

For bursts near the surface, venting will occur and therefore a portion of the thermal radiation will still escape. On this basis one would expect a curve of efficiency versus scaled depth of burst to be similar to that of Fig. 7.13

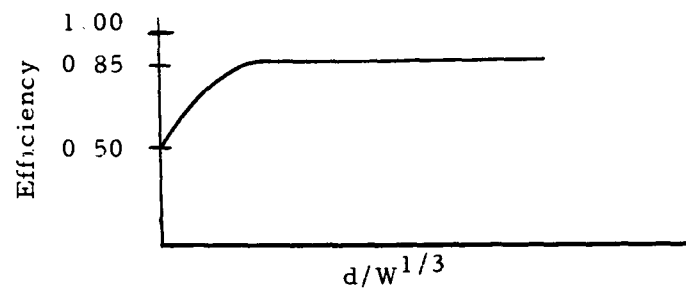


Figure 7.13 Percent of Efficiency vs Scaled Depth of Burst

7.2.3 Comparison with DANNY BOY Results

Maximum distances for fragments of various sizes have been computed by the methods of this chapter, using DANNY BOY explosion parameters as inputs. This was an 0.430-KT device buried at 110 ft in basalt. Predicted debris distances are plotted in Fig. 7.14 for various equivalence factors according to the methods described here.

SECRET

SECRET

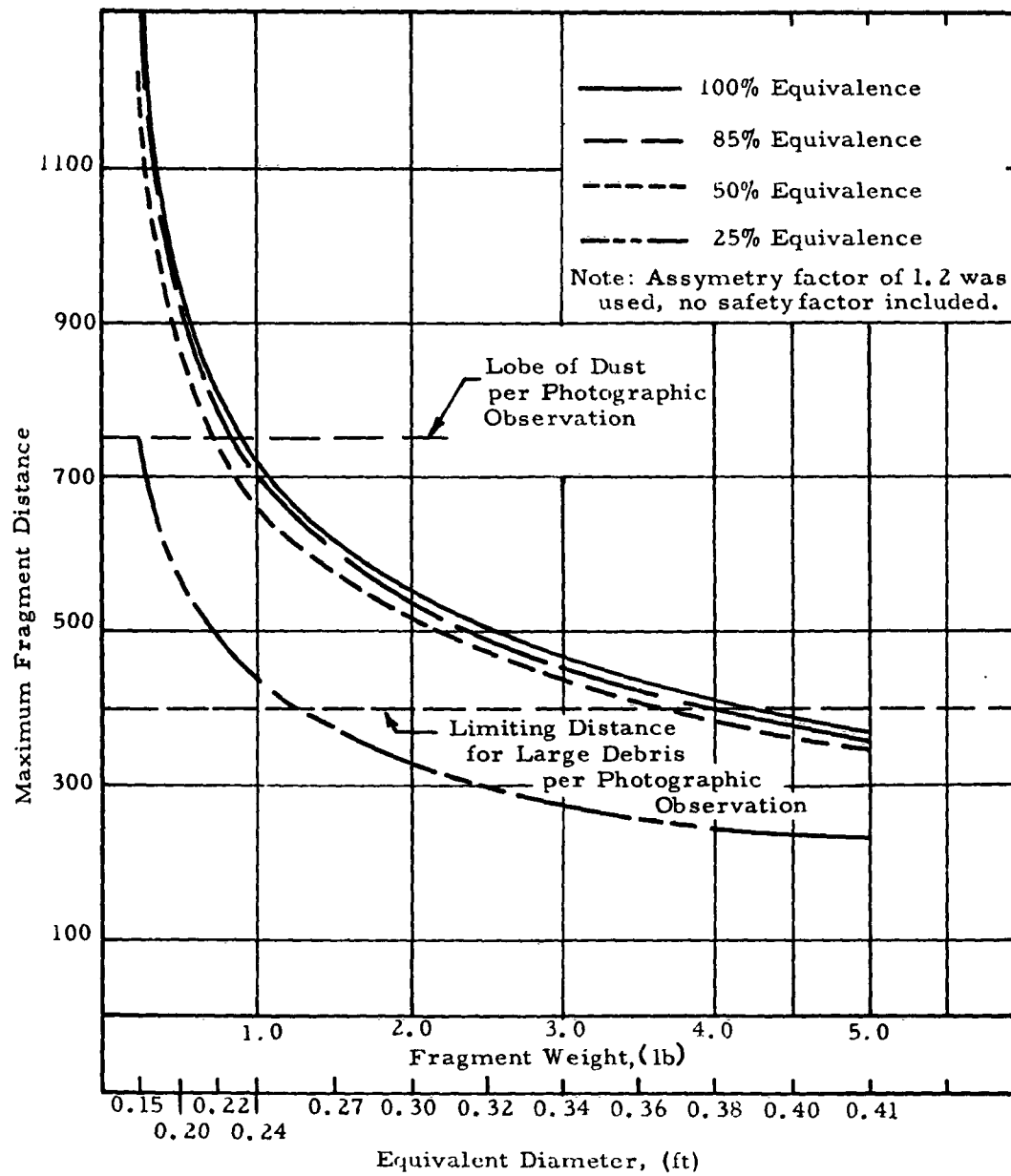


Figure 7.14 Estimated Maximum Fragment Distances for DANNY BOY Event

SECRET

SECRET

7.3 Throwout Debris from Stream-Bed Charges

Since energy partitioning for an explosion at the interface between two media is inversely proportional to the ratio of the densities of the media, the bottom burst of a stream-bed charge would be expected to impart more blast energy to the soil than a comparable surface burst at an air-soil interface. Thus, the stream-bed charge would dislodge more material for contribution to the debris, which we shall here regard only as the above-water ejecta. Initial velocities of the ejecta from stream-bed charges are unknown, but on the basis of energy partitioning we can concede, conservatively, that they may exceed initial velocities of ejecta from the comparable surface burst on land. Ejecta from the bottom burst may follow three paths, assuming the initial gas bubble does not break the surface.

- (1) Upward (nearly vertical) within the rising gas bubble into the atmosphere at relatively high velocities.
- (2) Upward (nearly vertical) through water, with considerable retardation.
- (3) Through the water at various angles to the water surface, with considerable retardation.

Bottom charges in deep stream beds would not be expected to throw debris to greater distances than comparable surface bursts on land, for only the debris rising through the gas bubble would be expected to reach the atmosphere at velocities comparable to those of the ejecta from surface bursts on land.

Although little consideration has been given crater throwout debris from underwater explosions or bottom bursts, either nuclear or high explosive, the following observation supports the above conclusions.

- (1) The displaced bottom material did not produce air-borne debris considered of consequence in the "Baker" test of OPERATION CROSSROADS. This event involved an explosion of a 20-KT device at 180-ft depth in the Bikini Lagoon, which is considered relatively shallow for that yield (Ref. 30).

SECRET

SECRET

- (2) Photographic observation of a series of tests involving underwater and bottom bursts of 300-lb HE charges showed plumes with decidedly vertical trajectories, (Ref. 31). This behavior is shown in Fig. 7.15 (from Ref. 31) and 7.16 (from Ref. 20).
- (3) Full-scale nuclear test experience has shown that if the depth of the underwater burst is not too great, the bubble remains intact until it rises to the water surface. At this point debris is expelled into the steam and fission gases (Ref. 29). Such debris would have predominantly vertical trajectories as shown in Fig. 7.16.

The problem of far-flung debris from underwater bursts is probably a hazard to field troops in cases of shallow streams only -- where the initial gas bubble breaks the surface and provides ejecta entering the atmosphere at all angles and with high initial velocities. Under these conditions the stream-bed charge placed either on or somewhat beneath the bottom -- on the basis of energy partitioning -- can conceivably produce ejecta which enters the atmosphere at initial velocities greater than that from the comparable surface or shallow-buried burst on land.

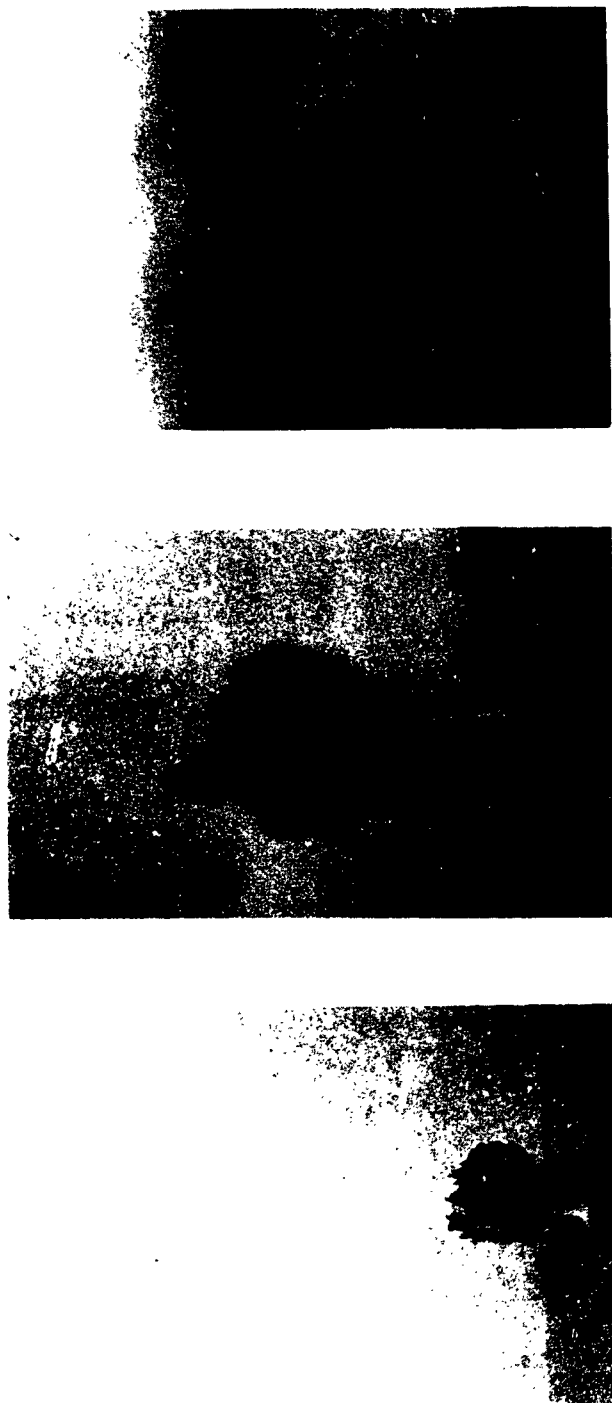
An analytic solution for initial velocities of the ejecta for either of the cases cited is beyond the scope of this portion of this investigation, and in fact, may be well beyond the scope of current knowledge. Experimentation to date can only contribute to rudimentary estimates of debris behavior from stream-bed charges.

For explosions where the gas bubble does not initially break the surface or approach the surface, we can probably neglect maximum debris distance in determining a safe line for personnel. In these cases radioactive spray from the plume itself, the condensation cloud and the base surge may extend farther than the ejected bottom material.

SECRET

SECRET

SECRET



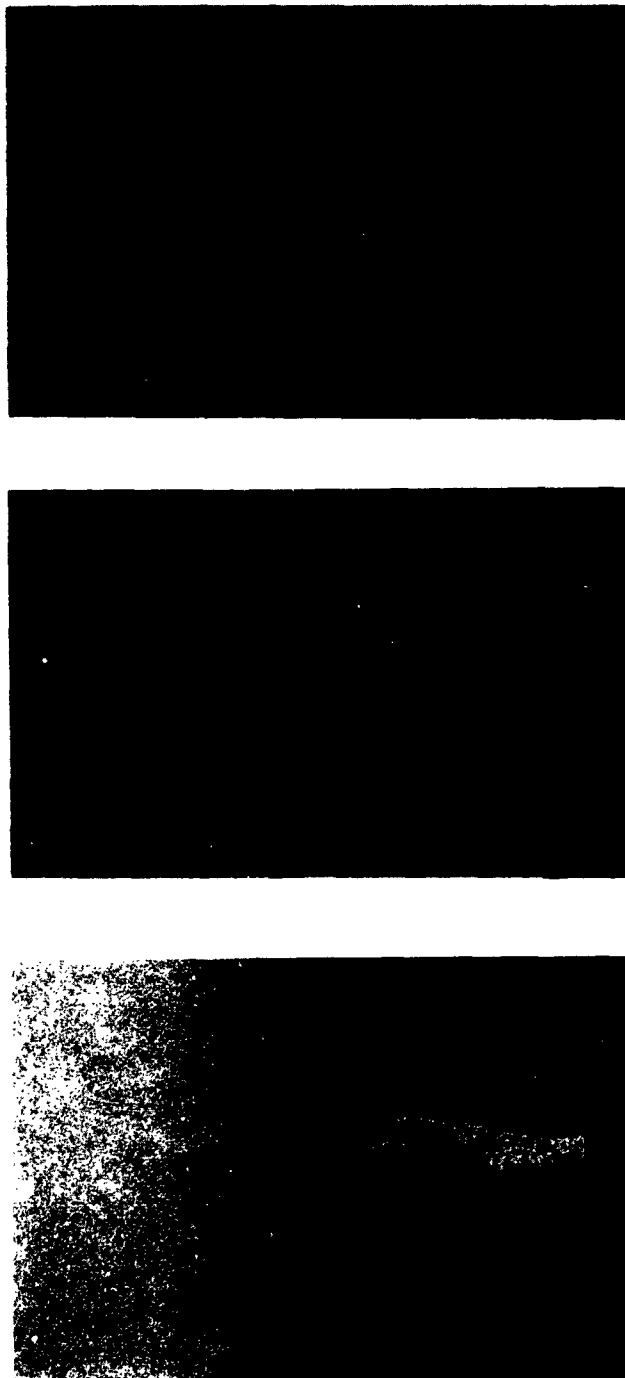
$W=300$ lbs	$D_b=2$ ft	$\lambda_c=0.30$ ft/lbs ^{1/3}	$W=300$ lbs	$D_b=2$ ft	$\lambda_c=0.30$ ft/lbs ^{1/3}
$D_f=4$ ft	$t_p=0.25$ sec	$h_p=120$ ft	$D_f=6$ ft	$t_p=0.25$ sec	$h_p=120$ ft
$R_p=17$ ft	$\tan^{-1} D_f/R_p=13^\circ$		$R_p=17$ ft	$\tan^{-1} D_f/R_p=19^\circ$	

(1/35th linear scale Bikini Test Baker)

Figure 7.15
Plumes From Low-Yield Underwater Explosions

Note:
 W = yield
 λ_c = scaled depth of charge
 t_p = time of plume photograph
 R_p = plume radius
 D_b = depth of burst below water surface
 D_f = depth of bottom
 h_p = reported plume height from photograph

SECRET



$W=300$ lbs	$D_b=4$ ft	$\lambda_c=0.60$ ft/lbs ^{1/3}	$W=300$ lbs	$D_b=5.5$ ft	$\lambda_c=0.82$ ft/lbs ^{1/3}
$D_f=6$ ft	$t_p=0.5$ sec	$h_p=120$ ft	$D_f=6$ ft	$t_p=0.5$ sec	$h_p=150$ ft
$R_p=15$ ft	$\tan^{-1} D_f/R_p=21^\circ$		$R_p=17$ ft	$\tan^{-1} D_f/R_p=19^\circ$	

(charge rested on bottom)

Figure 7.15 (Cont'd)
Plumes From Low-Yield Underwater Explosions

SECRET

SECRET

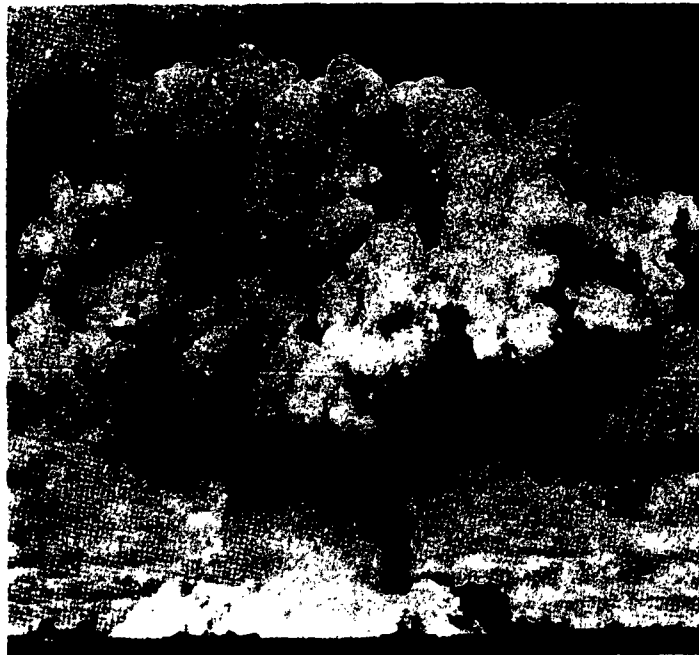
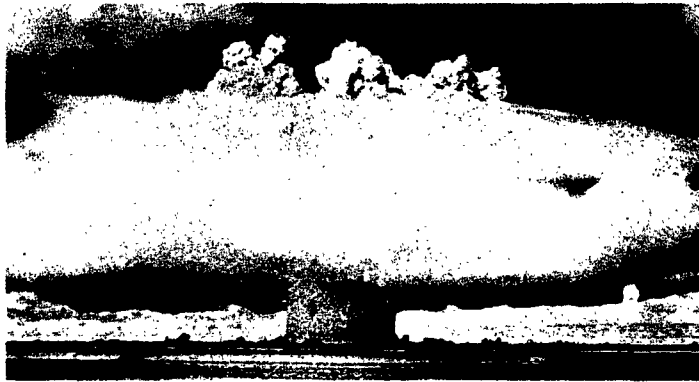


Figure 7.16
Plume From Shallow Underwater Nuclear Explosions

SECRET

SECRET

Among all the experimental work reviewed on cratering and debris, the Panama Canal tests of cratering charges in marine muck most closely resemble the configuration of the shallow stream-bed charge -- at least they assuredly provide a situation where the ejecta is not retarded in its trajectory by passing through water. Energy partitioning may not be exactly comparable to the stream-bed charge, for the immediate escape of the gas bubble would also cause more energy partitioning away from the bottom material.

In the absence of analytical methods for estimating debris behavior from bottom bursts, recourse is made to the available experimental data on crater tests in marine muck. Debris limits for stream-bed charges can be computed by estimating debris distances for basalt as prescribed earlier for cratering charges, and then applying a correction to account for the ratio of debris limits for basalt and bottom material. This correction factor,

$$\frac{\text{Debris diameter for bottom material}}{\text{Debris diameter for basalt}}$$

can be taken as the debris-diameter-ratio for marine muck in Fig. 7.11. In using Fig. 7.11 in this manner the scaled depth of burial of the charge should be taken relative to the stream bed. Thus for bottom bursts, scaled depth of burial will be zero.

SECRET

SECRET

REFERENCES

1. Ahlers, E. B., "Throwout Study of an Underground Nuclear Detonation", Interim Test Report DANNY BOY Project 1.5, POIR-1814 (ITR-1814), DASA Contract DA-49-146-XZ-097, Department of Defense-U.S. AEC, April 1962 (CONFIDENTIAL - Formerly RESTRICTED DATA).
2. Ahlers, E. B., "Throwout Study of an Underground Nuclear Detonation", Final Test Report DANNY BOY Project 1.5, POR-1814 (WT-1814), DASA Contract DA-49-146-XZ-097, Department of Defense-U.S. AEC, Sept. 1962 (CONFIDENTIAL - Formerly RESTRICTED DATA).
3. Anderson, D. and Fisher, R., "Hydrodynamic Analysis for a Buried Underground Nuclear Explosive", ARF Preliminary Report to DASA, Feb. 22, 1962 (SECRET).
4. Anderson, D., Fisher, R., and Wiedermann, A., "Post-Test Hydrodynamics Analysis of DANNY BOY", Final Report to DASA, Feb., 1963 (SECRET).
5. Vaile, Jr., R. B. and Salmon, V., "Evaluation of Missile Hazard, Underground Shot", Operation JANGLE, Project 4.5, Stanford Research Institute, Stanford, California, May 1952 (WT-338).
6. Robinson, C. S., "Explosions - Their Anatomy and Destructiveness", 1st Ed., McGraw-Hill Book Co., Inc., New York, 1944.
7. Assheton, R., "The History of Explosions", The Institute of Makers of Explosives", Wilmington, Del., 1930.
8. Armed Services Explosives Safety Board, Explosion Log. (Unpublished).
9. Hoy, R. B. and Foose, R. H., "Visual and Photographic On-Site Inspection", Project DANNY BOY, Project 7.5, Final Report POR-1823 (WT-1823), Stanford Research Institute, Dept. of Defense - U.S. AEC, April 1962.
10. Explosion Report File of Armed Services Explosives Safety Board (Unpublished).
11. Akst, I. B., Schuldt, H. S., and Self, D. C., "Wall Safe Test -- Propagation of a 2,000 Pound Explosion across 12-in. Concrete Bay Walls", Mason and Hanger - Silas Mason Co., Inc., for U.S. Army Ordnance Corps, 1960.
12. Robinson, C. S., "The Missile Hazard from Explosions", Tech. Paper No. 2, Army-Navy Explosives Safety Board, Washington, D. C., December 1945.
13. Bennett, J. G., Brown, R. L. and Crone, H. G., "Broken Coal-II. The Relation between Size Distribution and the Breakage Process", Jour. of the Institute of Fuel, Vol. XIV, No. 77, April 1941.

SECRET

SECRET

14. Grimshaw, H. O., "The Fragmentation Produced by Explosive Detonated in Stone Blocks".
15. Huber, G. B., Keough, D. D., Stallybrass, M. P. and Zabel, N. R., "Containment of Fragments from Runaway Reactor", Tech. Report No. 3, U.S. AEC Contract AT(04-3)-115 Project No. 2, Stanford Research Institute, Menlo Park, California, October 1959.
16. Huber, G. B. and Zabel, N. R., "Containment of Fragments from a Runaway Reactor", Tech. Report No. 4, U.S. AEC Contract AT(04-3)-115 Project No. 2, Stanford Research Institute, Menlo Park, California, October 1960.
17. Griffith, A. A., "The Phenomena of Rupture and Flow in Solids", Phil. Trans. Royal Soc., A221, 163, 1920.
18. Weibull, W., "A Statistical Theory of the Strength of Materials", Ing. Vetenskaps Akad. Handl. No. 151, 1939.
19. Air Force Special Weapons Center, Project 36, V-K, Railroad Equipment Shot 10, Film No. 16, 721.
20. Glasstone Samuel, E., Effects of Nuclear Weapons, U.S. AEC (1957).
21. Brown, A. A., et al., "Blast Damage to Trees -- Isolated Conifers", U.S. Dept. of Agriculture, Forest Service, Operation SNAPPER, Project 3.3, AFSWP-509, Armed Forces Specific Weapons Project, Washington D.C., January 1953.
22. Sauer, F. M., Fons, W. L. and Storey, T. G., "Blast Damage to Coniferous Tree Stands by Atomic Explosions", Operation UPSHOT-KNOTHOLE, Project 3.19, U.S. Dept. of Agriculture, Forest Service, WT-731, Armed Forces Special Weapons Project, Washington, D.C., January 1954.
23. Storey, T. G., Fons, W. L. and Sauer, F. M., "Crown Characteristics of Several Coniferous Tree Species", U.S. Department of Agriculture, Forest Service, Interim Tech. Report AFSWP-416, Armed Forces Special Weapons Project, Washington D.C., August 1955.
24. Johnson, R. B., "Effect of Geologic Factors on Cratering Experiments in Basalt", Tech. Letter: Area 18-1, U.S. Dept. of Interior, Geological Survey, August 8, 1962.
25. Roberts, W. B. and Blaylock, J. A., "Distribution of Debris Ejected by the Stagecoach Series of HE Cratering Bursts", Doc. No. D2-6955-1, Boeing Airplane Company, Seattle, Wash., October 3, 1961.
26. Carlson, R. H. and York, E. N., "Local Distribution of Material Ejected by Surface Explosions, White Tribe Interim Report, Doc. No. D2-6955-2, Boeing Airplane Co., Seattle, Wash., August 15, 1961.
27. Kempster, D. J., "Surface Burst of a 100-Ton TNT Hemispherical Charge (1961), Crater and Ejecta Deposit Measurements", DRB Project No. D89-16-01-12, Suffield Experimental Station, Ralston, Alberta, May 31, 1962.

SECRET

SECRET

28. Vaile, Jr., R.B., "Pacific Craters and Scaling Laws", Paper E, UCRL-6438, Proceedings of the Geographical Lab. - Lawrence Radiation Lab. Cratering Symposium, University of California, October 1961.
29. Darling, J.A., "Crater and Slope Tests with Explosives", I.C.S. Memo 282-P, The Panama Canal, Diablo Heights, C. Z., June, 1948.
30. "Effects of Explosions in Shallow Water", Final Report, Technical Memorandum No. 2-406, U.S. Army Corps of Engineers, Waterways Experiment Station, for Armed Forces Special Weapons Project, AFSWP-452, Vicksburg, Miss., April 1955.
31. Powell, J.H. and Hart, W.D., "The Effects Produced by the Explosion of Charges in Shallow Water with Particular Reference to the Atomic Bomb", Naval Construction Research Establishment, Report No. N.C.R.E./R 43, Rosyth, Gr. Brit.

SECRET

SECRET

APPENDIX A
MAXIMUM DEBRIS DISTANCE AND EXPLOSION PARAMETERS
FOR SELECTED EXPLOSIONS

SECRET

SECRET

MAXIMUM DEBRIS DISTANCE AND EXPLOSION PARAMETERS FOR SELECTED EXPLOSIONS

Site	Year	Explosive Material	Type of Confinement	Quantity of Explosive (tons)	Explosive TNT = 1.00	Equivalent Weight of Explosives (tons TNT)	W ^{1/3} (tons TNT) ^{1/3}	Maximum Debris Distance (ft)	W ^{1/3} -Scaled Maximum Debris Distance (ft/tons ^{1/3})	Assumed Impulse Distance, (ft)	Impulse, (lb-msec/in. ²)	W ^{1/3} -Scaled Impulse, (lb-msec/in. ²)
Camp Uijongbu, Korea	1947	Tetrytol	Tent	0.004	1.20	0.0048	0.169	30	178	3	248	1,468
Redstone Arsenal		Tetryl	Building	0.005	1.20	0.0060	0.182	600	3,300	15	406	3,332
Sunflower Ordnance Wks		JPN-C-2 Powder	Building	0.005	0.58	0.0029	0.142	35	246	8	110	768
Cugny Factory, France	1952	NG	Frame Building	0.0165	1.35	0.0223	0.281	82	292	15	176	624
Latrobe, Pa.	1951	Wet Mercury Fulminate	Barricaded Building	0.045	0.71	0.0320	0.322	250	787	15	132	414
C												
Honshu, Japan	1943	TNT	Unbarricaded Building	0.045	1.00	0.045	0.356	200	562	15	124	350
Arkansas Ordnance Plant	1945	Bombs	Unbarricaded Building	0.050	1.00	0.050	0.368	450	1,222	3	944	2,560
Ardeer, Scotland	1945	Tetryl, etc.	Burning Grate	0.075	1.14	0.0855	0.440	225	512	5	950	2,155
Mechanicsville, Md.	1884	Dynamite	Unbarricaded Building	0.100	0.79	0.079	0.429	310	723	15	186	434
	1955	Tetryl Graphite	Building	0.125	1.14	0.142	0.522	400	716	15	352	673
Rot herwas		TNT	Unbarricaded RDE Unit	0.150	1.00	0.150	0.530	825	1,558	10	729	1,370
Fairchance, Pa.	1943	Rifle Powder	Barricaded Building	0.200	0.58	0.116	0.488	360	738	12	447	916
Tenino, Wash.	1954	Nitro-Cotton	Unbarricaded Building	0.200	0.79	0.158	0.540	1,200	2,220	3	578	2,916
Dover, N.J.	1948	Propellant Stick Powd.	14-ft Cubicle	0.225	0.58	0.131	0.507	360	710	7	951	1,873
Bishopton, England	1945		Cordite House	0.225	1.20	0.270	0.646	300	464	15	655	1,013
Ayrshire, Scotland	1950	60% Dynamite	Barricaded Building	0.230	0.83	0.191	0.576	1,500	2,600	15	474	823
Pinole, Calif.	1907	Gelatin	Barricaded Building	0.250	1.35	0.338	0.695	1,200	1,727	15	794	1,139
Sherborne, England	1944	TNT	Mines in Truck	0.250	1.00	0.250	0.630	1,500	2,380	4	1,767	2,803
Sunflower Ordnance Wks	1944	Powder	Bug in Building	0.250	0.58	0.145	0.523	5,250	10,000	4	1,382	2,630
Moosic, Pa.		Black Powder	Unbarricaded Building	0.250	0.58	0.145	0.525	350	668	15	358	682
Perranporth, England	1902	Gelatin	Tram	0.267	1.35	0.360	0.711	1,050	1,476	4	2,067	2,905
Sunflower Ordnance Wks		Black Powder	Mixer in Building	0.334	0.58	0.194	0.578	5,280	9,140	1	2,020	3,491
Gibbstown, N.J.	1903	Dynamite	Barricaded Building	0.350	0.79	0.277	0.651	400	614	15	669	1,026
Upton Towans, England	1899	NG	Barricaded Building	0.380	1.35	0.513	0.800	600	750	15	1,103	1,377
Guinan, Samar, P.I.	1945	Frag. Bombs	Barge	0.400	1.00	0.400	0.736	300	408	20	558	758
Upton Towans, England	1899	Gelatin	Barricaded Building	0.450	1.35	0.608	0.850	1,500	1,771	15	1,247	1,472
Landing, N.I.	1909	Dynamite	Barricaded Building	0.450	0.79	0.306	0.673	900	1,336	15	828	1,169
Lower Hope Point, England	1902	NG	Barricaded Building	0.500	1.35	0.675	0.876	450	513	15	1,343	1,531
Uplee's Marshes, Faversham, England	1903	NG	Barricaded Building	0.500	1.35	0.675	0.876	150	171	15	1,343	1,531
Ashburn, Mo.	1906	NG	Tram	0.540	1.35	0.730	0.900	400	445	4	2,769	3,076
Savanna Ordnance Depot	1949	Fuzes, Mines, etc.	Earth-Covered Igloo	0.573	1.14	0.596	0.840	1,320	1,570	8	2,098	2,418
Kangnung, Korea	1947	Projectiles	Truck	0.650	1.00	0.650	0.866	300	346	4	4,643	2,051
Lewisburg, Ala.	1907	Dynamite	Building near Hill	0.650	0.79	0.514	0.800	500	625	15	1,104	1,378
Ashburn, Mo.	1906	Gelatin	Barricaded Building	0.650	1.35	0.878	0.956	1,040	1,089	15	1,602	1,899
Penson, Ariz.	1949	Low NG, High Am-mon. Nlt. Dyn.	Barricaded Crib, 8'x13'	0.663	0.53	0.351	0.705	1,100	1,560	4	2,046	2,899
Egyptian Powder Co.		Black Powder	Unbarricaded Shed	0.700	0.58	0.406	0.700	85	922	15	922	1,245
Schaghticoke, N.Y.	1912	Black Powder	Barricaded Building	0.750	0.58	0.435	0.757	800	1,057	15	922	1,245
Chattanooga, Tenn.	1903	Dynamite	Barricaded Building	0.750	0.79	0.592	0.840	800	952	15	922	1,245
Moosic, Pa.		Black Powder	Unbarricaded Building	0.800	0.58	0.464	0.774	750	969	15	922	1,245
Baraboo, Wis.	1943	E. C. Blank Fire Powd.	Barricaded Building	0.825	0.79	0.632	0.857	13,000	15,170	1	1,241	1,468
Ashburn, Mo.	1906	Dynamite	Barricaded Building	0.850	0.79	0.671	0.875	400	458	15	1,241	1,468
Pembrey		TNT	Barricaded Building	1.000	1.00	1.000	0.875	930	930	15	1,241	1,468
Chilworth, England	1879	Black Powder	Barricaded Building	1.000	0.58	0.580	0.833	600	720	15	1,241	1,468
Reynold, Pa.	1951	NG	Barricaded Building	1.010	1.35	1.108	1.108	1,000	904	15	1,241	1,468
Carney's Point		Shotgun Powder	Continuous Dryer	1.040	0.58	0.604	0.845	50	59	15	1,241	1,468
Umbogintwini, Natal	1909	NG	Barricaded Building	1.050	1.35	1.418	1.122	500	445	10	2,762	2,459
Cliffe, England	1904	NG	Barricaded Building	1.050	1.35	1.418	1.122	390	348	15	2,158	1,921

1901	Sunflower Ordnance Wks Gibbstown, N.J.	Black Powder Dynamite	0.334 0.350	0.58 0.79	0.194 0.277	0.578 0.651	9,170 9,280	4 15	2,067 2,491	2,905 3,491
1899	Upton Towans, England	Black Powder Dynamite	0.380 0.400	1.35 1.00	0.513 0.400	0.800 0.736	600 300	15 20	1,103 558	1,377 758
1945	Gunan, Samar, P.I.	Frag. Bombs								
1899	Upton Towans, England	Gelatin	0.450	1.35	0.608	0.850	1,500	15	1,247	1,472
1909	Landing, N.J.	Dynamite	0.450	0.79	0.306	0.673	900	15	1,343	1,169
1902	Lower Hope Point, England	Black Powder Dynamite	0.500	1.35	0.675	0.876	450	15	1,343	1,531
1903	Uplee's Marshes, Faversham, England	Black Powder Dynamite	0.500	1.35	0.675	0.876	150	15	1,343	1,531
1906	Ashburn, Mo.	Black Powder Dynamite	0.540	1.35	0.730	0.900	400	4	2,769	3,076
1949	Savanna Ordnance Depot Fangnung, Korea	Fuzes, Mines, etc. Projectiles	0.573 0.656	1.14 1.00	0.596 0.650	2,840 0.866	1,320 300	8 4	4,098 4,643	4,418 5,051
1907	Lewisburg, Ala.	Black Powder Dynamite	0.650	0.79	0.514	0.800	500	15	1,194	1,378
1906	Ashburn, Mo.	Black Powder Dynamite	0.650	1.35	0.878	0.956	1,040	15	1,602	1,873
1949	Penson, Ariz.	Black Powder Dynamite	0.663	0.53	0.351	0.706	1,100	15	2,046	2,399
1912	Egyptian Powder Co. Schaghticoke, N.Y.	Black Powder Dynamite	0.700	0.58	0.406	0.757	85	15	922	1,245
1903	Chattanooga, Tenn.	Black Powder Dynamite	0.750	0.58	0.435	0.757	800	15	973	1,284
1943	Baraboo, Wis.	Black Powder Dynamite	0.800	0.58	0.592	0.840	800	15	1,225	1,458
1906	Ashburn, Mo.	Black Powder Dynamite	0.825	0.79	0.632	0.857	750	8	1,764	2,278
1879	Pembrey	Dynamite	0.850	0.79	0.671	0.875	400	15	1,338	1,528
1951	Reynold, Pa.	TNT	1.000	1.00	1.000	1.000	930	15	1,743	1,743
1909	Umboingtini, Natal	Black Powder	1.010	1.35	1.362	0.833	720	15	1,206	1,446
1904	Cliffe, England	Black Powder	1.040	0.58	0.604	1.108	904	10	2,710	2,444
1905	Hazleton, Pa.	Black Powder	1.100	0.58	0.604	0.845	50	15	1,241	1,468
1944	Liberty Powder Co. Airfield, England	Black Powder Dynamite	1.100	1.00	1.100	1.031	2,620	5	3,115	3,018
1942	Mt. Braddock, Pa.	Black Powder Dynamite	1.100	1.35	1.418	1.122	445	10	2,762	2,459
1950	Eldred, Pa.	Black Powder Dynamite	1.100	1.35	1.418	1.122	348	15	2,158	1,921
1894	Waltham Abbey, England	Black Powder Dynamite	1.120	0.79	0.829	0.939	2,132	15	1,544	1,643
1913	Gibbstown, N.J.	Black Powder Dynamite	1.150	0.79	0.869	1.000	1,800	15	1,592	1,668
1907	Boulder, Colo.	Black Powder Dynamite	1.150	1.00	1.100	1.031	2,700	5	3,115	3,018
1904	Upton Towans, England	Black Powder Dynamite	1.200	0.79	0.814	0.932	1,500	15	1,592	1,668
1945	Kuba, Okinawa	Black Powder Dynamite	1.250	0.91	0.910	1.000	1,608	15	1,744	1,743
1892	Winsted, Conn.	Black Powder Dynamite	1.250	0.91	0.910	1.000	1,608	15	1,744	1,743
1911	Nanaimo, B.C.	Black Powder Dynamite	1.396	0.79	0.814	0.932	1,500	15	1,592	1,668
1926	Carney's Point, N.J.	Black Powder Dynamite	1.400	0.79	0.814	0.932	1,500	15	1,592	1,668
1951	Birmingham, Ala.	Black Powder Dynamite	1.484	0.79	0.814	0.932	1,500	15	1,592	1,668
1944	Moosic, Pa.	Black Powder Dynamite	1.500	0.79	0.814	0.932	1,500	15	1,592	1,668
1929	Gibbstown, N.J.	Black Powder Dynamite	1.500	0.79	0.814	0.932	1,500	15	1,592	1,668
1954	Radford Arsenal	Black Powder Dynamite	1.500	0.79	0.814	0.932	1,500	15	1,592	1,668
1953	Hercules, Calif.	Black Powder Dynamite	1.500	0.79	0.814	0.932	1,500	15	1,592	1,668
1910	Pinar Del Rio, Cuba	Black Powder Dynamite	1.500	0.79	0.814	0.932	1,500	15	1,592	1,668
1913	Martin, Pa.	Black Powder Dynamite	1.500	0.79	0.814	0.932	1,500	15	1,592	1,668
1943	Great Ashfield, England	Black Powder Dynamite	1.584	0.79	0.814	0.932	1,500	15	1,592	1,668
1953	Hercules, Calif.	Black Powder Dynamite	1.650	0.79	0.814	0.932	1,500	15	1,592	1,668
1898	Blackbeck, England	Black Powder Dynamite	1.750	0.79	0.814	0.932	1,500	15	1,592	1,668
1908	Gibbstown, N.J.	Black Powder Dynamite	1.750	0.79	0.814	0.932	1,500	15	1,592	1,668
1902	Ardeer, Scotland	Black Powder Dynamite	1.791	0.79	0.814	0.932	1,500	15	1,592	1,668
1948	Hercules, Calif.	Black Powder Dynamite	1.800	0.79	0.814	0.932	1,500	15	1,592	1,668
1945	Barge Pier, Korea	Black Powder Dynamite	2.000	0.79	0.814	0.932	1,500	15	1,592	1,668
1902	Ardeer, Scotland	Black Powder Dynamite	2.000	0.79	0.814	0.932	1,500	15	1,592	1,668
1905	Islemping, Mich.	Black Powder Dynamite	2.050	0.79	0.814	0.932	1,500	15	1,592	1,668
1914	Ardeer, Scotland	Black Powder Dynamite	2.090	0.79	0.814	0.932	1,500	15	1,592	1,668
1951	Seneca, Ill.	Black Powder Dynamite	2.100	0.79	0.814	0.932	1,500	15	1,592	1,668
1907	Barkdale, Wis.	Black Powder Dynamite	2.105	0.79	0.814	0.932	1,500	15	1,592	1,668
1908	Louviers, Colo.	Black Powder Dynamite	2.200	0.79	0.814	0.932	1,500	15	1,592	1,668
1943	A	Black Powder Dynamite	2.250	0.79	0.814	0.932	1,500	15	1,592	1,668
1912	Haskell, Okla.	Black Powder Dynamite	2.324	0.79	0.814	0.932	1,500	15	1,592	1,668
1916	Hoyle Factory	Black Powder Dynamite	2.400	0.79	0.814	0.932	1,500	15	1,592	1,668
1944	Wolf Creek	Black Powder Dynamite	2.400	0.79	0.814	0.932	1,500	15	1,592	1,668

SECRET

2

MAXIMUM DEBRIS DISTANCE AND EXPLOSION PARAM
FOR SELECTED EXP

1

Site	Year	Explosive Material	Type of Confinement	Quantity of Explosive, (tons)	Explosive Equivalence (TNT= 1.00)
Indiana Ordnance Wks		Smokeless Powder	Building	81.59	0.58
Beira, Portugal	1880	Black Powder	Mag.	82.50	0.58
Highland Station, Calif.	1892	Dynamite	Unbarricaded Building	103.6	0.79
Haskell, N. J.	1917	Smokeless Powder	Unbarricaded Building	117.0	0.58
Rio de Janeiro, Brazil	1925	Dynamic	Unbarricaded Building	124.0	0.79
Arco, Idaho	1945	50/50 Amatol	Barricaded Igloo	125.0	0.87
Savanna Ordnance Depot	1948	Tetrytol	Earth Covered Igloo	147.0	1.20
Kobe, Japan	1910	Dynamite	Barge	150.8	0.79
Manila, P. I.	1924	Dynamite, etc.	Unbarricaded Mag. 50x150	173.1	0.79
Indiana		Gun Powder	Frame Bldg. and RR Cars	177.6	0.58
		Rifle Powder	Magazine	179.2	0.58
Charleston		Ammon. Nitrate	Unbarricaded Building	193.0	0.42
Tessenderloo, Belgium					
Black Tom Island, N. Y. Harbor	1916	TNT	Freight Cars	200.0	1.00
Mindi Magazine, Canal Zone	1914	Dynamite	Unbarricaded Mag.	225.5	0.79
Sonemachi, Japan	1946	HE	Unbarricaded Dump	270.0	1.00
Baltimore, Md.	1913	Dynamite	Steamer	300.0	0.79
Acisate (Varese), Italy	1948	Ammo.	Underground Bunkers	350.0	1.00
Guadalcanal		Torpex	Steamer	400.0	1.25
Bari, Italy		Comp. B	Steamer	544.0	1.10
Hastings, Neb.		Torpex, TNT and DB Powder	Barricaded Bldg. 500 x 25	550.0	1.17
Pleasant Prairie, Wis.		Black Powder	Unbarricaded Mag.	587.5	0.58
Bombay, India	1944	HE .	Steamer	400.0	1.00
Lake Denmark, N. J.	1926	TNT	Unbarricaded Mag.	800.0	1.00
Bucharist, Rumania	1924	HE .	Building	1,000.0	1.00
Mt. Hood, Pacific Theatre	1944	HE	Steamer	1,000.0	1.00
Brest, France	1947	Ammonium Nitrate	Steamer	730.0	0.42
Texas City, Texas	1947	Ammonium Nitrate	Steamer	2,280.0	0.42
Port Chicago, Calif.	1944	HE	Steamer	2,136.0	1.00
Halifax, Nova Scotia	1917	HE	Steamer	2,600.0	1.00
Burton-on-Trent (Fauld)		Misc. Bombs	Barricade	2,670.0	1.00
Oppau, Germany	1921	Ammonium Nitrate	Open Pile	4,500.0	0.42

SECRET

MAXIMUM DEBRIS DISTANCE AND EXPLOSION PARAMETERS
FOR SELECTED EXPLOSIONS

2

SECRET

Type of Confinement	Quantity of Explosive, (tons)	Explosive Equivalence (TNT = 1.00)	Equivalent Weight of Explosives (tons TNT)	$W^{1/3}$, (tons TNT) ^{1/3}	Maximum Debris Distance (ft)	$W^{1/3}$ -Scaled Max. Debris Dis. (ft/tons ^{1/3})	Assumed Impulse Distance (ft)	Impulse (lb-msec/in. ²)	$W^{1/3}$ -Scaled Impulse, (lb-msec/in. ²) ^{1/3}
Building	81.59	0.58	43.75	3.62	900	249	15	11,268	3,119
Mag.	82.50	0.58	47.85	3.62	2,650	733	8	12,385	3,416
Unbarricaded Building	103.6	0.79	81.80	4.34	7,920	1,828	8	15,052	3,472
Unbarricaded Building	117.0	0.58	67.90	4.08	2,250	552	15	12,991	3,190
Unbarricaded Building	124.0	0.79	98.00	4.60	3,000	652	15	14,976	3,254
Barricaded Igloo	125.0	0.87	108.8	4.77	3,950	828	13	15,893	3,335
Earth Covered Igloo	147.0	1.20	176.3	5.60	6,000	1,071	13	19,023	3,398
Barge	150.8	0.79	119.0	4.91	17,920	3,650	20	15,383	3,131
Unbarricaded Mag. 50x150	173.1	0.79	136.9	5.15	1,800	350	25	15,510	3,015
Frame Bldg. and RR Cars	177.6	0.58	103.0	4.69	7,920	1,691	15	15,268	3,262
Magazine	179.2	0.58	104.0	4.70	2,400	511	8	16,241	3,492
Unbarricaded Building	193.0	0.42	81.05	4.32	5,280	1,220	15	13,921	3,221
Freight Cars	200.0	1.00	200.0	5.85	5,280	903	5	21,193	3,630
Unbarricaded Mag.	225.5	0.79	178.2	5.62	7,920	1,410	8	19,879	3,539
Unbarricaded Dump	270.0	1.00	270.0	6.46	2,400	372	30	19,650	3,046
Steamer	300.0	0.79	237.0	6.19	15,840	2,560	20	20,118	3,257
Underground Bunkers	350.0	1.00	75.0	4.21	1,500	356	24	12,189	2,894
Steamer	400.0	1.25	500.0	7.93	9,000	1,135	20	26,663	3,366
Steamer	544.0	1.10	599.0	8.42	4,500	535	20	28,498	3,389
Barricaded Bldg. 500 x 25	550.0	1.17	643.5	8.63	7,300	846	12	30,533	3,544
Unbarricaded Mag.	587.5	0.58	341.0	6.99	13,200	1,890	15	23,872	3,424
Steamer	400.0	1.00	400.0	7.36	3,900	530	20	24,532	3,336
Unbarricaded Mag.	800.0	1.00	800.0	9.28	5,280	569	15	32,495	3,508
Building	1,000.0	1.00	1,000.0	10.00	5,280	528	15	35,185	3,527
Steamer	1,000.0	1.00	1,000.0	10.00	6,600	660	20	34,395	3,447
Steamer	730.0	0.42	306.5	6.74	5,280	784	20	22,192	3,297
Steamer	2,280.0	0.42	958.0	9.85	11,500	1,168	20	33,857	3,443
Steamer	2,136.0	1.00	2,136.0	12.88	13,000	1,010	20	45,193	3,518
Steamer	2,600.0	1.00	2,600.0		18,480		20	50,528	
Barricade	2,670.0	1.00	2,670.0	13.86	4,346	314	20	48,924	3,536
Open Pile	4,500.0	0.42	1,890.0	12.34	4,920	399	70	35,737	2,898

SECRET

MAXIMUM DEBRIS DISTANCE AND EXPLOSION PARAMETERS FOR SELECTED EXPLOSIONS

Site	Year	Explosive Material	Type of Confinement	Quantity of (tons)	Explosive TNT = 1.00	Equivalent Weight of (tons TNT)	$W^{1/3}$ (tons TNT) ^{1/3}	Maximum Debris Distance (ft/tons ^{1/3})	$W^{1/3}$ -Scaled Max. Debris Distance (ft/tons ^{1/3})	Assumed Impulse (lb-msec/in. ²)	Impulse (lb-msec/in. ²)	$W^{1/3}$ -Scaled Impulse (lb-msec/in. ²)
King Powder Co. King's Mill, Ohio	1954	Black Powder	Barricaded Building	2,500	0.58	1,450	1.130	850	752	15	2,187	1,933
Furnace, Lochlyne, Scotland	1942	Black Powder	Barricaded Building	2,500	0.58	1,450	1.130	400	354	15	2,187	1,933
Essex, Ontario	1883	Black Powder	Unbarricaded Building	2,500	0.58	1,450	1.130	1,350	1,195	15	2,187	1,933
	1907	Dynamite	Freight Car	2,500	0.79	1,975	1.252	500	399	5	3,944	3,144
Offley Schaghticoke, N. Y.	1904	Comp. B	Truck	2,600	1.10	2,860	1.419	1,845	1,301	4	4,712	3,321
Cabot, Pa.	1910	Black Powder	Unbarricaded Building	2,900	0.58	1,682	1.188	300	253	15	2,384	2,005
Fairchance, Pa.	1942	Black Powder	Unbarricaded Building	3,000	0.58	1,740	1.202	500	415	15	2,431	2,022
Kankakee, Ill.	1943	Black Powder	2 Sides Barricaded Building	3,000	0.58	1,740	1.202	500	415	15	2,431	2,022
		Bi-Oil	Building	2,650	1.35	3,575	1.528	3,750	2,455	15	3,582	2,343
Norfolk, Va.	1943	Torpex	Bomb Trailer	3,025	1.25	3,781	1.555	1,000	644	4	5,231	3,360
Hazardville, Conn.	1913	Black Powder	Unbarricaded Building	3,350	0.58	1,939	1.246	900	642	15	2,587	2,074
Wilmington, Del.	1909	Black Powder	Barricaded Building	3,350	0.58	1,939	1.246	900	723	15	2,587	2,074
Faversham, England	1879	Black Powder	Unbarricaded Building	3,510	0.58	2,035	1.265	1,500	1,186	15	2,655	2,096
Sunflower Ordnance Wks.	1945	NG	Barricaded Building	3,700	1.35	4,995	1.707	2,425	1,422	15	4,228	2,475
Kenvil, N. J.	1943	NG	Barricaded Building	3,750	1.35	5,06	1.715	2,640	1,540	15	4,256	2,480
Hercules, Calif.	1953	Black Powder	Unbarricaded Building	3,750	0.58	2,175	1.295	5,280	4,080	15	2,754	2,126
Badger Ordnance Wks., Wis.	1945	NG	Unbarricaded Building	3,750	1.35	5,060	1.715	1,400	816	15	4,256	2,480
Marugame, Shikoku, Japan	1945	Picric Acid	Scrap Pile	3,750	1.11	4,160	1.607	300	187	5	5,268	3,276
Barkdale, Wis.	1945	NG	Barricaded Building	3,750	1.35	5,060	1.715	1,500	875	15	4,256	2,480
Hounslow, England	1887	Black Powder	Unbarricaded Building	3,750	0.58	2,175	1.295	930	719	15	2,754	2,126
Mt. Carmel, Calif.	1907	Black Powder	Unbarricaded Building	4,000	0.58	2,320	1.322	1,125	850	15	2,853	2,156
Selma, N. C.	1906	Tetryl and TNT	Truck	4,000	1.14	4,560	1.657	825	498	4	5,608	3,384
Mahanoy City, Pa.	1906	Dynamite	Tractor-Trailer	4,680	0.79	3,698	1.544	2,100	1,360	10	4,306	2,786
Barkdale, Wis.	1906	NG	Barricaded Building	4,835	1.35	6,525	1.866	500	268	15	4,806	2,573
Pittsburgh, Pa.	1894	Dynamite	Unbarricaded Mag.	5,000	0.79	3,950	1.580	1,000	633	8	4,718	2,986
Fairchance, Pa.	1944	Black Powder	Barricaded Building	5,000	0.58	2,900	1.425	1,050	737	15	3,214	2,254
Seneca, Ill.	1949	NG	Barricaded Building	5,174	1.35	6,990	1.910	5,280	2,765	15	4,961	2,597
Antwerp, Belgium	1889	Black Powder	Unbarricaded Building	6,000	0.58	3,480	1.512	2,640	1,745	15	3,532	2,331
Kenvil, N. J.	1948	NG	Barricaded Building	6,275	1.35	8,470	2,037	3,000	1,473	15	5,425	2,663
Wayne, N. J.	1916	Black Powder	Unbarricaded Building	6,438	0.58	3,735	1.550	2,000	1,290	15	3,660	2,360
Rainbow Factory, Essex	1945	Di-Nitro-Phenol	Barricaded Building	6,700	0.96	6,435	1.860	1,525	820	15	4,773	2,568
Railhead, Ordona, Italy	1945	TNT	Freight Car	6,800	1.00	6,800	1.893	2,000	1,058	5	6,340	3,348
La Jolla, Calif.	1945	Ammo. Van	Ammo. Van	7,250	1.00	7,250	1.935	1,675	866	4	6,649	3,438
Nebraska	1953	TNT	Trailer	8,085	1.00	8,085	2,003	1,000	499	4	6,918	3,449
McAlester, Okla.	1944	Torpex	Trailer in Front of Igloo	8,100	1.25	10,12	2.162	2,500	1,158	4	7,505	4,472
Allendorf, Germany	1944	Torpex	Unbarricaded Building	8,000	1.25	11,25	2.240	2,900	402	15	6,166	2,754
City Point, Va.	1864	Black Powder	Barges	9,000	0.58	4,640	1.667	1,500	900	20	3,462	2,077
Bradford, England	1917	Picric Acid	Unbarricaded Building	9,500	1.11	10,54	2.196	750	342	15	5,990	3,734
Kellogg, Ill.	1909	Black Powder	Barricaded Building	10,00	0.58	5,800	1.796	3,300	1,840	15	4,544	2,531
Holmes Park, Mo.	1908	Black Powder	Barricaded Building	10,00	0.58	5,800	1.796	1,000	557	15	4,544	2,531
Oakdale, Calif.	1908	Powder	Unbarricaded Mag.	10,00	0.58	5,800	1.796	1,400	779	8	5,526	3,075
Ce Elum, Wash.	1908	Black Powder	Unbarricaded Mag.	10,02	0.58	5,815	1.798	1,400	779	8	5,526	3,075
Wilpen, Minn.	1909	Black Powder	3 Sides Barricaded Building	10,50	0.58	6,095	1.827	6,600	3,614	15	4,651	2,548
Wilmington, Del.	1909	Black Powder	Unbarricaded Building	10,59	0.58	6,140	1.830	75	41	15	4,669	2,551
Oakdale, Pa.	1944	TNT	Building	12,00	1.00	12,00	2.286	2,640	1,155	15	5,526	3,075
Oahu, Hawaii	1944	Torpex	Loading Platform	12,00	1.25	15,00	2.465	2,000	811	20	6,166	2,754
Fontanet, Ind.	1907	Black Powder	Unbarricaded Building	12,50	0.58	7,250	1.935	375	194	15	5,526	3,075
Charleston	1908	Black Powder	Barricaded Mags.	12,50	0.58	7,250	1.935	1,200	621	8	4,651	2,548
Pindie, Calif.	1908	Dynamite	Barricaded Building	13,18	0.79	10,40	2.180	1,500	688	15	4,669	2,551
Newburgh Heights, Cleveland, Ohio	1912	Dynamite Black Powder	Unbarricaded Mags.	13,38	0.69	9,235	2.097	1,800	859	15	5,526	3,075
Gaçoigne Woods	1907	TNT	Unbarricaded	13,50	1.00	13,50	2.380	447	188	15	5,526	3,075
Reddick, Ill.	1907	Dynamite	Freight Car	15,00	0.79	11,85	2.280	7,920	3,474	5	7,783	4,783
Navajo Ordnance Depot	1949	Pentolite	Igloo	15,37	1.07	16,42	2.690	21,150	7,860	15	7,827	2,912
			Barricaded and Unbarricaded	16,40	1.14	19,48	2.690	21,150	7,860	15	7,827	2,912

A-5

MAXIMUM DEBRIS DISTANCE AND EXPLOSION PAF
FOR SELECTED EXPLOSIONS

1

Site	Year	Explosive Material	Type of Confinement	Quantity of Explosive (tons)	Explosive Equivalence
Indiana Ordnance Wks		Smokeless Powder	Building	81.59	0.5
Beira, Portugal	1880	Black Powder	Mag.	82.50	0.5
Highland Station, Calif.	1892	Dynamite	Unbarricaded Building	103.6	0.7
Haskell, N. J.	1917	Smokeless Powder	Unbarricaded Building	117.0	0.5
Rio de Janeiro, Brazil	1925	Dynamic	Unbarricaded Building	124.0	0.7
Arco, Idaho	1945	50/50 Amatol	Barricaded Igloo	125.0	0.8
Savanna Ordnance Depot	1948	Tetrytol	Earth Covered Igloo	147.0	1.2
Kobe, Japan	1910	Dynamite	Barge	150.8	0.7
Manila, P. I.	1924	Dynamite, etc.	Unbarricaded Mag. 50x150	173.1	0.7
Indiana		Gun Powder	Frame Bldg. and RR Cars	177.6	0.5
		Rifle Powder			
Charleston		Ammon. Nitrate	Magazine	179.2	0.5
Tessengerloo, Belgium			Unbarricaded Building	193.0	0.4
Black Tom Island, N. Y. Harbor	1916	TNT	Freight Cars	200.0	1.0
Mindi Magazine, Canal Zone	1914	Dynamite	Unbarricaded Mag.	225.5	0.7
Sonemachi, Japan	1946	HE	Unbarricaded Dump	270.0	1.0
Baltimore, Md.	1913	Dynamite	Steamer	300.0	0.7
Acisate (Varese), Italy	1948	Ammo.	Underground Bunkers	350.0	1.0
Guadalcanal		Torpex	Steamer	400.0	1.2
Bari, Italy		Comp. B	Steamer	544.0	1.1
Hastings, Neb.		Torpex, TNT and DB Powder	Barricaded Bldg. 500 x 25	550.0	1.1
Pleasant Prairie, Wis.		Black Powder	Unbarricaded Mag.	587.5	0.5
Bombay, India	1944	HE .	Steamer	400.0	1.0
Lake Denmark, N. J.	1926	TNT	Unbarricaded Mag.	800.0	1.0
Bucharist, Rumania	1924	HE .	Building	1,000.0	1.0
Mt. Hood, Pacific Theatre	1944	HE	Steamer	1,000.0	1.0
Brest, France	1947	Ammonium Nitrate	Steamer	730.0	0.4
Texas City, Texas	1947	Ammonium Nitrate	Steamer	2,280.0	0.4
Port Chicago, Calif.	1944	HE	Steamer	2,136.0	1.0
Halifax, Nova Scotia	1917	HE	Steamer	2,600.0	1.0
Burton-on-Trent (Fauld)		Misc. Bombs	Barricade	2,670.0	1.0
Oppau, Germany	1921	Ammonium Nitrate	Open Pile	4,500.0	0.4

SECRET

MAXIMUM DEBRIS DISTANCE AND EXPLOSION PARAMETERS
FOR SELECTED EXPLOSIONS

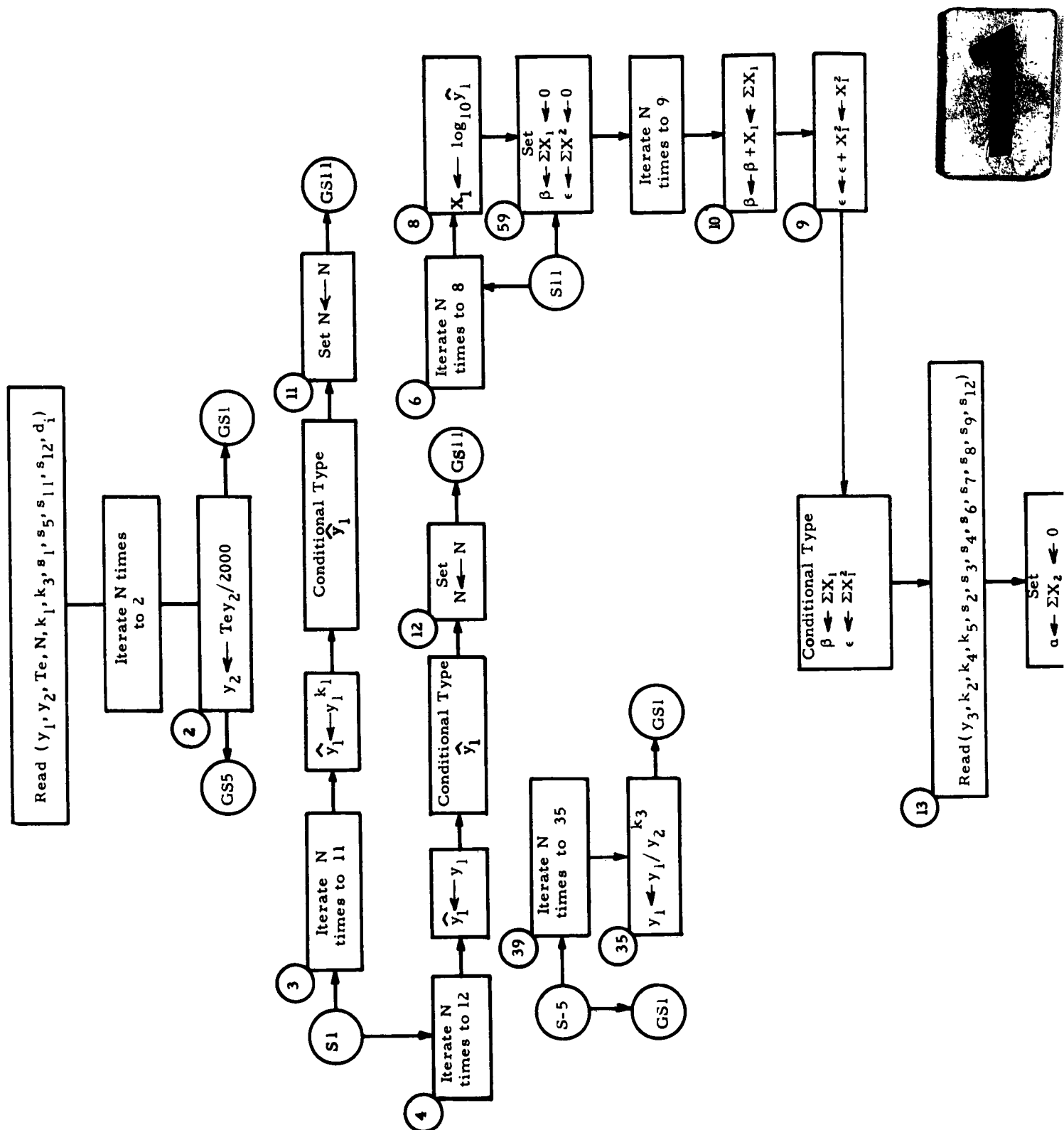
Type of Confinement	Quantity of Explosive, (tons)	Explosive Equivalence (TNT=1.00)	Equivalent Weight of Explosives (tons TNT)	$W^{1/3}$, (tons TNT) ^{1/3}	Maximum Debris Distance (ft)	$W^{1/3}$ -Scaled Max. Debris Dis. (ft/tons ^{1/3})	Assumed Impulse Distance (ft)	Impulse (lb-msec/in. ²)	$W^{1/3}$ -Scaled Im-pulse, (lb-msec/in. ² tons ^{1/3})
Building	81.59	0.58	43.75	3.62	900	249	15	11,268	3,119
Mag.	82.50	0.58	47.85	3.62	2,650	733	8	12,385	3,416
Unbarricaded Building	103.6	0.79	81.80	4.34	7,920	1,828	8	15,052	3,472
Unbarricaded Building	117.0	0.58	67.90	4.08	2,250	552	15	12,991	3,190
Unbarricaded Building	124.0	0.79	98.00	4.60	3,000	652	15	14,976	3,254
Barricaded Igloo	125.0	0.87	108.8	4.77	3,950	828	13	15,893	3,335
Earth Covered Igloo	147.0	1.20	176.3	5.60	6,000	1,071	13	19,023	3,398
Barge	150.8	0.79	119.0	4.91	17,920	3,650	20	15,383	3,131
Unbarricaded Mag. 50x150	173.1	0.79	136.9	5.15	1,800	350	25	15,510	3,015
Frame Bldg. and RR Cars	177.6	0.58	103.0	4.69	7,920	1,691	15	15,268	3,262
Magazine	179.2	0.58	104.0	4.70	2,400	511	8	16,241	3,492
Unbarricaded Building	193.0	0.42	81.05	4.32	5,280	1,220	15	13,921	3,221
Freight Cars	200.0	1.00	200.0	5.85	5,280	903	5	21,193	3,630
Unbarricaded Mag.	225.5	0.79	178.2	5.62	7,920	1,410	8	19,879	3,539
Unbarricaded Dump	270.0	1.00	270.0	6.46	2,400	372	30	19,650	3,046
Steamer	300.0	0.79	237.0	6.19	15,840	2,560	20	20,118	3,257
Underground Bunkers	350.0	1.00	75.0	4.21	1,500	356	24	12,189	2,894
Steamer	400.0	1.25	500.0	7.93	9,000	1,135	20	26,663	3,366
Steamer	544.0	1.10	599.0	8.42	4,500	535	20	28,498	3,389
Barricaded Bldg. 500 x 25	550.0	1.17	643.5	8.63	7,300	846	12	30,533	3,544
Unbarricaded Mag.	587.5	0.58	341.0	6.99	13,200	1,890	15	23,872	3,424
Steamer	400.0	1.00	400.0	7.36	3,900	530	20	24,532	3,336
Unbarricaded Mag.	800.0	1.00	800.0	9.28	5,280	569	15	32,495	3,508
Building	1,000.0	1.00	1,000.0	10.00	5,280	528	15	35,185	3,527
Steamer	1,000.0	1.00	1,000.0	10.00	6,600	660	20	34,395	3,447
Steamer	730.0	0.42	306.5	6.74	5,280	784	20	22,192	3,297
Steamer	2,280.0	0.42	958.0	9.85	11,500	1,168	20	33,857	3,443
Steamer	2,136.0	1.00	2,136.0	12.88	13,000	1,010	20	45,193	3,518
Steamer	2,600.0	1.00	2,600.0		18,480		20	50,528	
Barricade	2,670.0	1.00	2,670.0	13.86	4,346	314	20	48,924	3,536
Open Pile	4,500.0	0.42	1,890.0	12.34	4,920	399	70	35,737	2,898

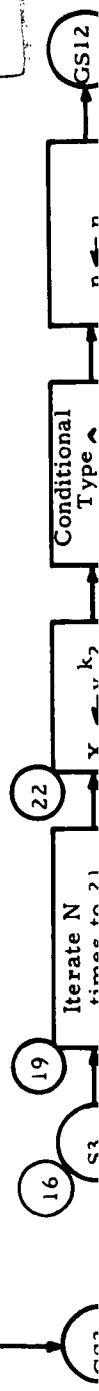
SECRET

APPENDIX B
COMPUTER PROGRAM FOR REGRESSION STUDY
OF HE EXPLOSIONS

SECRET

SECRET





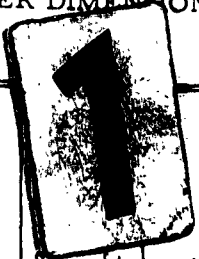


SECRET

APPENDIX C
MAXIMUM DEBRIS DISTANCE AND CRATER DIMENSIONS
FOR SELECTED EXPLOSIONS

SECRET

MAXIMUM DEBRIS DISTANCE AND CRATER DIMENSIONS FOR



Site	Year	Explosive Material	Quantity of Explosives, (tons)	Explosive Equivalence (TNT=1.00)	Equivalent Weight of Explosives, (tons TNT)	W ^{1/3} (tons T)	Crater Diameter, (ft)
Sunflower Ordnance Wks	1944	Powder	0.250	0.58	0.145	0.525	12.0
Perranporth, England	1902	Gelatin	0.266	1.35	0.360	0.711	17.0
Umbogintwini, Natal	1909	NG	1.050	1.35	1.418	1.122	18.0
Sherborne, England	1944	TNT	0.250	1.00	0.250	0.630	15.0
Lower Hope Point, England	1902	NG	0.500	1.35	0.675	0.876	16.0
Earle, N.J.	1946	Torpex	4.896	1.25	6.120	1.827	20.0
Cabot, Pa.	1910	Black Powder	3.000	0.58	1.740	1.201	25.0
Alconbury, England	1943	Bombs	1.250	1.00	1.250	1.077	22.5
Uplee's Marshes, England	1903	NG	0.50	1.35	0.675	0.876	30.0
Selma, N. C.	1942	Tetryl	4.000	1.14	4.560	1.657	14.3
Barksdale, Wis.	1906	NG	4.835	1.35	6.520	1.867	40.0
Honshu, Japan	1945	Bombs	0.050	1.00	0.050	0.368	30.0
Ikego Ammunition Depot	1947	Ammo	74.00	1.00	74.00	4.200	30.0
Winsted, Conn.	1892	Black Powder	1.250	0.58	0.725	0.898	30.0
Mt. Carmel, Pa.	1907	Black Powder	4.000	0.58	2.320	1.322	40.0
Badger Ordnance Wks., Wis.	1945	NG	3.750	1.35	5.060	1.715	47.0
Ft. Belvoir, Va.	1948	AN Cratering Explosive	0.160	1.00	0.160	0.543	39.5
Kurihama Naval Base, Japan	1945	Ammo	32.50	1.00	32.50	3.188	40.0
Nebraska	1953	TNT	8.085	1.00	8.085	2.010	51.5
Cleveland, Ohio	1912	Dynamite Black Powder	13.375	0.69	9.235	2.097	60.0
N. A. D., Oahu, Hawaii	1944	Torpex	12.000	1.25	15.00	2.464	60.0
Railhead, Ortona, Italy	1945	TNT	6.800	1.00	6.800	1.894	45.0
McAlester, Okla.	1908	Black Powder	22.47	0.58	13.036	2.372	50.0
Marugama, Shikoku, Japan	1945	Picric Acid	3.750	1.11	4.163	1.607	75.0
Sunflower Ordnance Wks	1945	NG	3.700	1.35	4.995	1.708	55.5
Highland Station, Calif.	1892	Dynamite	103.6	0.79	8.180	2.015	50.0
Gibbstown, N.J.	1929	NG	1.500	1.35	2.025	1.264	47.8
Chicago, Ill.	1886	Black Powder	81.00	0.58	46.98	3.606	95.0
Erith, England	1864	Black Powder	41.75	0.58	24.22	2.892	75.0
Kuba, Okinawa	1945	Dynamite	1.250	0.79	0.988	0.995	75.0
Manila, P.I.	1924	Dynamite	173.0	0.79	136.7	5.150	120.0
Antwerp, Belgium	1889	Black Powder	6.000	0.58	3.480	1.513	150.0
Reddick, Ill.	1907	Dynamite	15.00	0.79	11.85	2.279	120.0
Black Tom Island, N. Y. Harbor	1916	TNT - Picric Acid	200.0	1.06	212.0	5.958	275.0
Okinawa	1950	Dynamite	48.01	0.79	37.92	3.356	130.0
Johannesburg, So. Africa	1896	Gelatin	55.35	1.35	74.72	4.206	182.5

SECRET

SECRET

2

CRATER DISTANCE AND CRATER DIMENSIONS FOR SELECTED EXPLOSIONS

Quantity of Explosives, (tons)	Explosive Equivalence (TNT=1.00)	Equivalent Weight of Explosives, (tons TNT)	$W^{1/3}$, $(\text{tons TNT})^{1/3}$	Crater Diameter, (ft)	Crater Depth, (ft)	Crater Volume, (cu ft)	$W^{1/3}$ -Scaled Crater Dia. $(\text{ft/tons TNT})^{1/3}$	$W^{1/3}$ -Scaled Crater Depth, $(\text{ft/tons TNT})^{1/3}$	$W^{1/3}$ -Scaled Crater Volume, $(\text{cu ft/tons TNT})^{1/3}$	Maximum Debris Distance, (ft)	$W^{1/3}$ -Scaled Debris Distance, $(\text{ft/tons TNT})^{1/3}$
0.250	0.58	0.145	0.525	12.0	3.5	198	22.84	6.66	377	5,250	10,000
0.266	1.35	0.360	0.711	17.0	3.0	341	23.90	4.22	429	1,050	1,477
1.050	1.35	1.418	1.122	18.0	3.0	381	16.02	2.67	339	500	445
0.250	1.00	0.250	0.630	15.0	4.5	397	23.80	7.15	630	1,500	2,380
0.500	1.35	0.675	0.876	16.0	4.0	402	18.25	4.56	458	450	514
4.896	1.25	6.120	1.827	20.0	4.5	706	10.94	2.46	386	400	219
3.000	0.58	1.740	1.201	25.0	3.25	798	20.80	2.70	664	500	416
1.250	1.00	1.250	1.077	22.5	4.5	895	20.90	4.18	831	2,640	2,452
0.50	1.35	0.675	0.876	30.0	4.5	1,590	34.23	5.13	1,814	150	1,711
4.000	1.14	4.560	1.657	14.3	27.5	2,204	8.65	16.62	1,332	750	453
4.835	1.35	6.520	1.867	40.0	5.0	3,140	21.42	2.68	1,682	500	268
0.050	1.00	0.050	0.368	30.0	10.0	3,534	81.50	27.20	9,600	450	1,222
74.00	1.00	74.00	4.200	30.0	12.0	4,245	7.14	2.86	1,010	3,300	785
1.250	0.58	0.725	0.898	30.0	15.0	5,300	33.40	16.72	5,900	1,320	1,470
4.000	0.58	2.320	1.322	40.0	9.0	5,650	20.24	6.80	4,270	1,125	851
3.750	1.35	5.060	1.715	47.0	9.5	8,230	27.40	5.54	4,800	1,400	816
0.160	1.00	0.160	0.543	39.5	14.5	8,890	72.75	26.70	16,380	900	1,658
32.50	1.00	32.50	3.188	40.0	15.0	9,425	12.55	4.70	2,956	1,200	376
8.085	1.00	8.085	2.010	51.5	12.0	12,500	25.62	5.97	6,220	2,640	1,313
13.375	0.69	9.235	2.097	60.0	10.0	14,120	28.63	4.77	6,740	1,800	859
12.000	1.25	15.00	2.464	60.0	10.0	14,130	24.36	4.06	5,740	2,000	811
6.800	1.00	6.800	1.894	45.0	18.0	14,300	23.77	9.50	7,550	2,000	1,056
22.47	0.58	13.036	2.372	50.0	15.0	14,720	21.07	6.32	6,202	3,960	1,670
3.750	1.11	4.163	1.607	75.0	8.0	17,640	46.70	4.98	10,980	300	187
3.700	1.35	4.995	1.708	55.5	15.0	18,120	32.50	8.79	10,615	5,400	3,162
103.6	0.79	8.180	2.015	50.0	22.0	21,560	24.83	10.92	10,700	7,920	3,932
1.500	1.35	2.025	1.264	47.8	40.0	35,900	37.80	31.63	28,400	10,560	8,350
81.00	0.58	46.98	3.606	95.0	15.0	53,100	26.37	4.15	14,730	3,300	915
41.75	0.58	24.22	2.892	75.0	25.0	55,100	25.92	8.65	19,050	13,200	4,560
1.250	0.79	0.988	0.995	75.0	25.0	55,200	75.40	25.14	55,500	1,200	1,206
173.0	0.79	136.7	5.150	120.0	12.0	67,800	23.28	2.33	13,180	1,800	350
6.000	0.58	3.480	1.513	150.0	12.0	106,000	99.10	7.94	70,000	1,760	1,162
15.00	0.79	11.85	2.279	120.0	20.0	113,000	52.60	8.78	49,500	2,800	1,228
200.0	1.06	212.0	5.958	275.0	8.5	252,400	46.12	1.43	42,400	5,280	886
48.01	0.79	37.92	3.356	130.0	40.0	265,300	38.75	11.92	79,100	1,600	477
55.35	1.35	74.72	4.206	182.5	30.0	392,000	43.42	7.14	93,200	9,000	2,140

SECRET

APPENDIX D
FRAGMENT-SIZE DISTRIBUTION AND DISPERSION
OF FRAGMENTS
FROM PANTEX ORDNANCE PLANT EVENT

SECRET

SECRET

RECOVERY OF FRAGMENTS FOR A REINFORCED CONCRETE STRUCTURE
(Pantex Ordnance Plant Event)

SECRET

Fragment Size, (lb)	Number of Fragments Recovered at Various Ground Ranges, (ft)															Total: 0-1500
	0-100	100-200	200-300	300-400	400-500	500-600	600-700	700-800	800-900	900-1000	1000-1100	1100-1200	1200-1300	1300-1400	1400-1500	
1/16					1	5	11	12	7	7	4	4		4	1	56
1/8				840		8	31	6	4	5	4	3	2	2	1	906
1/4	3,755	2,228	1,349	3,043	4,404	2,043	659	360	174	76	37	4	2	4	1	18,138
1/3					1	1	1	1	1	2	2			2		12
1/2					1	6	12	7	5	4	1		1	2	1	40
3/4	312	2,237	1,195	1,356	195	239	178	89	27	9	17		3	1		5,858
1		1				5	9	5	6	2	3	1				32
1-1/4							2									1
1-1/2						6				2						10
2	338	449	335	417	265	250	178	145	80	24	15	6				2,502
2-1/2				7	1											8
3	311	602	303	367	416	307	107	132	81	43	10	1				2,680
3-1/3					1											1
3-1/2	10	4	1	2			2	4	2							14
4				3	6		2	1								12
5																2
6							1									1
7				1				3								1
8																1
9																1
10																7
12		7														106
14	3	101		1			1									13
15				13												2
18						2										9
20																1
40	1			1		1			1							4
50				1												1
60	39	22	43	22	26	13	23	32	8	10	2					240
70		5		11			1									17
75	1	2	2	5	3	2	11	5	8	1	1					41
80																1
90	54	26	42	38	55	22	1	6	3		1					248
95	1				1											2
100																6
150		1														1
180		23	6	2		1										81
225		1														1
4000																1
Totals:	4,874	5,720	3,286	6,130	5,376	2,912	1,230	808	407	185	97	19	9	15	4	31,072

SECRET

MATERIAL AND FRAGMENT DISPERSION FROM A REINFORCED CONCRETE STRUCTURE (Pantex Ordnance Plant Event)

Ground Range, (ft)	Area, (sq ft)	Number of Fragments,	Total Weight of Fragments, (lb)	Average Fragment Weight, (lb)	Specific Area, (sq ft/fragment)	Material Dispersion, (sq ft/lb)	Ground Range, (ft)	Area, (sq ft)	Number of Fragments	Total Weight of Fragments, (lb)	Average Fragment Weight, (lb)	Specific Area, (sq ft/fragment)	Material Dispersion, (sq ft/lb)
0-50	7,854	2,627	11,330	4.32	2.32	0.69	0-100	31,416	4,874	18,883	3.86	6.45	1.66
50-100	23,562	2,247	7,553	3.36	10.48	3.12	100-200	94,248	5,720	19,077	3.34	16.48	4.95
100-150	39,270	1,683	8,418	5.00	23.33	4.67	200-300	157,079	3,286	11,074	3.37	47.85	14.20
150-200	54,978	4,037	10,659	2.64	13.62	5.16	300-400	219,912	6,130	10,386	1.69	35.83	21.20
200-250	70,686	1,160	5,542	4.78	60.90	12.75	400-500	283,745	5,376	9,902	1.84	52.80	28.63
250-300	86,393	2,126	5,532	2.60	40.60	15.61	500-600	345,570	2,912	5,364	1.84	118.6	64.40
300-350	102,102	2,543	6,043	2.37	40.20	16.92	600-700	408,410	1,239	3,404	2.76	332.0	120.0
350-400	117,810	3,587	4,343	1.21	32.84	27.12	700-800	471,240	808	3,734	4.62	583.0	126.2
400-450	134,518	2,321	5,498	2.37	58.00	24.48	800-900	534,070	407	1,872	4.60	1,311	285.0
450-500	149,227	3,055	4,404	1.44	48.90	33.86	900-1000	596,900	185	887.1	4.80	3,225	673.0
500-550	164,930	1,135	3,196	1.50	77.20	51.50	1000-1100	659,740	97	371.3	3.83	6,800	1,778
550-600	180,640	777	2,167	2.79	232.4	87.40	1100-1200	722,560	19	17.87	0.940	38,040	40,500
600-650	196,350	619	1,139	1.85	317.6	172.3	1200-1300	785,400	9	4.50	0.500	87,267	174,500
650-700	212,060	611	2,265	3.71	346.7	93.60	1300-1400	848,230	15	3.92	0.261	56,549	216,300
700-750	227,770	456	2,581	5.66	499.0	88.10	1400-1500	911,060	4	1.35	0.338	227,765	675,000
750-800	243,470	352	1,153	3.28	691.0	211.0							
800-850	259,180	290	1,266	4.36	894.0	204.6							
850-900	274,890	117	606.3	5.18	2,350	451.0							
900-950	290,600	101	642.7	6.36	2,878	452.0							
950-1000	306,300	84	244.4	2.91	3,244	1,254							
1000-1050	322,020	76	141.4	1.86	4,310	2,278							
1050-1100	337,720	21	229.9	10.95	1,380	1,468							
1100-1150	353,430	9	8,062	0.896	39,270	43,800							
1150-1200	369,130	10	9,810	0.981	36,913	37,600							
1200-1250	384,850	7	4,125	0.589	54,880	53,300							
1250-1300	400,550	2	0.375	0.198	200,275	1,069,000							
1300-1350	416,260	8	2,334	0.292	52,030	178,500							
1350-1400	431,970	7	1,583	0.226	61,710	272,800							
1400-1450	447,680	4	1,348	0.337	111,920	332,000							
1450-1500	463,380	0	0	0	0	-							

SECRET

SECRET

**FRAGMENT-SIZE DISTRIBUTION FOR REINFORCED CONCRETE STRUCTURE
(Pantex Ordnance Plant Event)**

Fragment Size, (lb)	Number of Fragments	Percent of Total Fragments	Cumulative Number of Fragments	Cumulative Percent of Total Fragments	Weight of Fragments, (lb)	Percent of Total Weight	Cumulative Weight of Fragments, (lb)	Cumulative Percent of Total Weight
1/16	56	0.180	56	0.18	3.5	0.0041	3.5	0.004
1/8	906	2.916	962	3.10	113.25	0.133	116.75	0.137
1/4	18,138	58.374	19,100	61.47	4,534.5	5.324	4,651.25	5.461
1/3	12	0.039	19,112	61.51	4.0	0.005	4,655.25	5.466
1/2	40	0.129	19,152	61.64	20.0	0.023	4,675.25	5.490
3/4	5,858	18.853	25,010	80.49	4,393.5	5.159	9,068.75	10.64
1	32	0.103	24,042	80.59	32.0	0.038	9,100.75	10.69
1-1/4	1	0.003	25,043	80.60	1.25	0.001	9,102.0	10.69
1-1/2	10	0.032	25,053	80.63	15.0	0.018	9,117.0	10.71
2	2,502	8.052	27,555	88.68	5,004.0	5.876	14,121.0	16.58
2-1/2	8	0.026	27,563	88.71	20.0	0.023	14,141.0	16.60
3	2,680	8.625	30,243	97.33	8,040.0	9.440	22,181.0	26.04
3-1/3	1	0.003	30,244	97.34	3.33	0.004	22,184.0	26.05
3-1/2	14	0.045	30,258	97.38	49.0	0.058	22,233.0	26.11
4	12	0.039	30,270	97.42	48.0	0.056	22,281.0	26.16
5	2	0.006	30,272	97.43	10.0	0.012	22,291.0	26.17
6	13	0.042	30,285	97.47	78.0	0.092	22,369.0	26.27
7	1	0.003	30,286	97.47	7.0	0.008	22,376.0	26.27
8	3	0.010	30,289	97.48	24.0	0.028	22,400.0	26.30
9	1	0.003	30,290	97.48	9.0	0.011	22,409.0	26.31
10	7	0.023	30,297	97.51	70.0	0.082	22,479.0	26.39
12	106	0.341	30,403	97.85	1,272.0	1.493	23,751.0	27.89
14	13	0.042	30,416	97.89	182.0	0.214	23,933.0	28.10
15	2	0.006	30,418	97.90	30.0	0.035	23,963.0	28.14
18	9	0.029	30,427	97.92	162.0	0.190	24,125.0	28.33
20	1	0.003	30,428	97.93	20.0	0.023	24,145.0	28.35
40	4	0.0129	30,432	97.94	160.0	0.188	24,305.0	28.54
50	1	0.003	30,433	97.94	50.0	0.059	24,355.0	28.60
60	240	0.772	30,673	98.72	14,400.0	16.908	38,755.0	45.51
70	17	0.055	30,690	98.77	1,190.0	1.397	39,945.0	46.90
75	41	0.132	30,731	98.90	3,075.0	3.610	43,020.0	50.51
80	1	0.003	30,732	98.91	80.0	0.094	43,100.0	50.61
90	248	0.798	30,980	99.70	22,320.0	26.208	65,420.0	76.82
95	2	0.006	30,982	99.71	190.0	0.223	65,610.0	77.04
100	6	0.019	30,988	99.73	600.0	0.705	66,210.0	77.74
150	1	0.003	30,989	99.73	150.0	0.176	66,360.0	77.92
180	81	0.261	31,070	99.994	14,580.0	17.120	80,940.0	95.04
225	1	0.003	31,071	99.997	225.0	0.264	81,165.0	95.30
4000	1	0.003	31,072	100.000	4,000.0	4.697	85,165	100.00

SECRET

SECRET

APPENDIX E
FRAGMENTATION DATA
ON EXPLODED DRY SANDSTONE BLOCKS

SECRET

SECRET

FRAGMENTATION DATA ON EXPLODED DRY SANDSTONE BLOCKS

Test: B Block Dimensions: 18-in. diameter x 30-in. long
 Shothole Diameter: 3/4 in. Explosive: XL Hawkite
 Diameter of Explosive: 5/8 in. Weight of Explosive: 2 oz

Size Range of Fragments	Average Diameter, (in.)	Total Class Weight, (gm)	Total Class Weight, (lb)	Average Weight per Fragment, (lb)	Number of Fragments in Class	Cumulative Number of Fragments	Cumulative Percent of Total Fragments	Minimum Fragment Weight in Class, (lb)
Over 8 inch	(12)	57,400	126.5	62.9	2.013	2.013	0.0124	18.68
4 - 8 inch	6	44,700	98.5	7.86	12.51	14.52	0.0887	2.332
2 - 4 inch	3	43,800	96.5	0.983	98.15	112.7	0.688	0.2916
1 - 2 inch	1.5	31,800	70.1	0.1229	571.0	684.0	4.175	0.03644
1/2 - 1 inch	0.72	20,500	45.2	0.01535	2,945.0	3,629.0	22.18	0.00455
1/4 - 1/2 inch	0.375	11,100	24.5	0.00192	12,760.0	16,389.0	100.0	0.00057
1/16 - 1/4 inch		12,300						
500 microns - 1/16 inch		3,330						
251 - 500 microns		5,920						
124 - 251 microns		5,820						
66 - 124 microns		2,030						
20 - 66 microns		1,060						
10-20 microns		200						
5 - 10 microns		159						
2 - 5 microns		122						
Under 2 microns		68						
Total Weight of Recovered Material		240,309	530.0					
Total Weight of Material above 1/4-in. Fragment Size		209,300 (87.1%)	461.3					
Original Volume of Material (less shothole) cu. in.		7612						
Computed Density of Material, lb/cu. in.			0.0696					

SECRET

SECRET

FRAGMENTATION DATA ON EXPLODED DRY SANDSTONE BLOCKS

SECRET

Test: C Block Dimensions: 18-in. diameter x 30-in. long
 Shothole Diameter: 1 in. Explosive: XL Hawkite
 Diameter of Explosive: 7/8 in. Weight of Explosive: 2 oz

Size Range of Fragments	Average Diameter, (in.)	Total Class Weight, (gm)	Total Class Weight, (lb)	Average Weight per Fragment, (lb)	Number of Fragments in Class	Cumulative Number of Fragments	Cumulative Percent of Total Fragments	Minimum Fragment Weight in Class, (lb)
Over 8 inch	(12)	55,500	122.2	65.4	1.87	1.87	0.0063	19.38
4 - 8 inch	6	72,800	160.4	8.18	19.61	21.48	0.072	2.42
2 - 4 inch	3	43,300	95.5	1.022	93.45	115.0	0.386	0.313
1 - 2 inch	1.5	17,200	37.9	0.1278	296.0	411.0	1.38	0.038
1/2 - 1 inch	0.75	9,530	21.0	0.016	1,315.0	1,726	5.79	0.0047
1/4 - 1/2 inch	0.375	25,500	56.2	0.002	28,100.0	29,826	100.0	0.00059
1/16 - 1/4 inch		9,980						
500 microns - 1/16 inch		1,550						
251 - 500 microns		5,060						
124 - 251 microns		5,600						
66 - 124 microns		1,680						
20 - 66 microns		876						
10 - 20 microns		224						
5 - 10 microns		165						
2 - 5 microns		116						
Under 2 microns		72						
Total Weight of Recovered Material		249,153	549.5					
Total Weight of Material above 1/4-in. Fragment Size		223,830 (89.9%)	493.2					
Original Volume of Material (less shothole), cu.in.		7601						
Computed Density of Material, lb/cu.in.			0.0723					

SECRET

FRAGMENTATION DATA ON EXPLODED DRY SANDSTONE BLOCKS

SECRET

Test:	D	Block Dimensions: 18-in. diameter x 30-in. long						
Shothole Diameter:	3/4 in.	Explosive: Colex						
Diameter of Explosive	5/8 in.	Weight of Explosive: 2 oz.						
Size Range of Fragments	Average Diameter, (in.)	Total Class Weight, (gm)	Total Class Weight, (lb)	Average Weight per Fragment, (lb)	Number of Fragments in Class	Cumulative Number of Fragments	Cumulative Percent of Total Fragments	Minimum Fragment Weight in Class, (lb)
Over 8 inch	(12)	61,000	134.7	66.35	2.03	2.03	0.0132	19.65
4 - 8 inch	6	43,900	96.8	8.30	11.65	13.68	0.0892	2.46
2 - 4 inch	3	49,800	109.9	1.037	106.1	119.78	0.078	0.307
1 - 2 inch	1.5	37,500	82.9	0.130	636.0	756.0	4.93	0.0384
1/2 - 1 inch	0.75	23,200	51.2	0.0162	3,160.0	3,916.0	25.52	0.0048
1/4 - 1/2 inch	0.375	9,580	21.14	0.00203	11,405.0	15,331.0	100.0	0.0006
1/16 - 1/4 inch		11,400						
500 microns - 1/16 inch		3,950						
251 - 500 microns		7,110						
124-251 microns		5,730						
66 - 124 microns		1,780						
20 - 66 microns		750						
10 - 20 microns		174						
5 - 10 microns		165						
2 - 5 microns		127						
Under 2 microns		43						
Total Weight of Recovered Material		256,209	565.5					
Total Weight of Material above 1/4-in. Fragment Size		224,980 (87.9%)	496.4					
Original Volume of Material (less shothole), cu.in.		7612						
Computed Density of Material, lb/cu.in.			0.0734					

SECRET

FRAGMENTATION DATA ON EXPLODED DRY SANDSTONE BLOCKS

Test: E Block Dimensions: 18-in. diameter x 30-in. long
 Shothole Diameter: 3/4 in. Explosive: Colex
 Diameter of Explosive: 5/8 in. Weight of Explosive: 1 oz

Size Range of Fragments	Average Diameter, (in.)	Total Class Weight, (gm)	Total Class Weight, (lb)	Average Weight per Fragment, (lb)	Number of Fragments in Class	Cumulative Number of Fragments	Cumulative Percent of Total Fragments	Minimum Fragment Weight in Class, (lb)
Over 8 inch	(12)	94,400	208.0	62.8	3.32	3.32	0.0522	18.6
4 - 8 inch	6	60,100	132.5	7.85	16.89	20.21	0.318	2.325
2 - 4 inch	3	38,600	85.1	0.981	86.7	106.9	1.68	0.2906
1 - 2 inch	1.5	25,200	55.5	0.1226	452.0	559.0	8.78	0.0363
1/2 - 1 inch	0.75	6,690	14.7	0.0153	964.0	1,523.0	23.96	0.0045
1/4 - 1/2 inch	0.375	4,170	9.2	0.0019	4,835.0	6,358.0	100.0	0.00056
1/16 - 1/4 inch		3,490						
500 microns - 1/16 inch		1,560						
251 - 500 microns		2,230						
124 - 251 microns		1,810						
66 - 124 microns		567						
20 - 66 microns		262						
10-20 microns		74						
5 - 10 microns		67						
2 - 5 microns		42						
Under 2 microns		14						
Total Weight of Recovered Material		239,276	528.0					
Total Weight of Material above 1/4-in. Fragment Size		229,160 (95.8%)	505.0					
Original Volume of Material (less shothole), cu. in.		7.612						
Computed Density of Material, lb/cu. in.			0.0694					

SECRET

SECRET

FRAGMENTATION DATA ON EXPLODED DRY SANDSTONE BLOCKS

Test: F Block Dimensions: 18-in. diameter x 30-in. long
 Shothole Diameter: 5/8 in. Explosive: Rounkol
 Diameter of Explosive: 1/2 in. Weight of Explosive: 1 oz

Size Range of Fragments	Average Diameter, (in.)	Total Class Weight, (gm)	Total Class Weight, (lb)	Average Weight per Fragment, (lb)	Number of Fragments in Class	Cumulative Number of Fragments	Cumulative Percent of Total Fragments	Minimum Fragment Weight in Class, (lb)
Over 8 inch	(12)	102,000	225.0	66.2	3.40	3.40	0.058	19.6
4 - 8 inch	6	55,000	121.2	8.28	14.65	18.05	0.308	2.45
2 - 4 inch	3	46,000	101.5	1.035	98.1	116.15	1.982	0.3066
1 - 2 inch	1.5	29,900	66.0	0.1293	511.0	627.0	10.7	0.0384
1/2 - 1 inch	0.75	7,600	16.75	0.0162	1,036.0	1,663.0	28.3	0.0048
1/4 - 1/2 inch	0.375	3,860	8.51	0.00202	4,205.0	5,868.0	100.0	0.0006
1/16 - 1/4 inch		3,180						
500 microns - 1/16 inch		1,440						
251 - 500 microns		1,510						
124 - 251 microns		1,560						
66 - 124 microns		495						
20 - 66 microns		260						
10 - 20 microns		66						
5 - 10 microns		51						
2 - 5 microns		32						
Under 2 microns		18						
Total Weight of Recovered Material		252,972	557.2					
Total Weight of Material above 1/4 in. Fragment Size		244,360 (96.6%)	539.0					
Original Volume of Material (Less shothole), cu. in.		7,616						
Computed Density of Material, lb/cu. in.			0.0731					

SECRET

SECRET

FRAGMENTATION DATA ON EXPLODED DRY SANDSTONE BLOCKS

Test: G Block Dimensions: 18-in. diameter x 30-in. long
 Shothole Diameter: 1-1/4 in. Explosive: Runkol
 Diameter of Explosive: 1-1/8 in. Weight of Explosive: 1 oz

Size Range of Fragments	Average Diameter, (in.)	Total Class Weight, (gm)	Total Class Weight, (lb)	Average Weight per Fragment, (lb)	Number of Fragments in Class	Cumulative Number of Fragments	Cumulative Percent of Total Fragments	Minimum Fragment Weight in Class, (lb)
Over 8 inch	(12)	58,400	128.8	64.9	1.98	1.98	0.0368	19.54
4 - 8 inch	6	115,000	253.6	8.25	30.74	32.72	0.602	2.445
2 - 4 inch	3	35,900	79.1	1.031	76.7	109.0	2.004	0.3056
1 - 2 inch	1.5	21,700	47.8	0.129	371.0	480.0	8.83	0.0382
1/2 - 1 inch	0.75	9,430	20.8	0.016	1,290.0	1,770	32.55	0.00475
1/4 - 1/2 inch	0.375	3,330	7.3	0.002	3,670.0	5,440.0	100.0	0.00059
1/16 - 1/4 inch		2,690						
500 microns - 1/16 inch		1,330						
251 - 500 microns		1,470						
124 - 251 microns		1,430						
66 - 124 microns		389						
20 - 66 microns		189						
10 - 20 microns		45						
5 - 10 microns		23						
2 - 5 microns		21						
Under 2 microns		12						
Total Weight of Recovered Material		251,359	554.0					
Total Weight of Material above 1/4 in. Fragment Size		243,760 (97.0%)	537.4					
Original Volume of Material (less shothole), cu.in.		7,488						
Computed Density of Material, lb/cu.in.			0.0730					

SECRET

SECRET

FRAGMENTATION DATA ON EXPLODED DRY SANDSTONE BLOCKS

SECRET

Test: K Block Dimensions: 18-in. diameter x 30-in. long
 Shothole Diameter: 1-1/4 in. Explosive: Colex
 Diameter of Explosive: 5/8 in. Weight of Explosive: 1 oz

Size Range of Fragments	Average Diameter, (in.)	Total Class Weight, (gm)	Total Class Weight, (lb)	Average Weight per Fragment, (lb)	Number of Fragments in Class	Cumulative Number of Fragments	Cumulative Percent of Total Fragments	Minimum Fragment Weight in Class, (lb)
Over 8 inch	(12)	119,000	262.1	59.6	4,395	4.40	0.139	17.67
4 - 8 inch	6	53,300	117.5	7.45	15.79	20.19	0.636	2.208
2 - 4 inch	3	30,600	67.5	0.931	72.45	92.64	2.92	0.276
1 - 2 inch	1.5	14,300	31.5	0.1163	271.0	364.0	11.47	0.0345
1/2 - 1 inch	0.75	4,080	9.0	0.01456	618.0	982.0	30.92	0.00431
1/4 - 1/2 inch	0.375	1,810	4.0	0.00182	2,191.0	3,173.0	100.0	0.00054
1/16 - 1/4 inch		1,470						
500 microns - 1/16 inch		588						
251 - 500 microns		652						
124 - 251 microns		597						
66 - 124 microns		174						
20 - 66 microns		118						
10 - 20 microns		34						
5 - 10 microns		20						
2 - 5 microns		12						
Under 2 microns		8						
Total Weight of Recovered Material		226,763	499.5					
Total Weight of Material above 1/4-in. Fragment Size		223,090 (98.4%)	491.6					
Original Volume of Material (less shothole), cu. in.		7,588						
Computed Density of Material, lb/cu. in.			0.0659					

SECRET

FRAGMENTATION DATA ON EXPLODED DRY SANDSTONE BLOCKS

Test: M Block Dimensions: 18-in. diameter x 30-in. long
 Shot Hole Diameter: 3/4 in. Explosive: XL Hawkite
 Diameter of Explosive: 5/8 in. Weight of Explosive: 2 oz

Size Range of Fragments	Average Diameter, (in.)	Total Class Weight, (gm)	Total Class Weight, (lb)	Average Weight per Fragment, (lb)	Number of Fragments in Class	Cumulative Number of Fragments	Cumulative Percent of Total Fragments	Minimum Fragment Weight in Class, (lb)
Over 8 inch	(12)	18,100	39.9	63.05	0.63	0.63	0.007	18.7
4 - 8 inch	6	93,800	207.0	7.89	26.24	26.87	0.178	2.34
2 - 4 inch	3	39,700	87.6	0.986	88.9	115.8	0.769	0.292
1 - 2 inch	1.5	30,900	68.1	0.123	552.0	668.0	4.44	0.0365
1/2 - 1 inch	0.75	22,400	49.5	0.0154	3,205.0	3,873.0	25.7	0.00456
1/4 - 1/2 inch	0.375	9,750	21.5	0.00192	11,200.0	15,073.0	100.0	0.00057
1/16 - 1/4 inch		9,300						
500 microns - 1/16 inch								
251 - 500 microns		5,090						
124 - 251 microns		4,940						
66 - 124 microns		4,180						
20 - 66 microns		1,440						
10 - 20 microns		731						
5 - 10 microns		175						
2 - 5 microns		142						
Under 2 microns		76						
		58						
Total Weight of Recovered Material		240,782	530.8					
Total Weight of Material above 1/4-in. Fragment Size		214,650 (89.1%)	473.6					
Original Volume of Material (less shothole), cu.in.		7,612						
Computed Density of Material, lb/cu.in.			0.0697					

SECRET

SECRET

APPENDIX F
CONCRETE FRAGMENT WEIGHTS AND DIMENSIONS
FOR 1/24-SCALE SHIELDED REACTOR MODELS

SECRET

SECRET

CONCRETE FRAGMENT WEIGHTS AND DIMENSIONS FOR 1/24-SCALE SHIELDED REACTOR MODELS

Model No. 3

Event Simulated, 730 lb TNT, 1 msec, w/Pyrocore
Vessel 3/4 Full of Water

Piece Number	Individual Weight,		Group Weight,		Height, (in.)	Length, (in.)	Width, (in.)	Dist. of Fragments from Original Model Position, If > 10 ft		Remarks
	lb	oz	lb	oz				ft	in.	
44	39	15	39	15	6		12			Ring, 12-in. diam. with 4-1/2-in. diam. hole
43	11	2	11	2	7	9	4			
1	8	3			5	8	4			
4	8	1	16	4	6	6	4			
2	5	7			6	7	4			
6	5	7			6	4	4			
5	5	4			4	5	4			
8	5	1	21	3	6	5	4			
30	4	5	4	5	6	4	4			
16	3	11			4	5	4			
3	3	9			4-3/4	4	4			
15	3	4			6	6	4			
32	3	1	13	9	5-1/4	4	4			
12	2	15			4	5	4			
9	2	14			4	4	4			
7	2	13			4-1/2	4	4			
11	2	8			2-1/2	5-1/2	4			
37	2	5			5	3	4			
24	2	4	15	11	4-1/2	3-1/2	4			
23	1	15			4	3-1/2	3			
21	1	14			5	2-1/2	4	14	5	
17	1	13			4	4	3			
10	1	12			5	2-1/2	4			
20	1	9			5	3	2-1/2			
22	1	9			2-1/2	2-1/2	2			
27	1	9			2	4	4			
28	1	7			4	2-1/2	4			
31	1	7			4-3/4	2-1/2	4			
13	1	5			5-3/4	2	4			
14	1	5			2-1/2	4	4			
29	1	5			2	2-1/2	4			Approximately 50 small chunks of concrete
19	1	4			3	3	3			
33	1	4			4-3/4	2-1/2	4			
18	1	3	22	9	4	2-1/2	3			
40		15			4	2	2-3/4			
26		14			2	3-1/2	2-1/2			
36		13			4-1/2	1-3/4	3			
41		12			4-1/2	1-1/2	2			
25		11			2-1/2	1-1/2	4			
34		10			3/4	2	2-1/2			
38		10			4	1-1/2	3			
35		9			3-1/2	2	3			
39		7			4-1/2	1	2-3/4			
42		7			1-1/2	4	2			
45		6			1-1/2	2-1/4	1-1/2	18		
46		1/4			3/4	1	1/4	19	6	
-	4	1-3/4	11	4						

SECRET

SECRET

**CONCRETE FRAGMENT WEIGHTS AND DIMENSIONS
FOR 1/24-SCALE SHIELDED REACTOR MODELS**
Model No. 5 Event Simulated, 510 lb TNT, 1 msec, w/Pyrocore
Vessel Full of Water

Piece Number	Individual Weight,		Group Weight,		Height, (in.)	Length, (in.)	Width, (in.)	Remarks
	lb	oz	lb	oz				
9	32		32		4	15	10	
16	23	12			4	15	10	
18	23	12	47	8	4	15	8	
17	17		17		4	12	6	
2	8	6	8	6	4	10	4	
6	6	2	6	2	4	8	4	
8	5	14	5	14	4	10	3	
1	4	14			4	6	4	
21	4	14			4	6	4	
7	4	14			4	4	6	
22	4	8			2	4	7	
9	4	4			4	4	4	
3	4	2	27	8	4	4	4	
5	3	12			4	6	4	
4	3	6			4	6	3	
10	3	4	10	6	4	4	6	
11	2	4	2	4	4	4	3	
20	1	12			4	4	3	
12	1	4	3		4	6	1-1/2	
14		12			3	3	2	
13		12			3	2	2	
23		6			3	3	1/2	
15		2			1-1/2	1-1/2	1/2	
24	1	8	3	8				40 small chunks of concrete

SECRET

SECRET

CONCRETE FRAGMENT WEIGHTS AND DIMENSIONS
FOR 1/24-SCALE SHIELDED REACTOR MODELS

Model No. 14

Event Simulated, 160 lb TNT, 1 msec, w/Pyrocore
Vessel 3/4 Full of Water

Piece Number	Individual Weight,		Group Weight,		Height, (in.)	Length, (in.)	Width, (in.)	Remarks
	lb	oz	lb	oz				
1	140		140		18-1/2	12	12	Cylinder, 12-in. diam. with 4-1/4-in. diam. hole
2	19	14	19	14	3-1/2	12	12	

Model No. 15

Event Simulated, 150 lb TNT, 1 msec, w/Pyrocore
Vessel 3/4 Full of Water

Piece Number	Individual Weight,		Group Weight,		Height, (in.)	Length, (in.)	Width, (in.)	Remarks
	lb	oz	lb	oz				
15	142		142		18		12	Cylinder, with 4-1/4-in. diam. hole at center
1	3	8	7		2	6	5	
2	3	8			2-1/4	7	5	
3	1	15			2	5-1/4	3	
6	1	8			1-1/2	7-1/2	3-1/4	
5	1	6	8	8	2	4-1/2	3	
7	1	6			1-3/4	5	2-1/2	
4	1	5			1-3/4	6	2-1/4	
8	1				1-3/4	5-3/4	2-1/2	
9		13			2	2-3/4	2-3/4	
11		8			1-1/2	4	2-1/2	
12		6			1-1/2	3-1/2	2	
10		5			1-1/2	3-1/4	3	
13		5			1-3/4	2	1-1/2	
-		7	2	12				10 small chunks of concrete

SECRET

SECRET

**CONCRETE FRAGMENT WEIGHTS AND DIMENSIONS
FOR 1/24-SCALE SHIELDED REACTOR MODELS**

Model No. 16

Event Simulated, 210 lb TNT, 1 msec, w/MDF
Vessel Full of Water

Piece Number	Individual Weight,		Group Weight,		Height, (in.)	Length, (in.)	Width, (in.)	Dist. of Fragments from Original Model Position, If > 10 ft		Remarks
	lb	oz	lb	oz				ft	in.	
16	14	5	14	5	4	7	10			
19	13	10	13	10	4	11	6			
17	11	12			4	8	8			
18	11	4	23		4	5-1/2	9			
8	10	10	10	10	4	8	7			
7	9	10	9	10	4	6	6-1/2			
9	7	5	7	5	4	7	5			
6	4	4	4	4	4	6	4			
4	3	1	3	1	2-1/2	5	4-1/4			
10	2	13			3	4	4			
1	2	12			3-3/4	6	3-1/2			
3	2	12			3	6	3-3/4			
11	2	7			3	5-1/2	4-1/4			
21	2	5			2-1/4	5	4-1/2	18	6	
2	2				2-1/2	5	3-1/4			
22	2		17	1	2-1/4	5	4-1/2	11		
12	1	12			2-1/2	4-1/2	3			
13	1	12			3	3-1/2	3-1/2			
31	1	9			2-1/2	5	2-1/2			
14	1	3			2-1/2	4	2-1/2			
30	1	3			2	4	3-3/4			
15	1	2			1-1/2	5	2-1/2			
23	1				2	4	2-1/2	13		
26	1		10	9	2	4-1/2	2			
32		15			1-1/2	4-1/2	3			
39		15			1-3/4	5	2			
33		12			1-1/2	3	3			
27		11			1	3-1/2	2-1/2			
38		11			2-1/2	3	1-3/4			
24		9			2	3	2	15	9	
20		8			1-1/2	3-3/4	2			
25		8			2	2	2	13	9	
28		8			2	3	3	14		
36		6			2	3	2-1/2			
37		6			2	3	2-1/2			
29		5			2	2-1/2	1-3/4	13	6	
43		2-3/4			1-1/2	1-3/4	1-1/4	18	6	
46		2-3/4			1-1/2	2-1/2	1-1/2	11	9	
44		2-1/4			1	2	1	11	6	
45		2			1-1/2	1-3/4	1	10	3	
52		1-3/4			2-1/2	1-1/4	1	12		
47		1-1/2			1-1/4	1-1/4	1-1/2	11	5	
53		1-1/2			1-1/2	1-1/2	1	11	6	
48		1-1/4			1-1/2	1-1/2	3/4	14	6	
49		1			1/2	1-1/2	1/2	12	9	
50		1			1/2	2	1/2	12	9	
51		3/4			1/2	2	1	12		
54		1/2	8	5	1	1	3/4	10	9	
—			31	3						Approximately 200 small chunks of concrete (6 oz. to 1/2 oz range)
—			1	6						Approximately 125 very small chunks of concrete (below 1/2 oz in size)

SECRET

SECRET

CONCRETE FRAGMENT WEIGHTS AND DIMENSIONS
FOR 1/24-SCALE SHIELDED REACTOR MODELS

Model No. 17

Event Simulated, 160 lb TNT, 1 msec, w/Pyrocore
Vessel Full of Water

Piece Number	Individual Weight,		Group Weight,		Height, (in.)	Length, (in.)	Width, (in.)	Remarks
	lb	oz	lb	oz				
1	145		145		18-1/2	12	12	Cylinder, 12-in. diam. with 4-1/4-in. diam. hole
3	12	4	12	4	3	12	6	
4	4	1	4	1	2-1/2	6-1/2	5-3/4	
6	1	11	1	11	2-1/4	6	2-1/2	
2		7			1-1/2	2-1/2	2-1/4	
7		4			3/4	2	2-1/2	
5		2			1	2	3/4	
9		1-1/2			1/2	2	1-3/4	
8		1		15-1/2	1/2	2-1/2	1-1/4	

SECRET

SECRET

CONCRETE FRAGMENT WEIGHTS AND DIMENSIONS FOR 1/24-SCALE SHIELDED REACTOR MODELS

Model No. 19

Event Simulated, 210 lb TNT, 1 msec, w/MDF
Vessel 3/4 Full of Water

Piece Number	Individual Weight,		Group Weight,		Height, (in.)	Length, (in.)	Width, (in.)	Dist. of Fragments from Original Model Position, if > 10 ft		Remarks
	lb	oz	lb	oz				ft	in.	
26	21	14	21	14	5	12	4			
25	17	15	17	15	7	12	4			
8	8	10	8	10	6	7-1/2	4			
9	7	13			8	4-1/2	4			
7	7	11			6	7	4			
10	7	4	22	12	6	6-1/2	4			
11	6	10	6	10	5	8	4			
6	4	9	4	9	6	5-1/2	4			
12	3	6			5	6	3			
14	3	3	6	9	4	6	4	10	6	
5	2	13			4-1/2	5-1/2	3			
15	2	8			3-1/4	5	3-1/2			
13	2	7			6	4	4			
16	2	2			3	4	4			
3	2	1			2-1/2	4-1/2	3-1/2	10	9	
20	2	1			3	5	4			
4	2		16		3-1/4	5	2-3/4			
1	1	14			3	4	3-1/2			
2	1	14			2-1/2	4	3-1/2	19		
19	1	12			3	4-1/2	3			
18	1	9			3	5	3-1/2			
21	1	9			3	4-1/2	2-1/2			
22	1	6			3	4	3			
47	1	5			2-1/2	5	2-1/2			
44	1	4			3	5	2-1/2			
24	1	2			2-1/4	4	3			
30	1				2	5	1-3/4			
45	1				2	6	2			
49	1		16	11	2	6	2			
32	1	15			2	4-1/2	2			
48	1	15			2	5	2			
23	1	14			2	4	2	10	2	
28	1	14			2-1/2	3	2-1/2	10	3	
29	1	14			2	3-1/2	2-1/2	11	9	
31	1	14			2-1/2	4	2	12		
35	1	13			2	5	2			
56	1	13			2	4	2			
33	1	12			3	2-1/2	1-3/4	26		
50	1	11			2-1/2	4	2-1/2			
51	1	11			2-1/2	3-1/2	2-1/2			
57	1	11			2	3-1/2	2			
46	1	10			2	4-1/2	2			
54	1	10			3	3	2			
27	1	9			2	3-1/2	2	11	3	
34	1	9			2-1/2	2	2-1/4	13		
55	1	9			2	4	1-1/2			
58	1	9			2	4	2			
17	1	8			1	3	3			
52	1	8			2	2-1/2	2-1/2			
53	1	8			3	2-1/2	2-1/2			
59	1	7			1-1/2	3	1-1/2			
38	1	4-1/4			2	2	2	12	6	
39	1	2-1/4			2	1-1/2	1-1/2	13	6	
40	1	2-1/4			1	1	1	13	3	
41	1	1-3/4			1-3/4	1	1	14		
42	1	1/2			1	1	3/4	10	6	
43	1	1/2	16	7	1	1	3/4	15		
—			2	12						Approximately 110 small chunks of concrete (6 oz to 1/2 oz range)
—			2	12						Approximately 120 very small chunks of concrete (1/2 oz to 1/4 oz range)

SECRET

SECRET

APPENDIX G
CONCRETE FRAGMENT WEIGHTS AND DIMENSIONS
FOR 1/12-SCALE SHIELDED REACTOR MODELS

SECRET

SECRET

**CONCRETE FRAGMENT WEIGHTS AND DIMENSIONS
FOR 1/12-SCALE SHIELDED REACTOR MODELS**

Energy Source: Pyrocore

Period: 1 msec

Water in Vessel: 100%

Model No.	A	B	C	D	E	F
Event Simulated						
TNT (lb)	150	150	400	400	650	650
Megawatt-Seconds	280	280	750	750	1230	1230
Model Wt. (lb)	1308 (avg.)	1308 (avg.)	1292	1311	1286	1342
% Fragments						
< 1 lb	--	--	1.5	0.9	1.3	1.4
1 - 5 lb	--	--	1.4	0.5	3.4	1.4
5 - 10 lb	--	--	1.3	1.7	6.4	3.2
10 - 15 lb	--	--	1.9	1.1	11.4	6.1
15 - 20 lb	--	--	1.4	3.9	2.6	3.6
20 - 25 lb	2	--	8.7	13.2	10.5	8.0
> 25 lb	98	100	83.9	78.6	64.4	76.1
No. Fragments						
< 1 lb	--*	--	31(1616)	22(1050)	46(120)*	47(99)
1 - 5 lb	--	--	10	4	21	8
5 - 10 lb	--	--	2	3	11	6
10 - 15 lb	--	--	2	1	11	7
15 - 20 lb	--	--	1	3	2	3
20 - 25 lb	1	--	5	8	6	5
> 25 lb	4	6	12	14	20	20
No. Fragments Excluding Fines	5	6	63	55	117	96

* Figures in parentheses indicate "Fines".

SECRET

SECRET

APPENDIX H
TRAJECTORY OF AN AIR PARTICLE
DURING THE POSITIVE PHASE OF A NUCLEAR BLAST

SECRET

SECRET

APPENDIX H
TRAJECTORY OF AN AIR PARTICLE DURING THE POSITIVE PHASE
OF A NUCLEAR BLAST

Using the 1957 "The Effects of Nuclear Weapons" (Ref. 20), the velocity-time history of an air particle may be found at any fixed point on the ground surface for a surface burst of any yield. If we know the velocity of an air particle u_1 at one location, we can predict its new location after a short time interval Δt_1 (e. g., old location + $u_1 \Delta T_1$). Repeating this procedure enables us to establish the horizontal distance-time relationship of the particle. Because so many factors enter into the determination of the particle velocity as presented in reference 20, an otherwise straightforward integration becomes a rather involved bookkeeping problem. The following outline indicates the steps involved in the numerical integration:

- I. Select
 - A. Weapon Yield
 - B. Overpressure at front of forest, p_1
- II. Compute (Time: $T = 0$)
 - A. Shock Velocity U_1 for p_1 (see Fig. 3.80, Ref. 20)
 - B. Particle Velocity u_1 for p_1 (see Fig. 3.80, Ref. 20)
 - C. Distance from ground zero (GZ) to front of forest, x_0
 1. Fig. 3.94a; 1-KT surface burst; Ref. 20
 2. Scaling Law; Eq. 3.86.1 Ref. 20
- III. Select $T = \Delta T_1$
- IV. Compute
 - A. Distance traveled by particle in ΔT_1 $\Delta x_1 = u_1 \Delta T_1$
 - B. Distance traveled by shock front in T_1 $\Delta y_1 = U_1 \Delta T_1$
 - C. Time gap between shock front and particle:

$$t_1 = (U_1 - u_1) \Delta T_1 / U_1$$

SECRET

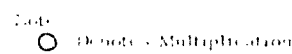
SECRET

- D. Overpressure at distance $x_0 + \Delta x_1$ from GZ: p_2'
 - 1. Fig. 3. 94a; 1-KT surface burst; Ref. 20
 - 2. Scaling Law; Eq. 3. 86. 1 Ref. 20
 - E. Overpressure at distance $x_0 + \Delta y_1$ from GZ: p_2
 - 1. Fig. 3. 94a; 1-KT Surface burst; Ref. 20
 - 2. Scaling Law; Eq. 3. 86. 1 Ref. 20
 - F. Shock Velocity U_2 for p_2 (see Fig. 3. 80, Ref. 20)
 - G. Duration of positive phase at $x_0 + \Delta x_1$: t_{1+}
 - 1. Fig. 3. 96; surface burst; Ref. 20
 - 2. Scaling from Art. 3. 88, Ref. 20
 - H. Overpressure behind shock front $p(t_1)$
 - 1. Compute t_1/t_{1+}
 - 2. Compute $p(t_1)$ from Eq. 3. 82. 1 (Ref. 20) using p_2'
 - I. Particle Velocity u_2 for $p(t_1)$; (Fig. 3. 80 Ref. 20)
- V. Select ($T = \Delta T_2$)
- VI. Compute
- A. $\Delta x_2 = u_2 \Delta T_2$
 - B. $\Delta y_2 = U_2 \Delta T_2$
 - C. $t_2 = [\Delta y_1 + \Delta y_3 - (\Delta x_1 + \Delta x_2)]/U_2$
 - D. p_3' at $x_0 + \Delta x_1 + \Delta x_2$ from GZ
 - E. p_3 at $x_0 + \Delta y_1 + \Delta y_2$ from GZ

The curves in the figures referred to in the outline were all fit with analytical expressions and the entire procedure was programmed for the UNIVAC 1105. Figure H-1 shows the detailed flow diagram of the program.

SECRET

—



SECRET

APPENDIX J
THE VULNERABILITY OF
ANTENNA SYSTEMS

SECRET

SECRET

APPENDIX J
THE VULNERABILITY OF ANTENNA SYSTEMS

The severity of the debris hazard to antenna systems is only one phase of debris problems associated with hardened sites, but it is used to describe the estimating procedures that can be applied to debris problems in general, using data collected in this report.

The approach used in this study made estimates in several manners and noted their consistency. First, estimates of the maximum range of antenna vulnerability were based on the correlation of maximum debris distance and equivalent yield observed in Chapter Two. Debris distribution data from the Pantex Ordnance Plant event were then scaled up to nuclear yields. This was done by scaling up the ground ranges according to the cube-root-of-yield scaling, although it may have been more appropriate to also scale up the total volume of fragments in a manner which accounted for the total material volume of the nuclear crater. The result was perhaps optimistic, resulting in fewer fragments. Next, debris environment was estimated independently by scaling up DANNY BOY findings to high yields. This was done by scaling both ground ranges and fragment densities according to cube-root-of-yield scaling. A third estimate of debris environment was based on use of the hydrodynamic model of crater formation developed by Brode and Bjork at RAND Corporation*. An analytical solution to the debris environment was obtained by considering peak velocities from the hydrodynamic model to be initial fragment velocities, and following the trajectories of the ejecta from the crater to ultimate impact with the ground. Results of these three approaches are consistent in predicting severe debris environments under likely hardening criteria.

* H. L. Brode and R. L. Bjork, "Cratering from a Megaton Surface Burst", Paper L, Proceedings of the Geophysical Laboratory - Lawrence Radiation Laboratory Cratering Symposium, UCRL-6438, University of California, October 1961.

SECRET

SECRET

There are two potential sources of debris hazards to antenna systems: throwout material from the crater and loose material or broken structure picked up and transported by the blast winds. The second source of debris can be eliminated by clearing an area around the antenna. No simple defense against crater throwout debris is apparent. This problem is therefore restricted to prediction of the debris hazard resulting from the crater throwout alone.

A comprehensive method of analysis of debris effects emanating from nuclear detonations has yet to be developed. To a great extent the character of the hardened sites is responsible for this state of affairs. The hardened missile silo with a reinforced concrete cover as the only exposed component was considered relatively invulnerable to debris damage. The sole problem was to predict the weight of debris on the closure after an attack so that sufficient power could be designed into the closure operating mechanism. Communications systems, however, pose entirely different problems. Components of antenna systems, for example, may be quite vulnerable to debris damage because of their electrical essentials. Thus, the hardened antenna design must be based on such criteria as density, size, and energy of debris particles to be expected at the antenna location.

Some studies which border on, or are corollary to, the problem have been performed. These include studies of missiles from accidental explosions (Chapter Two), studies of debris distribution from nuclear tests (JANGLE U and DANNY BOY), and analytical studies dealing with the crater formation problem (RAND). Each of these is used to estimate the debris hazard for the hypothetical antenna structure.

It should be emphasized that at present, it is only possible to assess the debris problem very roughly. Our intention is to objectively review the available data and to compare predictions based on different source material. Hopefully, the results will be consistent. We do not contend that this study completely settles the debris question for hardened sites. We do feel, however, that it is the most reasonable approach to the problem within the current state-of-the-art, -- i. e., short of further nuclear testing.

SECRET

SECRET

J-1 Estimates Based on High-Explosive Debris Data

The Armed Services Explosive Safety Board data on 206 HE detonations ranging in magnitude from 8-lb of tetrytol to 9,000,000 lb of ammonium nitrate were collected (Chapter Two). A statistical analysis relating the maximum missile distance to the weight of explosive (TNT equivalent) was made. On a log-log plot a linear regression line to best fit the data was found to be of the form,

$$\log_{10} D_M = 2.950 + 0.322 \log_{10} W \quad (J-1)$$

where

D_M = maximum missile distance, ft
 W = equivalent weight of TNT, lb.

Similarly, a quadratic regression line to best fit the data was found to be:

$$\log_{10} D_M = 2.960 + 0.347 \log_{10} W - 0.016 (\log_{10} W)^2 \quad (J-2)$$

Note that Eq. (J-1) indicates one should scale according to $W^{0.322}$. A standard error was found to be $2.47 D_M$. Equations (J-1) and (J-2) were applied to the antenna vulnerability problem using an equivalence factor of 0.50 to relate nuclear yield to TNT equivalent; the results are presented in Table J-1.

Table J-1
LIMIT OF ANTENNA VULNERABILITY BASED ON HE DATA

Weapon Yield, (MT)	Based on Linear Regression Line		Based on Quadratic Regression Line	
	Maximum Debris Distance, (miles)	Range of Maximum Debris Distance for One Standard Error (miles)	Maximum Debris Distance, (miles)	Range of Maximum Debris Distance for One Standard Error (miles)
5	19.4	7.9 to 48.0	6.4	2.6 to 15.7
10	24.2	9.8 to 59.9	6.8	2.8 to 16.8
20	30.3	12.3 to 75.0	7.6	3.1 to 18.9
50	40.7	16.5 to 100.7	8.4	3.4 to 20.8
100	50.9	20.6 to 121.0	9.1	3.7 to 22.4

SECRET

SECRET

It is interesting to note that a data point corresponding to 5,200,000 lb of TNT (2.60-KT nuclear weapon) was included and that the maximum missile distance for this point was 3.5 miles. Thus, we extrapolated four cycles from six cycles of data.

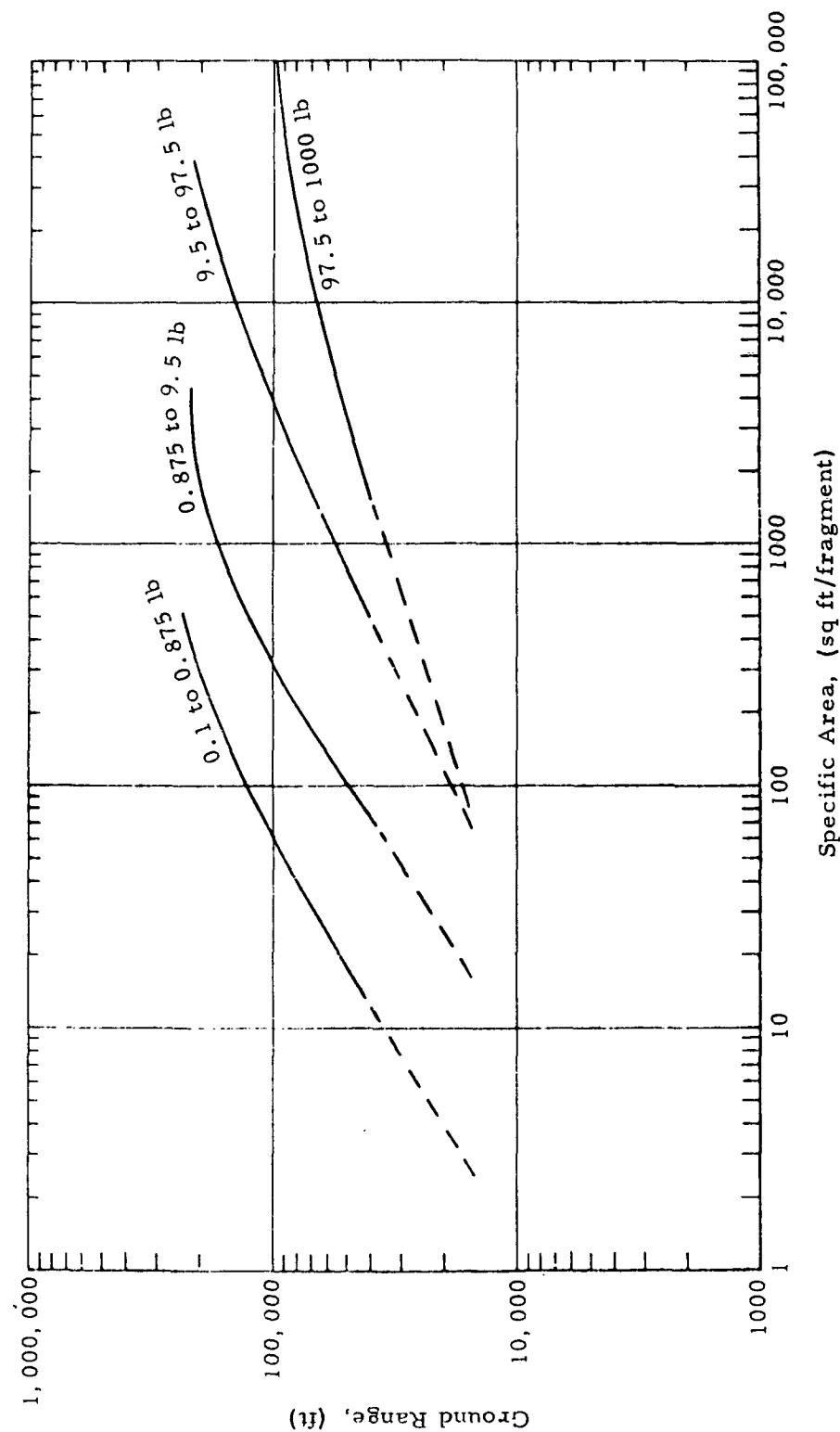
The relationship between the high explosion debris problem and the debris emanating from the crater of a nuclear weapon is certainly questionable. The HE debris generally results from buildings and equipment in the immediate vicinity of the explosions. The mechanism by which this debris is formed is different from mechanisms by which a crater is formed. Nuclear detonation is accompanied by rather substantial winds whereas in the HE explosion these winds are essentially absent. Nevertheless, it is desirable to take into consideration the large body of data that is available for the HE debris problem, particularly in view of the scarcity of nuclear test data. As a matter of fact, since essentially all debris associated with an HE detonation originates near the point of detonation, one can argue that this debris is, in fact, similar in origin to throwout debris.

The second item of interest is the distribution of debris outward from the point of the explosion. A detailed debris study which included complete descriptions and final locations of the debris was carried out at Pantex Ordnance Plant (Ref. 11). The explosive was 2000 lb of TNT detonated in a reinforced concrete bunker. For application to the antenna vulnerability problem, all reported ranges were scaled up by the cube-root-of-yield law. The total volume of fragments at the Pantex study was estimated to be 1000 cu ft, whereas the crater volume for, say a 20-MT weapon surface burst is about 3.7×10^9 cu ft. Rather than using the ratio of $3.7 \times 10^9 / 10^3$ to scale the number of fragments, we used the more optimistic (resulting in fewer fragments) cube-root-of-yield factor (215 for this case). The resulting missile density as a function of ground range is shown on Fig. J-1. The dashed portions of the curve are extrapolated to expected antenna locations. These results make it apparent that debris problems are critical for antenna systems.

SECRET

SECRET

9-J



Specific Area, (sq ft/fragment)

SECRET

Figure J-1 Fragment Distribution from 20-MT Weapon Based on Pantex Test

SECRET

J-2 Estimates Based on Nuclear Test Results

Armour Research Foundation (Ref. 2) recently completed an experimental study of crater throwout from an underground nuclear detonation; these results are derived completely from that work. This study was part of Project 7 DANNY BOY, a 0.43-KT nuclear device buried at a depth of 110 ft in basalt on the Buckboard Mesa at the Nevada test site. The expected crater zone was salted with a variety of objects which were located after the blast. In addition, the natural debris was tabulated in certain areas. Of particular interest here are the natural debris radial distribution charts reproduced from reference 2 in Fig. J-2, J-3, and J-4. Areas I, II, and III in these figures correspond to different orientations with respect to ground zero. The results must be scaled up to the cases of interest here. The ground ranges are reasonably scaled by the cube-root-of-yield law. Scaling of the fragment density expressed as fragments-per-square-foot requires some discussion. If the total number of fragments is assumed proportional to the crater volume, then the number of fragments scale directly as the weapon yield (crater diameter and depth each scale as the cube root of yield). The area over which these fragments are distributed scales as length square or as yield to the two-thirds power. Therefore, the fragment density scales as $W/W^{2/3}$ or as cube-root of yield. The results of Fig. J-2, J-3, and J-4 for the three sectors are averaged and scaled up to a 1-KT weapon as a standard. The result is shown on Fig. J-5. This is then used to determine debris density as a function of range for any weapon yield in kilotons.

This has been done for an antenna system location of 4.0 miles for selected weapon yields. Results are shown in Table J-2.

SECRET

SECRET

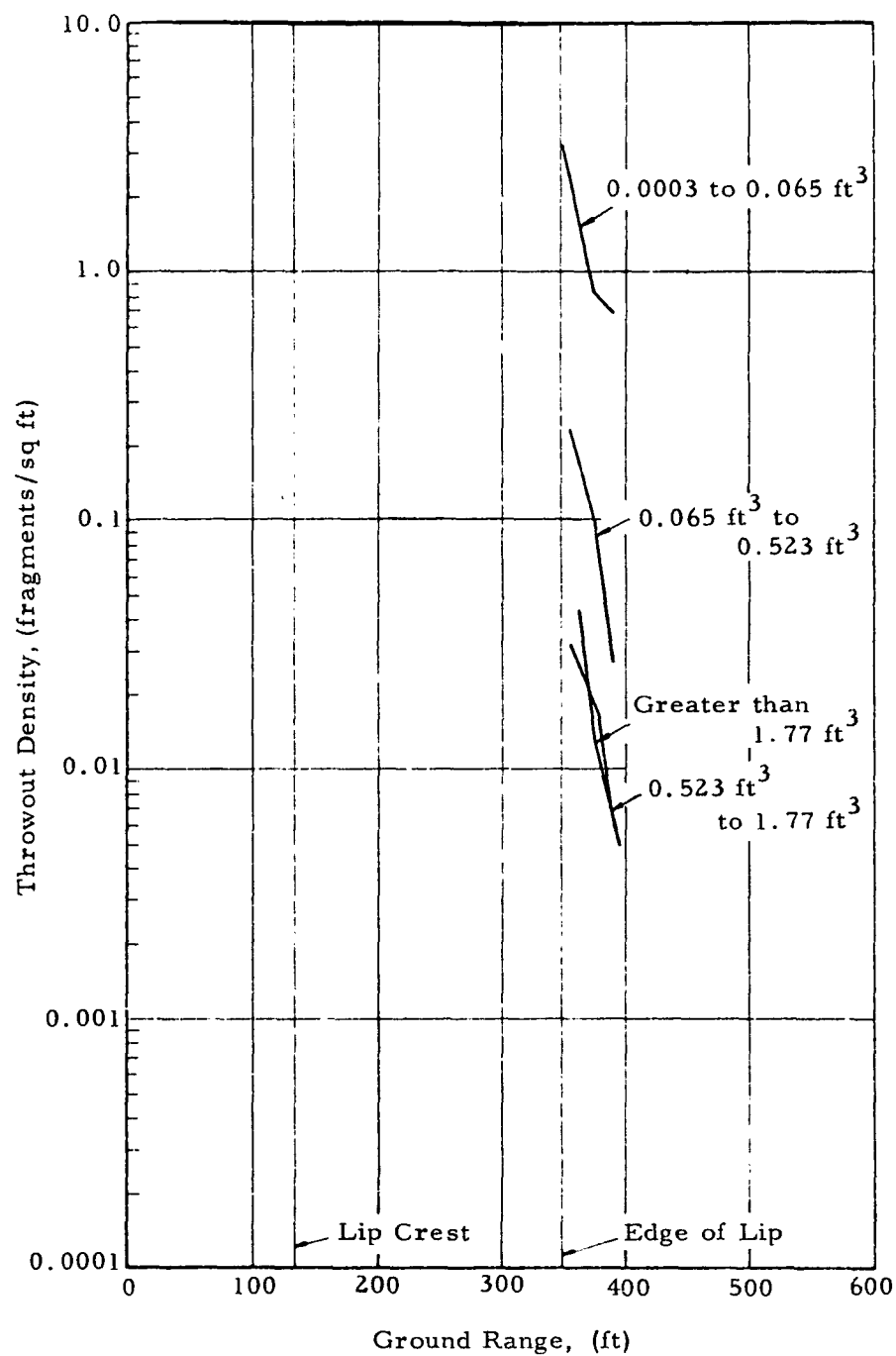


Figure J-2 Throwout Density, Area I, DANNY BOY Event

SECRET

SECRET

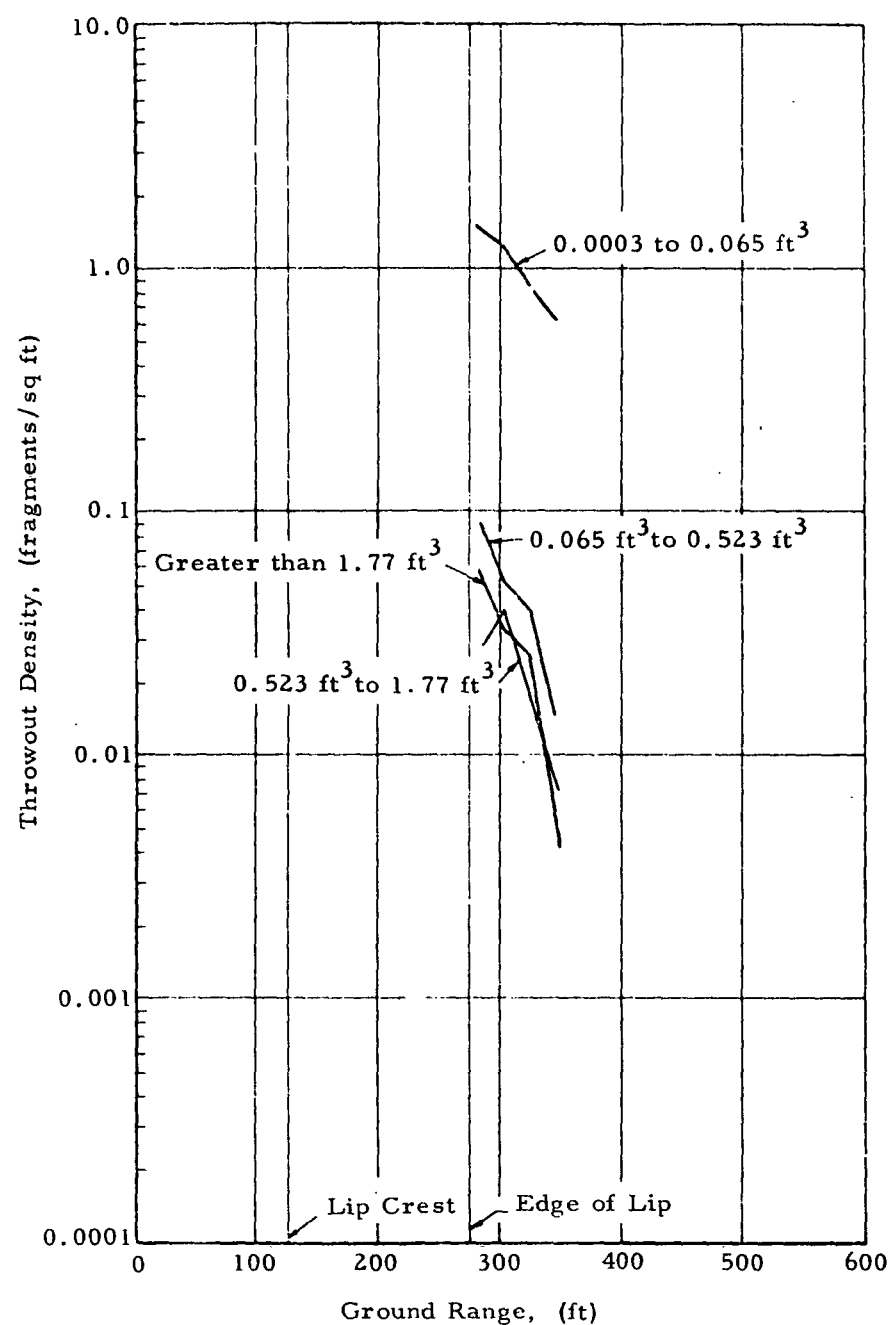


Figure J-3 Throwout Density, Area II, DANNY BOY Event

SECRET

SECRET

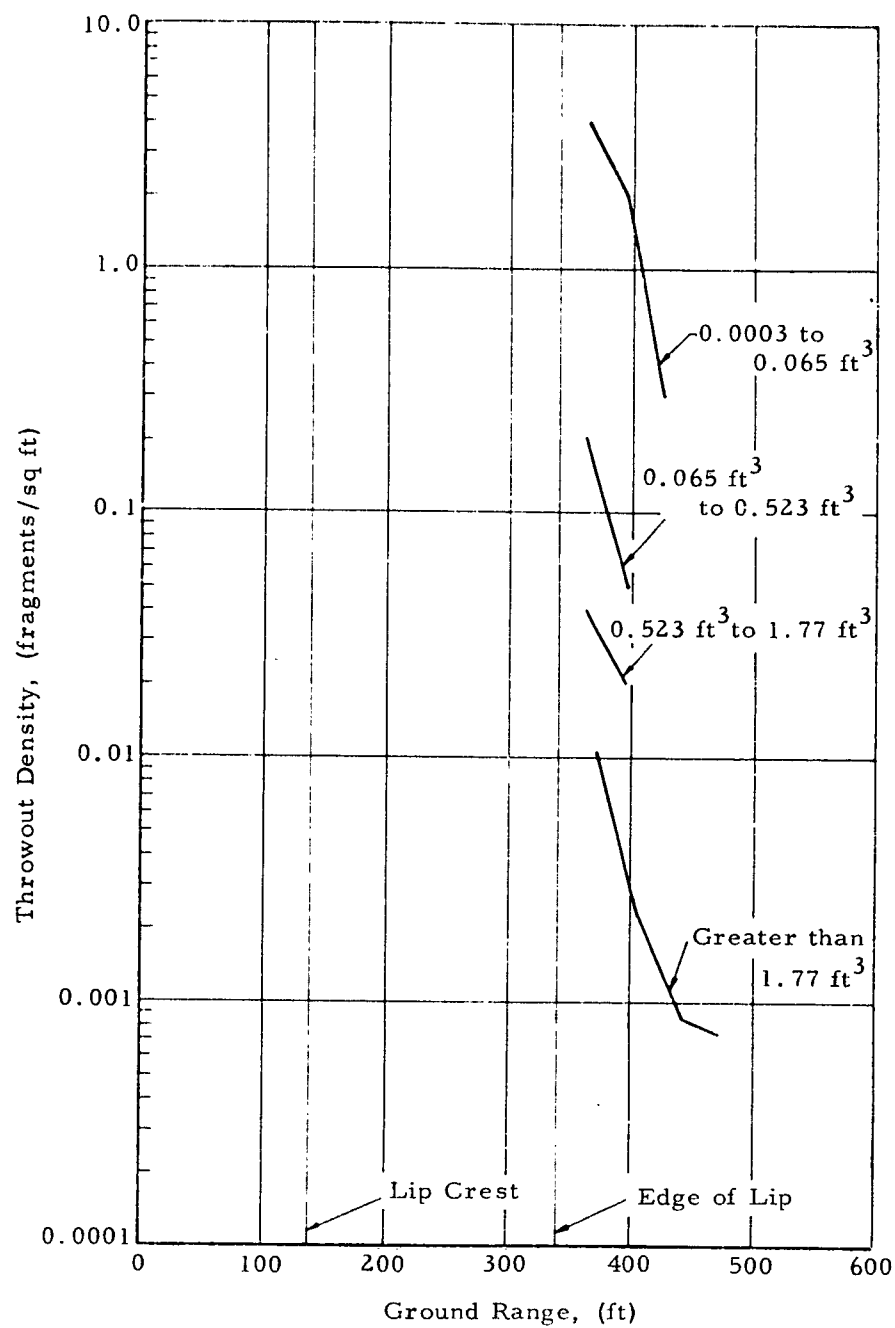


Figure J-4 Throwout Density, Area III, DANNY BOY Event

SECRET

SECRET

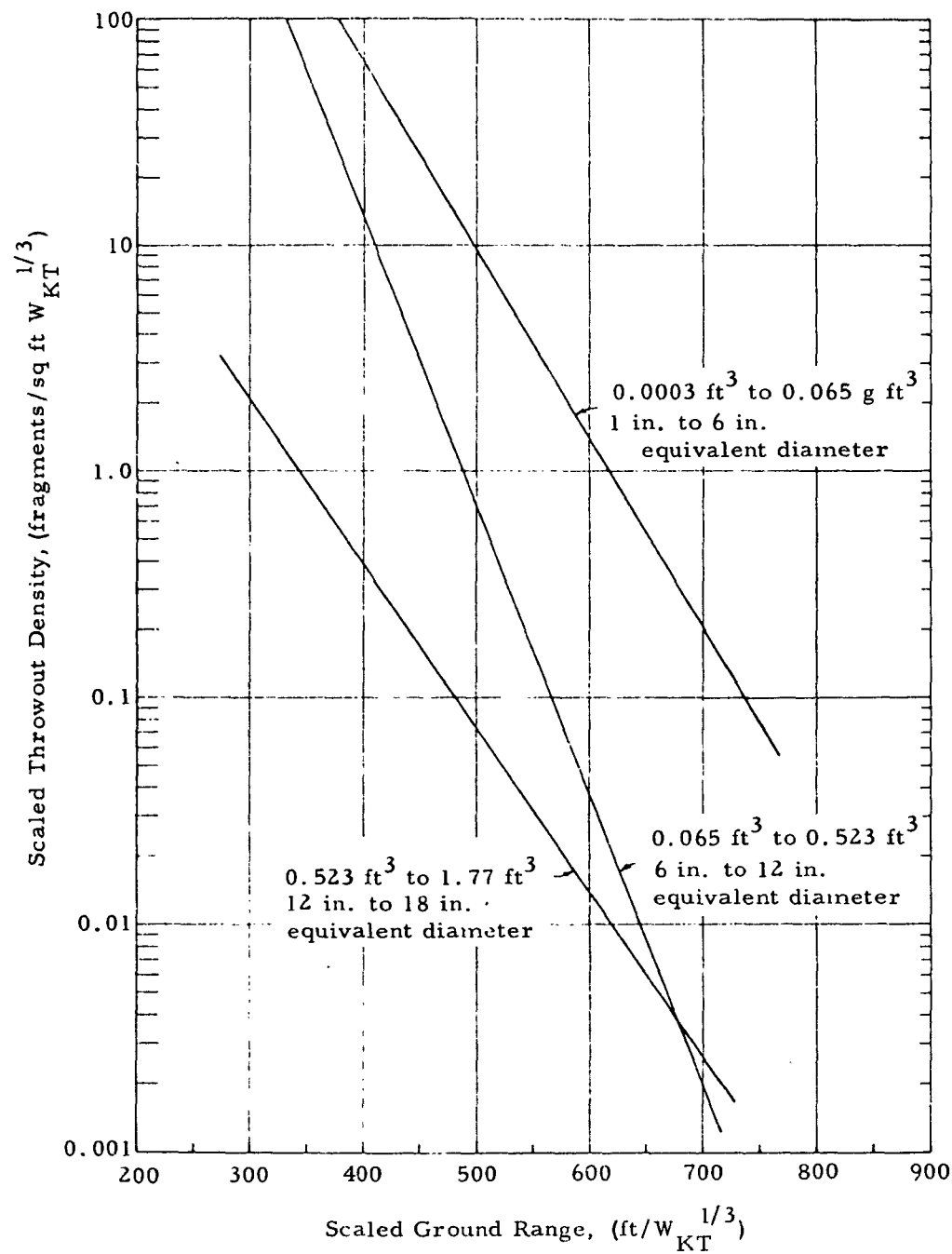


Figure J-5 Debris Density for 1-KT Weapon Based on DANNY BOY Results

SECRET

SECRET

Table J-2
DEBRIS DENSITY FOR ANTENNA SYSTEM LOCATION
AT 4.0 MILES GROUND RANGE
(Based on extrapolation of DANNY BOY data)

Weapon Yield, (MT)	Debris Density, (fragments/sq ft)		
	1 in. to 6 in. Equivalent Diameter (0.0003 to 0.065 ft ³)	6 in. to 12 in. Equivalent Diameter (0.065 to 0.523 ft ³)	12 in. to 18 in. Equivalent Diameter (0.523 to 1.77 ft ³)
10	0.86	0.00037	0.023
20	43.0	0.171	0.610
50	1,260.0	41.3	11.5
100	11,400.0	1,410.0	72.9

Based on the assumptions made with regard to scaling, it is obvious from Table J-2 that debris would pose a major problem. Note that particles of the size shown in Table J-2 were found in the DANNY BOY test. Thus, in applying the results of Table J-2 to antenna vulnerability problems, all three sizes of particles must be considered simultaneously. No attempt was made here to "scale" particle size which probably varies with both weapon yield and soil type.

These results are more severe than those predicted from HE data (Fig. J-2). Recall, however, that the number of fragments was scaled up by only the optimistic cube-root-of-yield scaling. Therefore, we feel the Table J-2 results are more significant.

J-3 Estimates Based on Analytical Studies

A completely analytical treatment of this problem depends primarily on a mathematical model to treat the crater formation problem. Such an analysis gives initial velocity vectors of material or particles leaving the crater, and the subsequent motion of these particles can be followed by means of standard trajectory analysis. We use a crater model devised at the RAND Corporation and then compute debris density at ranges from ground zero. The RAND model is first discussed, the trajectory analysis

SECRET

SECRET

is then presented, and finally, results are presented which are applicable to antenna systems.

J-3.1 Application of the RAND Crater Model

Brode and Bjork studied the formation of a crater resulting from a 2-MT weapon surface burst, assuming the material in the crater zone to be rock (tuff). Their interest was primarily in the early period of the crater formation when the pressure acting on the rock medium is very much greater than the shear strength of the rock. They, therefore, assumed the hydrodynamic model valid and numerically integrated the appropriate field equations. Pressure and velocity fields in the crater zone are presented. The velocity fields are reproduced here as Fig. J-6 through J-9.

The RAND model is formulated in Eulerian coordinates so that the velocity vectors represent the velocity of the mass currently at the point in space indicated by the base of the vector. It is therefore not possible from the available data to rigorously follow the motion of a specific mass of crater material. Rather we used these data by assuming that the peak velocity at each point in the crater is the initial velocity of the mass at that point.

A grid was established to roughly cover the crater and the data of Fig. J-6 through J-9 were used to determine peak velocities at each point of grid. The grid is shown in Fig. J-10 with grid points identified. The velocity vectors which are most severe from the viewpoint of throwout were selected; the resulting velocities are shown in Table J-3.

SECRET

SECRET

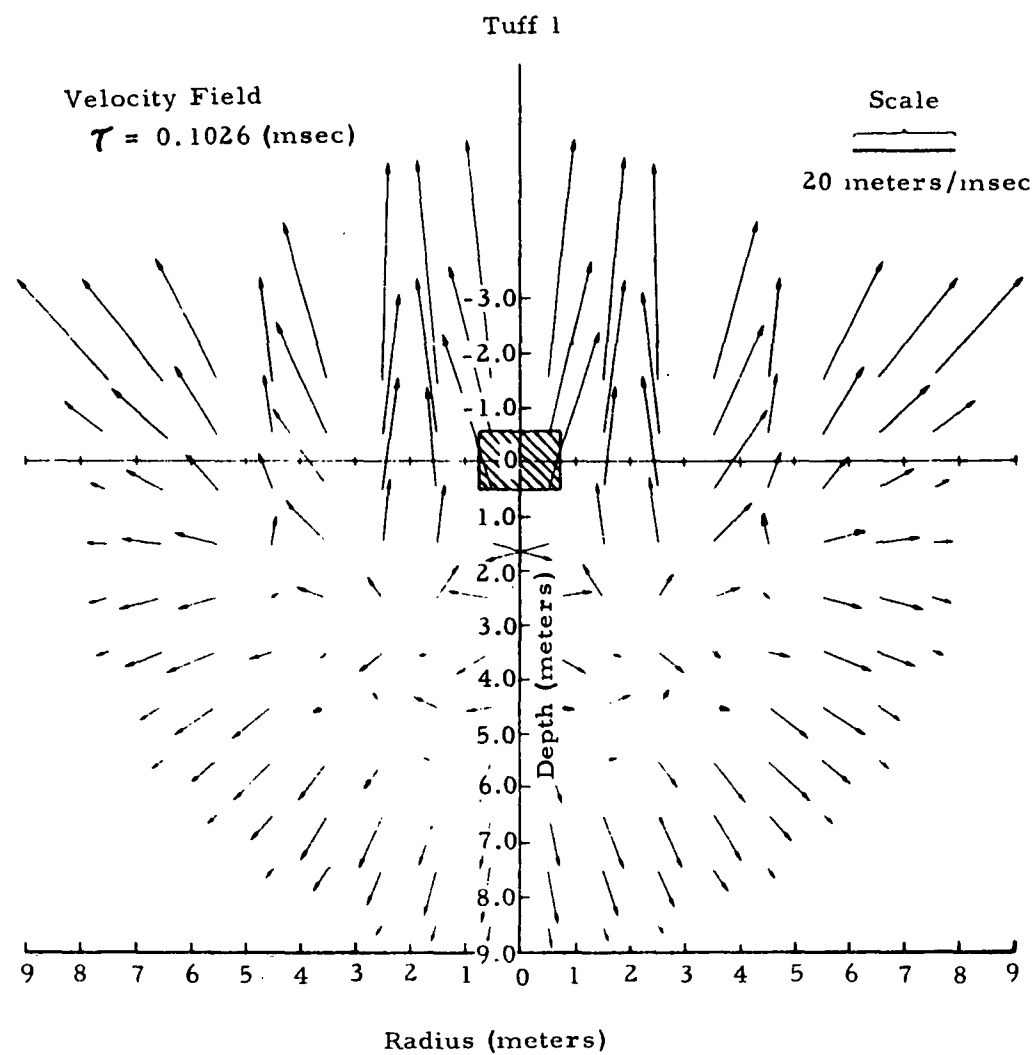


Figure J-6 Velocity Field in Crater ($\tau = 0.1026$ msec)

SECRET

SECRET

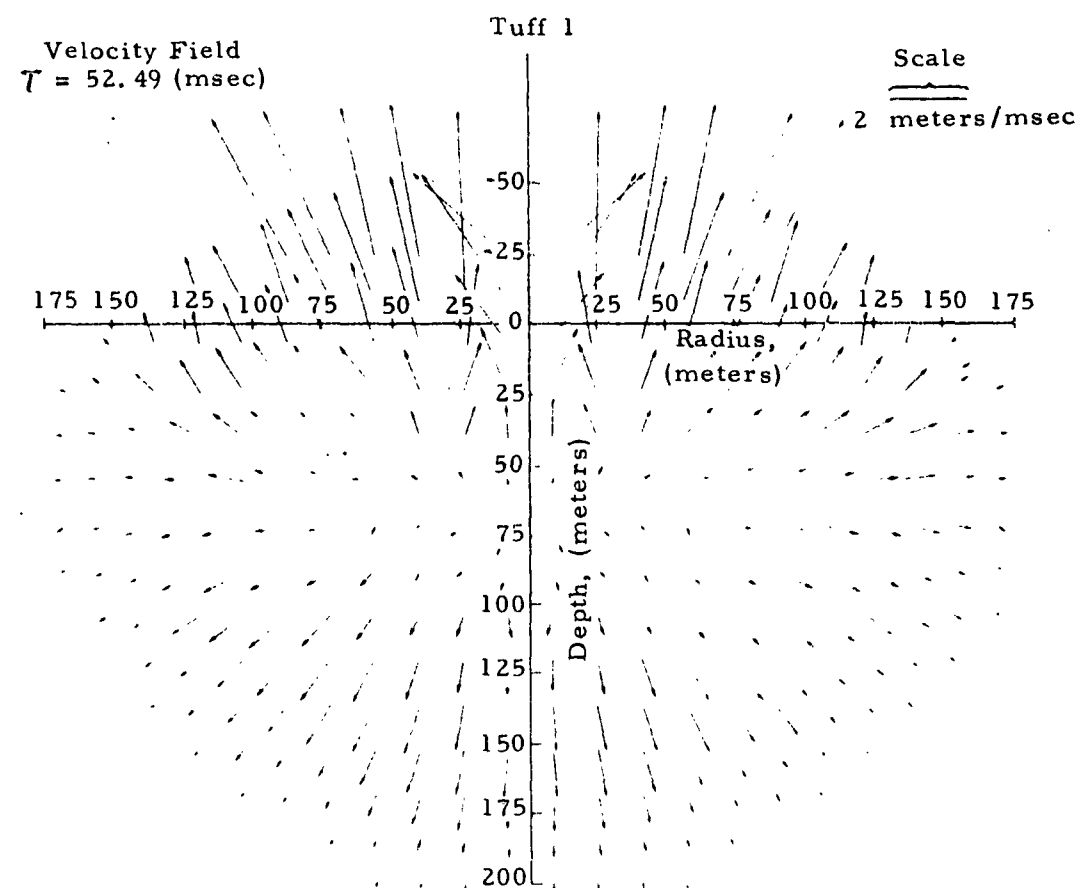


Figure C-7 Velocity Field in Crater ($\tau = 52.49$ msec)

SECRET

SECRET

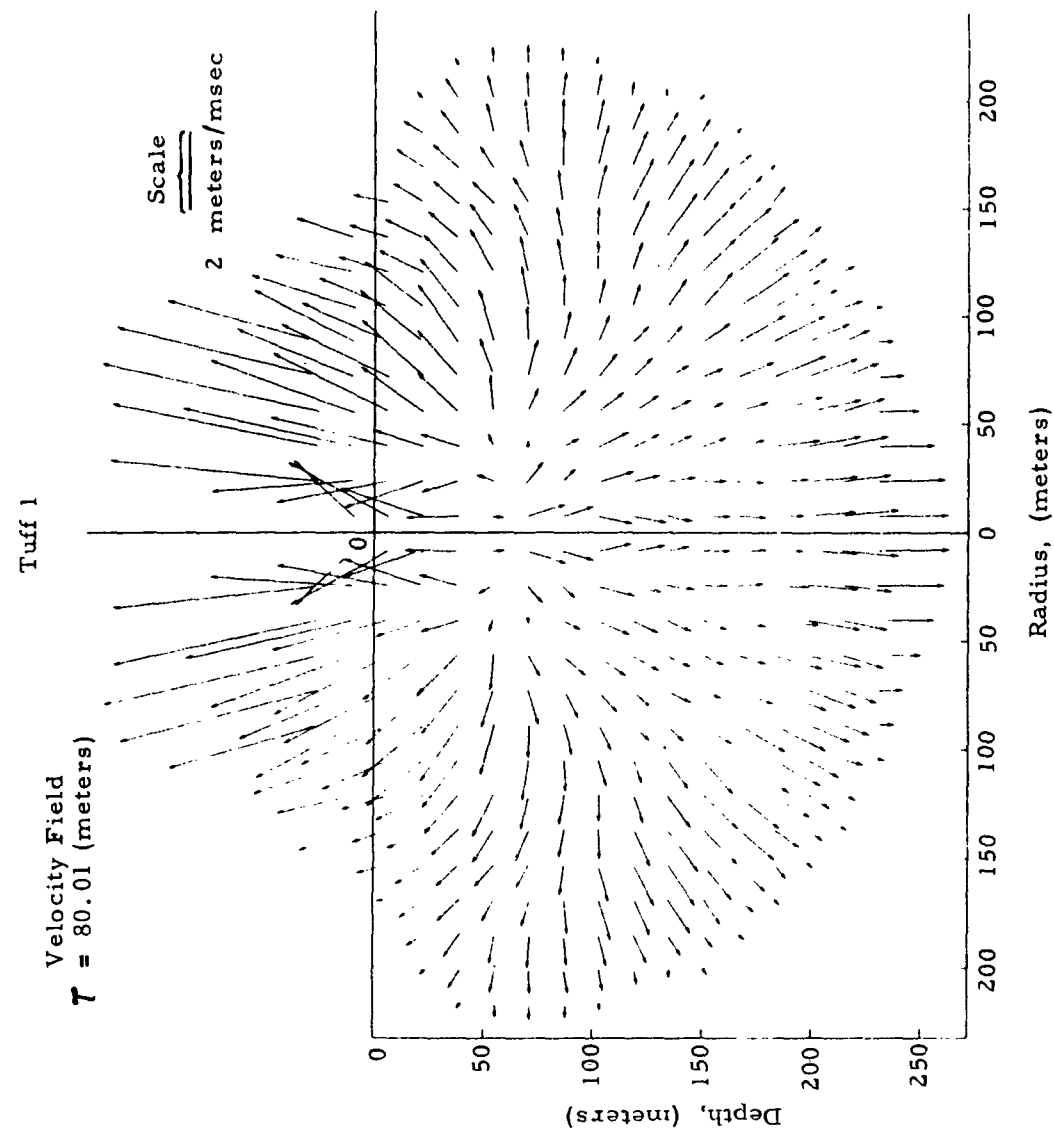


Figure J-8 Velocity in Crater ($\tau = 80.01$ msec)

SECRET

SECRET

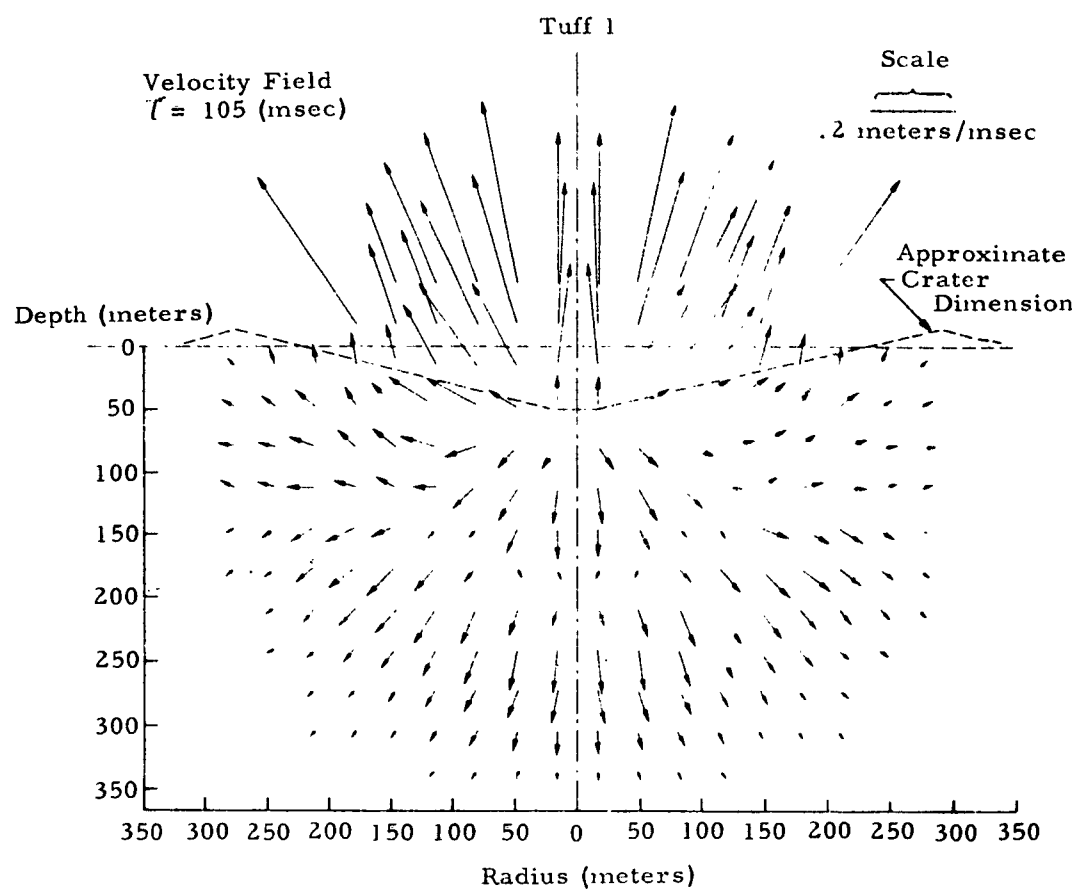
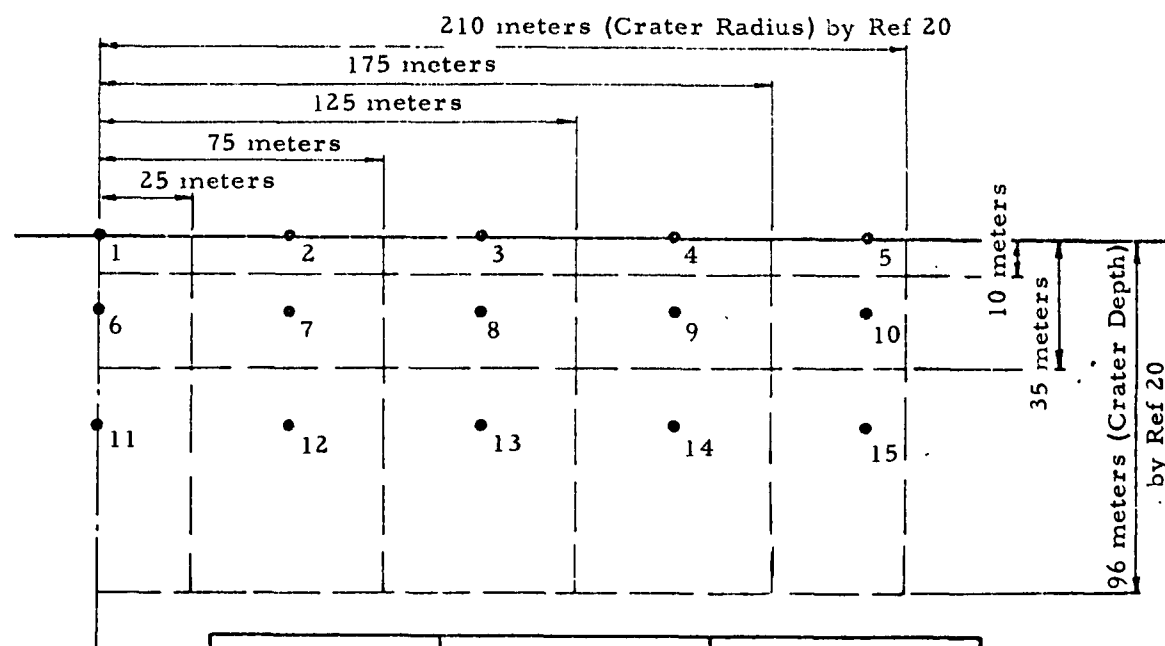


Figure J-9 Velocity Field in Crater ($T = 105$ msec)

SECRET

SECRET



Ring	Volume (cu meters)	Volume (cu ft)
1	1.96×10^4	11.8×10^5
2	15.6×10^4	94.0×10^5
3	31.7×10^4	191×10^5
4	46.7×10^4	281×10^5
5	42.6×10^4	257×10^5
6	2.94×10^4	17.7×10^5
7	23.4×10^4	141×10^5
8	47.6×10^4	287×10^5
9	70.0×10^4	422×10^5
10	64.0×10^4	386×10^5
11	11.9×10^4	71.6×10^5
12	95.0×10^4	572×10^5
13	193.2×10^4	1164×10^5
14	284.0×10^4	1710×10^5
15	260.0×10^4	1566×10^5

Figure J-10 Crater Divisions

SECRET

SECRET

Table J-3
INITIAL TABLE VELOCITY

Grid Point (see Fig. J-10 for Lo- cation in Crater)	Initial Horizontal Velocity, (meters/msec)	Initial Vertical Velocity, (meters/msec)
1	0.20	0.30
2	0.13	0.53
3	0.16	0.31
4	0.08	0.20
5	0.24	0.36
6	0.40	0.20
7	0.12	0.20
8	0.09	0.14
9	0.03	0.10
10	0.01	0.08
11	0.10	0.10
12	0	0
13	0	0
14	0	0
15	0	0

The velocity data in Table J-3 were used as the initial velocities in computing debris particle trajectories. Because the hydrodynamic model does not predict debris fragment size, trajectories were computed for a range of particle sizes.

J-3.2 Trajectory Analysis

Consider the motion of a particle through a medium such that the drag force acting on the particle is proportional to the square of the relative velocity between the particle and the air. It is assumed that the vertical and horizontal motion of the debris particle are decoupled. This is true if the center of pressure of the particle coincides with its centroid for all orientations so that no rotation occurs.

The equations of motion are then

$$\ddot{x} = \frac{k a \rho}{2} (u - \dot{x})^2 \quad (J-3)$$

$$\ddot{y} = \frac{k' a \rho}{2} \dot{y}^2 + g \quad (J-4)$$

SECRET

SECRET

where

x = horizontal coordinate

y = vertical coordinate, positive downward

$(\dot{})$ = differentiation with respect to time

a = aerodynamic coefficient, $\frac{(\text{projected area} \times \text{drag coefficient})}{\text{mass}}$

ρ = mass density of air

u = air particle velocity

g = gravitational constant

$$k = \begin{cases} +1 & ; u > x \\ -1 & ; u \leq x \end{cases}$$

$$k' = \begin{cases} +1 & ; y \leq 0 \\ -1 & , y > 0 \end{cases}$$

These are Riccati-type nonlinear differential equations, and can be linearized by a simple transformation of coordinates.

The horizontal equation of motion (J-3) can be linearized by the substitution,

$$x = -\frac{2}{k a \rho} \frac{\dot{s}}{s} \quad (\text{J-5})$$

Note that $x = -\frac{2}{k a \rho} \log_e s$,

thus,

$$\ddot{s} + k a \rho u \dot{s} + \frac{k^2 a^2 \rho^2}{4} u^2 s = 0. \quad (\text{J-6})$$

Equation (J-6) is a linear differential equation with variable coefficients because of the variation of particle velocity u and air density ρ with time. This could be numerically integrated but, because of our interest in relatively large times, the computation time would be prohibitive, and the resulting cumulative error undoubtedly sizable. Equation (J-6) is therefore solved by assuming that u and ρ are constant over an interval of time. The solution can then be extended in time by matching initial

SECRET

SECRET

conditions after each interval of time, and then changing u and ρ to a new constant value for the next interval. If u is constant, Eq. (J-6) has a solution

$$s = (C_1 + C_2 t) \exp \left[- \frac{u a \rho k}{2} t \right] \quad (J-7)$$

where

C_1 and C_2 are constants of integration.

The vertical equation-of-motion Eq. J-4 can be linearized by the substitution,

$$y = - \frac{2}{k' a \rho} \frac{\dot{z}}{z} \quad (J-8)$$

Then

$$y = - \frac{2}{k' a \rho} \log_e z \quad (J-9)$$

Then reduced equation then becomes,

$$\ddot{z} + k' \frac{a \rho g}{2} z = 0 \quad (J-10)$$

Recalling that $k' = +1$ for $y \leq 0$ and $k' = -1$ for $y > 0$, Eq. J-10 has the solution,

$$z = C_3 \cos \sqrt{\frac{a \rho g}{2}} t + C_4 \sin \sqrt{\frac{a \rho g}{2}} t \quad (J-11)$$

for $\dot{y} \leq 0$ (i. e., on way up)

and

$$z = C_5 \exp \left[\sqrt{\frac{a \rho g}{2}} t \right] + C_6 \exp \left[- \sqrt{\frac{a \rho g}{2}} t \right]$$

for $y > 0$ (i. e., on way down).

Equations (J-11) are used to compute the total time of flight for the particles, and then the total horizontal distance traveled is determined from the value of s , as computed from Eq. (J-7) at the time the particle hits the ground.

SECRET

SECRET

J-3.3 Numerical Results

The simultaneous solution of Eq. (J-6) and (J-11) was carried out on the UNIVAC 1105 digital computer. The initial velocities presented in Table J-3 were used as initial conditions and solutions were obtained for 1-in., 6-in., and 12-in. diameter particles.

The analytic forms of the weapon parameters used in the computer program are taken from reference 20. The actual values as taken from the computer program for a 20-MT weapon are plotted in Fig. J-11. For lack of better data, the close-in values for overpressure shock velocity and particle velocity were taken to be constant from ground zero out to a scaled ground range of 100 ft.

Solutions were obtained for particle velocity and air density assumed to be constant in 0.25-sec and 0.1-sec intervals. The numerical results differed by less than 2 percent so the computer runs were finally made using the 0.25-sec interval. Numerical results for flight time, horizontal distance traveled and final velocity are given in Table J-4.

These data were then converted to fragment density values. Consider the crater to be broken up into annular rings as shown in Fig. J-10. The material in each of the three horizontal layers was first distributed over the impact area. This was done by assuming that the material from each ring is spread at constant depth over a radial distance equal to the difference in the computed maximum trajectory distance of adjacent points. The fragment density in that region is then given as

$$N = \frac{V}{\frac{4}{3} \pi r_f^3} \frac{1}{\pi(r_o^2 - r_i^2)} \quad (J-12)$$

where

- N = fragment density
- V = volume in crater as given in Fig. J-10
- r_f = fragment radius
- r_o = outer radial distance for ring of interest
- r_i = inner radial distance for ring of interest.

SECRET

SECRET

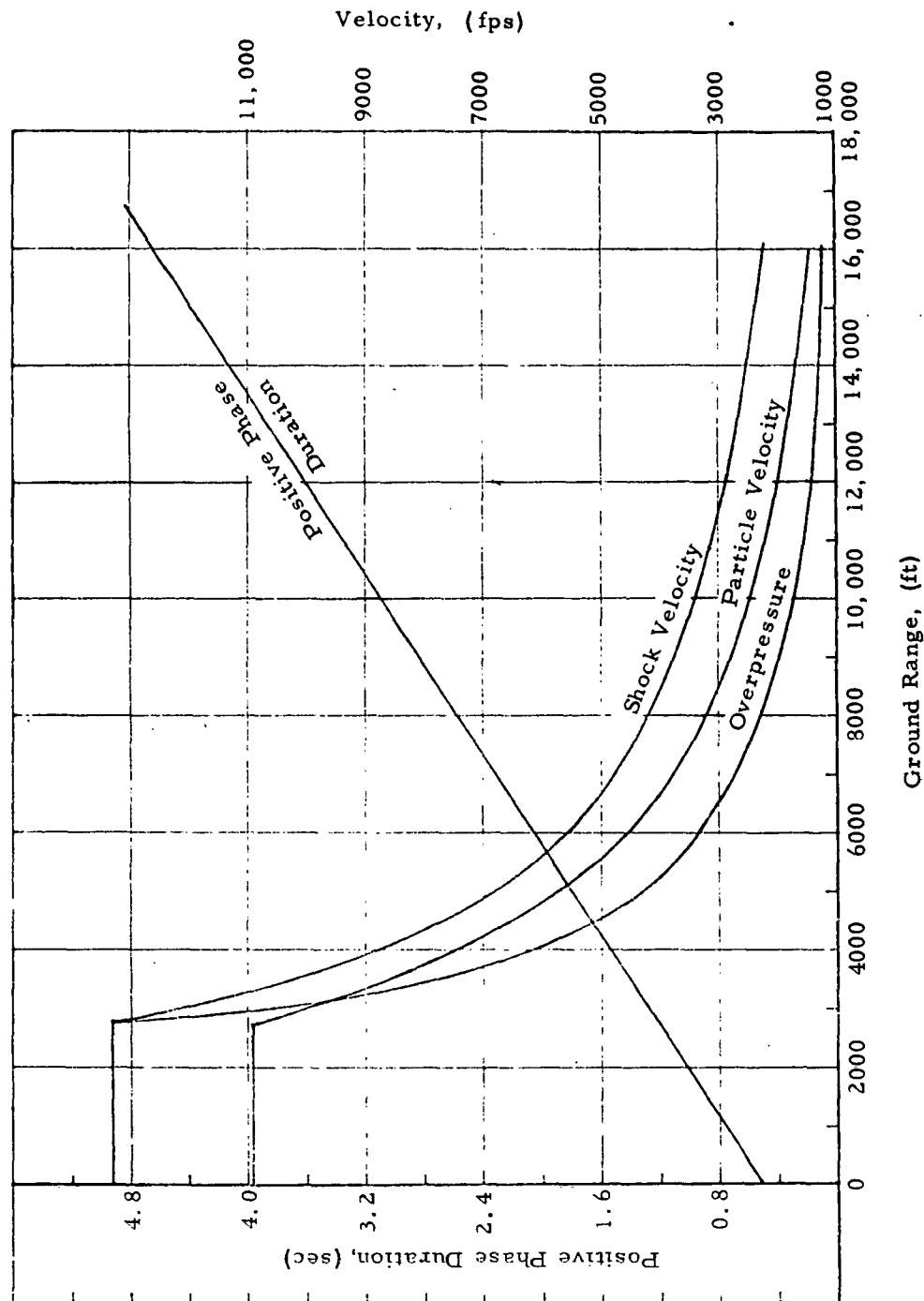


Figure J-11 Weapon Parameter for 20-MT Weapon

SECRET

SECRET

Table J-4
TRAJECTORY ANALYSIS FOR DATA FOR 20-MT WEAPON

Point in Crater (See Fig. J-10 for location)	One-Inch Particles			Six-Inch Particles			Twelve-Inch Particles		
	Final Location, (miles)	Final Velocity, (fps)	Flight Time, (sec)	Final Location, (miles)	Final Velocity, (fps)	Flight Time, (sec)	Final Location, (miles)	Final Velocity, (fps)	Flight Time, (sec)
1	2.9	1943	12.9	5.1	709	25.7	7.0	507	33.2
2	3.5	2131	14.4	5.5	723	29.4	7.5	504	38.4
3	2.9	1972	12.9	5.1	710	25.9	7.0	510	33.5
4	2.5	1611	11.8	4.6	705	23.1	6.6	532	29.6
5	3.0	2069	13.3	5.2	711	26.9	7.3	498	34.9
6	2.4	1580	11.8	4.6	696	23.1	7.0	505	29.6
7	2.5	1607	11.8	4.7	704	23.1	6.6	529	29.6
8	2.2	1336	10.9	4.4	702	20.8	6.2	553	26.3
9	2.1	1137	10.0	4.0	703	18.7	5.9	585	23.3
10	2.0	1137	10.0	4.0	703	18.7	5.9	586	23.2
11	2.0	1132	10.0	4.0	701	18.7	5.9	583	23.2

SECRET

SECRET

The effects of the three layers were then added.

The results of Table J-4 were then transposed to fragment density-distance curves and, for consistency, scaled down to a 1-KT weapon (both the range and fragment density were scaled as the cube root of yield). The result is plotted on Fig. J-12. It should be emphasized that the particle sizes on Fig. J-12 are not predicted by the model. Figure J-12 represents three solutions assuming that all of the crater material breaks up into the same size particles. Therefore, only one of the three curves in Fig. J-12 should be used at one time. This can be compared with the DANNY BOY results in Fig. J-5. The dashed line drawn in Fig. J-12 is from the DANNY BOY results, assuming that all debris fragments break up into one-inch radius particles. It is not surprising that the RAND model gives more severe results because of the assumed hydrodynamic behavior of the soil and the neglect of in-flight collisions between debris particles.

An interesting result was obtained while studying the trajectories of the debris leaving the crater. The total flight distance was found to be independent of the initial horizontal velocity component for the range of horizontal velocities predicted by the RAND model. In other words, the horizontal motion is determined completely by the blast winds for large weapons. The initial vertical velocity, of course, determines the time of flight upon which the total throw of a particle is very dependent. Based on this brief analysis, it appears that for a megaton-yield weapon, the surface burst (or perhaps partially buried burst) results in the most severe debris problem.

J-4 General Consistency of Results

Crater throwout debris was studied with particular emphasis on predicting its severity to antenna systems. The state-of-the-art is such that a completely reliable evaluation of this problem was not possible. The objective here was to examine available experimental data and analyses to establish bounds on the magnitude of the problem for antenna systems. First, the voluminous data which exist on debris resulting from high explosive detonation were studied. Results are presented in Fig. J-1 and Table J-1. It can be seen that the maximum missile distances predicted

SECRET

SECRET

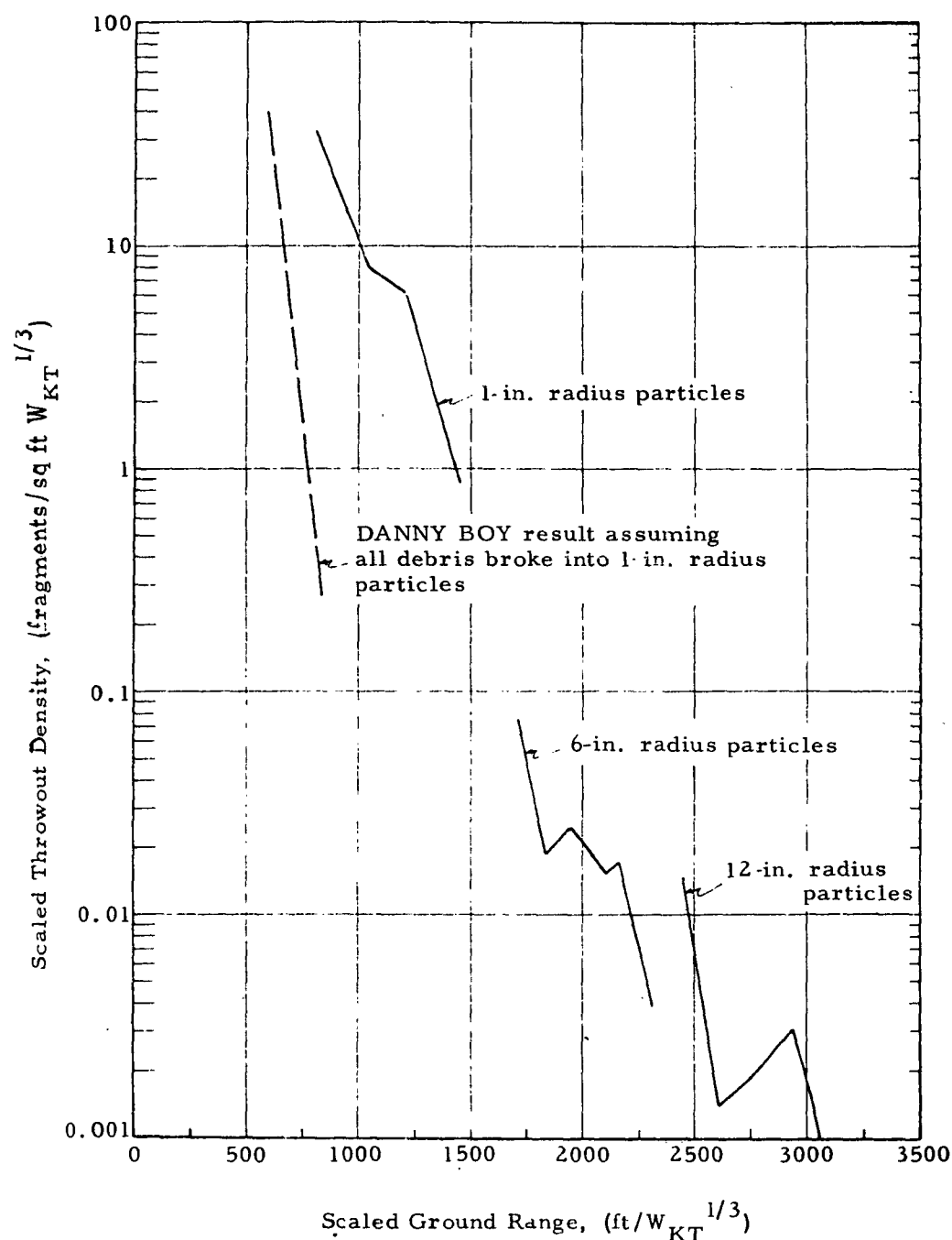


Figure J-12 Debris Density for 1-KT Weapon Based on Brode's Model of Crater Formation

SECRET

SECRET

are beyond likely antenna locations, and that at expected antenna locations the debris density is quite high. Secondly, the results of the DANNY BOY nuclear test are extrapolated to make predictions for antenna systems. It is assumed that both distance and fragment density scale as the cube root of yield. The resulting fragment density-distance curve for a 1-KT weapon is shown in Fig. J-5. This can be readily scaled up to real antenna situations and again a severe debris problem is predicted. Third, a completely analytical solution was obtained by following the motion of a particle from the crater to impact with the ground. Brode's hydrodynamic model was used for the crater formation phase of the motion. The resulting debris density-distance relationships, which indicated a relatively severe debris problem for expected antenna locations, are shown in Fig. J-12.

Therefore, while no conclusive evaluation of the problem was possible, all available data point to a very critical debris problem for antenna systems. There are two possible approaches to the design of antenna systems insofar as the debris problem is concerned.

First, locations could be restricted to those where the debris density was at a specified low level. Secondly, some degree of hardness could be provided against debris particles. At first look this would seem a most challenging task. The debris will have terminal velocities very close to the particle velocity, which can well be over 1000 fps. At these velocities it seems apparent that even quite small debris particles would be capable of damaging any fragile critical elements.

Certainly much has yet to be learned about the crater throwout problem. The soil type, depth of burial, and yield must all have some effect. None of this is understood at present. The results presented here are all based on a rock-like crater material. The debris particle size must certainly be a function of soil type. A sandy material should produce very small fragments that would tend to sand blast rather than fracture antenna elements. Also, as can be seen from Table J-4 sand would not be transported as far as a soil which breaks into large fragments.

SECRET

SECRET

The extremes of depth of burial were included in this study. DANNY BOY represents a completely buried shot at optimum depth* whereas the Brode crater model is for a surface burst. As remarked earlier, it appears that the surface burst will give the more critical debris problem for megaton range weapons.

The dependence on weapon yield (scaling) represents perhaps the most important unknown. Most of our results depend on an assumed cube-root-of-yield scaling law, although the analytical results were only scaled up from a two-megaton weapon.

Perhaps the most surprising result of this study is the consistency of the results of the three methods studied when so many unknown factors exist. This leads to some degree of confidence in the predictions of the study.

* Optimum depth of burial is that depth which produces maximum volume of apparent crater. It results in ejecta having trajectories with pronounced vertical components.

SECRET

UNCLASSIFIEDDISTRIBUTION LIST

Copies of this report are being distributed as follows.

<u>Copy No.</u>	<u>Recipient</u>	<u>Copy No.</u>	<u>Recipient</u>
1	Chief of Research and Development D/A Washington 25, D. C. Attn: Atomic Division	19	Commanding General USA Missile Command Huntsville, Alabama
2-4	Chief of Engineers D/A Washington 25, D. C. Attn: ENG CW-NE ENGTE-E ENGMC-E	20	Commanding General USA Munitions Command Dover, New Jersey
5-6	Commanding General U. S. Army Material Command Washington, D. C. Attn: AMCRD-DE-N	21	Commanding Officer U. S. Army Corps of Engineers Beach Erosion Board Washington, D. C.
7	Commanding General U. S. Continental Army Command Ft. Monroe, Virginia	22	Commanding Officer U. S. Army Nuclear Defense Laboratory Edgewood Arsenal Edgewood, Maryland Attn: Tech. Library
8	President U. S. Army Air Defense Board Ft. Bliss, Texas	23	Director Waterways Experiment Station U. S. Army Corps of Engineers Vicksburg, Mississippi Attn: Library
9	Commandant Command & General Staff College Ft. Leavenworth, Kansas Attn: Archieves	24	Director U. S. Army Corps of Engineers Nuclear Cratering Group Livermore, California
10	Commandant U. S. Army Air Defense School Ft. Bliss, Texas Attn: Command and Staff Dept.	25-26	Chief of Naval Operations ND Washington 25, D. C. Attn: OP-75 Attn: OP-03EG
11	Director Special Weapons Development Hq, CDC Ft. Bliss, Texas Attn: Chester I. Peterson	27	Director of Naval Intelligence ND Washington 25, D. C. Attn: OP-922V
12	Commanding General Aberdeen Proving Ground Aberdeen, Maryland Attn: Director, BRL	28	Director of Naval Intelligence ND Washington 25, D. C. Attn: OP-922V
13	Commanding General The Engineer Center Ft. Belvoir, Virginia Attn: Asst. Commandant, Engineer School	29-31	Chief Bureau of Naval Weapons ND Washington 25, D. C. Attn: F-121
14	Director U. S. Army Research and Development Laboratory Ft. Belvoir, Virginia Attn: Chief, Tech. Support Branch	32-33	Chief Bureau of Ships ND Washington 25, D. C. Attn: Code 372 Code 423
15	Commanding Officer U. S. Army Mobility Command Center Line, Michigan	34-35	Chief Bureau of Yards and Docks ND Washington 25, D. C. Attn: Code D-400 Code D-440
16	Commanding Officer Picatinny Arsenal Dover, New Jersey Attn: SMUPA-VC1	36	Chief of Naval Research ND Washington 25, D. C. Attn: Code 811
17	Commanding Officer Transportation Research Command Ft. Eustis, Virginia Attn: Chief, Tech. Info. Div.	37	Commander-in-Chief U. S. Pacific Fleet FPO San Francisco, California
18	Commanding General USA Electronic R&D Lab. Ft. Monmouth, New Jersey Attn: Technical Documents Center Evans Area	38	Commander-in-Chief U. S. Atlantic Fleet U. S. Naval Base Norfolk 11, Virginia

UNCLASSIFIED

UNCLASSIFIED

<u>Copy No.</u>	<u>Recipient</u>	<u>Copy No.</u>	<u>Recipient</u>
39-42	Commandant of the Marine Corps ND Washington 25, D. C. Attn: Code A03H	60	Hd, USAF (AFDRC/NE - Maj. Lowry) Washington 25, D. C.
43	President U. S. Naval War College Newport, Rhode Island	61	Hq, USAF (AFIAS-G-2) Washington 25, D. C.
44	Superintendent U. S. Naval Postgraduate School Monterey, California	62	Deputy Chief of Staff Plans and Programs Hq USAF Washington 25, D. C. Attn: War Plans Division
45	Commanding Officer Nuclear Weapons Training Center Atlantic, Naval Base Norfolk 11, Virginia Attn: Nuclear Warfare Dept.	63	Director of Research and Development DCS/D Hq USAF Washington 25, D. C. Attn: Guidance & Weapons Division
46	Commanding Officer U. S. Naval Schools Command U. S. Naval Station Treasure Island San Francisco, California	64	Air Force Intelligence Center Hq USAF ACS/I (AFCIN-3K2) Washington 25, D. C.
47-48	Commanding Officer Nuclear Weapons Training Center Pacific, Naval Station North Island San Diego 35, California	65	Commander-in-Chief Strategic Air Command Offutt AFB, Nebraska Attn: OAWS
49	Commanding Officer U. S. Naval Damage Control Training Center Naval Base Philadelphia 12, Pennsylvania Attn: ABC Defense Course	66	Commander Tactical Air Command Langley AFB, Virginia Attn: Document Security Branch
50-52	Commander U. S. Naval Ordnance Laboratory Silver Spring 19, Maryland Attn: EA EU E	67	ASD Wright Patterson AFB Ohio
53	Commander U. S. Naval Ordnance Test Station China Lake, California	68-70	Commander Air Force Logistics Command Wright-Patterson AFB, Ohio Attn: MCASS
54	Commanding Officer & Director U. S. Naval Civil Engineering Laboratory Port Hueneme, California Attn: Code L31	71-72	AFSC Andrews Air Force Base Washington 25, D. C. Attn: RDRWA SCIZ
55	Director U. S. Naval Research Laboratory Washington 25, D. C.	73-74	Director Air University Library Maxwell AFB, Alabama
56	Commanding Officer & Director Naval Electronics Laboratory San Diego 52, California	75	AFCLR L. G. Hanscom Field Bedford, Massachusetts Attn: CRQST-2
57	Commanding Officer U. S. Naval Radiological Defense Laboratory San Francisco, California Attn: Tech. Info. Division	76	AFSWC (SWRS) Kirtland Air Force Base New Mexico
58	Commanding Officer & Director David W. Taylor Model Basin Washington 7, D. C. Attn: Library	77	Commandant Institute of Technology Wright-Patterson AFB, Ohio Attn: MCLI-ITRIDL
59	Underwater Explosions Research Division DTMB Norfolk Naval Shipyard Portsmouth, Virginia	78	BSD Norton AFB, California
		79	Director USAF Project Rand, Via: U. S. Air Force Liaison Office The Rand Corporation 1700 Main Street Santa Monica, California

UNCLASSIFIED

UNCLASSIFIED

<u>Copy No.</u>	<u>Recipient</u>	<u>Copy No.</u>	<u>Recipient</u>
80	Director of Civil Engineering Hq USAF Washington 25, D. C. Attn: AFOCE	115	Officer-in-Charge U. S. Naval School Civil Engineering Corps Officers U. S. Naval Construction Battalion Port Hueneme, California
81	Hqs, Ogden Air Materiel Area Hill AFB, Utah Attn: Mr. Harry D. Mytinger	116	Los Alamos Scientific Laboratory P. O. Box 1663 Los Alamos, New Mexico Attn: Report Librarian (for Dr. A. C. Graves)
82	Hqs, Space Systems Division USAF AF Unit Post Office Los Angeles 45, California Attn: Mr. Earl I. Shain	117-118	Administrator National Aeronautics & Space Administration 1512 H Street, N. W. Washington 25, D. C. Attn: Mr. G. D. McCanley NASA Safety and Health Officer
83	Hqs, Air Proving Ground Center Eglin AFB, Florida Attn: PGBME	119	Langley Research Center NASA Langley Field Hampton, Virginia Attn: Mr. Philip Donely
84	Director of Defense Research & Engineering Washington 25, D. C. Attn: Tech. Library	120	Chief, Classified Technical Library Technical Information Service U. S. Atomic Energy Commission Washington 25, D. C. Attn: Mrs. Jean O'Leary (for Dr. Paul C. Fine)
85	U. S. Documents Officer Office of the United States National Military Representative-SHAPE APO-55 New York, New York	121	Chief, Classified Technical Library Technical Information Service U. S. Atomic Energy Commission Washington 25, D. C. Attn: Mrs. Jean O'Leary
86	Commander-in-Chief Pacific, Fleet Post Office San Francisco, California	122	Dr. Walker Bleakney Forestal Research Center Library Aeronautical Sciences Building Princeton University Princeton, New Jersey Attn: Librarian
87	Director Weapons Systems Evaluation Group OSD, Room 1E880 The Pentagon Washington 25, D. C.	123	Manager Albuquerque Operations Office U. S. Atomic Energy Commission P. O. Box 5400 Albuquerque, New Mexico
88	Commandant Armed Forces Staff College Norfolk 11, Virginia Attn: Library	124	Dr. Robert J. Hansen Division of Industrial Cooperation Massachusetts Institute of Technology 77 Massachusetts Avenue Cambridge, Massachusetts (Send TS to 244 Wood St., Lexington, Mass.)
89-104	Commander Field Command, DASA Sandia Base Albuquerque, New Mexico	125	Dr. Bruce G. Johnston The University of Michigan University Research Security Office Lobby 1, East Engineering Building Ann Arbor, Michigan (Do not sent TOP SECRET to this addressee)
105-106	Commander Field Command, DASA Sandia Base Albuquerque, New Mexico Attn: FCWT FCTG	126	Sandia Corporation Sandia Base Albuquerque, New Mexico Attn: Classified Document Division (for Dr. M. L. Merritt)
107-111	Chief Defense Atomic Support Agency Washington 25, D. C.	127	Dr. Nathan M. Newmark University of Illinois Room 207, Talbot Laboratory Urbana, Illinois (No TOP SECRET to this addressee)
112	Commandant Army War College Carlisle Barracks, Pennsylvania Attn: Library	128-147	Defense Documentation Center (DDC) Arlington Hall Station Arlington 12, Virginia Attn: TISIA-21 (No TOP SECRET to this addressee)
113	Commandant National War College Washington 25, D. C. Attn: Class Rec. Library		
114	Commandant The Industrial College of the Armed Forces Ft. McNair Washington 25, D. C.		

UNCLASSIFIED

UNCLASSIFIED

<u>Copy No.</u>	<u>Recipient</u>
148	Holmes & Narver, Inc. AEC Facilities Division 849 South Broadway Los Angeles 14, California Attn: Mr. Frank Galbreth
149	Professor Robert V. Whitman Massachusetts Institute of Technology Room 1-343 Cambridge 39, Massachusetts
150	Mr. Kenneth Kaplan United Research Services 1811 Trousdale Drive Burlingame, California
151	Stanford Research Institute Menlo Park, California Attn: Dr. Rubin
152	Dr. Robert C. DeHart Southwest Research Institute Post Office Box 28281 San Antonio 6, Texas
153	Dr. Neidhardt General American Transportation Corporation 7501 N. Natchez Avenue Niles, Illinois
154	Mr. J. Baston Space Technology Laboratories, Inc. 5500 West El Segunda Blvd. Los Angeles 45, California
155	Dr. Frank Shelton Kaman Nuclear Colorado Springs, Colorado
156	The Lovelace Foundation 4800 Gibson Boulevard, S. E. Albuquerque, New Mexico Attn: Document Librarian
157	Sandia Corporation P. O. Box 969 Livermore, California Attn: Mr. Mesnard
158	Aerojet-General Corporation 11711 South Woodruff Avenue Downey, California Attn: Mr. Glenn L. Roark Dept. 1312, Downey-Cleta Facility Propellant Physics Dept.
159-160	The Boeing Company Seattle 24, Washington Attn: Mr. Glen T. McNew Mr. W. E. Crist, Jr.
161	United Technology Center P. O. Box 358 Sunnyvale, California Attn: Mr. Gerald Conch
162-163	Office of Civil Defense (OCD) Washington 25, D. C.
164-165	Armed Services Explosives Safety Board Building TEMPO-7, 2073 Gravelly Point, Virginia

UNCLASSIFIED